UNIVERSITY OF SOUTHAMPTON

Mode-Locked Vertical-External-Cavity Surface Emitting Lasers

by

Hannah D. Foreman

A thesis submitted in partial fulfillment for the degree of Doctor of Philosophy

in the

Faculty of Engineering, Science and Mathematics

School of Physics and Astronomy

November 2006

UNIVERSITY OF SOUTHAMPTON

ABSTRACT

FACULTY OF ENGINEERING, SCIENCE AND MATHEMATICS
SCHOOL OF PHYSICS AND ASTRONOMY

Doctor of Philosophy

by Hannah D. Foreman

Vertical-external-cavity surface-emitting lasers (VECSELs) incorporate a semiconductor-based gain chip within an external cavity to form a unique category of laser. These devices draw upon the advantages of both semiconductor diode lasers; with broad gain bandwidths, spectral flexibility with design, and inexpensive fabrication, and the solid state laser family; with functional versatility provided by the external cavity, high power operation enabled by optical pumping, and high beam quality even at high powers. Following the important achievement of mode-locking of using a semiconductor saturable-absorber mirror (SESAM), this thesis is an experimental investigation of the further development and application of VECSELs emitting at wavelengths around 1 μm.

In the work presented here, the fabrication of VECSEL chips to optimise their performance is investigated: satellite pulses in the autocorrelation of a ML-VECSEL pulse are eliminated through back-surface polishing of gain and SESAM chips and thermal management of VECSELs is investigated, concentrating on 2 key approaches; intracavity heatspreader windows, and substrate removal. A ML-VECSEL is used to seed for a high power master-oscillator power amplifier. The seed pulses are amplified to an average power of 184 W with 77% efficiency. Peak powers of 28 kW are demonstrated, and pulse compression to 291 fs is achieved. Finally, development of a micro-imprint lithography method for the realisation of high repetition-rate (>100 GHz) operation of ML-VECSELs is presented. Focusing structures fabricated in GaAs are demonstrated, successfully overgrown and characterised.

Contents

Table of Contents ii

List of Figures vi

Declaration of Authorship x

Acknowledgements xi

1 Introduction 1
1.1 VECSELs: the bridge between the semiconductor diode and solid state lasers . . . 1
1.1.1 VECSEL Wavelength coverage . . . 6
1.1.2 Mode-locking of VECSELs . . . 7
1.2 Introduction to the work in this thesis . . . 8

Bibliography 10

2 Theory of VECSELs 14
2.1 Introduction . . . 14
2.2 VECSEL Active Mirror Design . . . 15
2.2.1 Material Choice . . . 15
2.2.2 Distributed Bragg Reflector . . . 17
2.2.3 Quantum Well Gain Region . . . 20
2.2.3.1 Quantum Wells . . . 20
2.2.3.2 The Microcavity . . . 26
2.3 Structural Properties of VECSELs . . . 27
2.3.1 Microcavity Enhancement Factor . . . 28
2.3.2 Fabry-Perot Sub-Cavity . . . 29
2.3.3 VECSEL Thermal Response . . . 33
2.3.4 Group Delay Dispersion . . . 35
2.4 Mode-Locking VECSELs . . . 36
2.4.1 SESAM Mode-Locking . . . 38
2.4.1.1 SESAM Mode-Locked VECSELs . . . 40
2.4.2 Sub-Picosecond Pulses from a ML-VECSEL . . . 41
2.4.2.1 Optical Stark Effect . . . 42
2.4.2.2 Fast Surface Recombination . . . 43
2.4.2.3 Stark SESAM Design . . . 44
2.4.2.4 Lasing Results . . . 44

2.4.2.5 Stark SESAMs at other wavelengths: a case study 47
2.5 Conclusion 50

Bibliography 51

3 Wafer Characterisation 55
3.1 Introduction 55
3.2 Wafer Growth and Sample Selection 56
3.3 Reflectivity Spectra 57
3.4 Photo-Luminescence Characterisation 59
3.4.1 Edge Photo-Luminescence Spectra 59
3.4.1.1 Thermal Resistance 62
3.4.2 Top Photo-Luminescence Measurements 63
3.4.2.1 Internal Quantum Efficiency 65
3.5 Sample Lasing Properties 68
3.5.1 Slope Efficiency 70
3.5.2 Fixed Losses 72
3.5.3 Characteristic Temperature 73
3.6 SESAM Characterisation 74
3.6.1 SESAM Photo-Luminescence Characterisation 74
3.6.2 Further SESAM Analysis 76
3.7 Conclusions 78

Bibliography 79

4 Wafer Fabrication 81
4.1 Introduction 81
4.2 Substrate Reflections 82
4.2.1 Polishing GaAs 83
4.2.2 Back-Surface Angle-Polished ML-VECSEL Results 87
4.3 Thermal Properties of VECSELs 88
4.3.1 Analytical Model 89
4.4 Heat-Sinking 'As-Grown' Samples 91
4.5 Crystalline Heat-Spreaders 92
4.5.1 Fabricating a Heat-Spreader Device 93
4.5.1.1 Mathematical Model 95
4.5.2 Surface Preparation 96
4.5.3 Direct Bonding Procedure 98
4.5.4 Bonding Results 99
4.5.5 Suitability of heat-spreader devices for mode-locked operation . . . 100
4.6 Substrate Removal as a technique of thermal management in VECSELs . 102
4.6.1 Sample Design for Substrate Removal 103
4.6.2 The Soldering Process 104
4.6.3 Substrate Removal Etching Process 107
4.6.4 Substrate-Removal Results 111
4.7 Conclusions 112

Bibliography 114

5 **Fibre Amplification of VECSEL Pulses** **119**
5.1 Introduction . . . 119
5.2 Yb-Doped Fibre Amplifier Theory . . . 120
5.2.1 Ytterbium Fibre Spectroscopy . . . 120
5.2.2 Pumping Considerations . . . 122
5.2.3 Pumping Geometry . . . 122
5.2.4 Fibre Characteristics . . . 123
5.2.5 Gain Saturation Model . . . 125
5.2.6 Pulse Propagation in Optical Fibre . . . 127
5.2.6.1 Chromatic Dispersion . . . 127
5.2.6.2 Fibre Nonlinearities . . . 128
5.2.7 Amplified Spontaneous Emission . . . 130
5.2.8 Accessing the Parabolic Regime . . . 130
5.3 Preliminary Experiments: 1035 nm VECSEL with near-single-mode YDFA 131
5.3.1 1052 nm VECSEL with Near Single-Mode YDFA . . . 135
5.4 VECSEL-MOPA: 1055 nm VECSEL with near-single-mode cladding pumped power amplifier stage . . . 138
5.4.1 1055 nm VECSEL Seed . . . 138
5.4.2 Pre-Amplifier . . . 140
5.4.3 High Power Amplifier . . . 140
5.4.4 VECSEL-MOPA Results . . . 140
5.4.5 External Pulse Compression . . . 142
5.4.6 Limitations and Damage . . . 146
5.5 Conclusions . . . 148

Bibliography **150**

6 **High repetition rate VECSEL** **153**
6.1 Introduction . . . 153
6.2 Challenges of high repetition rate VECSEL design . . . 154
6.2.1 10 GHz VECSEL . . . 155
6.2.2 Alternative Saturable Absorbers as a route to 50 GHz . . . 156
6.2.3 Limitations above 50 GHz repetition rates . . . 158
6.3 Focussing gain region VECSEL as a route to 100 GHz . . . 160
6.4 Fabricating Optical-Quality Focussing Structures in GaAs Substrates . . . 162
6.4.1 Direct Drilling of GaAs . . . 162
6.4.2 Imprint Lithography . . . 166
6.4.2.1 Imprint Lithography: Historical Aspect . . . 167
6.4.3 Southampton Micro-Imprint Technique . . . 168
6.4.4 Pattern transfer into the GaAs substrate via dry-etching techniques 175
6.4.4.1 Inductively Coupled Plasma (ICP) Etching Method . . . 176
6.4.4.2 Southampton-Sheffield ICP Etch Recipe . . . 178
6.4.4.3 ICP Etch Results . . . 179
6.5 Overgrowth and Characterisation . . . 180
6.5.1 Optical Characterisation of the Overgrown Structure . . . 183
6.6 Focusing Gain Region VECSEL Device Outlook . . . 186
6.6.1 Mode-Locking of the focusing Gain Region VECSEL . . . 186

6.6.1.1 Saturation Fluence Considerations 186
6.6.2 Future steps for the High Repetition Rate Stark ML-VECSEL project 187
6.6.2.1 SESAM Output Coupler 190
6.7 Conclusion 191

Bibliography **193**

7 Conclusions **199**
7.1 Characterisation of VECSEL Samples 199
7.2 Post-Growth Processing of VECSELs 200
7.3 Fibre Amplification of VECSEL Pulses 201
7.4 High Repetition Rate VECSELs 201
7.5 Future Work 202

Bibliography **204**

A Multilayer Calculations **205**

B VECSEL Cavity Design **208**

C Selected Publications **213**

List of Figures

1.1 Schematic drawing of a typical edge emitting semiconductor diode laser . 2
1.2 Diagram showing the geometry of a VCSEL 4
1.3 Schematic of a simple VECSEL cavity 5
1.4 Graph to show the current wavelength coverage of VECSELs 7

2.1 Bandgap energies vs lattice constant for various III-V semiconductors at room temperature. 16
2.2 Diagram to show the principles of operation that enable a DBR to demonstrate its characteristic high reflectivity 18
2.3 Calculated reflectivity spectrum of the DBR structure designed in this section. 19
2.4 Diagram of the quantized energy levels within a quantum well structure, and the corresponding wavefunctions. 22
2.5 Graphical comparison of the density of states in a quantum well with that of bulk semiconductor. 24
2.6 Diagram of the strain compensated QWs incorporated in the gain structures presented in this thesis. 25
2.7 Diagram showing the structure and $|E^2|$ intensity distribution within the gain sample active region. 27
2.8 Design of the gain structures incorporated in the VECSEL devices presented in this thesis. 28
2.9 Calculated and experimentally derived microcavity enhancement factors of the antiresonant VECSEL structure as a function of wavelength. 29
2.10 Spatial and spectral distributions of $|E^2|$ in resonant and antiresonant VECSEL gain structures. 31
2.11 Spatial and spectral $|E^2|$ distributions in the near-antiresonant VECSEL gain structures designed in this chapter. 32
2.12 Spectra of quantum well emission, sample reflectivity and lasing spectrum for three values of sample temperature. 34
2.13 Graph to show how the GDD introduced by the antiresonant gain sample design varies with wavelength. 36
2.14 Diagram showing the principle of operation of a slow saturable absorber. . 39
2.15 Design of the Stark SESAM 45
2.16 4-mirror, Z-cavity design used for the VECSEL mode-locking presented in this thesis. 45
2.17 Pulse autocorrelation and lasing spectrum of a ML-VECSEL operating in the Stark regime. 46
2.18 Design of Stark SESAM for operation at 840 nm. 49

3.1 Reflectivity spectrum of sample QT1544 58
3.2 Edge photo-luminescence experimental setup 60
3.3 Edge photo-luminescence spectra of sample QT1544 61
3.4 Integrated photo-luminescence experimental setup 63
3.5 Integrated photo-luminescence spectra of sample QT1873 64
3.6 Internal quantum efficiency of sample QT1712 as a function of incident pump power. 67
3.7 CW lasing cavity setup 68
3.8 Graph of the stability calculation for the straight cavity. 69
3.9 Slope efficiency plots at incremental sample temperatures for sample QT1544 in a 2 mirror cavity completed with a) a 0.8% transmission output coupler, and b) a 1.5% transmission output coupler. 71
3.10 Plot of threshold pump power variation with temperature for the 0.8% output coupling, CW lasing cavity, with calculated values of characteristc temperature inset. 73
3.11 Diagram of the setup used for PL characterisation of a SESAM 75
3.12 PL data taken from Stark SESAM QT1861A at low excitation 76

4.1 Wide-span autocorrelation and optical spectrum of a Stark ML-VECSEL pulse, showing the presence of satellite pulses resulting from sample back-surface reflections. 83
4.2 Sample preparation, and machine configuration for polishing GaAs 86
4.3 Wide-span autocorrelation and optical spectrum of a pulse from a ML-VECSEL in which the back-surface of the GaAs substrate of the gain and SESAM samples has been polished at an angle to eliminate satellite pulses resulting from sample back-surface reflections. 87
4.4 Schematic representation of two heat flow geometries considered for the analytical thermal model of VECSELs 89
4.5 Thermal mounting of VECSEL samples described in this thesis 91
4.6 Diagram showing the Liau model of capillary bonding. 95
4.7 Diagram to represent the strengthening of bonds between sample and heat-spreader with time, showing the hydrogen bridges that can form to strengthen the bond 96
4.8 Schematic representation of the bonding method 98
4.9 Pictures of some bonding results 100
4.10 Layer sequencing in reverse-grown sample for substrate removal 104
4.11 Metal layers deposited for RF solder of reverse-grown sample to copper submount 106
4.12 photograph of jet etcher 109
4.13 photograph of etched, mounted sample 110
4.14 CW lasing performance of QT1770 112

5.1 Ytterbium fibre spectroscopy 121
5.2 A fibre section showing the cladding pumping geometry. 123
5.3 Fibre cross-section and index profile 124
5.4 Calculated SPM-broadened frequency spectra for a Gaussian pulse. 129
5.5 Simulation results showing the evolution of a pulse propagating in the parabolic regime. 131

5.6 Preliminary YDFA setup . . . 132
5.7 1035 nm VECSEL seed intensity autocorrelation . . . 133
5.8 Output optical spectrum from YDFA seeded with a 1040 nm VECSEL. . 134
5.9 Map of peak photoluminescence measured across the surface of an unoptimised VECSEL sample. . . . 135
5.10 Pulse intensity autocorrelation and optical spectrum of 1052 nm seed VECSEL. . . . 136
5.11 Amplified 1052 nm VECSEL results . . . 137
5.12 Experimental setup for high power VECSEL-MOPA experiments. . . . 138
5.13 Pulse intensity autocorrelation and optical spectrum of 1055 nm seed VECSEL. . . . 139
5.14 VECSEL-MOPA optical-to-optical efficiency. . . . 141
5.15 Intensity autocorrelation of amplified output pulse from VECSEL-MOPA at an average power of 160 W. . . . 141
5.16 Optical spectra of amplified output from VECSEL-MOPA. . . . 143
5.17 Schematic of pulse compression setup. . . . 144
5.18 Compressed pulse from VECSEL-MOPA at 160 W average power. . . . 145
5.19 Compressed pulse length as a function of average VECSEL-MOPA output power. . . . 145
5.20 Images of damaged fibre ends. . . . 147

6.1 High repetition rate cavity configurations for tens of GHz devices. . . . 156
6.2 Representations of ML-VECSEL output showing the potential for pulse overlap as higher repetition rates are accessed by the devices. . . . 159
6.3 Schematics of the proposed 100 GHz concept VECSEL cavities. . . . 161
6.4 Cross-section of a proposed curved structure to be fabricated in GaAs. . . 162
6.5 Stability calculation for the proposed 100 GHz cavity . . . 163
6.6 Results of attempts to drill GaAs with ball-lens drill and sodium hypochlorite solution. . . . 165
6.7 Results of attempts to drill GaAs via a chemo-mechanical method. . . . 165
6.8 Schematic detailing the steps in the process developed to create focussing optical quality structures in GaAs. . . . 167
6.9 Diagram and photograph of the rig used for micro-imprinting of resist spun on GaAs substrate. . . . 170
6.10 Spin characteristics of PMMA 950 A11 photoresist . . . 171
6.11 1.5 μm ball lens imprint in 1813 resist on Si substrate. . . . 172
6.12 Various examples of unsuccessful imprintings. . . . 173
6.13 Profile and microscope image showing the relaxation of resist back into the centre of the imprint after removal of the mould . . . 174
6.14 Profile and AFM image showing the transferral of the pattern of relaxed resist following etching. . . . 174
6.15 Profile of 1.7 μm-thick PMMA on n-doped GaAs, imprinted with 300 μm diameter ball-lens jig. . . . 175
6.16 Schematic of an inductively coupled plasma reactive ion etching chamber 177
6.17 Profile of ICP etched imprint, showing comparison with pre-etch profile. . 180
6.18 Profile and microscope image of overgrown imprinted GaAs sample. . . . 182
6.19 Experimental setup for optical characterisation of overgrown imprinted GaAs sample. . . . 183

6.20 Photographs of the images produced by the reflected beam when projected onto the screen at an arbitrary distance from the sample. 185
6.21 Spatial beam intensity profiles of HeNe beam reflected by the imprinted and overgrown structure 185
6.22 Stability calculations for overgrown structure. 188
6.23 Configurations of SESAM output coupler for the 100 GHz VECSEL device190

B.1 Four mirror VECSEL cavity 208

Acknowledgements

First and foremost, I must thank Prof. Anne Tropper, not only for her continued guidance and unwavering support as my PhD supervisor, but also for all the opportunities she has encouraged me to embrace, and for being an inspiring role model, mentor and friend. I would like to thank Dr. Keith Wilcox for accompanying me on this journey, for the many valued discussions, fun in the lab, shared 'eureka!' moments. Thanks also to Dr. Sjoerd Hoogland for teaching me everything I needed to know to build a ML-VECSEL, and so much more.

To Pascal Dupriez, thanks for making even the longest days hunched over a fibre amplifier an enjoyable experience. Thank you also to Dr. Andy Malinowski for teaching me all the fibre amplifier essentials. A huge thank you to Dr. Corin Gawith for taking me on as his direct bonding apprentice, and for being a great friend. Thanks also to Dave Sager for all those clean-room hours, and valuable discussions, and to Dr. Pier Sazio for sharing his wealth of processing knowledge. Thanks to Dr. Tim May-Smith for all the polishing room antics!

Thanks to all the technical staff who have helped me along the way, notably 'Uncle' Colin and Vince for never failing to make me feel welcome in the basement, to Tom, Justin, Chad and all the guys in the workshop, is there anything that you can't do?! Thanks to Chris, Alan and Adam for all those equipment loans.

Thanks to Dr. Geoff Hill, Dr. John Roberts, and Dr. Andriy Krysa at Sheffield University for countless growths, processing and advice. Thanks to Dr. Alex Aschwanden and Dr. Dirk Lorenser at ETH Zurich for an enjoyable few days processing. And to Dr. Maxim Shkunov at Merck for allowing me to use their profiler.

Thank you to Pearl John and members of the Southampton University Student Chapter of the OSA for encouraging and supporting me to develop my outreach portfolio, and for all the laughs had in doing so.

Of course, a huge thank you to all my friends for their support and friendship. For sharing the ups and the downs, and for putting up with my insatiable desire to make a social event out of everything! To my ex-housemates for resisting the temptation to ask me how writing is going, to the Wardens for putting up with my incoherent ramblings

at 10pm wind-down time, and to 'the boys' for being the best lunchtime (and all the time actually) companions I can imagine! Thanks also to my new friends and colleagues in Glasgow for their support in these last few months. And a special thank you to Ian and Corin for helping me to get here in the first place, and again to Ian for ALL those pep talks and e-mails.

And finally, thank you to my family. Their pride and interest in me is a real driving force. Mum and Dad, you are truly special and precious people! Thank you so much for your continued support, for always being there at the end of the phone when I need you, for motivation when I'm feeling apathetic, for focus when I procrastinate, for lifting me when I'm down, and for sharing those oh-so-special highs. I cannot express how valuable your support has been, I am so lucky to have you!

To Mum, Dad and Rachel

Chapter 1

Introduction

1.1 VECSELs: the bridge between the semiconductor diode and solid state lasers

In recent years, there has been increasing interest in the development of a novel type of laser: the vertical-external-cavity surface-emitting laser (VECSEL) was born from two established laser technologies, inheriting the desirable properties of both. VECSELs incorporate a semiconductor quantum well-based gain element, similar to that of a semiconductor diode laser, in an external cavity with geometry similar to that of a diode-pumped solid-state laser (DP-SSL). Thus incorporating the flexible design and spectral coverage afforded semiconductor-based lasers, with the excellent beam quality and functional versatility of their solid-state laser counterparts.

Today, semiconductor diode lasers are the most widely used class of laser, with applications ranging from incorporation in simple CD players to the most advanced telecommunications technologies, and as high power pump sources for DP-SSLs. The spectral coverage of this class of devices is broad, with emission wavelength diversity provided by band gap engineering of the semiconductor through material composition and quantum well design. CW emission from blue (410 nm emission from InGaN-based diodes [1]) through to the mid-infrared (using a quantum cascade design [2]) has been achieved, and more recently, even the THz region of the spectrum has been directly accessed [3].

Moreover, the semiconductor growth techniques employed, and wafer-scale fabrication of these devices make them cheap, mass-producible sources. For the active medium, a direct-gap material is required, so the elemental semiconductors, silicon and germanium, are not suitable. Instead, combinations of elements from the third (Ga, Al, In) and fifth (As, P, N, Sb) groups of the periodic table are employed, and are refered to as III-V compounds and alloys.

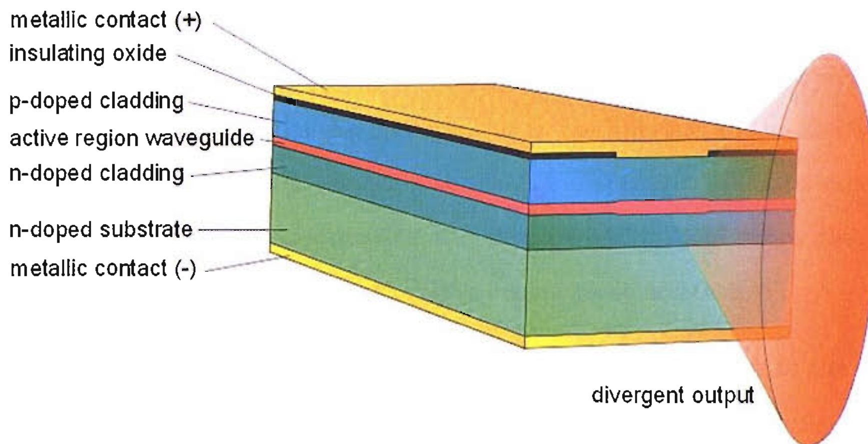

FIGURE 1.1: Schematic drawing of a typical edge emitting semiconductor diode laser, with characteristic divergent, astigmatic output beam.

Conventional semiconductor diode lasers have an edge-emitting geometry as shown in figure 1.1: a thin, un-doped active region, often composed of quantum wells (QWs), is sandwiched between layers of a different material which are, in turn, p-doped and n-doped. The devices are electrically pumped; current is injected via metallic contacts made to the p-n material. The resonator end-mirrors are formed by the cleaved facets at the end of the active region, and oscillation is perpendicular to the growth direction. Laser emission is from the edge of the active region from one of the facets, and it is herein that the major disadvantage of these devices lies: emission from this long, narrow aperture results in a highly astigmatic, divergent beam with poor modal quality.

Conversely, high power, high quality beams are readily achieved from the solid-state class of lasers. The gain element of these lasers is composed of a dielectric host material in glass or crystal form, which is impregnated with impurity ions from the transition

elements of the periodic table; typically rare-earth or transition-metal ions. The resonator geometry of such lasers is inherently versatile, and is constructed around an external cavity containing the doped crystal/glass usually in rod or disk form, optically pumped either by flash lamps or a suitable diode laser pump source. The external cavity facilitates control of the output beam, allowing high quality beams to be produced. Moreover, intracavity manipulation of the laser output is possible, through techniques such as mode-locking and frequency doubling [4].

In the disc geometry, SSLs exhibit power-scalable operation since they are cooled by one-dimensional heat flow, with the thermal gradient in the direction of the cavity optical axis. This dramatically reduces the negative thermal effects that might be experienced by the devices, such as thermal lensing and de-polarisation, and raises the damage threshold, permitting high quality, high power output to be achieved [5].

Despite these advantages, SSLs remain an expensive, bulky alternative to the semiconductor diode laser. Their active material is not suitable for cheap mass-production, and the constraints of the material system upon which they are based greatly limits the spectral coverage that they are able to provide (with the notable exception of some tunable sources such as the Ti:Sapphire laser). Moreover, the pump absorption band of such gain media is often narrow, greatly constraining the possible pump sources, and sometimes necessitating stabilisation of the pump wavelength.

Manipulation of the geometry of semiconductor lasers to provide improved output beam quality comparable with SSLs was achieved with the advent of the vertical-cavity surface-emitting laser (VCSEL) [6], shown in figure 1.2. Possessing an epitaxial structure very similar to that of a diode laser, with doped layers for current injection, the VCESL has one major difference: it has a vertical cavity, with oscillation parallel to the growth direction. The end-mirrors of the resonator are formed by highly reflective distributed Bragg reflectors (DBRs) grown either side of the QW-based active region, and laser emission is through the top surface of the device. Thus, the output beam is free from the divergent effects of the narrow aperture of a conventional edge-emitting diode, and emission in a single transverse mode (TEM_{00}) is possible. The positioning of the quantum wells within the active region is designed so that the QWs are located at the antinodes of the

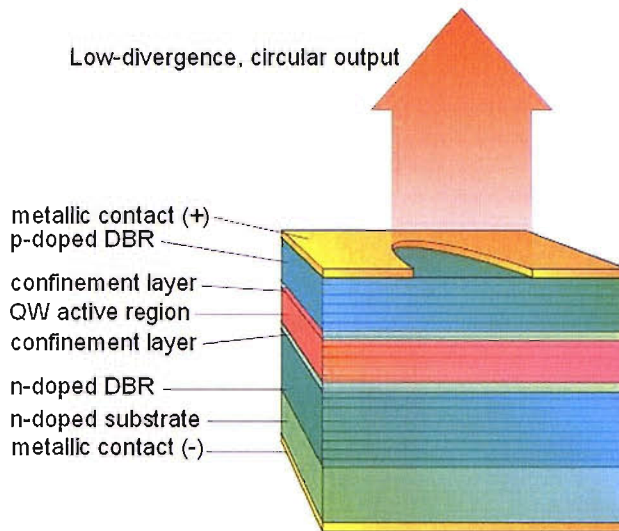

FIGURE 1.2: Diagram showing the geometry of a VCSEL: a low-divergence, circularly symmetric beam is emitted through the top DBR of the structure.

$|E^2|$ distribution at the lasing wavelength, referred to as resonant periodic gain (RPG) [7].

Unfortunately, at most, only a few milliwatts of fundamental mode output power are achievable from these electrically pumped VCSELs before the effects of carrier filamentation, where only pockets of the pumped region are seen to be active, and carrier separation, where electrons and holes are forced to separate by internal electric fields induced by electrical pumping, dominate. Moreover, versatility is sacrificed for compactness of these devices as their wholly epitaxial structure does not permit intracavity manipulation in an external cavity.

The potential of obtaining the full functionality of a SSL from a semiconductor-based resonator is realised in the form of a vertical-external-cavity surface-emitting laser. The VECSEL cavity geometry resembles that of a solid-state disk laser [5], and is shown in figure 1.3. The VECSEL gain chip exhibits the excellent thermal properties attributed to such thin disk lasers, and a power scalable device may, in principle, be achieved. The gain medium itself is reminiscent of that of a VCSEL, with an RPG QW-based active region grown on top of a DBR, however, the top DBR is not grown, and instead, the cavity is completed with an external, curved, dielectric mirror which enforces fundamental mode operation even at high powers, and/or with a large mode on the gain sample.

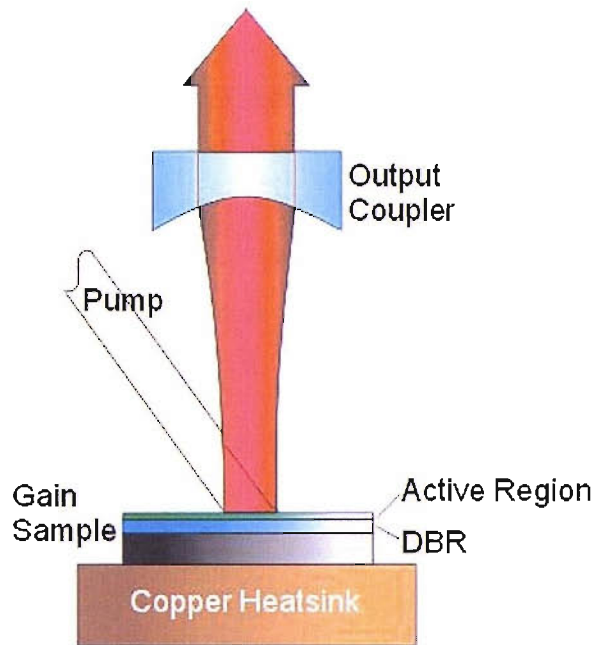

FIGURE 1.3: Schematic of a simple VECSEL cavity. The optically pumped gain sample forms one end mirror of the resonator, whilst the other is a spherical output coupler.

The VECSEL gain chip is optically pumped, defying convention within the semiconductor laser field [8]. The large absorption band of the bulk semiconductor QW barriers gives great versatility in pump source selection, unlike in some SSLs. Moreover, optical pumping provides freedom from the negative effects experienced by VCSELs at high powers, providing a controlled and uniform pump power distribution on the active layers. However, there is still some interest in electrically pumped VECSELs to create more compact devices for low power applications [9].

The advantages of semiconductor material system tailorability are maintained, and with careful design, a broad range of wavelengths can be accessed by these devices. This range is further increased by the affinity of these devices to intracavity frequency doubling due to the high intracavity powers produced [10]. Moreover, the broad gain bandwidth of these semiconductor-based devices lends them to tunable operation for spectroscopic purposes [11], and when coupled with insertion of a SESAM into the external cavity, permits passively mode-locked operation to give ultra short pulses [12, 13].

1.1.1 VECSEL Wavelength coverage

The majority of the early VECSEL work demonstrated emission at wavelengths around 1 μm [10, 12, 14], and 860 nm [15, 16]. It is here that the III-V semiconductor material system is most readily engineered, with GaAs substrates supporting lattice-matched AlAs/AlGaAs DBRs for both, employing the already well-characterised quantum well systems of GaAs/AlGaAs for 860 nm emission and InGaAs/GaAs for 1 μm. Suitable diode pumps are readily available for both.

However, wavelength coverage is not limited to these regions, and as the field has developed, so the emission range covered by VECSELs has widened. Figure 1.4 shows the current wavelength coverage provided by VECSELs: at 1.3 μm, the dilute nitrides have provided suitable emission [17], the InP-based material system developed for telecoms applications around 1.5 μm has lent itself to VECSEL technology, with emission being provided by InGaAsP quantum wells [18], and further migrations into the infra-red have been achieved using antimonide-based quantum wells [19, 20]. Visible VECSELs have been realised emitting in the blue, based on GaN systems [21], and the red, based on AlInGaP [22], although these devices are currently limited by the availability of suitable pump diodes.

The techniques demonstrated at one wavelength in VECSELs (often at 1 μm and 860 nm because of the ease of design and growth at these wavelengths) can be transferred to other wavelengths with ease. These techniques include intracavity frequency doubling, notably with the recent generation of UV light via this method, further increasing the spectral coverage of VECSELs [24], high power (Watt-level) operation [25, 26], tunable operation [20], single frequency operation [27], and mode-locked operation [28]. Moreover, VECSELs are now commercially available; one such source being the Coherent Inc. Sapphire, frequency doubled, green VECSEL capable of output powers as high as 500 mW at λ=488 nm [29].

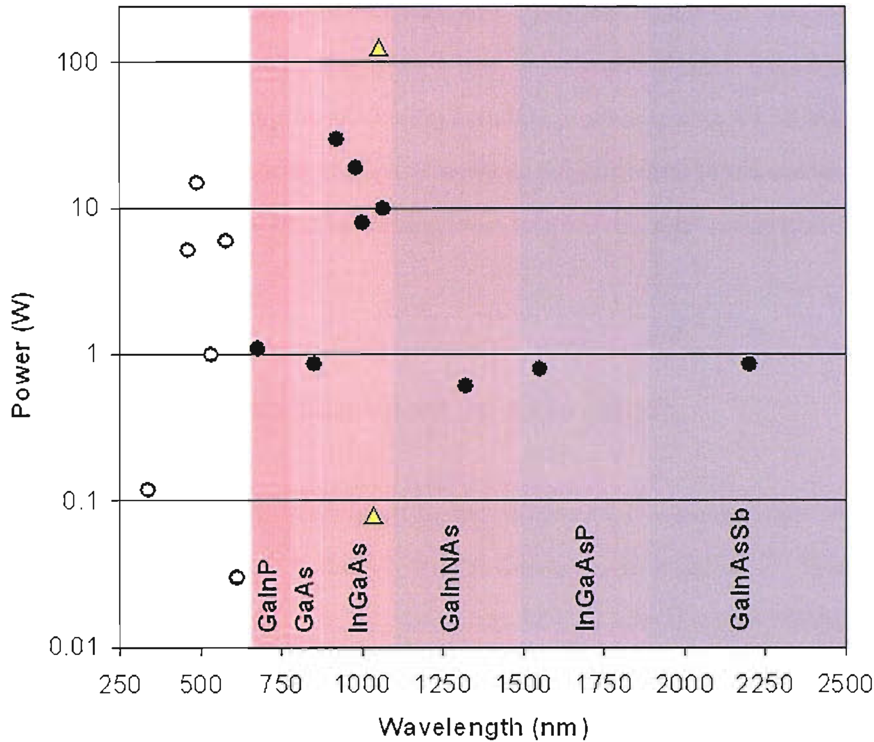

FIGURE 1.4: Graph to show the current wavelength coverage of VECSEL emission as a function of output power achieved, modified from [23]. Filled circles denote direct emission, open circles denote frequency doubled VECSELs, yellow traingles denote the work presented in this thesis.

1.1.2 Mode-locking of VECSELs

The external cavity of a VECSEL is ideal for insertion of an intracavity element to mode-lock the laser output. The gain bandwidth exhibited by a semiconductor system is broad, conducive to production of ultra-short pulses. The first mode-locked (ML) diode-pumped VECSEL was achieved in 1999 by Holm et al, using an intracavity acousto-optical modulator to actively mode-lock an 850 nm VECSEL [30]. Prior to this, mode-locked operation had been achieved in a less than optimal fashion, through synchronous pumping using a solid-state laser [8]. However, the demonstration of passive mode-locking of a DP-VECSEL using a semiconductor saturable absorber mirror (SESAM [12]) at 1 μm in 2000 by Hoogland et al set a precedent, and VECSEL mode-locking is now dominated by this technique [31].

Further development of SESAMs for VECSEL mode-locking has seen the demonstration

of passively mode-locked VECSELs emitting at 1.5 μm [28], and more recently, 1.3 μm [32]. Further reductions in pulse length have also been achieved with the advent of the Stark SESAM from Southampton University, enabling sub-ps pulses to be achieved for the first time [13]. The potential of these sources to generate low jitter, stable trains of pulses has been identified, enabled by locking to an external electronic reference oscillator [33].

1.2 Introduction to the work in this thesis

This thesis concentrates on the optimisation and application of mode-locked VECSELs at wavelengths around 1 μm. It builds on the development of passively mode-locked sources at this wavelength, particularly that of the Stark mode-locked VECSEL producing sub-ps pulses [13]. Further optimisations of such devices are considered, and their applications are investigated.

Chapter 2 discusses the main principles behind VECSEL operation, with particular focus on mode-locking. Each element of a VECSEL gain sample and SESAM is considered individually, and resonator design and optimisation around these samples is explained. The processes that lie behind characteristic behaviour exhibited by ML-VECSELs are explained, and design of gain and SESAM samples to optimise this behaviour is outlined.

Chapter 3 describes the experimental techniques used in this thesis to characterise VECSEL gain and SESAM samples post-growth to assess their quality and similarity to design. Results from various VECSEL samples, all with the same design, but different growths, are included to demonstrate the growth-to-growth variance, and importance of these characterisation steps. Methods to observe the reflectivity of the DBR, emission of the quantum wells independently, and effect of the whole structure combined are discussed, as well as characterisations of the samples performed in a CW lasing cavity. Mode-locking results are also presented.

Chapter 4 focuses on post-growth processing of VECSEL samples to achieve optimal operation. A method for eliminating satellite pulses in the output of a ML-VECSEL is presented, with pre and post-processing data demonstrating the results of the process.

Thermal management of VECSELs is discussed, motivated by enabling of high power operation through efficient heat removal from the VECSEL active region. Achievements in the field are reviewed, and two approaches to thermal management are presented: substrate removal, and bonding to an intracavity heat-spreader window.

Chapter 5 describes the application of the ML-VECSELs designed and built in this thesis as seeds for high power master-oscillator power-amplifiers (MOPAs) based on ytterbium-doped fibre amplifier (YDFA) technology. The construction of suitable ML-VECSELs is described, with initial low-power results demonstrating the necessity for careful selection of gain sample to provide the desired seed emission wavelength. A final VECSEL-MOPA system is investigated; the characteristics of the resulting output pulses are described, and external pulse compression is employed to achieve sub-300 fs pulses.

Chapter 6 presents the processing techniques developed as part of the work contained in this thesis to produce a high repetition rate VECSEL. A review of high repetition rate VECSEL operation is performed, and the challenges of realising such devices are discussed at length. Progress made in this thesis is presented, and the steps that are still to be completed in order to realise a final high repetition rate device are considered.

Chapter 7 concludes the thesis, reviewing the work contained, and milestones achieved. Future work following on from the achievements presented is detailed with the impact of the resulting devices considered.

Bibliography

[1] Nakamura, S. *et al.* InGaN-based multi-quantum-well-structure laser diodes. *Japanese Journal of Applied Physics* **35**, L74–L76 (1996).

[2] Faist, J. *et al.* Quantum cascade laser. *Science* **264**, 553–556 (1994).

[3] Barbieri, S. *et al.* Continuous-wave operation of terahertz quantum-cascade lasers. *IEEE Journal of Quantum Electronics* **39**, 586–591 (2003).

[4] Svelto, O. *Principles of Lasers* (Plenum Press, New York, 1998), fourth edn.

[5] Brauch, U., Giesen, A., Karszewski, M. & Stewen, C. Multiwatt diode-pumped Yb:YAG thin disk laser continuously tunable between 1018 and 1053 nm. *Optics Letters* **20**, 713–715 (1995).

[6] Jewell, J. L., Harbison, J. P., Scherer, A., Lee, Y. H. & Florez, L. T. Vertical-cavity surface-emitting lasers: Design, growth, fabrication, characterization. *IEEE Journal of Quantum Electronics* **27**, 1332–1346 (1991).

[7] Raja, M. Y. A. *et al.* Surface-emitting, multiple quantum well GaAs/AlGaAs laser with wavelength-resonant periodic gain medium,. *Applied Physics Letters* **53**, 1678–1680 (1988).

[8] Tropper, A. C., Foreman, H. D., Garnache, A., Wilcox, K. G. & Hoogland, S. H. Vertical-external-cavity semiconductor lasers. *Journal of Physics D: Applied Physics* **37**, R75–R85 (2004).

[9] Jasim, K. *et al.* Picosecond pulse generation from passively modelocked vertical cavity diode laser at up to 15 GHz pulse repetition rate. *Electronics Letters* **40**, 34–36 (2004).

[10] Raymond, T. D., Alford, W. J., Crawford, M. H. & Allerman, A. A. Intracavity frequency doubling of a diode-pumped external-cavity surface-emitting semiconductor laser. *Optics Letters* **24**, 1127–1129 (1999).

[11] Garnache, A., Kachanov, A. A., Stoeckel, F. & Houdre, R. Diode-pumped broadband vertical-external-cavity surface-emitting semiconductor laser applied to high-sensitivity intracavity absorption spectroscopy. *Journal- Optical Society of America B* **17**, 1589–1598 (2000).

[12] Hoogland, S. *et al.* Passively mode-locked diode-pumped surface-emitting semiconductor laser. *IEEE Photonics Technology Letters* **12**, 1135–1137 (2000).

[13] Garnache, A. *et al.* Sub-500-fs soliton-like pulse in a passively mode-locked broadband surface-emitting laser with 100 mW average power. *Applied Physics Letters* **80**, 3892–3894 (2002).

[14] Kuznetsov, M., Hakimi, F., Sprague, R. & Mooradian, A. High-power (>0.5-W cw) diode-pumped vertical-external-cavity surface-emitting semiconductor lasers with circular TEM_{00} beams. *IEEE Photonics Technology Letters* **9**, 1063–1065 (1997).

[15] Holm, M. A., Burns, D., Ferguson, A. I. & Dawson, M. D. Actively stabilized single-frequency vertical-external-cavity AlGaAs laser. *IEEE Photonics technology letters* **11**, 1551–1553 (1999).

[16] Holm, M. A., Burns, D., Cusumano, P., Ferguson, A. I. & Dawson, M. D. High-power diode-pumped AlGaAs surface-emitting laser. *Applied Optics* **38**, 5781–5784 (1999).

[17] Calvez, S. *et al.* GaInNAs/GaAs bragg-mirror-based structures for novel 1.3 μm device applications. *Journal of Crystal Growth* **268** (2004).

[18] Symonds, C. *et al.* Continuous-wave operation of monolithically grown 1.5-μm optically pumped vertical-external-cavity surface-emitting lasers. *Applied Optics* **42**, 6678–6681 (2003).

[19] Cerutti, L., Granache, A., Genty, F., Ouvrard, A. & Alibert, C. Low threshold, room temperature laser diode pumped Sb-based vecsel emitting around 2.1 micron. *Electronics Letters* **39**, 290–292 (2003).

[20] Hopkins, J.-M. *et al.* Tunable, single-frequency, diode-pumped 2.3 μm vecsel. In *Conference on Lasers and Electro-Optics (CLEO) 2006*, CThM3 (Long Beach, California, U.S.A., 2006).

[21] Park, S. H. *et al.* Room-temperature GaN vertical-cavity surface-emitting laser operation in an extended cavity scheme. *Applied Physics Letters* **83**, 2121–2123 (2003).

[22] Hastie, J. E. *et al.* High power CW red VECSEL with linearly polarized TEM_{00} output beam. *Optics Express* **13**, 77–81 (2005).

[23] Hastie, J. E. Data collated for presentation by J. E. Hastie (2006).

[24] Morton, L. G., Hastie, J. E., Dawson, M. D., Krysa, A. B. & Roberts, J. S. 1W CW red vecsel frequency-doubled to generate 60mW in the ultraviolet. In *Conference on Lasers and Electro-Optics (CLEO)*, JWB16 (Long Beach, California, USA, 2006).

[25] Lutgen, S. *et al.* 8-W high-efficiency continuous-wave semiconductor disk laser at 1000 nm. *Applied Physics Letters* **82**, 3620–3622 (2003).

[26] Chilla, J. *et al.* High power optically pumped semiconductor lasers. In *Photonics West: Solid State Lasers XIII* (San Jose, California, USA, 2004).

[27] Holm, M. A., Burns, D., Ferguson, A. I. & Dawson, M. D. Single-frequency second-harmonic generation in a vertical external-cavity semiconductor laser. In *Conference on Lasers and Electro-Optics US 2000*, 440–441 (San Francisco, U.S.A., 2000).

[28] Garnache, S. H. A. *et al.* Picosecond pulse generation with 1.5 μm passively mode-locked surface-emitting semiconductor laser. *Electronics Letters* **39**, 846–847 (2003).

[29] Coherent. Website (2006). URL `http://www.coherent.com/`.

[30] Holm, M. A., Cusumano, P., Burns, D., Ferguson, A. I. & Dawson, M. D. Mode-locked operation of a diode-pumped external-cavity GaAs/AlGaAs surface-emitting laser. In *Conference on Lasers and Electro Optics (CLEO) '99*, CtuK63 (Baltimore, Maryland, 1999).

[31] Keller, U. *et al.* Pushing the high-pulse-repetition-rate frontier using a new regime of inverse saturable absorption and novel low saturation fluence SESAMs. In *Advanced Solid State Photonics (ASSP) 2006*, TuA3 (Lake Tahoe, U.S.A., 2006).

[32] Rutz, A. *et al.* Passively modelocked GaInNAs VECSEL at centre wavelength around 1.3 μm. *Electronics letters* **42**, 926–927 (2006).

[33] Wilcox, K. G., Foreman, H. D., Roberts, J. S. & Tropper, A. C. Timing jitter of 897 MHz optical pulse train from actively stabilised passively modelocked surface-emitting semiconductor laser. *IEEE Journal of Quantum Electronics* **42**, 159–160 (2006).

Chapter 2

Theory of VECSELs

2.1 Introduction

The VECSELs presented in this thesis are designed to operate in the applications window at wavelengths around one micrometer, where the well-characterised, flexible, high quality InGaAs/GaAs/AlGaAs material system is at our disposal. The VECSEL is composed of an active mirror providing gain, and acting as an end mirror of the cavity. Then, as presented in chapter 1, the cavity constructed around this mirror may contain several intracavity elements; in the work presented here, a semiconductor saturable absorber mirror (SESAM [1]) for mode-locking of the devices is inserted. The cavity is completed with a curved output coupler which promotes the excellent modal quality that is characteristic of a VECSEL.

The active mirror and SESAM chips are both semiconductor multilayer structures. In order to provide emission and saturable absorption in the 1 μm wavelength region, both structures are based on the GaAs/AlGaAs III-V semiconductor material system which provides materials with bandgaps around this wavelength, for which the growth techniques are well established. InGaAs/GaAs quantum wells are included in the structure to provide gain.

This chapter describes the VECSEL structure and how mode-locking is achieved with such a structure as the gain medium. Both the gain sample and the SESAM's structural

properties and material compositions are discussed, introducing each element of the samples individually. Sample design methods are outlined, and the structural properties of gain mirror and SESAM are explored, with particular focus on application in a mode-locked (ML) VECSEL.

2.2 VECSEL Active Mirror Design

Design of the active mirror (or gain sample/chip) for a VECSEL cavity is crucial to its operation. It is a complex, multilayer, multi-functional structure, but for the purposes of growth, it must be kept as simple as possible. There are many factors to take into account when designing such a structure, particularly in a mode-locked VECSEL.

The structure bears strong resemblance to a VCSEL (described in chapter 1), but with one of the mirrors removed, leaving a highly reflecting Bragg mirror with a quantum well-based active region on top. The structure is optically pumped, which simplifies its design and growth in that no doping is required as would be for an electrically pumped device, however, the absorption of pump radiation must be considered. For efficient design, the potential pump sources should be identified prior to design to ensure that the absorption length of the active region of the quantum well gain structure is sufficient.

In mode-locked operation, the effects of the structure on the pulse as it propagates through must also be considered. As this section will demonstrate, the criteria for a structure that will be employed in a ML-VECSEL differ from those applied in a CW device, and high gain may be sacrificed for gain bandwidth in a ML-VECSEL design.

2.2.1 Material Choice

When deciding which material system to base the VECSELs described in this thesis on, the choice was clear: the close lattice match between GaAs and AlAs shown in figure 2.1 gives the $Al_xGa_{1-x}As$ system clear advantages over other choices, allowing multilayer structures with different compositions of AlGaAs to be grown without the problem of strain induced between the layers which can lead to degradation of the structure. The

advantages of this choice are further enhanced by the availability of GaAs substrates upon which to grow the layers, and the wealth of established methods for the processing of these materials, enhanced by the suitability of relatively low cost silicon detectors to devices emitting at the wavelengths defined by the AlGaAs system. Moreover, as will be described in chapter 5, this wavelength range also overlaps with the emission spectrum of rare-earth-doped fibres indicating the ML-VECSEL as a suitable seed source for Yb-doped fibre amplifiers.

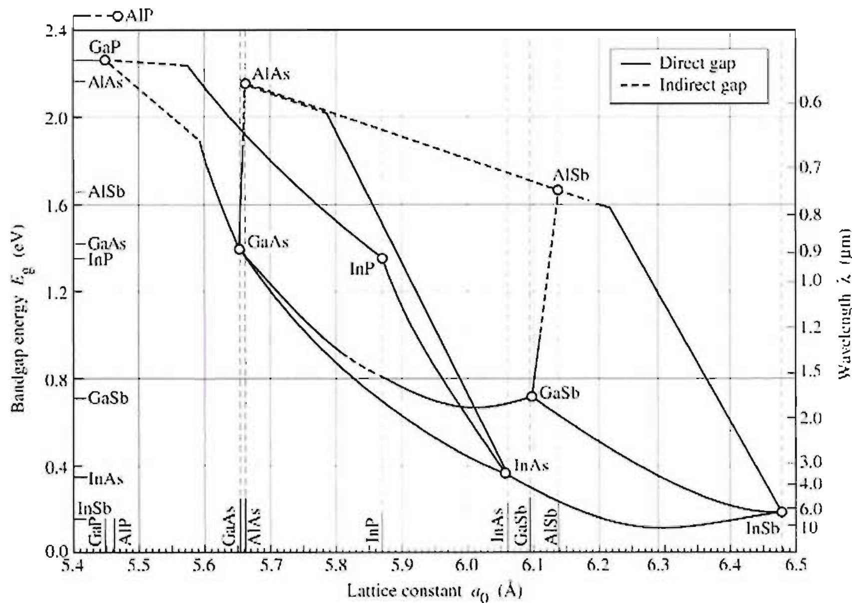

FIGURE 2.1: Bandgap energies vs lattice constant for various III-V semiconductors at room temperature [2], showing the advantageous lattice matching between GaAs and AlAs and corresponding range of possible material bandgaps.

Suitable quantum well (QW) structures to provide gain and saturable absorption in these $Al_xGa_{1-x}As$-based devices are sourced from the InGaAs/GaAs quantum well system. These QWs are well characterised, and have been shown to exhibit high gain and low thresholds, ideal for incorporation into the structures described here [3]. The characteristics of these QWs will be discussed in section 2.2.3.

For sample design, it is also important to consider the dispersive nature of the materials used. An analytical expression for the refractive index of $Al_xGa_{1-x}As$ is given in [4], achieved by fitting to experimental results obtained in [5], and is as follows:

$$n(E,x) = 3.3 + 0.09x - (0.08{+}0.7x)E + (0.19{+}0.16x)E^2 + \frac{0.00023}{(E-(1.42+1.25x))^2 + 0.003} \quad (2.2.1)$$

where E is the photon energy and x is the Al concentration. It is clear from this relation that different wavelengths of light passing through the structure will experience different refractive indices. The effects of this dispersion in a ML-VECSEL will be considered in section 2.3.4. Moreover, the tuning of the bandgap of semiconductors with temperature gives a tuning of E, and hence the temperature-dependence of refractive index of the layers must be considered. This effect is considered in section 2.3.3.

2.2.2 Distributed Bragg Reflector

In order to construct a laser cavity in the VECSEL configuration, the demands upon the mirror structure contained in the gain sample are clear: it must provide high reflectivity (>99.9%) and, since it is integral to the active device, it must be possible to deposit active layers on top of it. A distributed bragg reflector (DBR) constructed using the $Al_xGa_{1-x}As$ material system fulfills these requirements.

A DBR is composed of several layers of alternating high-to-low refractive index materials, in the case of the samples described here, the high index material is GaAs ($n_1 = 3.48$ calculated from equation 2.2.1) or $Al_{0.2}Ga_{0.8}As$ ($n_1 = 3.37$), an alternative that absorbs less pump than GaAs and hence reduces localised heating of the sample, and the low index material is AlAs ($n_2 = 2.95$). The reflectivity of such a mirror is wavelength-dependent, and its reflectivity spectrum can be tailored by altering the thickness of its layers. The basic principle behind the achievement of high reflectivity in such a structure is shown in figure 2.2a. The layers are one quarter of the design wavelength thick (optical thickness), and the structure repeats every 2 layers. So as the light traverses the structure, its phase has shifted by $\pi/2$ every time it reaches a new layer. In addition, there is a reflection at each interface: at interfaces where the light passes from low to high indices, a phase shift of π is induced in reflection, at high to low interfaces, no phase shift is induced. The result of these two factors is that all the reflected waves within the

structure experience $2m\pi$ phase shifts relative to the incident light (m is an integer), returning to the cavity in phase to interfere constructively, and all the transmitted waves interfere desconstructively, in theory, resulting in 100% reflectivity achievabe from the structure at the design wavelength.

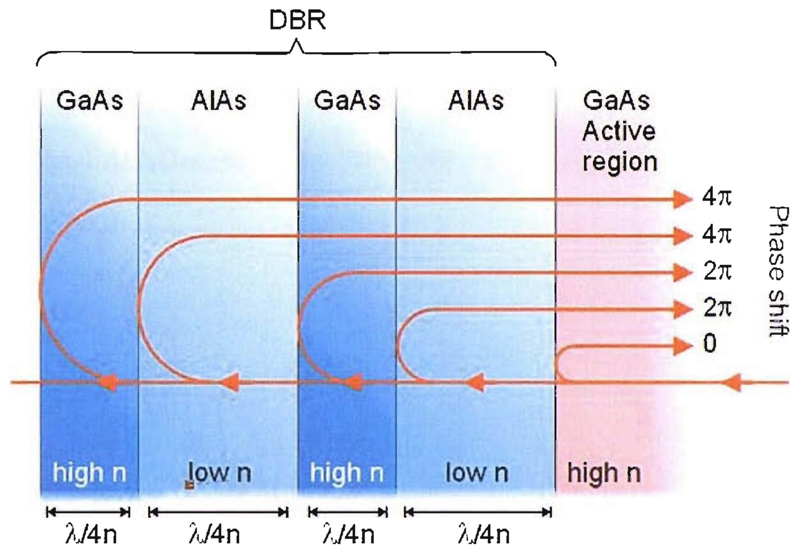

FIGURE 2.2: Diagram to show the basic principles that give a DBR its characteristic high reflectivity; all of the reflected waves experience phase shifts of $2m\pi$, and so constructively interfere to give high reflectivity.

The calculated reflectivity spectrum for the VECSEL design presented in this chapter is shown in figure 2.3. The spectrum shows a large region ($\Delta\lambda \approx$100 nm) of close to 100% reflectivity centred at the design wavelength (λ_0). This characteristic feature of the DBR is called the stop band, and is a result of the fact that the phase change at wavelengths around the design wavelength remains small. The bandwidth of the stop band and its reflectivity is determined by the number of layers that compose the DBR and the index contrast between them; higher index contrast and more layers gives a larger bandwidth of high reflectivity. The reflectivity at the design wavelength of a DBR with $2N+1$ layers can be expressed as:

$$R_N = \left(\frac{n_s - \left[\frac{n_1^2}{n_3}\right]\left[\frac{n_1}{n_2}\right]^{2N}}{n_s + \left[\frac{n_1^2}{n_3}\right]\left[\frac{n_1}{n_2}\right]^{2N}} \right)^2, \tag{2.2.2}$$

where n_s is the refractive index of the substrate (GaAs in this case), and n_3 is the refractive index of the incident medium (GaAs of the active region). To achieve the desired reflectivity, greater than 99.9% at the design wavelength, a minimum of 24 layers of GaAs/AlAs must be used. Beyond this point, there is a trade-off between the bandwidth of the stopband, and the complexity of the growth, both of which increase with increasing numbers of layers asymptotically to a steady state. For the samples presented in this thesis, $N = 54$ layers were chosen, providing broad stopbands for both GaAs/AlAs and $Al_{0.2}Ga_{0.8}As$/AlAs DBRs whilst remaining simpler to grow.

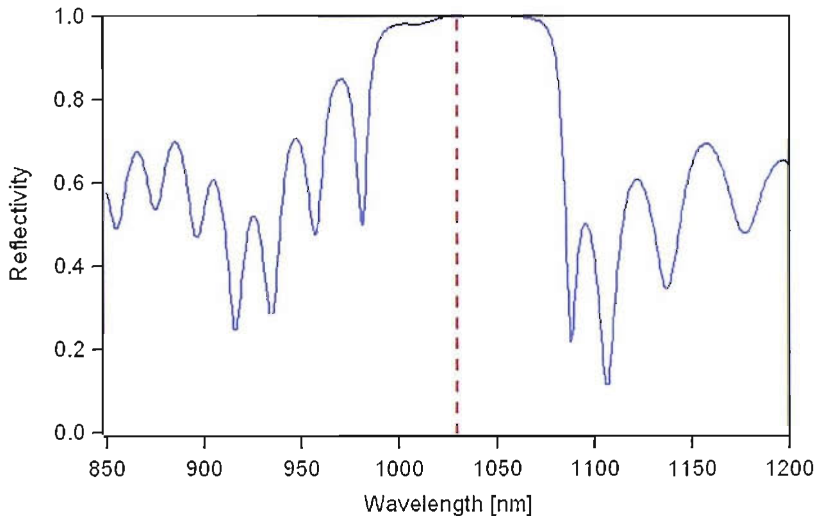

FIGURE 2.3: Calculated reflectivity spectrum of the DBR structure designed in this section (blue), showing the distinctive stopband feature with ~100% reflectivity spanning ~100 nm centred at the design wavelength (red). The spectrum is calculated using the multilayer methods presented in [6] (appendix A)

As will be discussed later in this chapter, the broadband reflectivity of the stopband is particularly important in mode-locked VECSELs, since a broad spectrum ($\Delta\lambda \approx$3 nm) is necessary to give short pulses, and high reflectivity across this spectrum is required. Moreover, the wavelength tuning desired in a Stark mode-locked VECSEL dictates that high reflectivity should be available over the whole gain spectrum of the VECSEL active medium, some 20-30 nm.

2.2.3 Quantum Well Gain Region

Gain in a VECSEL device is provided by the quantum well-based active region grown on top of the DBR. In design of this structure, both the lasing wavelength and the pump wavelength must be considered. It is necessary to design a quantum well structure that absorbs radiation efficiently at the pump wavelength, whilst also giving gain and emitting radiation at the desired lasing wavelength. The VECSELs used in this thesis are designed to emit at 1030 nm. The pump source selected is a λ=830 nm commercial diode, emitting up to 1-W of power.

2.2.3.1 Quantum Wells

The quantum well (QW) structures incorporated into the active region consist of a thin layer of material with bandgap energy E_{gm}, sandwiched between barrier layers of material with a larger bandgap energy E_{gb}. Electrons in the conduction band and holes in the valence band of the well are consequently confined in one direction, leading to a quantization of their energy; the carriers may only exist in a set of discrete states with discrete energies. The well's z-dimension (L_c) is comparable to the de Broglie wavelength of the electron or hole.

In order to understand the advantages of a quantum well as a gain medium over bulk semiconductor, it is necessary to consider the wavefunction of an electron in the semiconductor ($\psi(z)$), and the Schrödinger equation, of which it is a solution:

$$\left[\frac{1}{m^*}\frac{d^2}{dz^2} + V(z)\right]\psi(z) = E\psi(z) \tag{2.2.3}$$

where m* is the effective mass of the electron (m^*_w in the well, and m^*_b in the barrier), and E is its energy [3]. V(z) describes the confinement potential of the well, and is given by:

$$\begin{aligned} V(z) &= 0 \quad |z| < L_c/2 \\ &= V_0 \quad |z| \geq L_c/2 \end{aligned} \tag{2.2.4}$$

which takes into account the fact that the well barriers are not infinite. For this reason, the wavefunction penetrates into the well barrier, and it is necessary to consider the Schrödinger equation solutions in the region of the well separately from the barriers. The solution within the well takes on the form

$$\begin{aligned} \psi(z) &= \sqrt{\tfrac{2}{L_c}} cos(k_n z), \quad n\ even, \\ &= \sqrt{\tfrac{2}{L_c}} sin(k_n z), \quad n\ odd, \end{aligned} \tag{2.2.5}$$

where k_n are the wavenumbers given by $k_n = n\pi/L_c$. Meanwhile, outside the well, $\psi(z)$ becomes:

$$\psi(z) = C_{\pm} exp(K_z^z), \ where\ K_z^2 = \frac{2m*_b}{\hbar^2}(V_c - E). \tag{2.2.6}$$

The wavefunction must be continuous at the boundary of the well, so it is necessary to match the solutions and their derivatives at the well/barrier interface. Thus, the even states are given by

$$\begin{aligned} \psi(z) &= C_2 cos k_z z, \quad &|z| \leq L_c/2 \\ &= C_3 exp(-K_z|z|), \quad &|z| > L_c/2. \end{aligned} \tag{2.2.7}$$

with the condition

$$\sqrt{E}\ tan\left[\frac{\sqrt{m^{*}E}}{2\hbar^{2}}L_c\right] = \sqrt{V_c - E}, \tag{2.2.8}$$

the solutions of which give the energies of the even states. Similar solutions exist for the odd states, where

$$\begin{aligned} \psi(z) &= C_1 sink_z z, & |z| \leq L_c/2 \\ &= C_3 exp(-K_z|z|), & |z| > L_c/2. \end{aligned} \tag{2.2.9}$$

with the condition

$$-\sqrt{E}\ cot\left[\frac{\sqrt{m^{*}E}}{2\hbar^{2}}L_c\right] = \sqrt{V_c - E}, \tag{2.2.10}$$

yielding a picture of the quantum well with finite barriers that takes the form of figure 2.4.

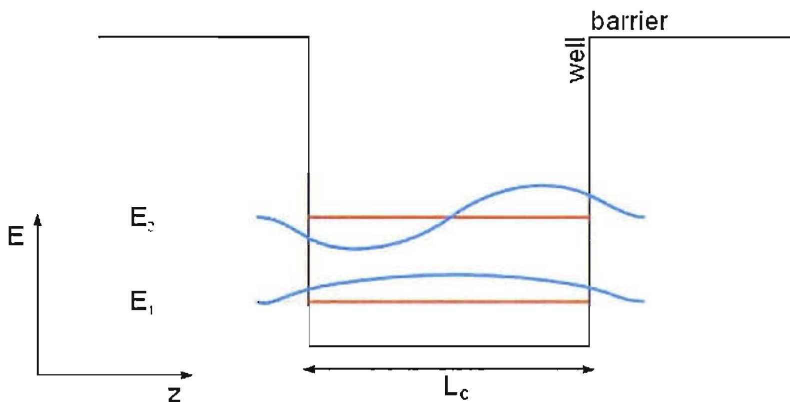

FIGURE 2.4: Diagram of the quantized energy levels (red) within a quantum well structure, and the corresponding wavefunctions (blue). Note the penetration of the wavefunction into the quantum well barrier since the barriers are not infinite.

We can understand the advantages of a quantum well over bulk semiconductor as a gain medium in terms of this quantization of energies by considering the density of states in each case. In bulk, the dimensions of the semiconductor are huge compared with the de Broglie wavelength, thus, the allowed momentum states of the carriers can be treated

as continuous variables, yielding a density of states in the conduction or valence band ($\rho(E)$) of the form [7]:

$$\rho(E)dE = \left(\frac{1}{2\pi^2}\right)\left(\frac{2m^*}{\hbar^2}\right)^{3/2}\left(E^{1/2}dE\right) \quad (2.2.11)$$

where the energy E is measured from the band edge up into the conduction band, or down into the valence band, m* is the effective mass of an electron in the conduction band, or a hole in the valence band as before, and $\hbar$ is the reduced Planck's constant.

In the QW, the reduction in the z-dimension of the well to a length comparable with the de Broglie wavelength, and corresponding quantization of energies restricts the consideration of the momentum in the z-direction, so that it can no-longer be treated as continuous. Thus the density of states for the energy interval dE becomes:

$$\rho(E)dE = \left(\frac{1}{2\pi^2}\right)\left(\frac{2m^*}{\hbar^2}\right)\left(\frac{\pi}{L_z}\right)dE, \quad E > E_1. \quad (2.2.12)$$

So, providing the energy is larger than the first allowed state (E_1), found by solving equation 2.2.10, the density of states is constant until the energy is sufficiently large to move to E_2, found by solving equation 2.2.8, and so on. The description above applies to both electrons in the conduction band and the holes in the valence band, but it must be noted that there are two types of holes present; light holes and heavy holes, with correspondingly different effective masses (m*). For our purposes, only heavy holes need be considered since the first energy state for light holes is far into the band in comparison.

The two resulting plots of density of states for bulk semiconductor and a quantum well are shown in figure 2.5. The advantages of the quantum well over bulk semiconductor as a gain medium are now clear: in the restricted state enforced in a quantum well, a larger number of electrons of the inverted population have the same energy within the conduction band, hence an incoming electromagnetic wave of the corresponding energy stimulates them much more effectively than if they were smeared out over a range of energies as in the bulk. Thus, the number of carriers required to reach transparency

is reduced. Further confinement in the remaining 2 dimensions to produce quantum wires and even dots would reduce this number further, however, such gain media are not employed here since a corresponding reduction in gain bandwidth is also observed, unsuitable for mode-locking.

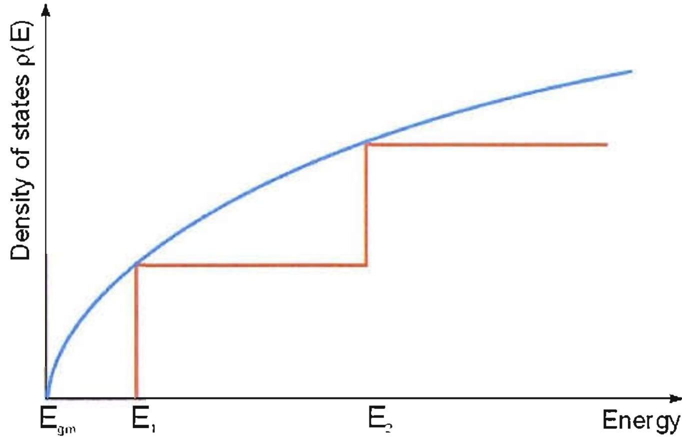

FIGURE 2.5: Graphical comparison of the density of states in a quantum well (red) with that of bulk semiconductor (blue) as a function of energy. The one-dimensional confinement of the quantum well results in a 'stair-step' density of states that lies within the parabolic density of states of the bulk. Note that E_1, the first allowed energy within the quantum well, is higher than the lowest energy bulk states, and is referred to as the confinement energy of the quantum well.

A diagram of a quantum well from the structures described in this thesis is shown in figure 2.6. E_1 is often referred to as the confinement energy of the well, and is added to the bulk bangap of the semiconductor material that composes the quantum well (E_{gm}) to give the QW bandgap energy, E_{gQW}. Thus, it can be seen in equation 2.2.10 that by varying the thickness of the quantum well (L_c), we can tailor the value of E_1 and hence E_{gQW}. Of course, E_{gQW} can also be varied by changing E_{gm}; using different alloy compositions for the well material.

For the design chosen here, the quantum well material is $In_{0.23}Ga_{0.77}As$ ($E_{gm} = 1.081$ eV [8]), whist the barriers are GaAs ($E_gb = 1.42$ eV [8]). The pump radiation ($h\nu = 1.494$ eV) is absorbed in the GaAs and the generated carriers drop down and become trapped in the QW. The requirement for gain at the design wavelength (photon energy $h\nu_0$) is that [8]:

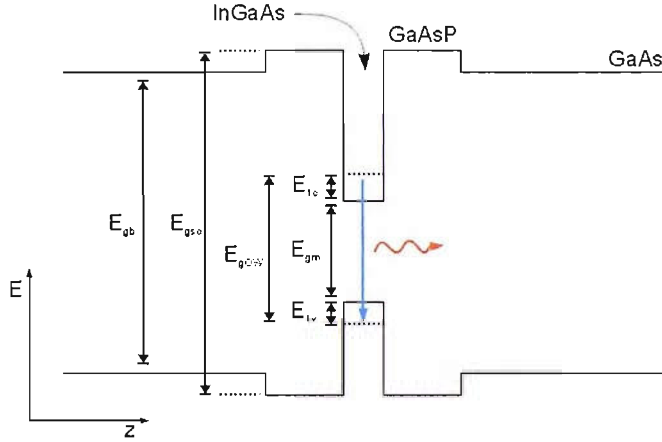

FIGURE 2.6: Diagram of the strain compensated QWs incorporated in the gain structures presented in this thesis, showing energy changes through the QW structure in the z-direction. E_{gb} is the bandgap energy of the QW barrier material which absorbs the pump light. E_{gsc} is the bandgap of the strain compensating layers. E_{gQW} is the effective bandgap of the quantum well that results from energy quantization. E_{1c} and E_{1v} are the confinement energies of the conduction and valence bands respectively. E_{gm} is the bulk bandgap energy of the quantum well material.

$$E_{gQW} \leq h\nu_0 < E_{fc} - E_{fv} \tag{2.2.13}$$

where E_{fc} and E_{fv} are the quasi fermi levels for the conduction band and valence band respectively.

From figure 2.1, it can be seen that the well/barrier materials are not lattice-matched, inducing strain in the structure, which can be advantageous in that it reduces the transparency electron density of the device [8]. However the lattice mismatch reduces the material stability, and can result in unsuccessful growth, or lattice relaxation effects that rapidly degrade the laser performance. To avoid these effects in the VECSELs presented here, $GaAs_{0.94}P_{0.06}$ strain compensation layers (the intermediate layers shown in figure 2.6) are grown either side of the quantum well, consequently, the QWs considered in this thesis are unstrained.

$GaAs_{0.94}P_{0.06}$ has a larger bandgap energy (E_{gsc} = 1.478 eV [9]) than GaAs, creating a small potential barrier for the carriers of approximately 54 meV, but the high capture efficiency of the quantum well, and relatively large diffusion distance of the carriers is thought to overcome this [9]. The quantum well thickness (L_c) was therefore selected

to be 8 nm giving a quantum well transition energy (E_{gQW}) of 1.218 eV, considering a $GaAs_{0.94}P_{0.06}/In_{0.23}Ga_{0.77}As/GaAs_{0.94}P_{0.06}$ QW, corresponding to the design wavelength of 1020 nm, to account for the faster shift of QW emission wavelength with temperature to be measured in chapter 3. The L_c parameter is fine-tuned by the grower in several test growth runs with corresponding PL measurements to compensate for any shifts from the theoretical value due to growth temperature and strain.

2.2.3.2 The Microcavity

In order achieve efficient performance from the VECSEL sample, it is necessary to ensure optimal pumping of the quantum wells within the active region. The design of the region of absorbing GaAs barriers and InGaAs quantum wells plays a crucial role in this optimisation: to extract maximum gain, the positioning of the quantum wells within the active region must be considered, as well as the length of the region itself.

To avoid unnecessary waste of the incident pump radiation, the active region must be long enough to ensure that the majority has been absorbed by the time it reaches the DBR. Furthermore, any light that does penetrate through to the DBR will be absorbed in the GaAs DBR layers, causing heating which could be detrimental to the laser performance. The absorption coefficient of the GaAs barriers for light with at wavelength of 830 nm is 15.1×10^3 cm^{-1}, and for the strain compensating GaAsP layers, 8.4×10^3 cm^{-1} [10], so the sample designs described in this thesis contain an active region that is $7\lambda_0/2$ long (λ_0 = VECSEL design wavelength), allowing absorption of 79% of the pump before the DBR is reached.

The active region is sandwiched between an AlAs window layer, and the DBR. Within this front section of the sample, the double-pass of the laser mode establishes a standing wave pattern, with an anti-node defined at the front surface of the DBR for the lasing wavelength as shown in figure 2.7. This dictates the suitable positions for the quantum wells; at the subsequent antinodes within the active region, to ensure they see the maximum possible gain (a configuration often referred to as resonant periodic gain [11]). Moreover, in order to reduce laser threshold, and minimise parasitic losses, the proportion of excited carriers supplied to each well from the barriers should be equal,

hence, to compensate for the decrease in pump intensity due to absorption and subsequent reduction number of carriers generated as distance into the structure increases, the quantum wells are positioned in the biased manner depicted in figure 2.7, with 2 quantum wells under the first antinode of the microcavity standing wave, 1 QW each under the following three antinodes, an unoccupied antinode, and then one QW under the final antinode.

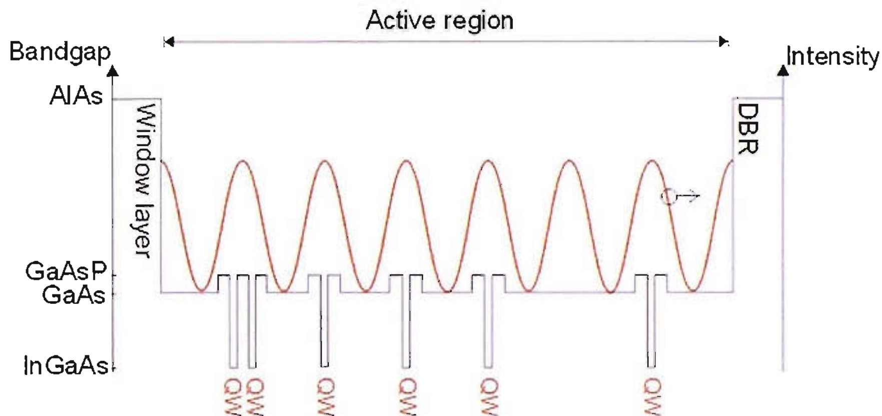

FIGURE 2.7: Diagram showing the structure as a function of material bandgap, and the $|E^2|$ intensity distribution (red) within the gain sample active region. The quantum wells are positioned at the antinodes of the $|E^2|$ standing wave in a biased fashion to allow for pump absorption as described in the text.

This total of 6 quantum wells is lower than the numbers used in VECSEL gain samples designed for high power operation [12]. The sample is designed for low power laser work, without the requirement for post-growth processing to achieve optimal operation: this low number of wells promotes a low lasing threshold with a high proportion of pump power per well, and consequently a lower transparency point, and reduced stimulated emission rates before this point is reached. However, the result of this low power design is that the rollover point (explained in section 2.3.3) is reached at a lower power, and the slope efficiency of the device is lower.

2.3 Structural Properties of VECSELs

The complete gain sample structure is shown in figure 2.8, including the active region and DBR already described. On top of the active region, an AlAs window layer is grown

to confine photo-excited carriers to the active region. The thickness of this layer can be altered to tailor the properties of the gain structure to compliment the function of the VECSEL into which it will be integrated. A small capping layer is grown on top of this window to protect the sample from degradation via oxidation of the aluminium containing layer. The following subsections will describe the effects of the multilayer structure on the properties of the laser, and highlight the design considerations necessary to optimise these effects.

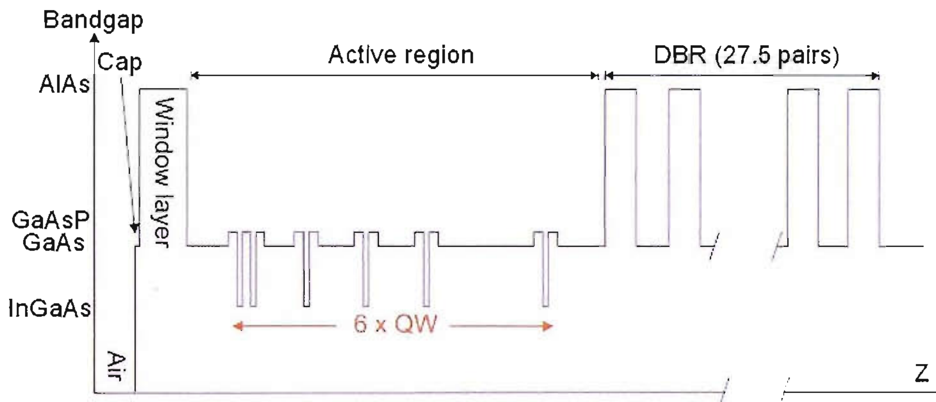

FIGURE 2.8: Design of the gain structures incorporated in the VECSEL devices presented in this thesis, consisting of a 27.5-pair AlAs/GaAs or AlAs/AlGaAs DBR structure grown behind a GaAs active region containing InGaAs QWs with GaAsP strain-compensating layers, capped with a variable thickness AlAs window layer and a 10 nm-thick GaAs protective capping layer.

2.3.1 Microcavity Enhancement Factor

It is clear that the positioning of the quantum wells under the antinodes of the standing wave is only accurate for the design wavelength; as emission wavelengths migrate away from this, the positions of the antinodes shift, so that the quantum wells emit decreasing quantities of stimulated photons at wavelengths with increasing migrations from design. This can limit the gain spectrum of the quantum well device, but also act to enhance performance at the design wavelength.

This effect can be quantified either experimentally, by dividing the top photoluminescence (measurement described in section 3.4.2) by the edge-emitted photoluminescence (measurement described in section 3.4.1), or by calculation using the multilayer method

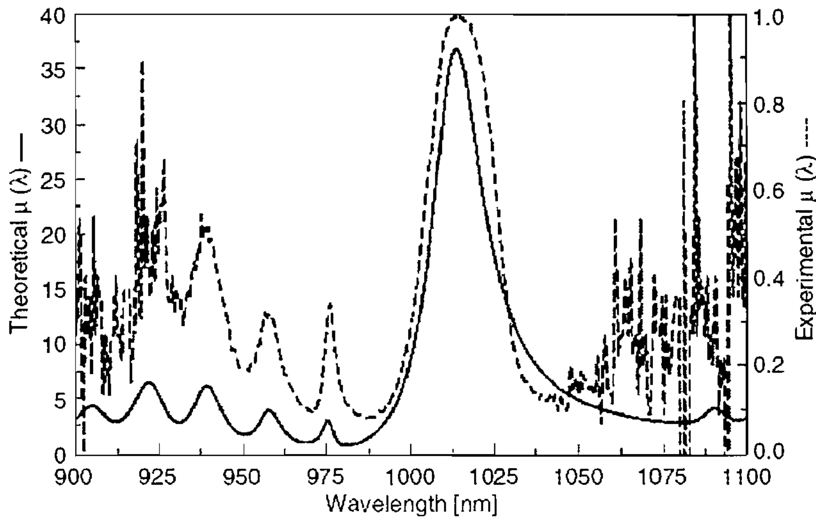

FIGURE 2.9: Calculated and experimentally derived microcavity enhancement factors of the antiresonant VECSEL structure (sample QT1544 analysed) as a function of wavelength, described in the text, taken from [6].

described in [6] (see appendix A). These experiments and the calculation were carried out in [6] for sample QT1544, a near-antiresonant VECSEL grown to the design presented in this chapter, defining a quantity known as the microcavity enhancement factor ($\mu(\lambda)$) for the sample. The microcavity enhancement spectrum obtained is shown in figure 2.9. Outside of the region around the enhancement peak, the experimental spectrum is dominated by noise and is inaccurate, moreover, the experimental spectrum shows the shape of the enhancement, but not the absolute value, with a reduction in the ratio between the height of the peak to the side-lobes, this is attributed to growth discrepancies in the structure causing layer thicknesses to vary slightly from design. The microcavity enhancement factor ($\mu(\lambda) = 25$) was determined from these data, taken as 75% of the calculated peak to account for the growth discrepancy, and will be used in section 3.4.2.1 in calculaton of the quantum efficiency of the sample.

2.3.2 Fabry-Perot Sub-Cavity

From the structure design shown in figure 2.8, it can be seen that a subcavity can be formed between the front of the sample and the front of the DBR: the interface of the top semiconductor layer with air forms a highly reflective surface compared with the

semiconductor-semiconductor interfaces within the sample. Thus, a Fabry-Perot etalon is established in the subcavity, with corresponding intensity transmission peaks at its resonant wavelengths [13].

The samples grown from the designs proposed here are intended for integration into mode-locked VECSELs: the ultrashort pulses produced have broad spectra with bandwidths of several nanometers, and require spectral tunability to access the appropriate regime (to be discussed in section 2.4.2), thus, a gain sample with a correspondingly broad effective gain spectrum is required. The material gain of the semiconductor quantum well system designed for emission at 1020 nm is amply broad (20-30 nm), however, the microcavity properties of the sample structure described in the previous section, and the Fabry-Perot cavity modify this gain spectrum, giving much narrower effective gain.

The Fabry-Perot properties of the subcavity dictate that the longer the subcavity, and the more reflective the interfaces at either end, the more defined its transmission peak, and hence the narrower the effective gain spectrum. The relatively short active region of the samples described here compared with other structures helps to overcome this gain narrowing issue, however, it is possible to control coupling into the Fabry-Perot subcavity, and achieve much more stringent gain spectrum control.

There are two extreme Fabry-Perot cases: resonant and antiresonant [14], depicted in figure 2.10. In the resonant case (figure 2.10a), the AlAs window layer at the front of the active region is designed to be an integer multiple of $\lambda_0/2$ thick (λ_0 = design wavelength). Thus, with an antinode already defined at the front surface of the DBR, and an active region that is $7\lambda_0/2$ thick, another antinode is located at the front surface of the sample. As a result, the subcavity operates on resonance at the design wavelength, and the effective gain bandwidth is limited by the width of the resonance. However, such a structure gives strong coupling of the incident electric field intensity ($|E^2|$) into the structure, resulting in $|E^2|$ in the wells that is 3-4 times that of an off-resonant structure. This is advantageous in reducing the threshold of the device. Such resonant samples are suitable for application in high power, CW, narrow-linewidth VECSELs. However, careful sample design and thermal management is required to ensure that

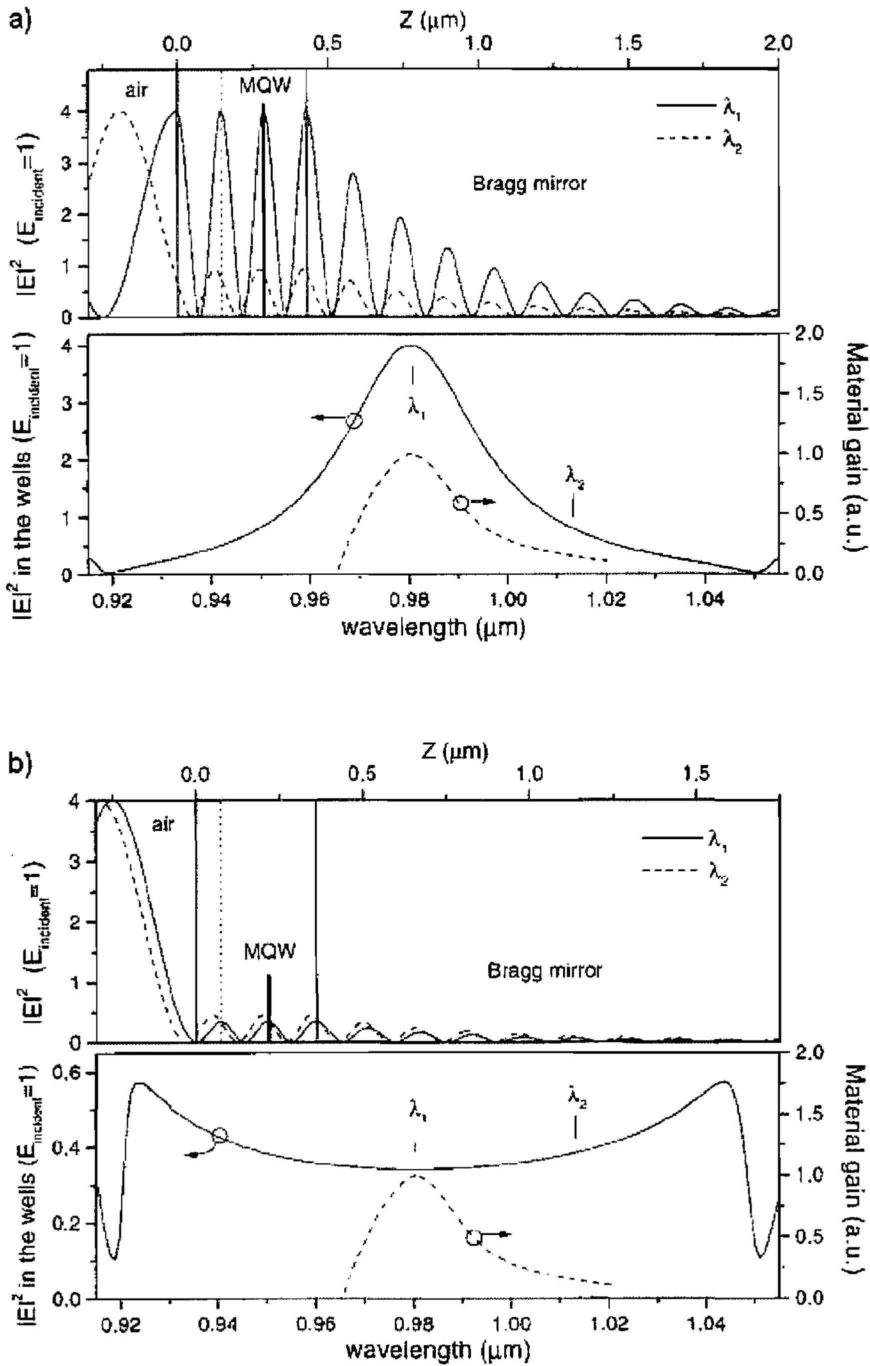

FIGURE 2.10: Spatial and spectral distributions of $|E^2|$ in a) resonant and b) antiresonant VECSEL gain structures taken from [14]. Note the strong coupling of the $|E^2|$ into the resonant structure compared with the antiresonant, and the corresponding narrowing of the $|E^2|$ spectrum as a result of the resonance. The material gain is also shown (dashed) and its relationship described in the text.

at maximum power, the material gain peak and resonance conditions coincide. The wavelength tunablity of such devices is significantly reduced.

In the case of antiresonant design (figure 2.10b), the AlAs window has a thickness of an odd number of $\lambda_0/4$. This defines a node at the front surface of the sample, and thus the $|E^2|$ coupling into the structure is weak ($1/n_{GaAs}$), giving a high threshold. However, the wavelength dependence of the $|E^2|$ on the wells is dramatically reduced, coinciding with the broad minimum of the Fabry-Perot transmission spectrum at the design wavelength; the effective gain profile now strongly resembles that of the material gain.

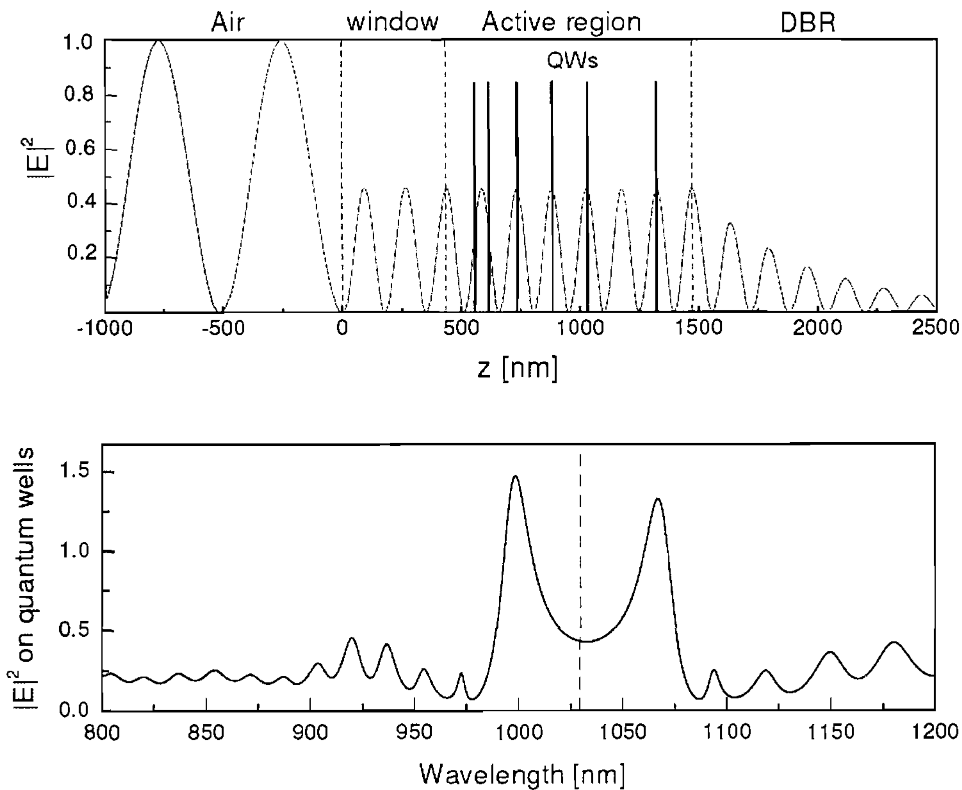

FIGURE 2.11: Spatial and spectral $|E^2|$ distributions in the near-antiresonant VECSEL gain structures designed in this chapter, modified from [9], for comparison with figure 2.10.

The gain samples used in the work contained in this thesis have subcavities designed to operate at a compromise between these two Fabry-Perot cases, drawing on the advantages of both. The AlAs window thickness is 1.45 $\lambda_0/4$, resulting in an off-resonant subcavity, with an average $|E^2|$ spectrum on the quantum wells shown in figure 2.11.

The intensity spectrum is broad around the design wavelength, rising to resonance peaks at approximately 30 nm from the design wavelength on either side. The stronger $|E^2|$ coupling at wavelengths away from the design wavelength acts to compensate for the reduction in material gain at these migrations, resulting in an effective gain spectrum that is broader than the material gain, permitting broad lasing spectra suitable for short-pulse mode-locking, and great wavelength tunability of the resulting devices.

2.3.3 VECSEL Thermal Response

When designing a VECSEL structure, it is important to consider the thermal response of its various components; the gain structure will be subjected to heating of the DBR layers via absorption here of any residual pump light not absorbed in the active region. Moreover, non-radiative effects and spontaneous emission act to drain available pump power, and cause further heating of the structure. Temperature dependent spectral shifts of quantum well emission and refractive index of the constituent layers of the structure are observed in response to these heating effects: the temperature-dependent changes in the bangap of the quantum wells and barriers gives a shift in QW emission of 0.33 nm/K, whilst the thermal expansion and refractive index changes of the various layers composing the sample leads to a shift in structure emission wavelength of 0.1 nm/K [15]. Methods used to measure these shifts are presented in chapter 3.

The result of these effects is a thermal misalignment of the sample's emission characteristics, shown schematically in figure 2.12. The quantum well emission (blue) is seen to 'walk through' the QW-absorption enhanced microcavity resonance (indicated by the dip in the stopband reflectivity curve shown in black). Lasing (red) is at the absorption-enhanced microcavity resonance wavelength, so it is most efficient, and capable of yielding the highest power when the QW peak PL wavelength and the microcavity resonance wavelength coincide. Either side of this point, the amount of energy lost to fluorescence and non-radiative effects is increased. This effect is much more prevalent for resonant-grown VECSELs, where the effective gain bandwidth is greatly reduced. For these devices, post-growth processing for thermal management is often required, as will be discussed in chapter 4.

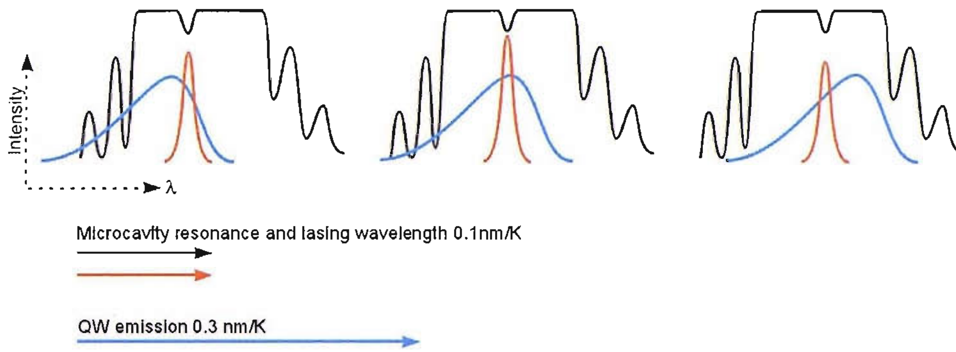

FIGURE 2.12: Spectra of quantum well emission (blue), sample reflectivity (black) and lasing spectrum (red) for three values of sample temperature, showing the rollover effect described in the text.

Eventually, as pumping and hence heating of the structure is increased, the output power of the VECSEL is seen to 'rollover', passing through a maximum, and then decreasing back to zero as a result of this thermal misalignment. Furthermore, other contributions to this rollover come from an increase in the non-radiative recombination rate. Auger recombination is a power-dependent non-radiative recombination effect observed in semiconductor devices [16]. This is a many-body effect where two energetic electrons collide, promoting one further into the conduction band whilst the other, as dictated by energy conservation, falls down to the valence band. The promoted electron eventually thermalizes back down to the bottom of the conduction band, releasing its extra energy as thermal energy, acting to heat the semiconductor. The reverse case happens for holes in the heavy hole band. Since this effect is carrier-density dependent, its effect on the output power and efficiency of the device increases with more pumping, and can eventually dominate over stimulated emission rates whilst also causing extra heating. The effects of thermal rollover are observed in chapter 3.

To compensate for these effects, and ensure that the QW emission and the desired microcavity configuration coincide at high pump power at room temperature, the design wavelengths of the quantum wells and the rest of the structure are offset both from each other, and from the desired lasing wavelength.

2.3.4 Group Delay Dispersion

Since the sample designs presented here are for application in pulsed VECSELs, it is necessary to consider the effects that a pulse will experience when it encounters the structure. Mode-locking theory in relation to these samples will be discussed in later sections: as already highlighted, the spectrum of a short pulse is broad, and whilst the use of antiresonant design, and the broad gain bandwidth available from the semiconductor system permit the VECSEL gain sample to support such pulses, it is also necessary to consider the dispersion of the structure.

In section 2.2.1, equation 2.2.1 shows the wavelength-dependency of the refractive index of $Al_xGa_{1-x}As$, known as its dispersion relation $\beta(\omega)$. Thus, it is apparent that as a pulse with a broad spectrum $(\Delta\omega_L)$, centred at the lasing frequency ω_L, passes through a structure, different spectral regions of the pulse will travel with different velocities, resulting in a temporal broadening of the pulse. The E-field of the output wave can be written as $E = A_0 expj(\omega t - \beta z)$, where A_0 is a constant [13]. The total phase of the wave is now $\phi_t = \omega t - \beta z$.

Observation of the dispersion relation in equation 2.2.1 shows that the relation between ϕ and ω can be approximated by a parabolic law such that

$$\phi = \phi_L + \left(\frac{d\phi}{d\omega}\right)_{\omega_L} (\omega - \omega_L) + \frac{1}{2}\left(\frac{d^2\phi}{d\omega^2}\right)_{\omega_L} (\omega - \omega_L)^2 \qquad (2.3.1)$$

where ϕ_L is a constant phase shift which has no effect on the pulse, $\frac{d\phi}{d\omega}$ gives a shift of the pulse in time, and $\frac{d^2\phi}{d\omega^2}$ describes the time delay between the fastest and slowest spectral components of the pulse, i.e. the pulse broadening. Thus the pulse broadening $(\Delta\tau)$ due to dispersion experienced by a pulse passing through a length l of material can be written as

$$\Delta\tau \cong l\left|\left(\frac{d^2\phi}{d\omega^2}\right)\omega_L\right|\Delta\omega_L = |\phi''(\omega_L)|\Delta\omega_L. \qquad (2.3.2)$$

$\phi''(\omega_L)$ is the group delay dispersion (GDD) of the material at frequency ω_L. A theoretical calculation of the GDD of the near-antiresonant gain structure design presented in this chapter using the multilayer calculation method presented in [6] (see appendix A), yields the data shown in figure 2.13. At the desired lasing wavelength (λ_{stark}) the GDD is small (a few hundreds of fs^2) and positive. Thermal tuning of the lasing wavelength allows tuning of the GDD to achieve the shortest pulses. GDD is also introduced by the cavity mirrors ($\sim$ 20fs^2), and the SESAM (varying from -10 fs^2 to -40 fs^2, also tunable, for the Stark SESAM described in section 2.4.2). The ideal total value of GDD to be introduced into a VECSEL cavity in order to produce unchirped pulses has been modelled to be small and positive [17], with optimal pulse lengths with minimal chirp being achieved experimentally at GDD values between +200 and +500 fs^2 [18].

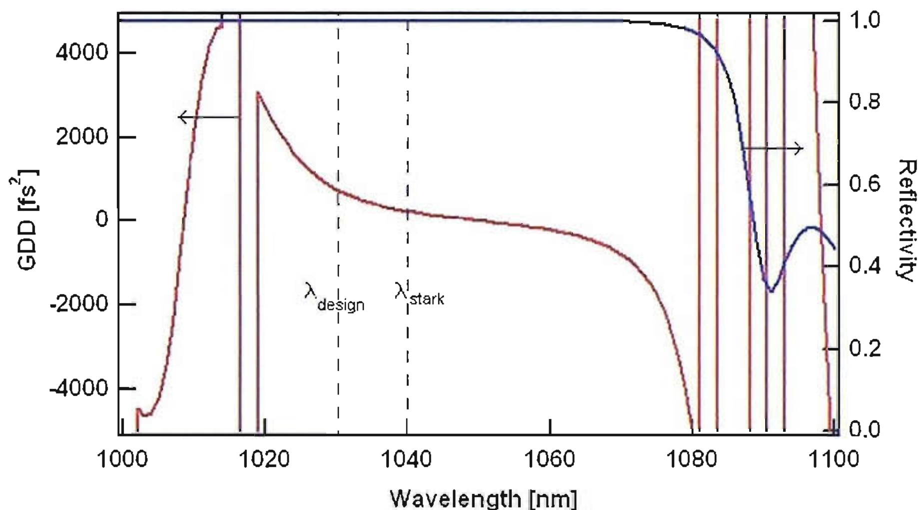

FIGURE 2.13: Graph to show how the GDD introduced by the antiresonant gain sample design varies with wavelength (red), and the corresponding reflectivity of the sample (blue). Note the broad region of slowly varying GDD around the Stark and design wavelengths (λ_{Stark} and λ_{design}), allowing temperature tuning of the GDD introduced by the sample around these wavelengths to optimise pulse characteristics as discussed in the text.

2.4 Mode-Locking VECSELs

This thesis primarily considers mode-locked operation of VECSELs. In CW operation, a laser may oscillate in a large number (N) of longitudinal modes, equally spaced in frequency with $\Delta\nu$ separation between consecutive modes, giving a total oscillating

bandwidth, $\Delta\nu_L$ of $N\Delta\nu$ [13]. All of the longitudinal modes have random phase, but equal amplitude (E_0), resulting in a random time behaviour of the laser intensity which appears as a random sequence of light pulses in the output waveform. Despite this randomness, these properties of the laser waveform dictate that it has features characteristic of a Fourier series: it is periodic with a period of $\tau_p = 1/\Delta\nu$.

If the laser is now modified in some way to force the longitudinal modes to oscillate with a definite relationship between their phases, the oscillating modes interfere, producing a train of evenly spaced pulses in the output waveform. This process is known as mode-locking. Each pulse has a duration $\Delta\tau_p$ which is $\approx 1/\Delta\nu_L$. Thus, it is clear that for a laser with a very large gain bandwidth, it is possible for $\Delta\nu_L$ also to be very large, resulting in very short pulses in the output waveform. Thus, the large gain bandwidth of the semiconductor quantum well system described above is suitable for producing short pulses of the order of pico- or femto-seconds in length, and the importance of maximising the effective gain bandwidth of the gain chip through the design considerations incorporated above can be appreciated.

It is important to consider that in a real system, the modes tend not to have equal amplitudes, but instead have some distribution about a central mode with maximum amplitude. This is reflected in the temporal pulse envelope, which in the ideal case is a Fourier transform of the amplitude distribution. Thus, the pulse width ($\Delta\tau_p$) is related to the width of the laser spectrum by $\Delta\tau_p = \beta/\Delta\nu_L$, where β is a numerical factor called the time-bandwidth product. Values of β for ideal Gaussian and hyperbolic secant shaped pulses are 0.441 and 0.315 respectively [19], if a pulse of a certain shape has the corresponding β, it is said to be Fourier-limited. Often, additional phase shifts will increase the pulse length, resulting in chirped pulses with an increased β value. In order to realise the shortest possible pulse for the available lasing bandwidth, it is necessary to compensate for these phase shifts, one method for doing so is the GDD control described in section 2.3.4.

In order to establish the phase relationship between the modes of the cavity, and hence mode-lock the laser, an intracavity fast shutter is required. The shutter may be active or passive; the former being driven by an external source, whilst the latter employs a

nonlinear optical response of a material. In a passively mode-locked laser, the largest spike in the noise sees the least attenuation at the shutter, becoming stronger each time it passes the shutter whilst the rest of the noise is suppressed. In this picture, a pulse builds up from the noise of the laser, and eventually, the output of the laser is a train of pulses separated by the cavity round-trip time.

In this system, it is important that the shutter closes quickly after the pulse has passed, so it is essential that the non-linear response of the material recovers quickly. The pulse length and shape are greatly affected both by the length of time that the shutter is open, and by this recovery time and shape. In an actively mode-locked device, the stability of the pulse train is reliant on that of the external driver and the feedback mechanism that controls it. Consequently, passive mode-locking is the preferred choice for producing stable, ultrashort pulses. Passive mode-locking of the VECSELs presented in this thesis is achieved by inserting a semiconductor saturable absorber mirror (SESAM) into the cavity. The operation of these devices is described in the following section.

2.4.1 SESAM Mode-Locking

The SESAM was introduced in the early 1990s as a device to passively mode-lock solid-state lasers to achieve ultrashort pulses [1, 20]. Their operation relies on the saturation effects of semiconductor quantum wells; as the pulse passes the quantum well, the bands fill up with carriers, and its absorption coefficient falls, the pulse is then reflected by a DBR grown behind the quantum well and experiences minimal attenuation by the QWs. Once the pulse has passed, the quantum well recovers and begins absorbing again. The operation of the device is independent of wavelength providing that the centre wavelength of the pulse is above the quantum well bandgap. The only requirement is that the incident energy per unit area is sufficient to saturate the SESAM; this threshold value is referred to as the saturation fluence (F_{sat}) of the device.

Typically, the recovery of the quantum well is bi-temporal [21]: there is an ultra-fast decay of the order of tens of femtoseconds arising from intraband carrier-carrier scattering and thermalization processes whilst a longer recovery time of the order of picoseconds to nanoseconds arises from interband trapping and recombination processes. This longer

recovery time is a drawback of the quantum well for use as a mode-locking shutter as it creates a bottle-neck for the carriers, and does not close the shutter quickly, limiting the shortest pulse lengths possible. Investigations into reducing this recovery time have had some success in forcing carriers to recombine via defects in the crystal lattice created for example by introducing dislocations and impurities through low temperature growth [20], proton bombardment [22] or ion implantation [23]. The SESAMs used in this thesis to achieve 4-ps pulses employ low temperature growth, whilst in the case of the Stark SESAM used to produce sub-ps pulses in section 2.4.2, a fast surface recombination effect is employed which will be explained in section 2.4.2.2.

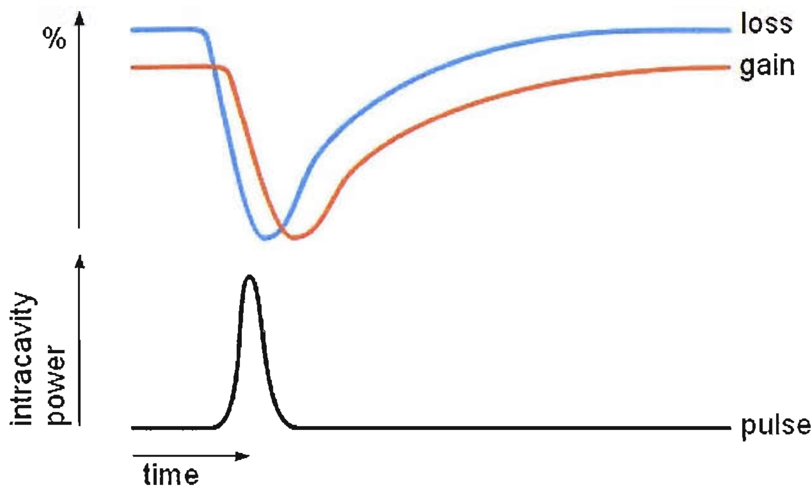

FIGURE 2.14: Diagram showing the principle of operation of a slow saturable absorber in the steady state; the loss introduced by the saturable absorber (total cavity loss is shown in blue) saturates before the gain (total cavity gain shown in red) when the pulse (black) is incident, creating a window of net gain. Both recover to a steady state where loss is greater than gain so there is no lasing between pulses.

Stable, passively mode-locked trains of short pulses are achieved by using the SESAM as an end mirror of the cavity. This creates a window of net gain at the point in time when the pulse is incident on the SESAM, achieved through the slow saturable absorber effect and dynamic gain saturation [24]. The mechanism is depicted in figure 2.14: the SESAM saturates faster than the gain, forming the window of net gain as the cavity loss falls below the cavity gain. The fast recovery of the SESAM allows this loss to rapidly rise again, closing the net gain window, and allowing the gain to recover slowly, staying below the loss until the next pulse arrives. The slower recovery component of

the SESAM defines the extent of the pulse and its shape since the pulse is sensitive to the net loss immediately before and after the gain window.

Since the SESAM incorporates the saturable absorber on top of a mirror, the percentage of the saturable loss of the device, referred to as its modulation depth, can also be considered as the change in reflectivity of the mirror, ΔR. ΔR must be sufficiently large to allow the SESAM to have a strong effect, and hence the mode-locking onset time to be short enough that spectral condensation that occurs during lasing build up, which narrows the available bandwidth for mode-locking, is not too far advanced. However, such large ΔRs increase the likelihood of Q-switching instabilities in the laser, particularly at high repetition rates [25]: there is a clear trade-off between the two effects, and ΔR typically has a value of $\leq$1%. In addition to the saturable losses of the SESAM, non-saturable losses are also present, it is essential to keep these to a minimum ($<$ 1% in the case of ML-VECSELs) since they reduce the saturable loss of the device, and increase its insertion loss.

A typical SESAM for use in lasers emitting at wavelengths around 1 μm contains one InGaAs/GaAs QW grown at $\sim$300 ^oC in a GaAs subcavity on top of a GaAs/AlAs DBR similar to that described in section 2.2.2. The positioning of the QW within the subcavity allows tailoring of the modulation depth and saturation fluence of the SESAM by altering the $|E^2|$ on the QW, control of this property is crucial for application of SESAMs in high repetition rate VECSELs as will be described in chapter 6. Typical saturation fluences of such SESAMs are of the order of some tens of $\mu J/cm^2$.

2.4.1.1 SESAM Mode-Locked VECSELs

VECSELs are well suited to mode-locking with a SESAM: their external cavity allows insertion of the SESAM device to create an all-semiconductor ML laser. The high differential gain of the quantum well gain medium of a VECSEL provides freedom from the Q-switching instabilities exhibited by its SESAM mode-locked solid-state counterparts even at low-GHz repetition rates [10] (although this may become a problem for higher repetition rate VECSELs discussed in chapter 6), permitting greater freedom in SESAM design.

In order to successfully mode-lock a VECSEL using a SESAM, the bandwidth and GDD restrictions already discussed apply, but it is also important to consider the saturation of the SESAM. The window of net gain depicted in figure 2.14 is created as the SESAM saturates before the gain. In a ML-VECSEL, the SESAM and gain chip are both based on semiconductor quantum well systems, and thus have very similar saturation energies, this is not the case for the solid-state counterparts of the VECSEL which typically have saturation energies three orders of magnitude larger than the quantum well [6]. Thus, it is necessary to focus the cavity mode more tightly on the SESAM than the gain chip, increasing the energy fluence on the SESAM compared with the gain chip; achieved in the lasers presented in this thesis by using the Z-cavity configuration as described in section 2.4.2 and appendix B. The ratio of the modal areas is around 1:10-20, providing a fluence on the SESAM of the order of some hundreds of $\mu J/cm^2$, amply saturating it before the gain.

The first passively mode-locked VECSEL was demonstrated in 2000 in a collaboration between Southampton University and ETH Zurich [26]. The authors achieved 22 ps-long pulses with a central wavelength of 1030 nm at a repetition rate of ~4 GHz. A low-temperature grown SESAM was used, which had a bitemporal response with a 130 fs fast component and a 4 ps 1/e recovery time. Mode-locking using a similar SESAM was carried out as part of the work described in this thesis in sections 5.3.1 and 5.4.1, where 4 ps pulses were achieved. This improvement in pulse length is attributed to the use of a near-antiresonant designed gain sample as described earlier in this chapter and better growth, similar pulse lengths using low-temperature SESAM designs have been observed elsewhere [27, 28].

2.4.2 Sub-Picosecond Pulses from a ML-VECSEL

As discussed in chapter 1, the potential advantages of a VECSEL over its solid state counterparts are clear. However, there is still much scope for improvement in the VECSEL field before some solid state laser achievements are realised, let alone surpassed by the VECSEL. Mode-locked solid state lasers producing pulses as short as a few femtoseconds have been demonstrated [29]; until such short pulses can be realised from a

VECSEL, solid state lasers will continue to dominate as sources of ultra-short pulses for a broad range of applications. In ML-VECSELs employing the low-temperature grown SESAM described in the previous section, the pulse length remains limited by the inherent carrier-dependent recovery time of the SESAM, restricted to pulse lengths around 4 ps. It is necessary to employ other effects in the SESAM to achieve further decreases in pulse length.

The following sections describe the modified design of SESAM used in a ML-VECSEL to achieve sub-500 fs pulses. Initially the structure of this modified absorber appears similar to that of a slow saturable absorber. However, in addition to the effects of slow saturable absorption, two other key effects are exploited to produce shorter pulses. These are the optical Stark effect, and the effect of fast surface carrier recombination. The use of such a SESAM to mode-lock a VECSEL was first reported in [18]: this remains the shortest reported pulse achieved directly from a passively mode-locked VECSEL.

2.4.2.1 Optical Stark Effect

The optical Stark effect was first observed in GaAs/AlGaAs quantum well structures by Mysyrowicz et al in 1986 [30]. They observed a sub-picosecond blue-shift of the spectrum of the exciton in the presence of a short optical pulse. After the shift, the system returned to its original state without delay, indicating that no population of excitons or carriers is produced during the shift. The effect operated over a bandwidth measured to be approximately 3 nm.

In the SESAMs described here, the optical Stark effect is employed as a pulse shaping mechanism. The SESAM is designed so that the lasing wavelength lies just at the edge of the exciton wavelength. Mode-locking is initiated and builds up via the slow saturable absorber effect described in section 2.4.1. Once the pulse is sufficiently strong, it starts to excite the Stark shifting of the exciton resonance. This blue shifts the exciton out of the pulse spectrum and enhances the reduction in absorption seen by the pulse, acting as an additional fast shaping effect. The strength of the Stark effect is intensity dependent, and consequently provides shortening of the pulse beyond that of the saturable absorption effect with the more intense peak of the pulse seeing a

more dramatic reduction in absorption. The femtosecond response times and immediate restoration of the system to its original condition further enhance the pulse shaping effect since there is no 'recovery time' of the effect.

The use of the Stark effect in this way makes the SESAM wavelength-dependent, and consequently limits the wavelength versatility of the SESAM itself to within the 3 nm bandwidth of the Stark effect. The wavelength tunability of the gain sample with temperature allows the operator to tune the laser to operate in the Stark regime. The problem is further addressed by incorporating a quantum well in the SESAM that has the same design as those in the gain sample, aside from strain compensation which is deemed unnecessary for such a structure where any extra dislocations added by strain would actually be advantageous to the operation as indicated in the next section.

2.4.2.2 Fast Surface Recombination

Outside of the Stark bandwidth, the Stark SESAM still demonstrates the saturable absorber effect, and can mode-lock the laser to produce 2.3 ps pulses as described in [31], still shorter than those achieved from the low-temperature grown SESAM used previously. These shorter pulses are achieved through another improvement to the SESAM: fast surface recombination. Previously, slow saturable absorbers have demonstrated recovery times into the hundreds of picoseconds providing the longer recovery component of their bitemporal response. This arises from the slow recombination of carriers trapped in the quantum well back out into the quantum well barriers. In the Stark SESAM shown here, this longer response is eliminated by the inclusion of fast recombination sites for the carriers, which accelerate the excited carrier recovery time of the SESAM through QW carrier tunnelling and trapping to surface states of the device.

The sites are achieved by positioning the quantum well in very close proximity to the front surface of the structure, the order of the evanescent wave penetration depth of the excitons from the GaAs/air interface, allowing carriers to tunnel out to the arsenic anti-sites located there. The resulting total carrier lifetime measured in the literature of an InGaAs quantum well located 2 nm from the sample surface with GaAs barriers

has been measured to be 21 ps, compared with lifetimes of the order of 100-200 ps for deeper quantum wells [32].

The Stark SESAM used to produce the sub-500 fs pulses presented in this thesis and in [18] operating in the Stark regime, and 2.3 ps pulses presented in [31] operating outside of the Stark regime, was characterised in a similar way to the low-temperature grown SESAM, and yielded a 1/e recovery time of ~2.1 ps. This indicates that the improvement in pulse length achieved using this device outside of the Stark regime from 4 ps to 2.3 ps pulses can be attributed to the fast surface recombination effect. This measurement will be described in section 3.6.2.

2.4.2.3 Stark SESAM Design

The design of a SESAM for mode-locked operation in the Stark regime at 1040nm is shown in figure 2.15. It combines the elements outlined above. The DBR has the same design as that of the gain sample, with 30 pairs of GaAs/AlAs layers and a broad stopband, but this time centred at the desired lasing wavelength of 1040nm since there will be no heating of the SESAM by pump radiation. On top of this is a simple subcavity designed to be 0.68 $\lambda/4$ long. One InGaAs quantum well without strain compensating layers, designed for 1030 nm to allow for heating of the quantum well by the absorption it will perform, is grown with a 2 nm GaAs capping layer on top completing the well.

2.4.2.4 Lasing Results

The Stark SESAM was inserted into a VECSEL cavity containing a gain sample grown to the near-antiresonant design presented in this chapter. A z-cavity design was used, shown schematically in figure 2.16: the gain sample was pumped normal to its surface, and acted as a folding mirror, with one arm going to a 50 mm radius of curvature 0.8% output coupler, and the other at approximately 12° to it to a 25 mm radius of curvature focusing high reflector, then to the SESAM at approximately 6°. The design method for such a cavity is shown for completeness in appendix B, and uses the ABCD matrix approach [13]. The cavity configuration was closer to that of a concentric resonator, as

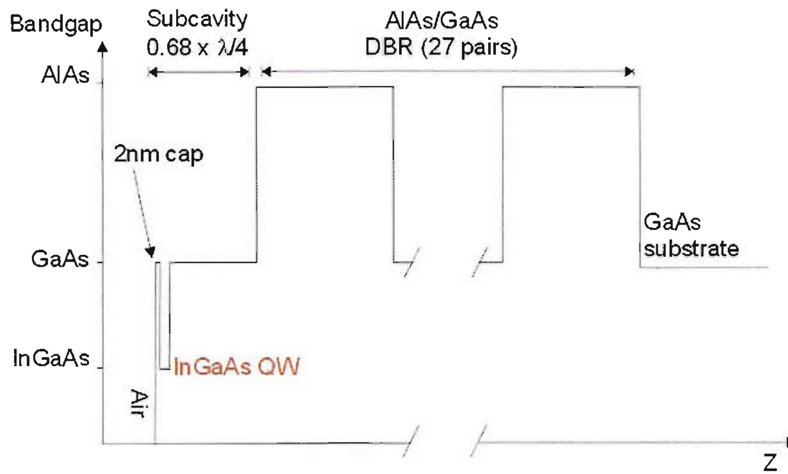

FIGURE 2.15: Design of the Stark SESAM, showing the InGaAs QW placed 2 nm from the front of the sample to enable fast surface recombination as described in the text. The QW is contained within a 0.68 × $\lambda/4$ GaAs subcavity grown on top of a GaAs/AlAs DBR.

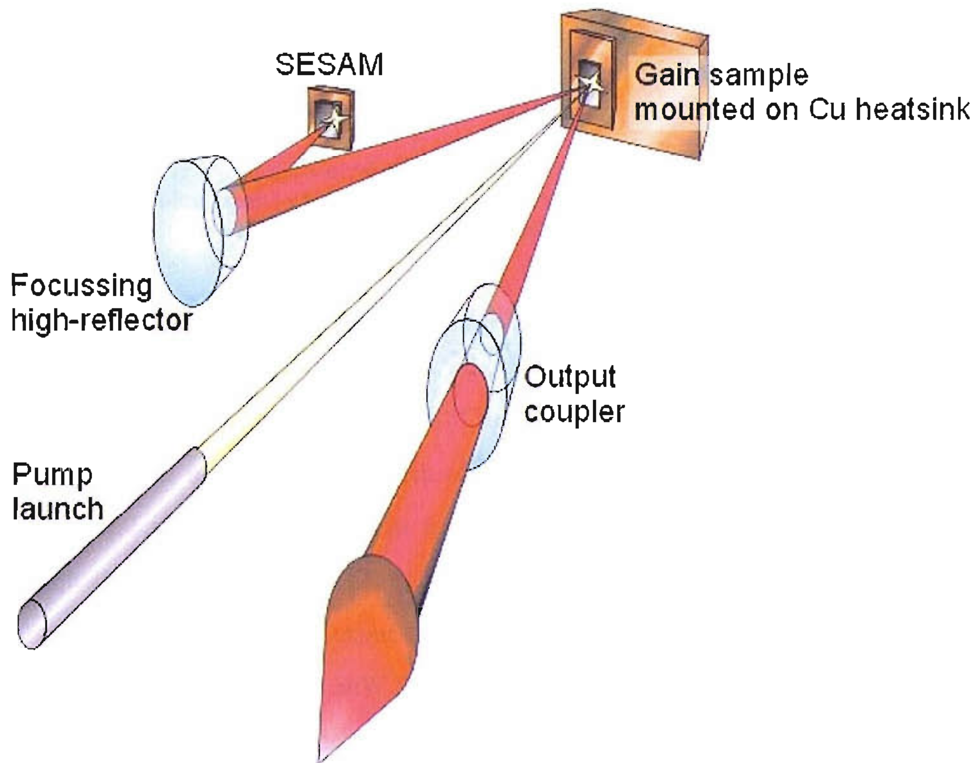

FIGURE 2.16: 4-mirror, Z-cavity design used for the VECSEL mode-locking presented in this thesis, incorporating a near-antiresonant VECSEL gain sample chip, suitable dielectrically coated mirrors and a SESAM as described in the text.

opposed to a more stable confocal configuration; here, Stark-enhanced ML was possible. The cavity mode was determined at the gain sample to mode-match with the focussed pump spot with a waist radius of 60 μm. Thus, using the cavity design calculations presented in appendix B, the spot on the SESAM had a waist radius of ~20 μm.

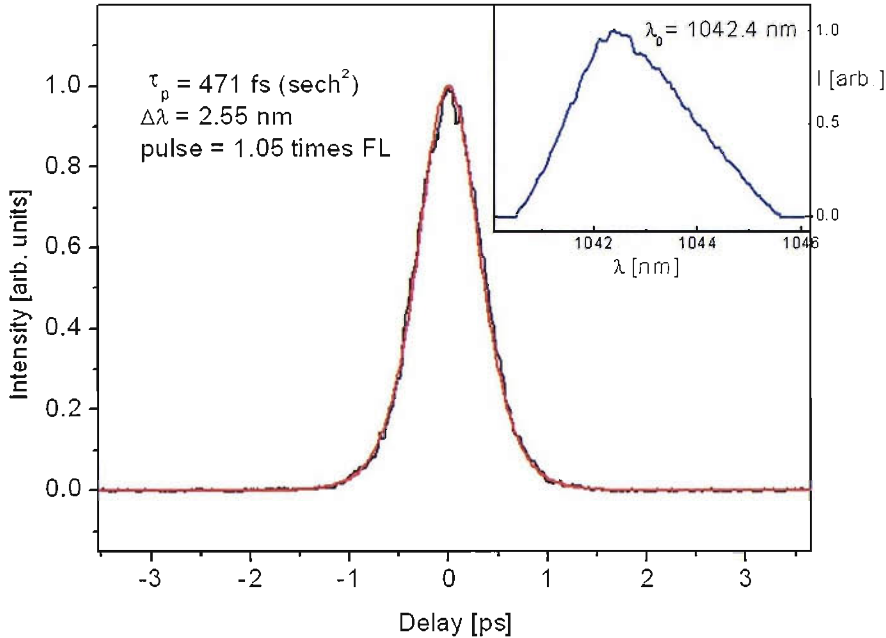

FIGURE 2.17: Pulse autocorrelation (black) with calculated sech^2 fit (red) and lasing spectrum (blue, inset) of a ML-VECSEL operating in the Stark regime. τ_p = pulse width (FWHM), $\Delta\lambda$ = spectrum bandwidth (FWHM), FL = Fourier limit.

The resulting pulse autocorrelation and spectrum are shown in figure 2.17. The cavity was optimised via temperature tuning and component positioning to yield a minimum sech^2 pulse autocorrelation length of 471 fs. The spectrum, centred at a wavelength of 1042.4 nm, had a FWHM bandwidth of 2.55 nm, corresponding to a time-bandwidth product that was 1.05 times Fourier limited (see section 2.4). In order to achieve these high quality pulses, the VECSEL gain sample was cooled to 0°C, the pump power was 650 mW and the VECSEL output power was correspondingly low (4.5 mW). Average output powers as high as 44 mW were achieved in the same cavity, but with a corresponding increase in pulse length and reduction in pulse quality thought to be caused by thermal de-tuning of the lasing wavelength from the optimal GDD introduced by the gain sample.

2.4.2.5 Stark SESAMs at other wavelengths: a case study

The GaAs/AlGaAs material system provides somewhat of a luxury when designing a Stark SESAM. When applying the design principles outlined above to other wavelengths, a SESAM incorporating fast surface recombination is not so readily realised. A peripheral project of this thesis was the design a Stark SESAM for use in a ML-VECSEL with a lasing wavelength of 840 nm for application in THz generation using low temperature-grown GaAs antennae: the design is detailed in this section, but unfortunately, the structure had not been grown before the completion of the work contained in this thesis, and so could not be tested.

Continuous wave VECSELs operating at 850 nm are well documented by Hastie et al [33, 34, 35, 36], incorporating VECSEL gain structures with GaAs quantum wells, $Al_{0.2}Ga_{0.8}As$ barriers, and $Al_{0.2}Ga_{0.8}As$/AlAs DBRs. It would be possible to adapt this design for a suitable antiresonant gain sample at a design wavelength of 840 nm. Indeed, the DBR layers could also be applied to a Stark SESAM at this wavelength. The design of the front subcavity requires more consideration though.

The initial problem encountered in the design of the SESAM is that of the 2 nm capping layer. In the Stark SESAMs designed for application at wavelengths around 1 μm, the InGaAs QW cap is a 2 nm-thick layer of GaAs, protecting the sample from surface contamination, and also acts as the barrier material of the quantum well forming a symmetrical well. The QW structures proposed for application at 840 nm have GaAs QWs with AlGaAs barriers. Thus, GaAs is eliminated as a barrier material, whilst the proposed barrier material readily oxidises due to its aluminium content, and so is not a suitable cap.

Suitable cap materials can be sourced from incorporation of indium and phosphide-containing layers into the structure. InP itself would provide a resilient capping layer, but is not lattice-matched to GaAs; inclusion of gallium into the InP overcomes this problem. The semiconductor materials in the $In_{1-x}Ga_xAs_yP_{1-y}$ group are lattice matched to GaAs when [37]:

$$x = \frac{1+y}{2.08 - 0.08y}. \tag{2.4.1}$$

In turn, the bandgap energy of those materials can be calculated using the following equation [37]:

$$E_g = 1.91 - 1.44y + 2.87y^2 - 3.23y^3 + 1.31y^4. \tag{2.4.2}$$

Using equations 2.4.1 and 2.4.2, the lattice matched material composition is found to be $In_{0.52}Ga_{0.48}P$, with a corresponding bandgap energy of 1.91 eV compared with 1.67 eV for the AlGaAs barriers in the gain sample. With such large bangap barriers, it would be necessary to include some aluminium into the GaAs quantum well to raise its bandgap.

However, the use of phosphide-based material is detrimental to the fast surface recombination process that is vital to the rapid recovery of these SESAMs. It is the arsenic vacancies in GaAs at the sample surface of the Stark SESAM that give it its characteristic recovery time. InP-based growth produces a lower surface state density, and thus a longer surface recombination time. The carrier lifetime in InP-based samples with an InGaAs QW positioned 1.5 nm from the sample surface has been measured to be 80 ps, compared with the 21 ps for the analogous AlGaAs-based device [32]. Asymmetric well design has improved on this problem, where the barrier material at the front of the sample has a lower bandgap that that behind the quantum well, decreasing carrier confinement in the well towards the surface of the sample, and increasing the tunnelling probability.

To apply this 'barrier tipping' technique to the Stark SESAM design for the 840 nm VECSEL, it is intuitive that the cap barrier material should contain more arsenic than the barrier behind the quantum well and should also have a lower bandgap. Thus, the design depicted in 2.18 was decided upon. The $In_{0.7}Ga_{0.63}As_{0.3}P_{0.37}$ barrier behind the quantum well has a bangap energy of 1.66 eV, close to the 1.67 eV of the AlGaAs barriers

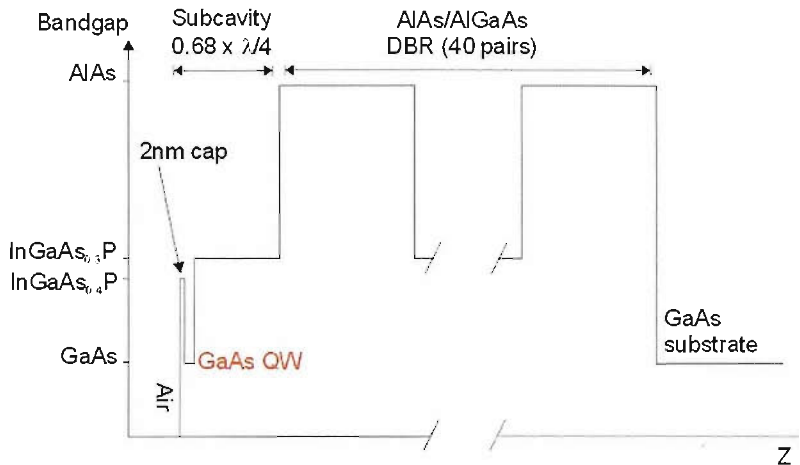

FIGURE 2.18: Design of Stark SESAM for operation at 840 nm, employing a suitable AlAs/AlGaAs DBR with 40 pairs, and biased QW barriers to encourage fast surface recombination as described in the text.

in the gain sample, so the GaAs quantum well design requires little modification. Meanwhile, the $In_{0.6}Ga_{0.68}As_{0.4}P_{0.32}$ cap barrier has a lower bandgap of 1.62 eV, and a larger As concentration, providing the asymmetric well bias towards surface recombination.

The refractive index of AlGaAs was calculated using equation 2.2.1 in section 2.2.1. For $In_{1-x}Ga_xAs_yP_{1-y}$, the analogous equation is

$$n = 17.987 - 20.74E_g + 9.634E_g^2 - 1.469E_g^3 \tag{2.4.3}$$

where E_g is the bandgap of the material [38]. Thus, the refractive indices of 30% and 40% arsenic InGaAsP, and GaAs at 840 nm are calculated to be 3.39, 3.43 and 3.63 respectively. To ensure that the QW is positioned in the $|E^2|$ as before, the sub-cavity is again designed to be $0.68\lambda/4$ thick. A second SESAM design was also produced with a thinner sub-cavity to increase the saturation fluence of the SESAM as described in section 2.4.2.3 for comparison of the mode-locking dynamics.

2.5 Conclusion

The basic principles behind the operation of a ML-VECSEL have been presented. Each element of both the gain sample and SESAM has been described individually in the context of the final device. The process for material selection was outlined, with the necessary lattice-matching equations provided. The gain sample design was detailed, focusing on its function as an active mirror, explaining the operation of a DBR, and the intricacies of the quantum well gain region.

The structural properties of VECSELs were discussed: microcavity enhancement and the Fabry-Perot sub-cavity, with particular attention to the lasing properties that are observed as a result. The expected thermal response of a gain sample was explained, highlighting the necessity to account for heating effects in sample design. Structural effects on a pulse in a ML-VECSEL were also considered.

The processes involved in the mode-locking of a VECSEL were described. The VECSELs presented in this thesis are mode-locked using a SESAM: the operation of such a device was detailed. The method for achieving sub-ps pulses from a VECSEL demonstrated at Southampton, and in this thesis was explained and the design of a SESAM to perform this ultrashort mode-locking was detailed, explaining the interplay of two important effects; the optical Stark effect, and fast surface recombination. The design of a SESAM to achieve both was described with lasing results presented and adaptation of such a design for application at 850 nm detailed.

Bibliography

[1] Keller, U. *et al.* Semiconductor saturable absorber mirrors (SESAMs) for femtosecond to nanosecond pulse generation in solid-state lasers. *IEEE Journal of Selected Topics in Quantum Electronics* **2**, 435–453 (1996).

[2] Kressel, H. & Butler, J. *Semiconductor laser and heterojunction on LEDs* (Academic Press, New York, 1977).

[3] Chow, W. W., Koch, S. W. & III, M. S. *Semiconductor Laser Physics* (Springer-Verlag, Berlin Heidelberg, 1994).

[4] Kokubo, Y. & Ohta, I. Refractive index as a functon of photon energy for AlGaAs between 1.2 and 1.8 eV. *Journal of Applied Physics* **81**, 2042 (1997).

[5] Jr., H. C., Sell, D. & Panish, M. Refractive index of $Al_xGa_{1-x}As$ between 1.2 and 1.8 eV. *Applied Physics Letters* **24** (1974).

[6] Tropper, A. C. & Hoogland, S. H. Extended cavity surface-emitting semiconductor lasers. *Progress in Quantum Electronics* **30**, 1–143 (2006).

[7] Verdeyen, J. T. *Laser Electronics* (Prentice Hall, 1995), third edn.

[8] Zory, P. S. *Quantum Well Lasers* (Academic Press Ltd., 1993).

[9] Hoogland, S. *Optically pumped Vertical-External-Cavity Surface-Emitting Semiconductor Lasers.* Ph.D. thesis, University of Southampton, Southampton, UK (2003).

[10] Tropper, A. C., Foreman, H. D., Garnache, A., Wilcox, K. G. & Hoogland, S. H. Vertical-external-cavity semiconductor lasers. *Journal of Physics D: Applied Physics* **37**, R75–R85 (2004).

[11] Raja, M. Y. A. *et al.* Surface-emitting, multiple quantum well GaAs/AlGaAs laser with wavelength-resonant periodic gain medium,. *Applied Physics Letters* **53**, 1678–1680 (1988).

[12] Alford, W. J., Raymond, T. D. & Allerman, A. A. High power and good beam quality at 980 nm from a vertical external-cavity surface-emitting laser. *Journal of the Optical Society of America B* **19**, 663–666 (2002).

[13] Svelto, O. *Principles of Lasers* (Plenum Press, New York, 1998), fourth edn.

[14] Garnache, A., Kachanov, A. A., Stoeckel, F. & Houdre, R. Diode-pumped broadband vertical-external-cavity surface-emitting semiconductor laser applied to high-sensitivity intracavity absorption spectroscopy. *Journal- Optical Society of America B* **17**, 1589–1598 (2000).

[15] Holm, M. A., Burns, D., Cusumano, P., Ferguson, A. I. & Dawson, M. D. High-power diode-pumped AlGaAs surface-emitting laser. *Applied Optics* **38**, 5781–5784 (1999).

[16] Coldren, L. A. & Corzine, S. W. *Diode Lasers and Photonic integrated Circuits* (John Wiley and Sons Inc., 1995).

[17] Paschotta, R. *et al.* Soliton-like pulse-shaping mechanism in passively mode-locked surface-emitting semiconductor lasers. *Applied Physics B: Lasers and Optics* **75**, 445–452 (2002).

[18] Garnache, A. *et al.* Sub-500-fs soliton-like pulse in a passively mode-locked broadband surface-emitting laser with 100 mW average power. *Applied Physics Letters* **80**, 3892–3894 (2002).

[19] Hirlimann, C. *Femtosecond laser pulses - principles and experiments* (N/K, 1998).

[20] Keller, U. *et al.* Solid-state low-loss intracavity saturable absorber for Nd:YLF lasers: an antiresonant semiconductor fabry-perot saturable absorber. *Optics letters* **17**, 505–507 (1992).

[21] Keller, U. *et al.* Pushing the high-pulse-repetition-rate frontier using a new regime of inverse saturable absorption and novel low saturation fluence SESAMs. In *Advanced Solid State Photonics (ASSP) 2006*, TuA3 (Lake Tahoe, U.S.A., 2006).

[22] Gopinath, J. *et al.* Recovery dynamics in proton-bombarded semiconductor saturable absorber mirrors. *Applied Physics Letters* **78**, 3409 (2001).

[23] Lederer, M. J. *et al.* Multipulse operation of a Ti:sapphire laser mode locked by an ion-implanted semiconductor saturable-absorber mirror. *Journal- Optical Society of America B* **16**, 895–904 (1999).

[24] Haus, H. A. Mode-locking of lasers. *IEEE Jounal on Selected Topics in Quantum Electronics* **6**, 1173–1185 (2000).

[25] Hönninger, C., Paschotta, R., Morier-Genoud, F., Moser, M. & Keller, U. Q-switching stability limits of continuous-wave passive mode locking. *Journal of the Optical Society of America B* **16**, 46–56 (1999).

[26] Hoogland, S. *et al.* Passively mode-locked diode-pumped surface-emitting semiconductor laser. *IEEE Photonics Technology Letters* **12**, 1135–1137 (2000).

[27] Häring, R. *et al.* Picosecond surface-emitting semiconductor laser with >200mW average power. *Electronics Letters* **37**, 766–767 (2001).

[28] Häring, R. *et al.* High-power passively mode-locked semiconductor lasers. *IEEE Journal of Quantum Electronics* **38**, 1268–1275 (2002).

[29] Keller, U. Recent developments in compact ultrafast lasers. *Nature* **424**, 831–838 (2003).

[30] Mysyrowicz, A. *et al.* 'dressed excitons' in a multiple-quantum-well structure: Evidence for an optical stark effect with femtosecond response time. *Physical review letters* **56**, 2748–2751 (1986).

[31] Wilcox, K. G., Foreman, H. D., Roberts, J. S. & Tropper, A. C. Timing jitter of 897 MHz optical pulse train from actively stabilised passively modelocked surface-emitting semiconductor laser. *IEEE Journal of Quantum Electronics* **42**, 159–160 (2006).

[32] Garnache, A., Sermage, B., Teissier, R., Saint-Girons, G. & Sagnes, I. A new kind of fast quantum-well semiconductor saturable absorber mirror with low losses for ps pulse generation. In *IEEE IndiumPhosphide-Realted-Materials*, 247–250 (Santa-Barbara, CA, USA, 2003).

[33] Hastie, J. E. *et al.* A 0.5W, 850nm $Al_xGa_{1-x}As$ vecsel with intra-cavity silicon carbide heatspreader. In *Annual Meeting of the IEEE Lasers and Electro-Optics Society*, TuAA2 (Glasgow, Scotland, UK, 2002).

[34] Hastie, J. E. *et al.* 0.5-W single transverse-mode operation of an 850-nm diode-pumped surface-emitting semiconductor laser. *IEEE Photonics Technology Letters* **15**, 894–896 (2003).

[35] Hastie, J. E. *et al.* Microchip vertical external cavity surface emitting lasers. *Electronic Letters* **39** (2003).

[36] Hastie, J. E. *et al.* A 0.5W, 850nm $Al_xGa_{1-x}As$ vecsel with intra-cavity silicon carbide heatspreader. *SPIE proceedings* **5137**, 201–206 (2003).

[37] Ioffe physico-technical institute: New semiconductor materials. characteristics and properties. Website (1996-2005). URL `http://www.ioffe.rssi.ru/SVA/NSM`.

[38] Wallace, S. G. *et al.* Refractive indices of InGaAsP lattice-matched to GaAs at wavelengths relevant to device design. *Applied Physics Letters* **76**, 2791–2793 (2000).

Chapter 3

Wafer Characterisation

3.1 Introduction

The work contained in this thesis focusses on the design and application of mode-locked VECSELs. These devices are composed of a semiconductor gain sample, and an external cavity into which SESAM is inserted in order to mode-lock the laser. The structures of these samples are described in sections 2.2 and 2.4.1 respectively. The gain structures and ac-stark SESAM samples described were designed at Southampton, but in the absence of the required growth facilities in-house, were grown off-site at the EPSRC III-V Central Facility at Sheffield University by Dr John Roberts. When new samples are received, it is important to characterise them fully to ascertain their properties in relation to the original design and determine whether the growth has been successful. The characterisation of QT1544, the near-antiresonant VECSEL structure used to produce the sub-500 fs pulses described in 2.4.2, was carried out and is documented in [1] and [2]. For completeness, in this chapter, these methods are outlined, and applied to various VECSEL and SESAM samples.

The experiments allow investigation of the properties of the structure as a whole, and the individual components that form the VECSEL active mirror, as well as the passive SESAM element. The structures' reflectivities are characterised to show the properties of the DBR. For the gain sample, the edge photo-luminescence spectrum (edge PL) of

the sample is characterised in order to probe the quantum wells of the active region directly, without the influence of the active region microcavity or the DBR. The top-surface photo-luminescence spectrum (top PL) of the structure is measured, showing the photoluminescence of the quantum wells modulated by the many-layer interference effects of the structure, and its temperature response. Finally, the continuous-wave (CW) lasing properties of the structure are investigated in a simple 2-mirror cavity configuration. This section details each of these characterisation steps. Characterisation of the SESAM involves PL measurement as well as DBR characterisation. More complex methods of SESAM characterisation are also discussed.

3.2 Wafer Growth and Sample Selection

Most of the wafers used in the work in this thesis were grown at the EPSRC III-V Semiconductor Facility at the University of Sheffield by Metal Organic Chemical Vapour Deposition (MOCVD). In the MOCVD process, the GaAs substrate is exposed to volatile metal-organic gas-phase precursors which react and decompose on the substrate surface to produce the desired film [3]. The process is carried out in a reaction chamber held at 2-100 kPa, at a temperature of 690 ^oC. Examples of precursors for gallium, arsenic, indium and aluminium are trimethyl gallium ($(CH_3)_3Ga$), arsine (AsH_3), trimethyl indium ($(CH_3)_3In$) and trimethyl aluminium ($(CH_3)_3Al$) respectively. The vapours are transported to the chamber by a carrier gas, usually nitrogen or hydrogen, and the toxic waste products removed via a gas exhaust and cleaning system. Growth of a typical VECSEL structure such as that described in section 2.2 takes approximately 8 hours.

Often, a map of the photo-luminescence peak wavelength across the wafer taken by the grower is supplied with the grown wafer. The map is taken using an Accent RPM2000 PL setup with a 633 nm or 532 nm excitation source. From this, and by direct observation of the wafer surface, it is possible to identify areas of uniform growth with the desired photo-luminescence properties. Typically, these areas are located in the central region of the wafer where growth is optimised, and inherently more uniform. From this characterisation, suitable areas from which a sample should be cleaved are identified. If

the sample is particularly non-uniform, or a suitable area is not initially identifiable, the characterisations described in this chapter may be carried out at various points across the wafer with the wafer intact to find a suitable area, although this makes handling and mounting awkward, and is not desirable.

Samples of approximately 3 mm $\times$ 5 mm are cleaved. These are then bonded to a copper mounting plate using conductive silver paint. This mounting plate can then be thermally contacted to a peltier-cooled heat sink to control the sample temperature.

3.3 Reflectivity Spectra

In the previous chapter, the elements that compose a VECSEL active mirror were introduced. The first element to characterise is the DBR. In section 2.2, theoretical calculations of the DBR stopband and reflectivity spectrum were performed. Here, experimental reflectivity spectra of the sample are compared with the predictions.

Reflectivity spectra are taken using a Perkin Elmer UV/VIS/NIR Lambda 9 spectrometer. A reflectivity rig is used to gain measurements. It has a horizontal plate with a 1 mm diameter aperture which is covered with the sample to be measured face down. Light from the spectrometer tungsten lamp is directed at the sample, and the reflection collected and measured in the spectrometer by a monochromator used in conjunction with a holographic grating with 1053 lines per mm, giving a wavelength precision of $\pm$0.1 nm [4].

A calibration trace is first taken using a silver mirror which has a flat, highly reflective spectrum across the wavelength region to be measured. This is placed face-down on the aperture, and the reflectivity spectrum taken, logged by the Perkin Elmer Lambda 19 winlab software. This is used to normalise further spectra. The sample is then placed in the spectrometer, face down on the aperture, and the spectrum taken over the 850nm to 1200nm range.

A reflectivity spectrum for sample QT1544, grown to the antiresonant VECSEL design described in section 2.2 is shown in figure 3.1. This can be compared with the predicted

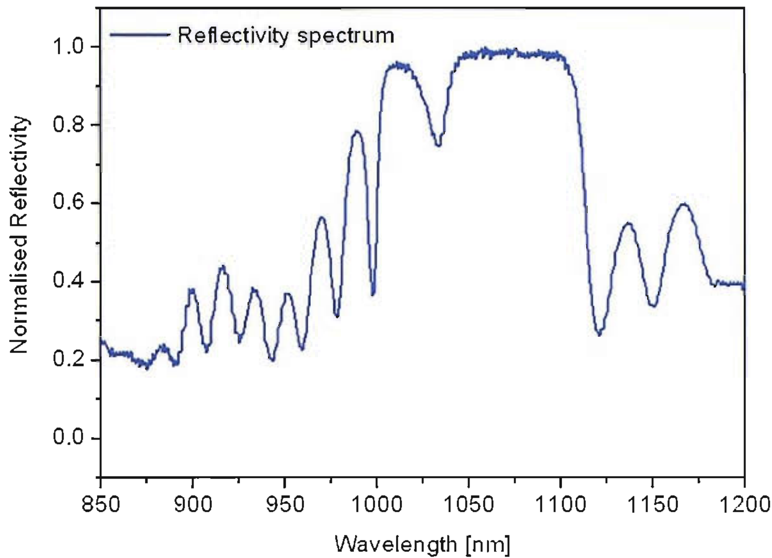

FIGURE 3.1: Reflectivity spectrum of near antiresonant VECSEL sample QT1544, showing the distinctive stopband feature with ~100% reflectivity from ~1000-1100 nm. The absorption feature of the microcavity resonance is also apparent at ~1033 nm.

reflectivity spectrum shown in figure 2.3 in section 2.2. It clearly shows the DBR stop band, in good agreement with calculation, showing close to 100% reflectivity across the whole stopband, as desired for the broadband reflectivity of the device. The stopband is centred at 1060 nm, and spans a wavelength range of 110 nm. Although as wide as the calculated stopband, it is apparent from this reflectivity spectrum that the DBR has been grown approximately 25 nm long of the desired centre wavelength of 1035 nm. The stopband is, however, broad enough to cope with this discrepancy, and still gives the desired high reflectivity at the desired lasing wavelength.

A feature is apparent in the measured spectrum centred at 1033 nm; a 25% dip in reflectivity which does not appear in the calculated spectrum. This dip indicates a resonance of the microcavity of the structure as discussed in section 2.2.3.2, enhanced by absorption in the quantum wells. In a resonantly designed structure, the absorption would be more pronounced.

Reflectivity spectra provide immediate information about the success of the growth, and the sample's properties. Composed of more than 50 layers, the DBR is arguably the most difficult component in the VECSEL structure to grow, so its characterisation allows assessment of the quality of the structure. Coupled with the initial information

it provides about the microcavity, the reflectivity spectrum is a powerful tool in the characterisation of samples.

3.4 Photo-Luminescence Characterisation

To probe the emission characteristics of the structure, the sample can be illuminated with pump light, and the quantum well emission analysed. This section describes two different photo-luminescence techniques used to characterise the quantum wells alone, and the effect of the whole structure on their emission.

3.4.1 Edge Photo-Luminescence Spectra

The edge photo-luminescence spectrum (Edge PL) of the structure provides a means to directly observe the intrinsic properties of the quantum well gain region of the structure. A spot at the very edge of the sample is pumped, and photoluminescence from this spot is collected from the side of the sample using a microscope objective. PL collected in this way is free from any modulation or waveguiding effects of the complex multi-layer structure.

The setup is shown in figure 3.2. The pump laser used is a fibre-coupled diode laser, emitting up to 1 W of power at a wavelength of 830 nm from a 30 μm core-radius fibre. The fibre output is collimated with a 35 mm focal length doublet lens, and focussed down to a 60 μm radius spot on the sample surface by a 75 mm focal length doublet lens. It is important to ensure that the fluorescence collected by the microscope objective has not been guided down the waveguide formed by the microcavity, and so the objective is positioned at an approximately 10° angle behind the front surface. The collected light is launched into a grating spectrometer with a Si photodiode array detector.

Edge PL spectra for the antiresonant VECSEL gain structure at -5, 5 and 20 ^{o}C and 81, 317 and 789 mW pump power are shown in figure 3.3. The spectra have similar profiles, with a large peak at 830 nm due to scattered pump. They show a clear peak in photo-luminescence at the design wavelength of $\sim$1030 nm, caused by the radiative

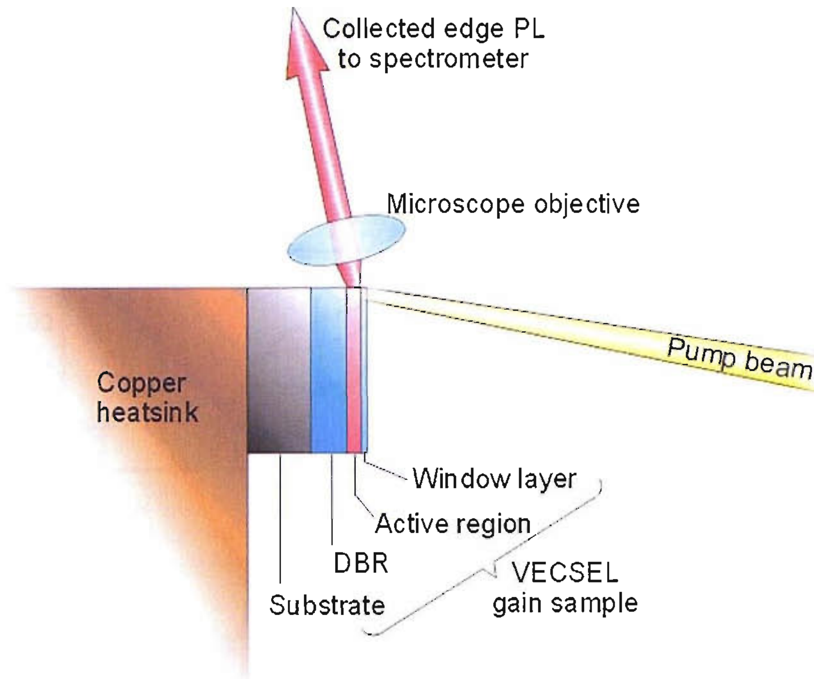

FIGURE 3.2: Edge photo-luminescence experimental setup: the sample is illuminated by the focussed pump light. Photo-luminescence is collected from the edge of the sample by the microscope objective, which is placed at a slight angle in order to avoid collecting light which has been modified by the sample structure. The PL is directed to a spectrometer for analysis.

recombination between the conduction band and the heavy hole band. A shoulder in the PL is also present at ~950 nm, attributable to radiative recombination between the conduction band and the light-hole band. A further, reduced peak is also observed at ~890 nm, close to the bangap of GaAs, indicative of some recombination of carriers in the GaAs barriers of the active region. However, this peak is much smaller than the quantum well peaks indicating good confinement of carriers in the quantum wells.

Varying the sample temperature (T_{sample}) and amount of pump power (P_{pump}) allows us to probe the thermal response of the quantum wells. As the temperature is increased at fixed pump power, the peak in the edge PL spectrum broadens due to the increase in the thermal energy of the carriers, and shifts to longer wavelength in accordance with the thermal shift of the band edge. An edge PL shift of 0.30 nm/K with heat sink temperature is calculated for low excitation of the structure investigated using the data shown in figure 3.3. The band edges for each temperature are determined by identifying

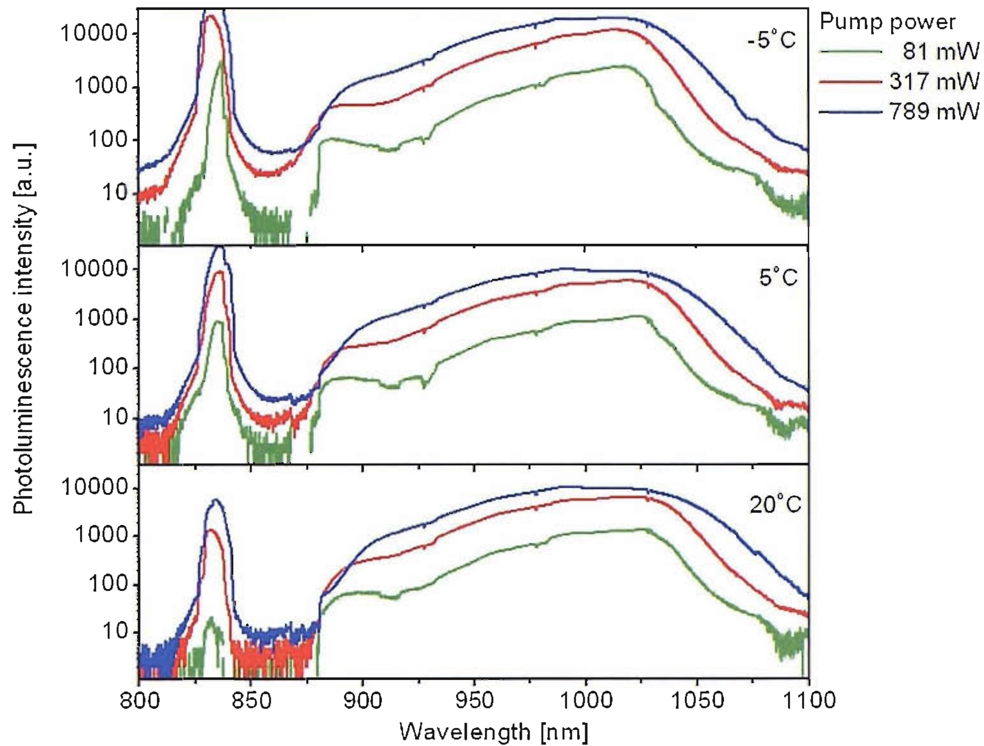

FIGURE 3.3: Edge PL spectra of sample QT1544. Spectra are taken at three different temperatures and powers to characterise the PL shifts with increased heating of the wells. The shape of the graphs is described in the text.

the shoulder in the spectrum on the long wavelength side, and using a linear fit function to these points in the Origin 7.0 program.

For increased pumping at constant temperature, broadening of the quantum well emission peak is also observed. This is caused by the filling of the QW bands by the increasing numbers of carriers created with increased pumping and a corresponding rise in transitions from the E_2 and higher levels (see chapter 2). A 9.16 nm/W shift in quantum well emission is observed at low temperature as pump power is increased. This is attributable to the screening of the atomic attractive forces by the carrier charges at the higher carrier densities generated by the increased pumping [5].

The low excitation (81 mW pump power), room temperature (20 ^{o}C sample temperature) peak emission wavelength of the quantum wells shown in the edge PL spectrum is measured to be ~1027 nm. This is longer than the quantum well design wavelength of 1020 nm. As discussed in section 2.2, the design wavelength is chosen to be shorter

than the desired operating wavelength to compensate for the thermal response of the sample and permit room temperature lasing at high pump powers. A measured quantum well emission longer than this value will lead to thermal misalignment of the structure components at high pump powers or sample temperatures, resulting in reduced lasing power.

3.4.1.1 Thermal Resistance

It is possible to estimate the thermal resistance (Z_{th}) of the active layers from these two experimentally determined rates via the following calculation:

$$Z_{th} = \frac{\delta\lambda}{\delta P_{abs}} . \frac{1}{\frac{\delta\lambda}{\delta T_{sample}}} \tag{3.4.1}$$

where Z_{th} is the thermal resistance, $\delta\lambda/\delta P_{abs}$ is the change in wavelength per Watt of pump power absorbed, and $\delta\lambda/\delta T_{sample}$ is the temperature shift required to increase the emission wavelength by 1 nm. In order to convert from incident pump power (P_{pump}) to absorbed pump power (P_{abs}), the pump power must be multiplied by a factor of 0.47. This arises from a 68% transmission of pump light at the sample surface, derived from the Fresnel formula [6]. Using a Beer-Lambert law calculation, and assuming absorption coefficients at the pump wavelength in the GaAs barriers and the AlGaAs strain-compensating layers of 15.1×10^3 cm^{-1} and 8.4×10^3 cm^{-1} respectively, it is estimated that of this transmitted light, 69% is absorbed [1], resulting in a total of 47% of the incident pump light being absorbed. Therefore, for the measured values of edge PL shift with sample temperature and pump power for QT1544 above, the thermal resistance of the active layers of QT1544 is calculated to be 30.4 K/W. In the following section, this value will be compared to the thermal resistance of the VECSEL structure as a whole.

3.4.2 Top Photo-Luminescence Measurements

The top PL spectrum of the structure is taken to characterise the modulation effects of the active region microcavity resonances on the sample's photoluminescence. This allows direct observation of the spectral shift of the emission of the structure with increased pumping at various temperatures. Measurements of the photo-luminescence power are also taken to characterise the efficiency of the structure, and determine its optimal operating conditions.

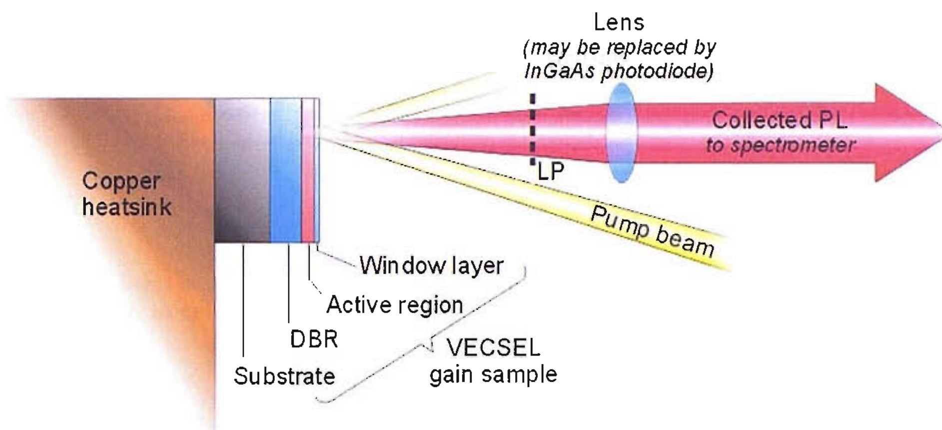

FIGURE 3.4: Integrated photo-luminescence experimental setup. The sample is pumped at an angle to allow PL to be collected from the top surface of the sample. PL is either collimated by a lens and directed to a spectrometer, or incident on a photodiode. A long pass filter (LP) allows only light with wavelength longer that 950 nm through, eliminating scattered pump light from the measurements.

The top photo-luminescence setup is shown in figure 3.4. The sample is pumped at an angle with the 830 nm fibre-coupled diode, and emits PL over the whole 4π solid angle. Some PL is collected and collimated by a lens placed at its focal length away from the sample, normal to the surface. This is coupled into the grating spectrometer used for the edge PL measurements. Following this, the lens is removed, and an InGaAs photodiode is put in its place to measure the photo-luminescence power through a 950 nm long-pass filter to eliminate any signal from scattered pump.

The room temperature top PL spectra of VECSEL gain sample QT1873 are shown in figure 3.5. QT1873 and QT1544 are different growths of the same structure design, and so should contain the same number of layers of the same thickness with the same

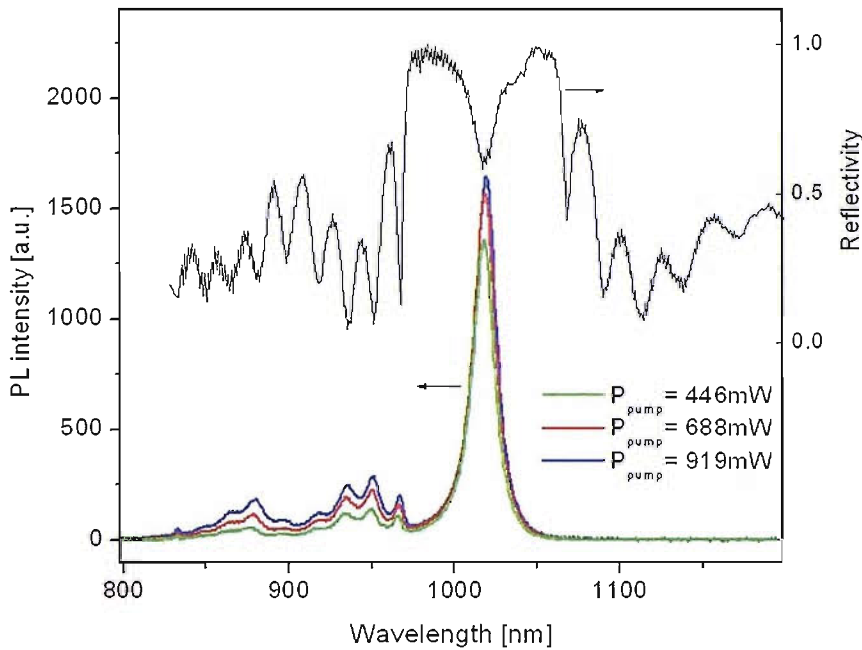

FIGURE 3.5: Integrated photo-luminescence spectra of the emission from the antiresonant gain sample QT1873, shown with the reflectivity spectrum of the structure for reference. The spectral shape is described in the text.

material concentrations. Some discrepancies between the two are apparent, but they are expected to have very similar thermal properties. The sample's room temperature reflectivity spectrum is also shown for reference. The main peak in the top PL centred at approximately 1018 nm corresponds to the quantum well fluorescence enhanced by the resonance of the active region microcavity. The corresponding absorption dip in the reflectivity spectrum is clearly identifiable at the same wavelength. Lower intensity modulated peaks in the top PL spectrum are apparent at shorter wavelengths outside the DBR stopband. These are caused by structural modulation of the quantum well photoluminescence, corresponding to modulations in the reflectivity spectrum of the sample.

As the pump power is increased, the peak of the PL shifts to longer wavelengths at a rate of 3.78nm/W. The response of the top PL to increases in sample temperature is not shown in the data collected for QT1873, but a top PL thermal shift of 0.1 nm/K was measured by Holm et al in [7] as a result of the thermal misalignment effects described in chapter 2. This rate is different from the 0.3 nm/K expected for the edge PL since

the two are governed by different effects; the edge PL being dependent on the thermal shifts of the quantum well bandgap, and the top PL on thermally induced changes in the optical path length.

Using equation 3.4.1, it is possible to calculate the thermal resistance of the whole active structure from the measured PL shifts with pump power and sample temperature. For QT1873 the whole active structure thermal resistance is calculated to be 35.5 K/W. This is larger than the thermal resistance calculated from the edge PL measured for QT1544 in section 3.4.1, showing that the DBR layers of the structure increase its thermal resistance.

The thermal performance of the unprocessed chip is poor, and the wavelength dependence on sample temperature and pump power undesirable for some applications. However, in the cases of the mode-locked devices presented in this thesis, these thermal shifts in emission wavelength are used to provide broad wavelength tunability of the sources, and tuning into various pulse regimes, increasing the versatility of the devices. Moreover, the antiresonant designs used for the mode-locked devices presented here, with their broadband gain in comparison with resonant structures, provide a greater tolerance to shift of QW PL peak wavelength relative to top PL before lasing performance is compromised as discussed in section 2.2.3.2.

3.4.2.1 Internal Quantum Efficiency

The internal quantum efficiency ($\eta_{internal}$) of a structure is defined as the ratio between the number of emitted photons (N_{QW}) and the number of absorbed photons (N_{abs}) [1].

$$\eta_{QW} = \frac{N_{QW}}{N_{abs}}. \tag{3.4.2}$$

Calculation of values of quantum efficiency of a structure allow assessment of the thermal loading of the structure with increased pumping, a fundamental parameter in indication of the efficiency of the sample. The experimental setup is the same as that shown in

figure 3.4, with a photodiode used in place of the spectrometer to measure the photoluminescence power in terms of the number of photons incident on it.

The model considers a pumped QW in the active region as a point emitter emitting over a 4π steradian solid angle. Of this emission, the number of photons per solid angle measured by the photodiode is given by

$$N_{PD} = \frac{aN_{QW}}{4\pi nD^2} \int f(\lambda)\mu(\lambda)T(\lambda)d(\lambda) \tag{3.4.3}$$

where a is the area of the photodiode aperture, D is the distance of the photodiode from the sample surface, n is the refractive index of the layer in which the well is embedded, and N_{QW} is the overall emission rate of the quantum well which has a spectral distribution according to the function $f(\lambda)$, normalised such that $\int f(\lambda)d(\lambda) = 1$. The functions $\mu(\lambda)$ and $T(\lambda)$ are the microcavity enhancement factor (defined in section 2.2.3.2), and transmission spectrum of the long-pass filter respectively. The microcavity enhancement factor at the main peak in top PL for QT1544 was described in section 2.3.1 and is taken to be $\mu(\lambda) = 25$ [1]. Equation 3.4.3 is kept simple by assuming that the angles involved are small enough that for the Snell's law factor $sin\theta \approx \theta$. N_{PD} is derived from the voltage generated by the photodiode taking into account the gain of the pre-amplifier used and the efficiency of the photodiode.

The number of absorbed photons, N_{abs}, is calculated by dividing the absorbed pump power by the pump photon energy. The amount of pump energy that is absorbed is equal to the incident pump power corrected by Fresnel and Beer-Lambert factors as in section 3.4.1.1.

The quantum efficiency of sample QT1712, grown to the near-antiresonant design detailed in section 2.2, has been calculated using equation 3.4.2, and is shown as a function of incident pump power in figure 3.6. The quantum efficiency increases rapidly to begin with, but at pump powers of approximately 200 mW, it is seen to peak, and then begins to fall as non-radiative processes start to become more dominant. Also, at high pump powers, the high carrier densities cause band filling in the quantum wells, causing a saturation in the number of photons emitted. This does not occur in the GaAs barriers

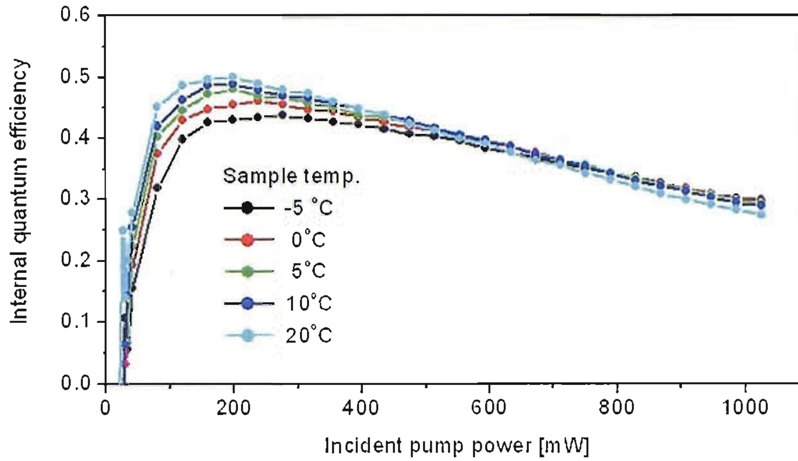

FIGURE 3.6: Internal quantum efficiency of sample QT1712 as a function of incident pump power for different sample temperatures.

where the pump photons are absorbed since this has a much larger volume than the quantum wells. The observation of these effects in the quantum efficiency highlights the importance of thermal management of the VECSEL structure in order to achieve high power lasing discussed in chapter 4.

Such a measurement was carried out to determine the quantum efficiency of sample QT1544 in [1], where it was observed that at higher sample temperatures, the quantum efficiency of the sample was lower than at low temperatures due to the poor thermal properties of the sample. In the measurement of QT1712, at low incident pump powers, contrary to prediction, the higher sample temperature measurement appears more efficient, attributable to higher carrier mobility in the barriers caused by the increased sample temperature. However, it can be seen that at higher sample temperatures, the quantum efficiency decreases at a faster rate after the maximum efficiency is reached, and as incident pump power increases, the lower sample temperatures are more efficient, as expected. The maximum quantum efficiency measured for sample QT1712 is ~0.5, lower than the measured value for QT1544 of >0.6 [1], supported by the CW lasing behaviour of QT1712, which demonstrated a low rollover point, and poor slope efficiency in comparison with that of QT1544 (QT1544 data presented in the following section).

3.5 Sample Lasing Properties

The final characterisation is that of the continuous-wave (CW) lasing properties of the sample. The sample is used in a simple, two mirror, confocal cavity as shown in figure 3.7. As with the PL measurements, an 830-nm, 1-W fibre-coupled diode laser is used to pump the VECSEL gain structure. The gain structure DBR forms one end-mirror of the cavity. The other mirror is a curved dielectric output coupler with a focal length of 50 mm and reflectivity of 99.2%, which completes the cavity. The optimal distance at which this output coupler should be placed from the gain sample is determined using a stability calculation, the procedure for which uses a ray matrix method as shown in apendix B.

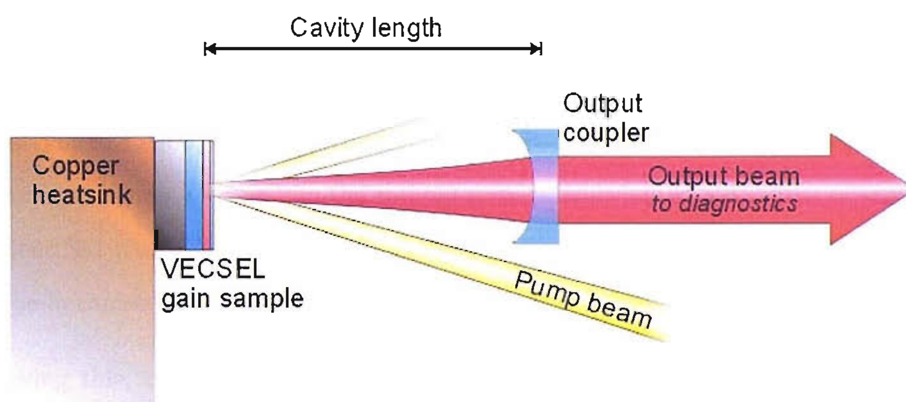

FIGURE 3.7: CW lasing cavity setup. The cavity design and alignment is described in the text.

The stability curve for this straight cavity is shown in figure 3.8, a result of the calculation in appendix B. It can be seen that the optimal position for the output coupler to provide mode-matching with the 60 μm radius pump spot on the gain sample is at 47.5 mm from the gain sample. To allow experimental optimisation of this factor, the output coupler is mounted on a micrometer-controlled translation stage to allow optimisation of its position during lasing. Pumping is at an angle to allow positioning of the output coupler normal to the sample surface. This angle is minimised as much as possible to reduce the ellipticity of the pump beam and provide the best possible mode-matching with the Gaussian cavity mode.

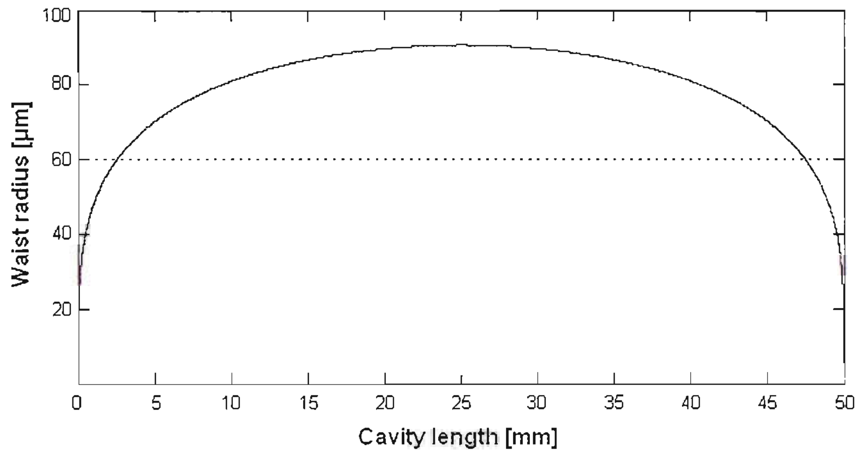

FIGURE 3.8: Graph of waist spot size versus cavity length for a straight cavity [calculated using the methods outlined in B, output coupler radius of curvature $R_{oc} = 50$ mm]

To align the cavity, first the pump beam is positioned. The fibre-coupled launch is located at 75 mm from the sample surface at the desired angle (approximately 5° from the normal) to allow room for the output coupler. The pump spot is observed using a microscope camera focussed on the sample surface, allowing a 'clean' area of sample to be identified with minimal scattering losses. In this way, the pump spot focusing can also be optimised by direct observation of the spot.

Following this, the sample is cooled to 0 ^oC and pumped with in excess of 800 mW pump power to ensure that pumping is not below the expected threshold of the device. The output coupler is positioned at 47.5 mm from the sample surface and normal to it by eye, to achieve optimal mode-matching on the sample surface between pump and VECSEL modes, and hence most efficient use of the incident pump energy. An infra-red sensitive camera is used to observe the sample through the output coupler. A 950 nm long-pass filter is used to eliminate scattered pump light from the image. The multiple reflections of fluorescence from the pumped spot as well as the fluorescing spot itself can be seen. The output coupler is moved and tilted until these spots lie on top of each other, at which point an increase in the amplification of the fluorescence can be observed, and possibly even lasing. If no lasing is achieved, the output coupler is traversed away from the gain sample to reach the edge of stability at 50 mm from the sample, where its edge appears illuminated by the multiple reflections since they are the same size as the

output coupler at this point. From here, the output coupler is traversed back towards the sample, making fine adjustments to its tilt until lasing is achieved, identified by a large increase in light detected by the camera. Following this, the cavity alignment and pump spot location are optimised for the lowest threshold in fundamental transverse mode operation.

3.5.1 Slope Efficiency

Various properties of the sample, and the VECSEL device as a whole can be characterised in this CW, confocal oscillator configuration. The first is the slope efficiency of the VECSEL. Starting from a cavity optimised for low threshold and fundamental mode operation, the pump power is increased incrementally, and values of VECSEL output power are recorded for each increment. This is repeated for various sample temperatures, and output coupling.

Graphs of VECSEL power as a function of pump power for sample QT1544 are shown in figure 3.9. Two different output couplers were used to complete the cavity with 0.8% and 1.5% transmissions. Efficiency plots for each are shown in figures 3.9 a) and 3.9 b) respectively. The experimental data are shown as a series of colour-coded points, with a bold, solid line showing a linear fit to the data (before rollover) performed by the 'Origin' mathematical program. Graphs of these measured slope efficiencies at the different sample temperatures are inset.

In figure 3.9a, data from the cavity completed with a 0.8% ouput coupler show that the optimal lasing efficiency (16.7%) is achieved at a sample operating temperature of 0 ^{o}C. The effects of thermal rollover are not seen in these conditions, and the maximum output power of 128 mW achieved from the VECSEL is limited by the maximum amount of pump power of 1.025 W available. Indeed, it is not until sample temperatures above 10 ^{o}C are reached that the maximum powers achieved cease to be limited by the available pump, and the effects of thermal rollover (discussed in chapter 2) are observed. The effect is clearly identifiable for the 20 ^{o}C sample temperature data, with rollover occurring at a pump power of approximately 950 mW, corresponding to a maximum output power of 64 mW achieved. The changes in slope efficiency can be identified in the inset graph,

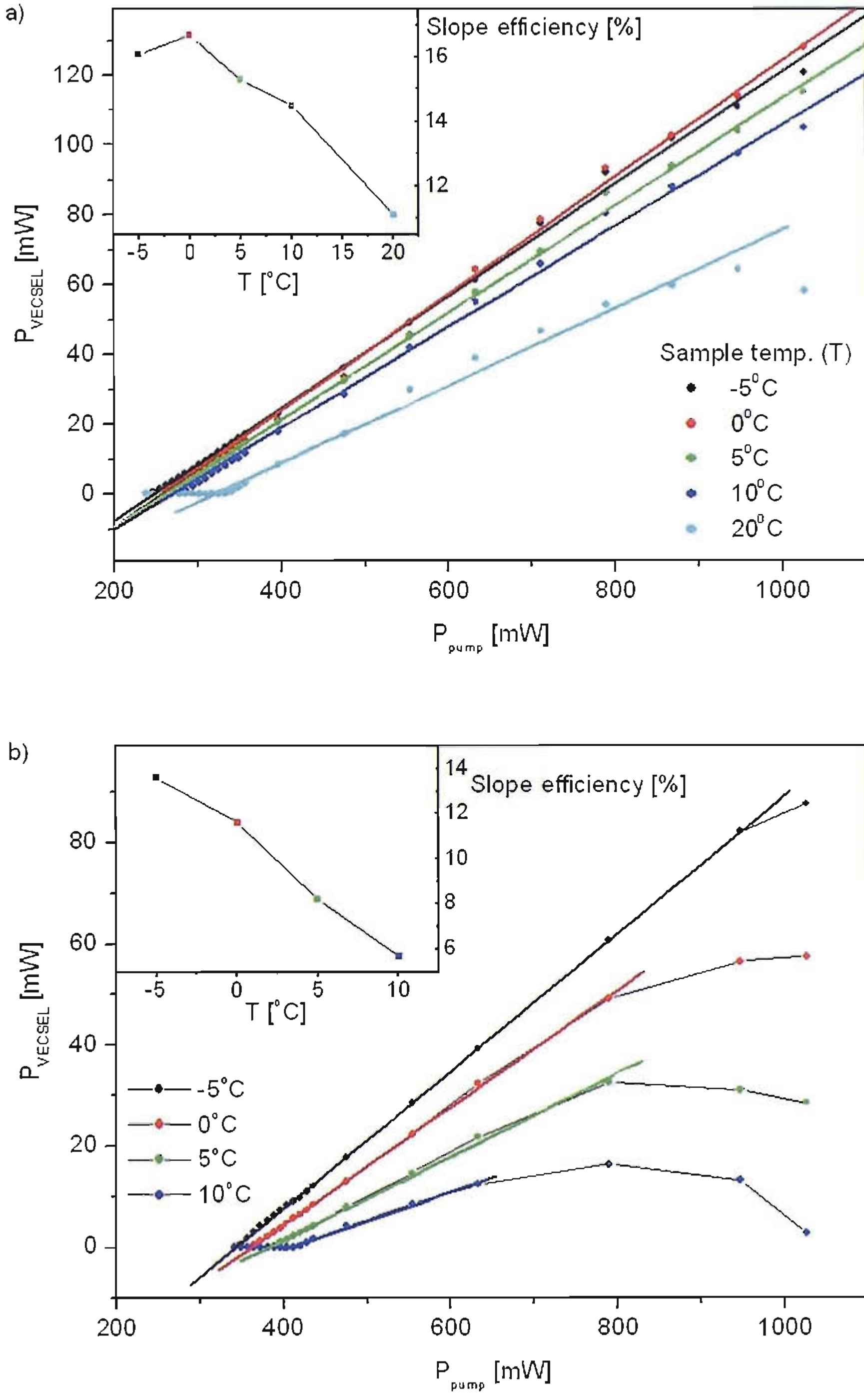

FIGURE 3.9: Slope efficiency plots at incremental sample temperatures for sample QT1544 in a 2 mirror cavity completed with a) a 0.8% transmission output coupler, and b) a 1.5% transmission output coupler. The experimental data points are shown as coloured dots, with solid colour lines showing linear fits to the data used to determine slope efficiency. Plots of slope efficiency as a functon of sample temperature are inset for each. The maximum slope efficiency obtained was 16.7% for 0.8% ouput coupling at 0 ^{o}C.

clearly showing the decrease in slope efficiency of the device as operating temperature is increased after the maximum at 0 ^{o}C.

For the cavity completed by a 1.5% transmitting output coupler, shown in figure 3.9b, it should be noted that at sample temperatures above 10 ^{o}C, it was not possible to obtain any lasing action as the gain available at this temperature was not sufficient to overcome the higher loss of the output coupler, and lasing threshold was never reached. At lower temperatures, the effects of thermal rollover are much more apparent than for 0.8% output coupling, indeed, the results are not pump power limited at all, and the maximum slope efficiency of 13.6% is achieved at the coldest sample temperature of -5 ^{o}C, corresponding to a maximum output power of $\sim$88 mW at the maximum pump power of 1.025 W. The inset graph clearly shows the decrease in slope efficiency with increasing temperature from this point until lasing is no longer achievable.

3.5.2 Fixed Losses

The output coupling for a VECSEL cavity is low, and only small losses can be tolerated by the device. With such a low loss requirement for the cavity, it is useful to know the fixed internal losses of a VECSEL sample to ascertain the tolerances of a device using the gain sample in question for insertion of various elements, in the case of the cavities in this thesis, a SESAM to mode-lock the VECSEL.

In order to ascertain the fixed losses of a sample, it is necessary to produce a Findlay-Clay plot for the laser [8]. The output coupling of the cavity is varied, and a plot of ln(R), where R is the reflectivity of the output coupler, versus the threshold pump power is produced. The y-intersect of this plot corresponds to the fixed losses. Unfortunately, for the experiments in this thesis, only two output couplers were available; 0.8% and 1.5%, and the insertion loss of any variable output coupling device was too high to be of use. Consequently the Findlay-Clay plots for the device only have two points. However, a value of fixed loss of the sample QT1544 was obtained through this crude experiment of $\sim$1 %. This is thought to be caused by oxidation of the sample and scattering losses at the surface, and may also be attributable to a poor growth. The effect of larger fixed loss is that the lasing threshold of the cavity containing the sample is higher since more

pump power is required to raise the gain high enough to equal the larger loss. Only small percentages of ouput coupling can be tolerated limiting the output power achievable, and elements to be inserted into the cavity must have very low insertion losses.

3.5.3 Characteristic Temperature

In the CW lasing characterisation of the sample, it is also possible to observe the temperature dependence of the threshold of the VECSEL. A plot of threshold pump power variation with temperature is shown for the 0.8% output coupling cavity in figure 3.10. An exponential fit to the graph is shown, and the threshold pump power shows good agreement with an exponential increase with sample temperature. The threshold pump power required at different temperatures depends on many factors, including the fixed losses of the sample itself, and all the temperature dependent effects discussed in previous sections of this chapter and section 2.3.3.

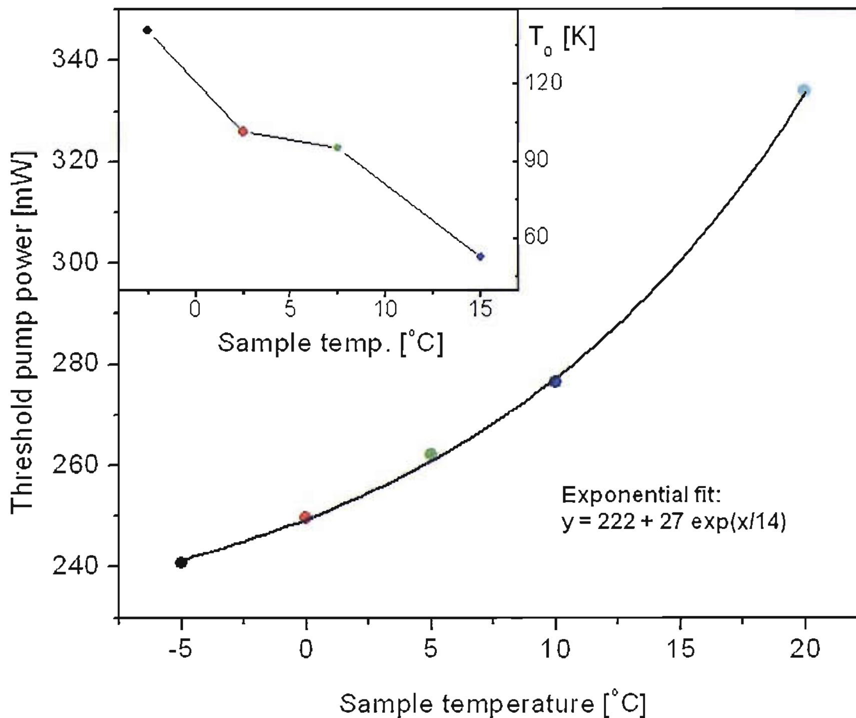

FIGURE 3.10: Plot of threshold pump power variation with temperature for the 0.8% output coupling, CW lasing cavity, with calculated values of characteristic temperature (T_0) inset. The threshold increases exponentially with sample temperature. The corresponding reduction in characteristic temperature is calculated using equation 3.5.1.

The combined effect of all these different processes on the temperature-dependence of the threshold of the device is conventionally characterised in diode laser literature by a figure of merit known as the characteristic temperature, T_0 [5]. The threshold of the laser is said to vary as exp(T/T_0), allowing T_0 to be calculated using the following equation:

$$P_{th}(T_f) = P_{th}(T_i)exp\left(\frac{T_f - T_i}{T_0}\right) \tag{3.5.1}$$

where P_{th} is the threshold pump power at a given temperature, and T_i and T_f are the initial and final temperatures respectively. In practice, it is common for the rate of increase of the threshold to be somewhat faster than exponential with temperature, and so values of T_0 are only useful if quoted with the corresponding temperature [1]. A plot of calculated T_0 for the range of temperatures measured is shown set into figure 3.10. The values of T_0 drop with increasing sample temperature from 140 K at -2.5 ^{o}C to 50 K at 15 ^{o}C. This indicates again that the sample will operate more favourably at lower temperatures, however, the values of T_0 are all low compared with the typical values for strained InGaAs quantum well lasers which are commonly $\geq$200 K [5], showing the high thermal dependence of the sample.

3.6 SESAM Characterisation

The characterisation performed for SESAM samples used in experiments in this thesis is less detailed. Since it is a passive element, and is not pumped, the SESAM's thermal properties are less critical. Moreover, the SESAM structure is much simpler than the gain sample, consisting only of a DBR and a single, surface quantum well (as described in section 2.4.2.3). The DBR stopband can be characterised as before with a reflectivity spectrum, to ensure that it has the required high reflectivity over the specified range.

3.6.1 SESAM Photo-Luminescence Characterisation

The PL of the quantum well can be observed directly through the top surface of the SESAM. The signal is weak as there is only one quantum well. So, in order to measure

the PL, a microscope is used in the setup shown in figure 3.11. The excitation source (the same 830 nm pump diode used for the gain sample characterisations described in this chapter) is launched into the microscope, and focussed onto the SESAM surface. The characterisation is performed at low excitation (~50 mW incident) to avoid thermal shifting of the QW PL. The PL is then collected by the microscope objective that delivered the excitation light, and separated from the excitation light using a beam splitter. Excess pump is filtered out using a GaAs substrate to absorb it, and the remaining PL signal is detected by a grating spectrometer.

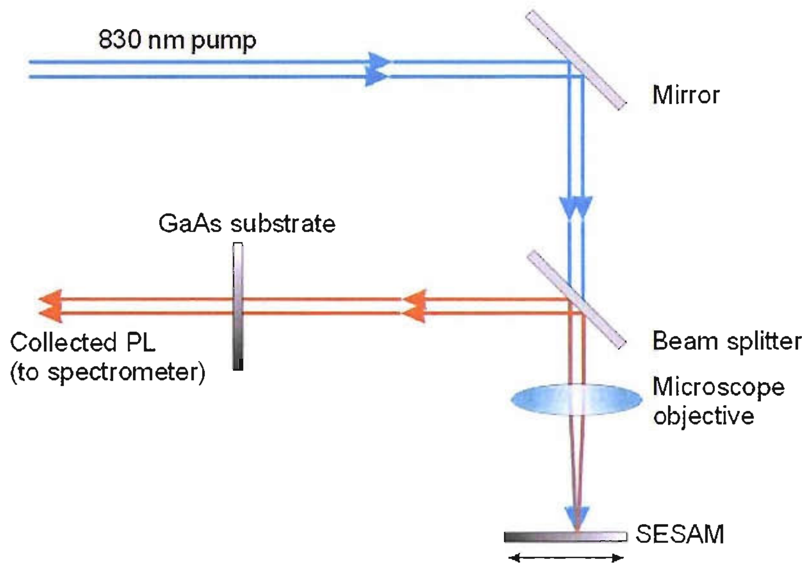

FIGURE 3.11: Diagram of the setup used for PL characterisation of a SESAM. Light from a VECSEL pump diode is focussed onto the sample in a microscope, and the emitted PL is collected by the microscope objective. A GaAs substrate is used to filter out any residual pump.

From this, the peak wavelength of the PL can be determined, and compared with the design wavelength to see if mode-locking will be successful using the device. This characterisation is particularly important for Stark SESAMs, where the band edge wavelength is crucial to the mode-locking since the Stark effect only has a predicted bandwidth of ~3 nm [9].

SESAM PL data for a Stark SESAM grown to the design detailed in 2.4.2.3 is shown in figure 3.12 along with reflectivity data for the DBR. The PL shows a characteristic Gaussian profile since it is not modulated by any structural features, and is emitted by

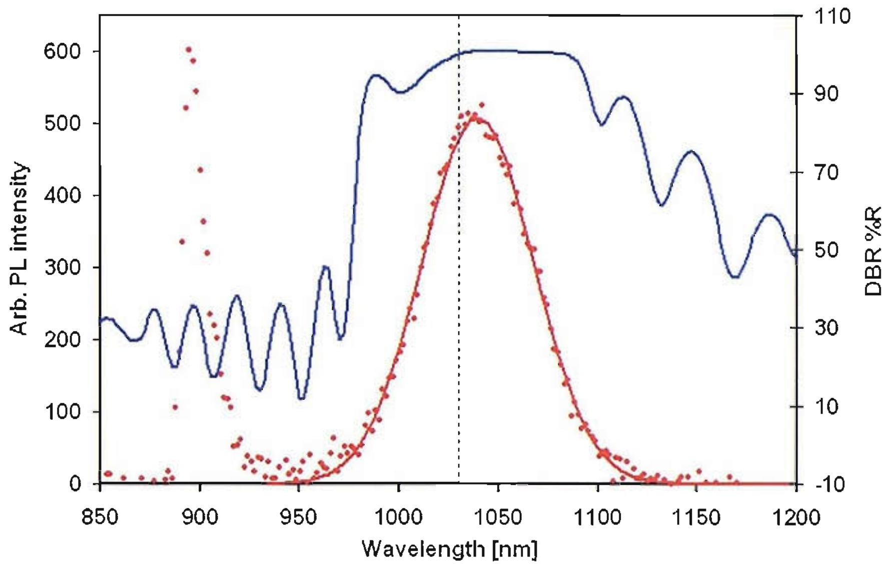

FIGURE 3.12: PL data taken from Stark SESAM QT1861A at low excitation (denoted by red points) with SESAM DBR reflectivity spectrum (blue) shown for reference. A Gaussian fit to the PL data is shown (red line) as well as the design wavelength (black, dashed line).

only one QW. The design wavelength of the Stark SESAM is 1030 nm, and it can be seen that the PL is long of this wavelength, and outside of the 3 nm bandwidth acceptance region of the Stark effect, indicating that this particular structure will not be successful in Stark mode-locking a VECSEL at 1040 nm.

3.6.2 Further SESAM Analysis

Further investigations of the SESAM are possible in the form of pump and probe measurements. These can give recovery times for the SESAM, its modulation depth, saturation fluence, reflectivity, and nonsaturable losses, as well as characterising the dynamics of the SESAM recovery. However, these measurements are by no means trivial to obtain, and it was not within the remit of this project to perform such a characterisation. Since the work of this thesis was completed, a piece of Stark SESAM has been analysed in a nonlinear optical characterisation rig and a pump-probe rig, both set up in the Keller group at ETH Zurich. The measurements were performed by Rachel Grange using the methods described in [10].

For both characterisations, the excitation source was a Time Bandwidth Product SESAM mode-locked Yb:YAG laser centred at 1030 nm, with a 0.5 nm spectral bandwidth, with 2.1 ps pulse duration at 77 MHz repetition rate and 215 mW output power. This matches very approximately the properties of the VECSEL into which the SESAM is inserted, with the power selected to simulate the fluences experienced by the SESAM in the VECSEL. In the nonlinear reflectivity measurement, the incident pulse fluence is varied using a variable attenuator, and the reflected and incident beams are compared using two suitably calibrated photodiodes to calculate the reflectivity for varying pulse fluences. In the pump probe experiment, a strong pump beam and weak probe beam both derived from the excitation source simultaneously are overlapped spatially on the sample. The pump beam is then delayed relative to the probe beam, and the reflectivity changes in the sample caused by the pump beam are evident in the probe beam reflection.

From this characterisation, the Stark SESAM was found to recover completely after approximately 10 ps, with a fast 1/e recovery time measurement between 1 ps at low excitation, and 5 ps at high excitation, limited by the resolution obtainable using the 2.1 ps excitation pulses. The saturation fluence was measured to be 56 μJ/cm^2, the modulation depth 0.32%, nonlinear reflectivity 99.46%, and the nonsaturable losses 0.22% [11]. Typically for slow saturable absorbers which do not employ the Stark effect, such as the one used to mode-lock the VECSEL described in chapter 5, the recovery time is bi-temporal with a 5-ps fast component, and a >100-ps slow recovery component; modulation depths are typically around 1%, and nonsaturable losses comparable to that of the Stark SESAM [12]. The faster recovery of the Stark SESAM and use of the Stark effect indicates that it is a suitable candidate for mode-locking to produce sub-ps pulses, as has already been reported [13]. The small modulation depth of the Stark SESAM is ideal for multi-GHz repetition rate mode-locking to suppress Q-switching instabilities [14].

3.7 Conclusions

The characterisation experiments described in this chapter allow insight into the unique properties of individual VECSEL samples to be gained. The reflectivity spectrum of the sample and PL measurements provide the necessary information to determine whether or not the sample growth has been successful in creating a structure close to design, whilst the top PL and CW lasing properties of the sample can be compared with other devices to ascertain the VECSEL's merits. These techniques are versatile and can be applied to any VECSEL sample design at any wavelength providing the necessary detectors and excitation sources are available.

The knowledge gained from sample characterisation allows a more accurate interpretation of the lasing characteristics observed of the mode-locked devices described in this thesis. Armed with knowledge of the thermal and spectral properties of the device, it is possible to predict the optimal lasing conditions for each sample individually. Necessary thermal management of the devices can be identified, and threshold conditions predicted. Characterisation of the SESAM gives the information required to understand the mode-locking dynamics of the device, providing insight into the pulsing regimes observed.

The results presented in this chapter show the critical dependence of VECSEL operation on the thermal management of the device. The samples employed in this thesis have been designed for low threshold, low power operation, and so thermal management of these samples is less complex. However, in order to access high power VECSEL operation, more careful control of the thermal properties is required. Thermal management of VECSELs will be discussed in the next chapter.

Bibliography

[1] Tropper, A. C. & Hoogland, S. H. Extended cavity surface-emitting semiconductor lasers. *Progress in Quantum Electronics* **30**, 1–143 (2006).

[2] Hoogland, S. *Optically pumped Vertical-External-Cavity Surface-Emitting Semiconductor Lasers*. Ph.D. thesis, University of Southampton, Southampton, UK (2003).

[3] Vossen, J. L. & Kern, W. *Thin Film Processes* (Academic Press Inc., 1978).

[4] Perkin Elmer technical information database. Website (1998-2006). URL `http://www.perkinelmer.com`.

[5] Coldren, L. A. & Corzine, S. W. *Diode Lasers and Photonic integrated Circuits* (John Wiley and Sons Inc., 1995).

[6] Hecht, E. *Optics* (Addison-Wesley Publishing Company, Inc., 1987), second edn.

[7] Holm, M. A., Burns, D., Cusumano, P., Ferguson, A. I. & Dawson, M. D. High-power diode-pumped AlGaAs surface-emitting laser. *Applied Optics* **38**, 5781–5784 (1999).

[8] Findlay, D. & Clay, R. A. The measurement of internal losses in 4-level lasers. *Physics Letters* **20**, 277–278 (1966).

[9] Mysyrowicz, A. *et al.* 'dressed excitons' in a multiple-quantum-well structure: Evidence for an optical stark effect with femtosecond response time. *Physical review letters* **56**, 2748–2751 (1986).

[10] Haiml, M., Grange, R. & Keller, U. Optical characterization of semiconductor saturable absorbers. *Applied Physics B: Lasers and Optics* **79**, 331–339 (2004).

[11] Grange, R. Nonlinear optical characterization of the SESAM QT1627 (2005). Private communication.

[12] Tropper, A. C., Foreman, H. D., Garnache, A., Wilcox, K. G. & Hoogland, S. H. Vertical-external-cavity semiconductor lasers. *Journal of Physics D: Applied Physics* **37**, R75–R85 (2004).

[13] Garnache, A. *et al.* Sub-500-fs soliton-like pulse in a passively mode-locked broadband surface-emitting laser with 100 mW average power. *Applied Physics Letters* **80**, 3892–3894 (2002).

[14] Grange, R. *et al.* New regime of inverse saturable absorption for self-stabilizing passively mode-locked lasers. *Applied Physics B: Lasers and Optics* **80**, 151–158 (2005).

Chapter 4

Wafer Fabrication

4.1 Introduction

A great advantage of the VECSEL is that if suitably designed, the wafer requires no post-growth processing in order to achieve lasing performance for low power laser work. Indeed, some of arguably the most significant results in the VECSEL mode-locking field have been obtained using samples simply cleaved from a grown wafer and inserted directly into a cavity [1, 2, 3, 4]. Notably, in the mode-locked VECSEL results presented in this thesis, a chip was simply cleaved from the as-grown wafer, and mounted on a copper heat-sink with silver-loaded electrically conductive paint, ready for use (results in section 2.4.2 and chapter 5).

However, in order to access high power lasing from a chip, some wafer processing and device fabrication may be required. In this chapter, adaptations of standard glass polishing methods for GaAs are demonstrated, and applied as a method for improving pulse characteristics in a ML-VECSEL cavity. The thermal properties of a VECSEL chip are discussed, and two different methods of thermal management of VECSELs are reviewed in conjunction with experiments carried out to assess their suitability to the ML-VECSEL devices presented in this thesis.

4.2 Substrate Reflections

For many potential applications of pulsed semiconductor lasers, both pulse shape, and the quality of the pulse train are important. The undesirable chirp and phase structure induced in mode-locked semiconductor diode laser pulse profiles where the pulse travels along a highly nonlinear waveguide to exit the laser limits the applications of these devices: the inability of these otherwise cheap, compact, desirable devices to meet the demands of pulse quality has prevented them from competing with their solid-state counterparts for some pulsed applications. However, VECSELs have challenged this inadequacy of mode-locked semiconductor lasers. Optical Stark effect mode-locking, employed in this thesis (section 2.4.2), produces clean, sub-500 fs, sech^2 pulses of quality comparable with pulses from conventional solid state lasers, but potentially at a fraction of the device cost [2, 5].

Realisation of this potential however may require some processing in order to optimise ML-VECSEL performance. Initial results of Stark mode-locking achieved in the work contained in this thesis showed satellite pulses separated at approximately 14 ps and multiples thereof from the main pulse autocorrelation, and corresponding modulations of the optical spectrum of the pulse (see figure 4.1). Calculations predicted that these satellites were a result of a back-surface reflection of a small amount of light that was transmitted through the back of the DBR of either the gain or SESAM sample, reflected off the back surface of the sample, and then re-entered the cavity to circulate and extract gain.

The 14 ps separation of the satellite (denoted by 'x' in figure 4.1) corresponds to a length in a vacuum of 4.2 mm. From equation 2.2.1 in chapter 2, we can calculate that the refractive index of GaAs at $\lambda = 1043$ nm is $n = 3.5$. Therefore, at this wavelength, 14 ps corresponds to a length of 1.2 mm in GaAs. This distance must be halved to account for the reflection, giving a distance of 0.6 mm in GaAs; the thickness of a sample wafer. The resulting modulations of the optical spectrum can be observed with a spacing of 0.26 nm, also in agreement with the calculated value.

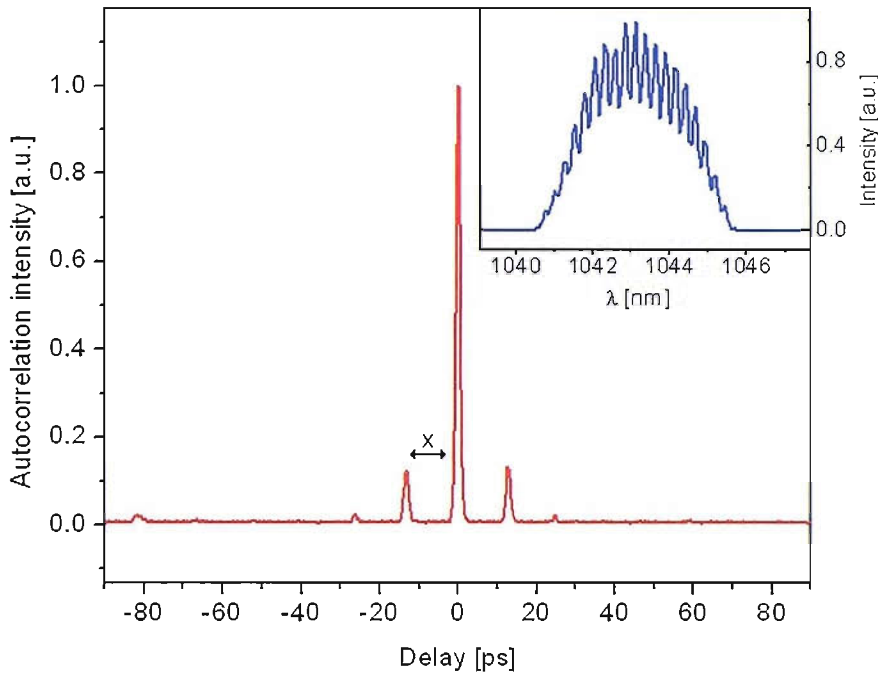

FIGURE 4.1: Wide-span autocorrelation (red) and optical spectrum (blue, inset) of a Stark ML-VECSEL pulse, showing the presence of satellite pulses resulting from sample back-surface reflections. 'x' denotes the delay of the satellite pulse from the main pulse.

Back surface reflections are stronger for wafers that are polished on both sides, but even for wafers that are only front-face polished, the rough back surface may scatter some of the transmitted light back into the laser mode. Therefore, the approach to eliminating back-surface reflection induced satellite pulses adopted in this thesis is angle polishing. The sample back surfaces are polished at a slight angle ($\approx$2 degrees), to reflect any stray light outside of the cavity mode, and hence eliminate it from the laser output. The highly polished surface has sufficient quality to avoid any scattering into the laser mode by imperfections.

4.2.1 Polishing GaAs

Standard polishing methods developed to polish silicon and other dielectrics employ several initial lapping stages; first using a large particle-size (600 μm) silicon carbide lapping slurry, followed by decreasing particle size calcined aluminium slurries (9 μm and 3 μm particle sizes in turn) to remove large thicknesses of material, and smooth, the

final step uses a chemo-mechanical polishing treatment called Syton (SF1), a colloidal suspension of silica nanoparticles in an alkaline solution, to etch and polish, leaving an optically-flat surface. GaAs responds quickly to standard lapping techniques; it is so brittle, that is is not necessary to use coarse-grade slurries unless dealing with millimetres of GaAs removal. However, GaAs is not successfully etched by SF1, hence, other methods of final polishing must be employed. The final polishing stage for all samples in this thesis is carried out using a finer calcined aluminium grit with particle size of 0.3 μm.

The process is carried out using a Logitech PM2A polishing machine, with interchangeable polishing plate. The sample is mounted on a Logitech PP5GT polishing jig [6]. The recipe for the GaAs polishing process is as follows:

1. The GaAs sample is mounted on a glass microscope slide with the surface to be polished facing up. In order to prevent a rounding of the sample edges by any rocking motion of the jig, or extra polishing at the sample edges, it is protected by packing with sacrificial pieces of GaAs substrate around the sample edges. Mounting is with quartz wax. The sample and sacrificial GaAs is positioned on the glass slide, this is then placed on a hotplate held just above the wax melting point (66-69 ^oC), and a few grams of wax particles are deposited on top, narrowly encasing the sample and sacrificial GaAs in molten wax (as in figure 4.2a) and b).
2. The glass slide, complete with sample is then mounted on to a polishing jig mount using molten wax again. This is then removed from the heat, and allowed to cool.
3. Once the wax is set, the mount is screwed on to the polishing jig, and positioned so that the sample falls just proud of the jig rest (shown by the green, dashed line in figure 4.2b) exerting minimal pressure upon it when it is placed on the lapping plate. At this point, if an angle polish is required, the polishing jig can be configured by the adjustment of 2 screws to hold the sample at the desired angle.
4. The lapping plate is prepared using the 3 μm polishing slurry to be used for the lapping stage. A lapping plate conditioning jig is used. The plate is rotated at 60 rpm for 20 minutes with slurry dripped on constantly to keep the plate just

wet enough to allow free movement of the jig, and providing an adequate coating of slurry particles on the plate for efficient lapping.

5. After conditioning, the plate is rinsed with de-ionized (DI) water, and re-coated with polishing slurry. The polishing jig with sample mounted is then placed on the plate, and the sample lowered down into contact with the plate. This setup is shown in figure 4.2c).

6. Depending on the amount of material to be removed, and the pressure exerted on the sample, the lapping stage duration varies. The lapping plate rotates at 30 rpm, and is lubricated with one drop of slurry per revolution. The sample surface is observed every 10-15 minutes to check the progress of the lapping, and allow prevention of the propagation of any damage or cracks across the sample surface. To lap an angle of a couple of degrees across the sample surface using 3 μm slurry and minimal pressure at 30 rpm takes approximately 1.5 hours, at a GaAs lapping rate of $\sim$20 μm/hour.

7. Once lapping is complete, the sample and jig are thoroughly doused with copious amounts of DI water to remove any remaining slurry particulates.

8. The lapping plate is exchanged for a polishing plate with a Hyprocel Pellon polishing cloth surface (available from Logitech [6]). The cloth is impregnated with 0.3 μm particle-size calcined aluminium oxide slurry, which drips as before on to the plate as it turns. The jig is positioned, and the plate is rotated at 10 rpm, slower than before to avoid rocking of the sample on the cloth surface.

9. The sample surface is regularly observed under a microscope to assess the surface quality. The required quality is achieved when the surface scratch density is low enough that a 120 μm pump spot can occupy an un-scratched area. This takes approximately two hours.

The lapping process is different from the process of grinding in that it uses a free-moving abrasive (the slurry) between two surfaces to wear the surfaces, instead of the abrasive material being held in the wheel, and cutting the sample. The lapping technique induces

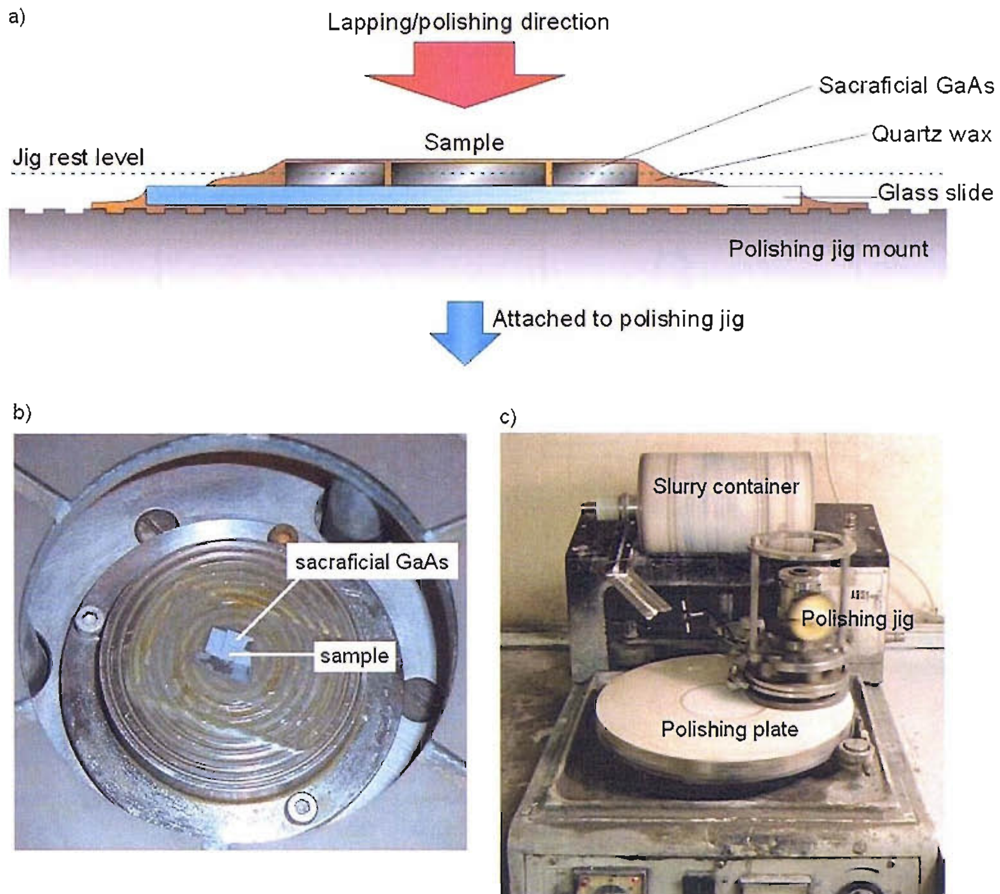

FIGURE 4.2: Polishing GaAs: a) Cross-section of mounted sample showing sacrificial GaAs packed around the sample, mounted on a glass slide, and attached to the polishing jig mount using quartz wax. The mount is positioned on the jig so that only the material above the jig rest level falls proud of the jig base. b) Photograph of the mounted sample showing the sacrificial GaAs packed around the sample. c) The Logitech PM2A polishing machine with pellon polishing cloth and 0.3 μm slurry. The polishing jig is held in place on the polishing plate by a moveable arm.

much less stress in the material being polished, and so is much more suitable for the polishing of inherently brittle GaAs samples [7].

However, this purely mechanical method of polishing is not optimal for the final steps in optical surface preparation, where a chemical method would produce favourable results. A chemo-mechanical method of polishing GaAs does exist. It relies on the use of Chemlox, a sodium hypochlorite-based polishing fluid supplied by Logitech [6], used in conjunction with a glass polishing plate. Sodium hypochlorite is a well-known etchant of GaAs [8]. However, the aggressive nature of Chemlox on other materials makes it

unsuitable for use with the polishing machine available, and so this technique was not employed for the work presented in this thesis.

4.2.2 Back-Surface Angle-Polished ML-VECSEL Results

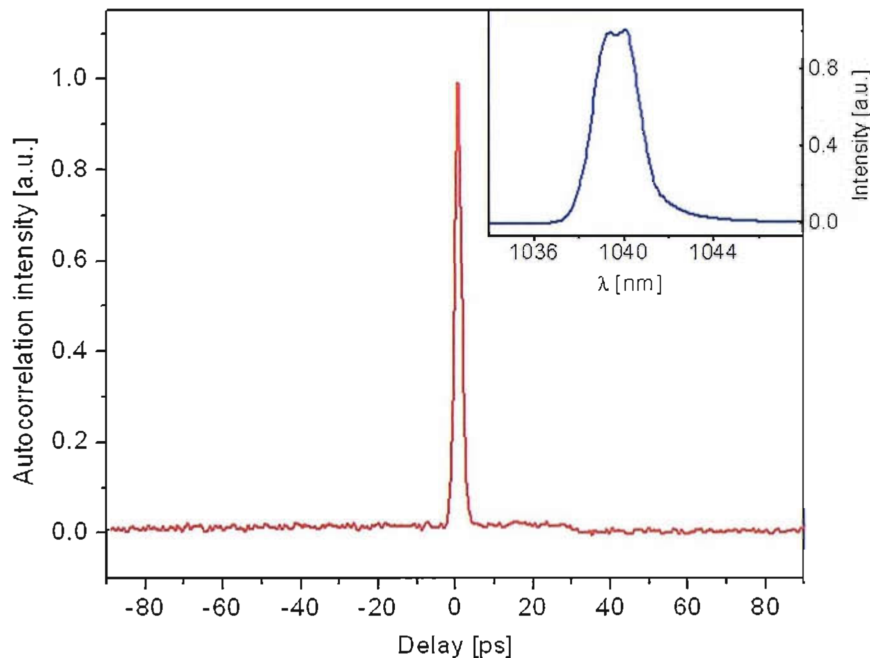

FIGURE 4.3: Wide-span autocorrelation (red) and optical spectrum (blue, inset) of a pulse from a ML-VECSEL in which the back-surface of the GaAs substrate of the gain and SESAM samples has been polished at an angle to eliminate satellite pulses resulting from sample back-surface reflections.

The back-surface angle-polished samples were mounted as before, with conductive silver paint on to a peltier temperature-controlled copper heat-sink, and returned to the VECSEL cavity. Lasing was achieved at 1040 nm with characteristic ~500 fs pulses. The wide-span autocorrelation and optical spectrum of the polished sample ML-VECSEL are shown in figure 4.3. Notably, the wide-span pulse autocorrelation shows an absence of the characteristic back-surface reflection satellites seen in the unpolished cavity results shown in figure 4.1, and the optical spectrum is no-longer modulated. The lasing wavelength is approximately 2 nm shorter than the wavelength emitted by the cavity that yielded the results in figure 4.3, this is attributable to pumping of a slightly different spot on the sample. It should be noted that in comparison of results achieved before and after polishing, the VECSEL output power was not reduced, and the front-surface

quality of the polished samples did not appear to have been degraded when observed under a microscope, indicating that no noticeable damage was incurred in the polishing process.

4.3 Thermal Properties of VECSELs

The thermal sensitivity of semiconductor light-emitting devices is well documented, and it is well known that devices tend to operate with greater efficiency at lower temperatures due to a decrease in carrier leakage with decreasing temperature [9]. In a VECSEL structure, however, thermal effects are more complex. Optical pumping introduces a quantum defect between pump and laser photons, producing excess heat in the gain structure which increases with increased pumping/VECSEL power, alongside the heating effects of non-radiative effects. As already discussed in chapters 2 and 3, it is important to account for the thermal misalignment of the VECSEL structure. In addition, with heating, the material will expand, causing a slight thermal lens to form.

Naturally, for most applications, room temperature operation is desirable, indeed, the less temperature sensitive a structure is around room temperature, the better. Consequently, the samples employed in this thesis are designed to account for the various temperature shifts they will experience, and give optimal lasing at room temperature with pumping (as in section 2.2). Ultimately, not only do these thermal effects limit the slope efficiency of a VECSEL, but they also have a significant effect on the maximum power obtainable from a structure by determining its rollover point as observable in the CW-lasing data shown in 3.9 in section 3.5. To overcome this effect, it is necessary to lower the thermal impedence of the chip. Two approaches to this are discussed in the remainder of this chapter. One other interesting approach not discussed here is that of in-band pumping, where pump absorption is in the quantum wells [10]. Thus the pump radiation wavelength is very close to that of the VECSEL, resulting in a low quantum defect, and hence reduced heating.

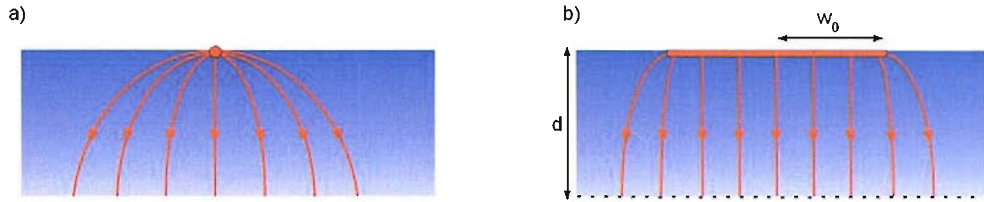

FIGURE 4.4: Schematic representation of two heat flow geometries considered for the analytical model: a) a point source of heat on a semi-infinite thermal conductor that is cooled on its bottom-surface, and b) a uniform heat input over a circular disk of radius w_0, on a slab of thickness d. The solid red lines show the flux distribution.

4.3.1 Analytical Model

Extensive modelling of the three dimensional heat flow within VECSEL structures has been carried out by several groups in order to analyse the merits of various thermal management techniques [11, 12, 13]. However, for our purposes, it is possible to demonstrate these merits through application of a simple analytical approach [14].

Sketches of two heat flow geometries are shown in figure 4.4. The first (figure 4.4a) is a point source of heat on a semi-infinite thermal conductor that is cooled on its bottom-surface. Approximate heat flux distribution lines are sketched on to the diagram to show the significant contribution to heat evacuation from lateral cooling in this geometry. The second (figure 4.4b) shows a uniform heat input over a circular disc of radius w_0 on a slab of thickness d. Here the flux distribution lines show a much closer to one-dimensional heat flow, with a much reduced contribution from lateral cooling. In this case, the thermal impedence of the device is larger, but the device benefits from being intrinsically power scalable.

In the case of the point heat source (figure 4.4a), it is possible to express the temperature distribution as a function of position in the conducting medium [14]:

$$\delta T(\mathrm{r}) = \frac{P}{2\pi\kappa\,|\mathrm{r}|}, \tag{4.3.1}$$

where P is the power of the point source of heat, and κ is the thermal conductivity of the conducting medium.

Material	κ [Wm^{1}K^{-1}]	
$Al_xGa_{1-x}As$	55 - 212x + 248x^2)	[16]
GaAs	55	[16]
AlAs	91	[16]
$Al_{0.2}Ga_{0.8}As$	22.52	[16]
Copper	401	[17]
Indium	81.8	[17]
YAG	11	[18]
Sapphire	44	[19]
SiC	490	[20]
Diamond	2000	[21]
Air	0.026	[22]

TABLE 4.1: Thermal conductivity values of some common heat sink materials, YAG is added for example of thin disk SSL comparison

For the second geometry, assuming one-dimensional heat flow, the temperature drop becomes [11]:

$$\delta T_{1D} = 2\frac{Pd}{\pi w_0^2 \kappa}. \tag{4.3.2}$$

The thermal properties of a VECSEL are very similar to those of a thin disk laser [15]; they exhibit the second thermal geometry (equation 4.3.2), with the thin disk representing the area of the active region pumped by the incident, top-hat profile pump beam that is launched from a multimode fibre. Hence, increasing the pump spot area (πw_0^2) allows linear scaling of the incident pump power since the extra heat is spread over a larger disk and 1-D heat flow is not compromised, ultimately allowing higher power operation than in the first geometry (equation 4.3.1).

It is also important to consider the thermal conductivity of the conducting medium that surrounds the pumped disk, κ. The inverse relationship between temperature rise and thermal conductivity in equation 4.3.2 dictates that the more thermally conductive the medium, the smaller the temperature rise in the active region of the sample for a given pump power and spot size. Thermal conductivity values of some common heat sink materials are shown in table 4.1. Methods of thermal management of VECSELs though manipulation of these properties will be discussed in sections 4.5 and 4.6.

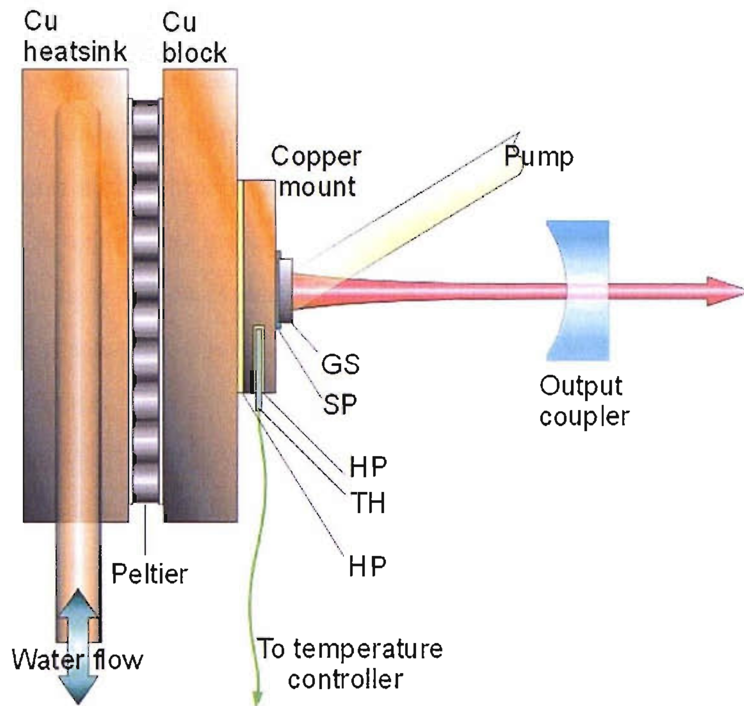

FIGURE 4.5: Thermal mounting of VECSEL samples described in this thesis. The gain sample (GS) is bonded to the copper mount with conductive silver paint (SP), this is in turn attached to the copper block which is temperature controlled by a Peltier device. Conductive heat paste (HP) ensures good thermal contact at all interfaces. The sample temperature is detected by a thermistor (TH) inserted into the copper mount. The back plate of the device is water-cooled.

4.4 Heat-Sinking 'As-Grown' Samples

The majority of the samples described in this thesis were simply cleaved directly from the freshly grown wafer, bonded on to a copper mount using conductive silver paint, attached to a cooled copper block, and inserted into the cavity. The copper block temperature is peltier controlled, with a Peltier device attached to a water-cooled copper heatsink. Figure 4.5 shows this mounting configuration.

However, this arrangement does not permit high power lasing to be achieved, and the gain structure is subjected to extensive heating effects. Indeed, if the samples contained more quantum wells to achieve higher power, and hence had a higher threshold, it may not even be possible to reach transparency before thermal rollover, and the laser may not oscillate at all, as discussed in section 2.2.

In a pumped sample, the heat must travel directly from its source in the gain region. Assuming one-dimensional heat flow, for an un-processed sample, the available routes are either out through the front-surface of the sample into air, or back through the DBR to the substrate and eventualy the heatsink. The extremely low thermal conductivity of air results in a negligible amount of heat being evacuated via this route. Instead, the majority of the heat dissipates through the DBR, which, due to its many-layer structure, and inclusion of some low thermal conductivity AlGaAs ($\kappa = 22.5\mathrm{Wm^{1}K^{-1}}$), has a high thermal impedence. Then the heat must travel through the bulky GaAs substrate, also with a low thermal conductivity, in order to reach the efficient copper heatsink to which it is attached. Fabrication methods to overcome these far-from optimal thermal properties have been investigated extensively in the VECSEL field. The following sections describe the two key techniques that have emerged: bonding to an intracavity heat-spreader, and substrate removal.

4.5 Crystalline Heat-Spreaders

Crystalline heat-spreaders have been widely used across the semiconductor laser diode industry to improve device efficiency, lower threshold currents and increase optical power output, with the added advantages of increased device lifetimes, higher reliability, and improved frequency stability [23]. For this purpose, diamond has been the somewhat expensive, but very effective material of choice, with its very high thermal conductivity, whilst other heat spreader materials include sapphire and silicon carbide (SiC) with thermal conductivities shown in table 4.1.

Crystalline heat-spreaders were first employed in VECSELs by Alford et al at Sandia [24]. They used a 2 mm-thick sapphire window which was directly bonded on to the front surface of the gain sample. Pumping through the sapphire window, they demonstrated powers exceeding 1.5 W, at a wavelength of 980 nm, in continuous-wave operation from a VECSEL, with an optical-to-optical efficiency of 19%. Further investigations into crystalline heatspreading were carried out by Hastie et al in [25, 26]. They investigated the merits of several different materials as VECSEL crystalline heat-spreader windows,

demonstrating that performance could be greatly improved using SiC and diamond with much higher thermal conductivities. The group have gone on to extensively model thermal management in VECSELs [12], and have incorporated the heatspreader technology into several 'microchip' VECSEL devices [27, 28].

The heat-spreader is directly bonded to the front surface of the sample, evacuating the majority of the heat through the sample front surface, avoiding the bulky substrate and high thermal impedence DBR layers of the VECSEL sample. Because the heat flow is predominantly through the front surface, this technology can be efficiently applied to VECSELs at any wavelength, regardless of their semiconductor layer composition, providing the heat-spreader material is transparent and non-absorbing at the lasing and pump wavelengths. This is a particularly attractive approach at wavelengths where the corresponding semiconductors have very low thermal conductivities, for example in antimonide VECSELs [29], or are difficult to etch selectively to remove the substrate.

4.5.1 Fabricating a Heat-Spreader Device

When considering VECSEL operation, the challenges for producing a reliable heat-spreader window device are clear. The device will experience some localised heating, and may be cooled to improve lasing action, so it is essential that the two substrate materials have similar coefficients of thermal expansion. Since the window is intracavity, with pump radiation also needing to pass through, the material must be transparent at both pump and laser wavelengths. Moreover, it must be of sufficient quality for lasing to be possible, taking into account the VECSEL's low tolerance of intracavity fixed losses. The same restrictions apply for the bond between the heat-spreader, and the VECSEL gain structure itself. It is imperative that the bond does not introduce any thermal resistance, and negligible optical losses. It is clear from these requirements, that use of any sort of adhesive is not suitable, and that the heat-spreader must be contacted directly to the gain sample with a lossless bond. Direct bonding using Van der Waals forces provides an attractive solution to this problem.

Direct bonding has been employed throughout the laser and optoelectronics fields as a method for joining one mirror-polished surface to another without the use of an adhesive

[30]. This method escapes the problems associated with the use of an adhesive layer, including a mismatch in thermal expansion coefficients that may result in cracking at high temperatures, etalon effects in the adhesion layer, impurities in the adhesive that lead to optical losses and absorption, diffusion of foreign atoms into the VECSEL and heat-spreader structures from the adhesive, structural weaknesses in the adhesive layer itself, and thermal impedence introduced by the layer and the additional interfaces. Moreover, direct bonding is much more suitable than conventional wafer fusion bonding [31], in that it is possible for bonds to be formed at room temperature and low pressure, avoiding the possibility of thermally and pressure induced damage in the VECSEL layer structure. With careful surface preparation pre-bond, it is possible to form a lossless, vacuum tight, seamless interfacial bond between two explicit materials, each maintaining their individual properties [32].

It was Yablonovitch et al who first observed the tendency for GaAs films to bond to any flat surface [33]. Then entitled 'Van der Waals bonding', Yablonovitch et al investigated this technique as a preferred alternative to lattice-mismatched heteroepitaxial growth for the amalgamation of different semiconductor layers. They noticed that the films they produced via epitaxial lift-off (see section 4.6) tended to bond to any smooth substrate by natural intermolecular forces. Furthermore, they noticed that the process was enhanced by the capillary forces exerted by the presence of a small amount of distilled water that remained after surface preparation.

The direct bonding of GaAs wafers on the scales described in this thesis was extensively studied by Liau in 2000 where the technique was termed 'liquid capillarity' [34]. He derived the criteria for surface tension, wafer flatness and elasticity as will be discussed in the next section. For the samples bonded in this thesis, sapphire was chosen as the heat-spreader material, since it is much cheaper than diamond, and far more robust than SiC, known to be particularly brittle. Moreover, with transparency ranging from wavelengths of 180 nm to 4.5 μm and a thermal expansion coefficient of 8.4×10^{-6} K^{-1} [35], similar to 5.73×10^{-6} K^{-1} for GaAs [16], Sapphire fulfills the other requirements of a suitable material.

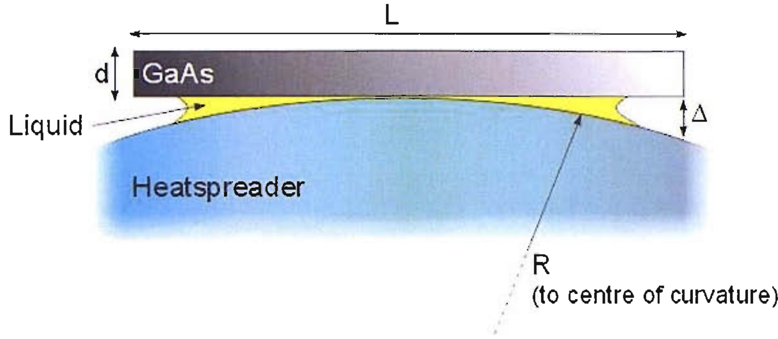

FIGURE 4.6: Diagram showing the Liau model of capillary bonding for use in conjunction with equation 4.5.1 adapted from [34]. The flat sample of thickness d, and length L, is bonded to the curved surface with radius R to the centre of curvature. The capillary liquid is shown in yellow, between the 2 surfaces separated by the distance δ.

4.5.1.1 Mathematical Model

The Liau model (after [34]) is based on the simplified concept of bonding a flat sample to a curved substrate as shown in figure 4.6. The strength of the surface tension (α) of the liquid used in the bonding process required to force the sample to deform to the substrate surface is given by:

$$\alpha > \frac{Ed^3}{32R^2}\ , \quad R = \frac{L^2}{8\Delta} \tag{4.5.1}$$

where E is the Young's modulus of the sample material (in this case, the GaAs VECSEL substrate), d is the thickness of the sample, R is the radius of curvature of the surface of the heat-spreader substrate material, L is the length of the sample ($L \gg R$), and Δ is the separation of the surfaces.

For the samples used in this thesis, d = 500 μm, E_{GaAs} = 8.53$\times$10^{-11} dyn/cm^2 [36] (1 dyn = 10^{-5} N). For the heat-spreader substrates, the sapphire supplier quoted Δ < 0.4 μm for L = 5 mm. Therefore, using equations 4.5.1, R = 7800 cm, and $\alpha >$ 0.054 dyn/cm. The values of α for water, methanol, acetone and IPA are 72.8 dyn/cm, 22.6 dyn/cm, 25.2 dyn/cm and 23.0 dyn/cm respectively [37], implying that all three are suitable liquids for the direct bonding of GaAs to sapphire via the Liau capillary

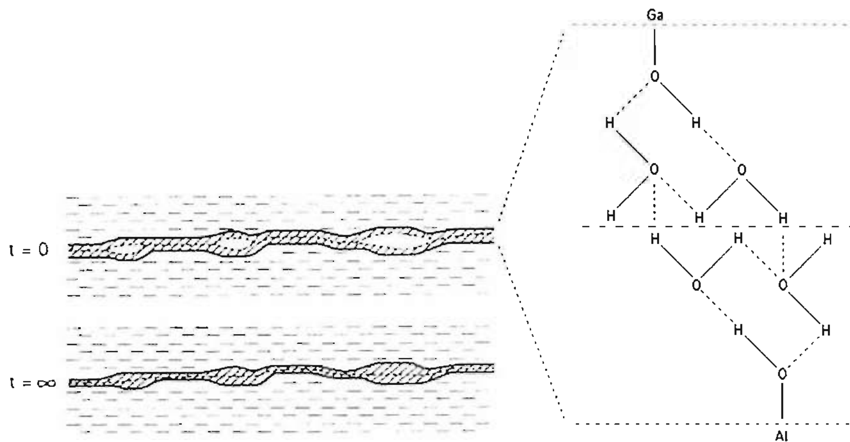

FIGURE 4.7: Diagram to represent the strengthening of bonds between sample and heat-spreader with time, showing the hydrogen bridges that can form on hydrophilic surfaces to strengthen the bond, adapted from [39].

bonding method. The surface of the VECSEL gain sample is assumed to be much flatter than the sapphire, with $\Delta \approx 2$ nm.

4.5.2 Surface Preparation

The chemical state of the substrates to be bonded is also critical [38]. The strength of the bond between the substrates increases steadily for some tens of hours of increase, and then reaches a steady state. At this point, the surfaces are in close contact, and in areas of atomic contact, hydrogen 'bridges' may form, providing additional strength to the bond surplus to that of the Van der Waals forces [39]. This process is shown schematically in figure 4.7. For this to happen, all native oxides, organic, inorganic and chemical impurities must be removed from the substrate surfaces, and GaAs, hydrophobic in nature, must be activated in some hydrophilic aqueous treatment.

Samples are always handled with clean, teflon, Lerloy® tweezers. The cleaning procedure adopted for the substrates comprising the samples described in this thesis was carried out in a class 1000 cleanroom. The method is as follows:

1. If the sample has been previously polished, it must be soaked in a beaker of Ecoclear^{TM} (a solvent designed specifically for wax removal) overnight, and any

large clumps of wax gently wiped away once weakened using a cleanroom bud soaked in Ecoclear^{TM}.

2. The sample surface is doused with a jet of Ecoclear^{TM} to remove any large particulates.

3. A cleanroom-grade cotton bud loaded with Ecoclear^{TM} is wiped across the sample surface to one designated corner, the bud is discarded after each wipe, and a new one selected, to avoid wiping contaminants back over the sample surface in a second wipe.

4. Submerse the sample in a small beaker of Ecoclear^{TM}, and place in an ultrasonic bath at 40°C for 20 minutes.

5. Remove the sample from the beaker and wash the surface in a jet of Ecoclear^{TM} to remove any contaminant residues.

6. Repeat steps 2 to 5 with first acetone, then isopropanol, then DI water.

7. Completely dry the sample surface with dry nitrogen.

8. The sample should be kept front-surface up during these procedures, and in any further storage, in a protective sample box, to avoid contact contamination.

Some difficulties were encountered when deciding how to render the sample surface hydrophilic. Common hydrophilic surface washes used in direct bonding technology are based on solutions of ammonium hydroxide (NH_4OH) and hydrogen peroxide (H_2O_2), or other alkaline solutions saturated with hydroxyl groups [40]. However, these substances strongly etch both GaAs and AlGaAs, and therefore are not suitable for use in the GaAs-based direct bonding technique. In fact, no substantial hydrophilic surface treatment is used in the bonding process described here. However, the cleaning process itself can act to render the GaAs hydrophilic.

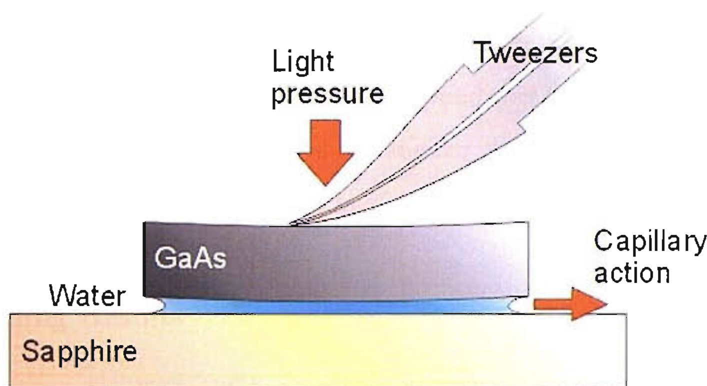

FIGURE 4.8: Schematic representation of the bonding method. The sapphire rests on a cleanroom tissue covering a glass slide to protect it from the structured cleanroom wet bench surface and any contaminants.

4.5.3 Direct Bonding Procedure

Following the cleaning procedure, the substrates can be bonded. The samples presented in this thesis consist of GaAs-based VECSEL samples or (for trial purposes) plain GaAs substrates bonded to sapphire substrates. The cleaned 1 cm × 1 cm × 0.5 mm sapphire substrate is placed clean-face-up on to a piece of cleanroom tissue over a microscope slide on the wet bench. A drop of DI water is dropped on to the sapphire. The VECSEL sample to be bonded (very approximately 3 mm × 5 mm × 0.5 mm) is then placed clean-face down on to the sapphire with the liquid between. Any excess liquid is blown away with dry nitrogen. The sample is then moved across the sapphire surface with gentle finger pressure (using the clean teflon tweezers), until a bond is felt to form, and the sample 'snatches' to the sapphire surface. This method is shown schematically in figure 4.8. The sample is then left overnight for the bond to strengthen, before turning over to assess the quality of the bond formed. An additional adhesive may be applied around the edges of the bonded area post-bond to aid and maintain adhesion, but the adhesive for this should be carefully selected so as not to jeopardise the bond in any way. For the samples presented in this thesis, a thick UHU super-glue was used that did not seep into the bond.

During bonding trials, it became apparent that the quality of the cleaved edges of the sample was of critical importance. Samples with poor quality edges did not bond, and

the best bonded regions formed closest to the sides with cleaner cleaves. Also from trial, sample shape was a contributing factor, the greater the ratio between the sides of the rectangle of the sample shape, the more likely a bond was to form. It is thought that this is because the improved flexibility a rectangular geometry over square allows the sample to deform to the sapphire surface more readily.

4.5.4 Bonding Results

Initial bonding trials were carried out using GaAs substrate samples, without any active layers grown. A sample of GaAs bonded to sapphire is shown in figure 4.9a. Once the method had been optimised to reproducibly yield samples with > 75 % of the surface successfully bonded (the final method given above), trials were attempted with active samples. The active samples were cleaved from the wafer QT1712, a structure designed to be identical to QT1544, chosen because it was grown most recently: 9 months prior to bonding trials, and hence was expected to have the least surface contamination and degradation. However, surface degradation caused by oxidation was already observable on QT1712's surface as shown in figure 4.9b. Samples were selected to have as little surface oxidation as possible, determined from microscope inspection, since the topography created by this oxidation may prevent bonding.

None of the active samples attempted bonded successfully. One such sample is shown in figure 4.9c. Newton rings are observable across the sample interface, indicating that the bond has not propagated from the top corner of the sample from which it appears to have initiated. It is thought that this is because the active samples tried did not have sufficient surface quality to give a low enough α in equation 4.5.1 to allow the surface tension of even DI water to bond them to the sapphire. No other, newer, less degraded samples were available to bond, however, it is expected that a new sample with a contamination and oxidation free surface would form a successful bond like the GaAs substrate shown in figure 4.9a.

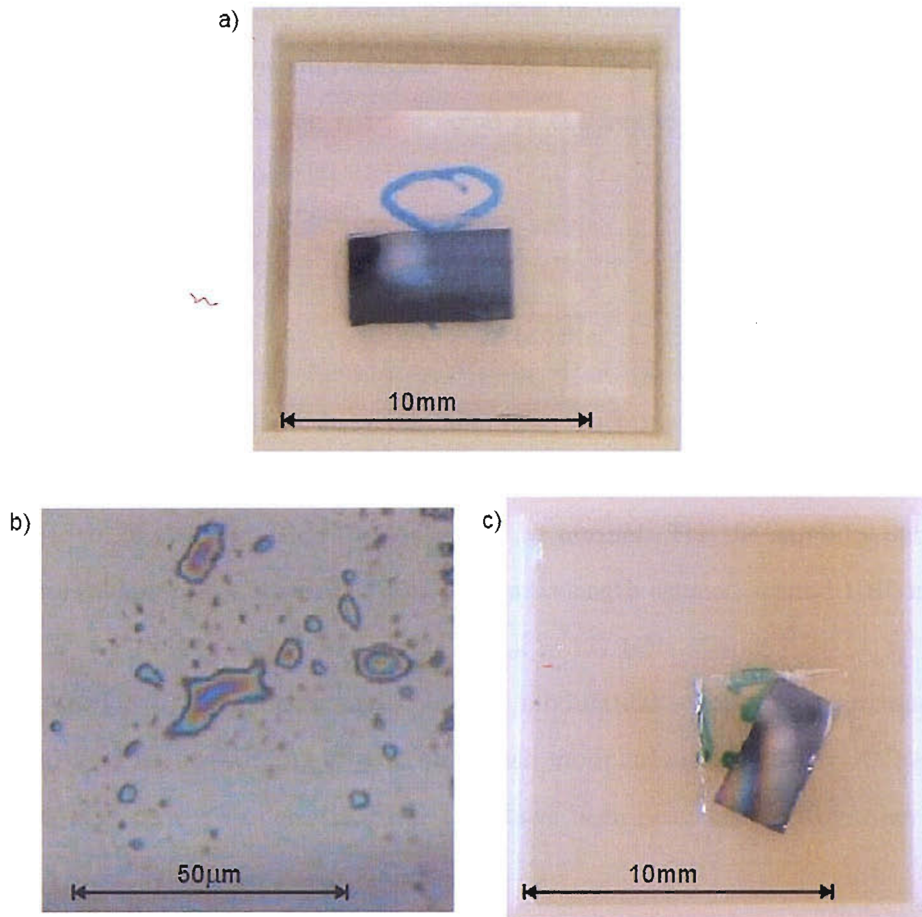

FIGURE 4.9: a) A sample of plain GaAs substrate bonded to sapphire with >75% of the surface successfully bonded (the dark region). The lighter, unbonded region is thought to originate from a cleavage imprefection at the edge of the sample. b) Surface oxidation on sample QT1712 which may act to prevent a bond from forming. c) An active VECSEL sample partially bonded to sapphire. Newton's rings can be seen across the sample surface indicating that only a partial bond has formed.

4.5.5 Suitability of heat-spreader devices for mode-locked operation

In section 2.4, the required operating conditions of a mode-locked VECSEL were explained. If a heat-spreader-bonded VECSEL active sample were to be inserted into a mode-locked cavity, considerations above and beyond those of loss in a CW cavity would have to be taken into account. The broad spectrum required for mode-locking of the device would have to be maintained, and the insertion of another material into the cavity through which the pulse must travel must be included when considering the dispersive effects of various cavity elements on the pulse.

The heat-spreader device has 2 reflecting surfaces; its interface with air, and the bonded interface between it and the gain sample. As such, it may act to modulate the spectrum of the laser with a modulation spacing equal to the free spectral range ($\Delta\nu_{fsr}$) of an analogous etalon, defined as [41]:

$$\Delta\nu_{fsr} = \frac{c}{2nLcos\theta} \tag{4.5.2}$$

where c is the speed of light in a vacuum, n is the refractive index of the medium between the reflecting surfaces, L is the distance between the reflecting surfaces, and θ is the angle of the ray inside the etalon to the normal. For the sapphire substrates used in this chapter, in a laser operating with wavelength centred around 1040 nm, L is 0.5 mm, $n \approx 1.75$ [42], and $\theta = 0$, giving $\Delta\nu_{fsr} = 171$ GHz. Using $\frac{\Delta\nu_{fsr}}{\nu} = \frac{\Delta\lambda}{\lambda}$, where λ is the wavelength of the laser, and $\Delta\lambda$ is the modulation spacing, this corresponds to a spectral modulation spacing of 0.62 nm. Such modulations are clearly visible in the spectra of CW heat-spreader VECSELs that have been demonstrated by other groups [25, 26].

The importance of a broad, clean spectrum for mode-locking to form short pulses was emphasised in section 2.4. The typical 500 fs-pulsed VECSEL spectrum is 2-3 nm broad, so it is clear that 0.62 nm modulations of this spectrum would have a noticeable effect on the mode-locking of such a device, destabilising mode-locking, producing a far from transform limited pulse, a pulse pedestal, or, in the case of deep modulations, a complete inability to achieve short pulses at all. In order to avoid such effects, it would be necessary to coat the faces of the heat spreader with a dielectric coating designed to give ~100% transmission at the laser wavelength to eliminate its etalon properties.

Alternatively, a thinner heat spreader substrate could be used to increase the free spectral range. This approach has been used by Lindberg et al who successfully mode-locked a heat-spreader VECSEL in [43]. A 50 μm thick diamond window, antireflection coated for the lasing wavelength, was bonded to the VECSEL substrate. The lasing wavelength was 1550 nm, and the mode-locked pulses achieved were 3.2 ps long, well within the free

spectral range of the diamond which corresponded to a modulation spacing of 10 nm under these conditions.

Another important property of the heat-spreader to consider in a mode-locked VECSEL is its dispersion. In section 2.4.2, the importance of the interplay between the group delay dispersion introduced by the gain sample and SESAM in the cavity on the pulse length achievable was discussed. A heat-spreader also contributes to this interplay. The second order dispersion of sapphire at $\lambda = 1040$ nm is calculated to be 31 fs^2mm^{-1}. With a total path length of 1 mm through the heat-spreader, assuming that it is adequately coated to prevent etalon effects, which would also dramatically contribute to the second order dispersion experienced by the pulse in the cavity, the total GDD contributed by the sapphire would be 31 fs^2. This is a relatively small value, however, with SESAM GDD values varying from -10 fs^2 to -50 fs^2 in the operation band of the Stark SESAM detailed in section 2.4.2, and the delicate balance of GDD in the cavity required for short pulsed, bandwidth limited operation [44], the small contribution to GDD of the sapphire could be enough to de-stabilise the short-pulse regime.

Ultimately, in future work, if a successful heatspreader device is to be realised in a ML-VECSEL at Southampton, new sample growths with good surface quality are required to obtain a bond to the heatspreader. The heatspreader material will require anti-reflection (AR) coatings on both sides, and a wedged profile to suppress its etalon effects in the cavity which may disrupt the mode-locking. Moreover, the additional dispersion of the heatspreader must be considered, and it may be necessary to compensate for this intracavity either by tuning the operating wavelength and hence the GDD introduced by the SESAM and gain chip, or insertion of an intra-cavity dispersion compensation element.

4.6 Substrate Removal as a technique of thermal management in VECSELs

The second technique investigated to improve the thermal properties of the VECSEL sample is etching and epitaxial liftoff. Here, the primary evacuation route for heat

from the gain region is through the DBR and the back surface of the sample as with unprocessed samples. However, extensive thinning and complete removal of the bulky, insulating GaAs substrate allows heat to be evacuated efficiently via this route in VECSELs operating at 1 μm since the semiconductor compositions used still have reasonable thermal conductivities [13, 29].

Substrate removal has proved itself a successful method for improving VECSEL chip thermal properties. Notably, at wavelengths of 1 μm, the first demonstration of a VECSEL by Kuznetsov et al in 1997 featured a thinning and etching of the substrate to achieve >0.5 W continuous wave (CW) operation [45]. Further improvements have been made by Lutgen et al, who demonstrated 8 W CW with 41% slope efficiency [46], and later by Chilla et al, who achieved 30 W CW [47]. In the mode-locking field, Aschwanden et al have recently demonstrated 2.1 W average power from a picosecond-pulsed mode-locked VECSEL at a wavelength of 1 μm [48]. These results show the great promise for this method of thermal management of VECSELs, however, they are very rigorous and intrusive for the VECSEL structure, and lead to reduced chip lifetimes. Moreover, for the CW results, the large pump areas used mean that the VECSEL beams produced are typically multimode and divergent.

The method used to fabricate the epitaxially lifted off devices presented in this thesis is similar to that used in [11]. The techniques described in the following sections were carried out at the Swiss Federal Institute of Technology (ETH) in Zurich, in collaboration with Professor Keller's group. The technique requires that the VECSEL structure be grown in reverse, with the DBR grown last. The sample is mounted on to a copper heatsink using an elaborate soldering process, and the substrate is thinned and ultimately removed entirely in a wet etching process. This leaves a thin, epitaxially-lifted-off active mirror, soldered directly to a copper heat-sinking device.

4.6.1 Sample Design for Substrate Removal

The gain sample design for an epitaxially lifted off structure remains the same as the antiresonant VECSEL design in section 2.2, but with layer order reversal and additional etch-stop layers to fulfill the fabrication requirements. The sample design is shown

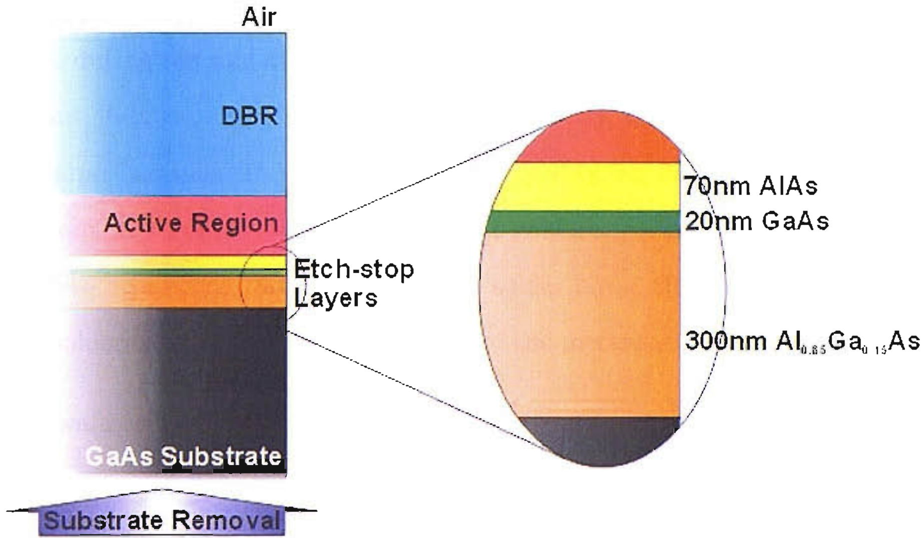

FIGURE 4.10: Layer sequencing in reverse-grown sample for substrate removal. First the three etch-stop layers are grown with 300 nm $Al_{0.85}Ga_{0.15}As$, 20 nm GaAs and 70 nm AlAs. This is followed by the capping layer, window layer and active region, and finally the DBR with an oxidation cap (not shown). The capping layer, window, active region and DBR are grown to the design in section 2.2, but in reverse order.

schematically in figure 4.10. Three etch-stop layers are grown directly on top of the substrate, first, 300 nm of $Al_{0.85}Ga_{0.15}As$, then 20 nm GaAs and finally 70 nm AlAs. This combination requires several highly selective etching steps, and so produces an excellent mirror finish. Next is the 10 nm GaAs capping layer of the active mirror, and then follows the gain structure, complete with window layer, quantum wells and strain compensation as described in section 2.2. And finally, the DBR is grown, with 27 pairs of $Al_{0.2}Ga_{0.8}As$/AlAs. A small GaAs capping layer is grown on top to protect the DBR from oxidation.

4.6.2 The Soldering Process

A small sample approximately 2 mm by 4 mm is cleaved from the wafer, and attached to a small copper submounting plate of 5 mm × 5 mm × 1 mm, using an elaborate composite soldering process. The soldered layer is critical, in that it must provide excellent thermal contact between the Peltier cooled copper heat-sinking device, and the back-surface of the DBR. But equally as critical is the mechanical support that it must provide to the sample during etching, and once it is thinned to its final thickness of

~6 μm on the heatsink, whilst also being soft enough not to induce stress and damage to the sample during the soldering process. Furthermore, the quality of the solder junction is important. Any gaps have lower thermal conductivity, and will be seen as burned spots on the pumped sample. To ensure the highest quality, an RF solder technique is used, adapted from [49]. For this technique, both the gain sample and the copper submount to which it is to be soldered are metalised with solder layers through a sputter technique, and then soldered together through melting of the metalisation layers.

The gain wafer surface (the back of the DBR) is cleaned via the standard procedure detailed in section 4.5.2. The layers deposited on this surface are shown in figure 4.11a and are as follows:

- First a 30 nm titanium layer is deposited to aid adhesion to the semiconductor. This layer has the same function as the flux commonly used in the soldering process, reducing the surface tension of the solder, and preventing the build-up of a solid oxide layer when the solder is in its molten phase. Titanium is chosen instead of flux to avoid the creation of any potential of low conductivity voids in the solder caused by trapped flux vapour. With a refractive index a little larger than 3, this layer also absorbs any 1040 nm radiation transmitted through the DBR eradicating any spurious back-reflections which may distort the pulse as in section 4.2.
- The next layer is 200 nm of platinum, providing a diffusion barrier for the following indium solder layer, preventing any diffusion of indium ions into the semiconductor, contaminating the back layers of the DBR.
- Then follows the 5000 nm indium solder layer. Indium is chosen for its low melting point of $156^{o}C$, reducing thermal stress on the sample, and also its high ductility, allowing it to incur the stress in cooling rather than the sample. However, its thermal conductivity is not optimal (see table 4.1), so its thickness is kept to a minimum.

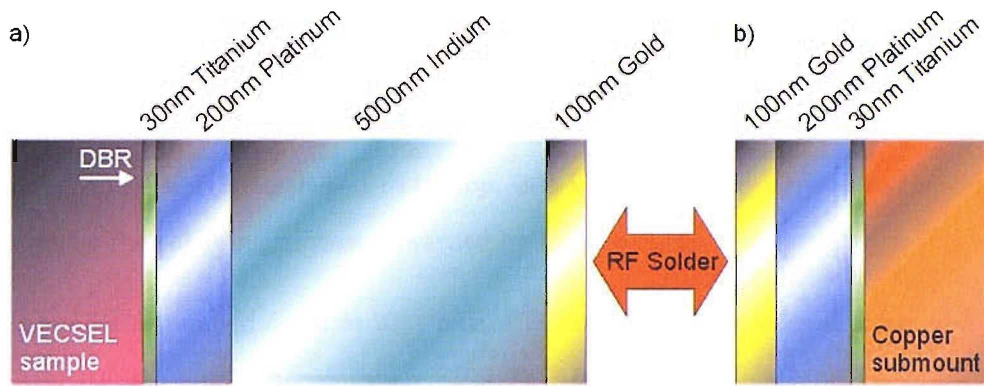

FIGURE 4.11: Metal layers deposited for RF solder of reverse-grown sample to copper submount for substrate removal technique. The function of each layer is described in the text.

- Finally, a 100 nm gold layer is deposited. At the gold-indium barrier, an intermetallic compound forms, $AuIn_2$. This compound acts as a protective layer, preventing the indium from oxidising before soldering when handled in air.

In preparation for its metalisation, the copper submount is first spark eroded, and then lapped down to a roughness less than the thickness of the indium solder layer ($\sim$1 μm peak to valley) via a method similar to that described in section 4.2.1. Following this, layers identical to the those deposited on the gain sample, omitting the indium, are sputtered on to the submount; a 30 nm layer of titanium, again to aid adhesion to the metal, then a 200 nm platinum diffusion barrier for the indium in the solder, and finally 100 nm of gold as a protective layer. These layers are shown in figure 4.11b. Both samples are stored in a nitrogen cabinet to prevent any oxidisation of the metalisation layers before soldering takes place.

Soldering is carried out by radio frequency (RF) heating in a vacuum chamber. The two metalised surfaces are cleaned with acetone and IPA. The copper submount is placed, metalised surface up, on top of a nickel block. The nickel couples well to the RF field, and acts as a hotplate in the soldering process, heated by RF eddy currents. The sample is placed on top of the Cu submount, with its metalised surface facing down, in contact with that of the submount. A graphite spacer is placed on top of this to prevent scratching of the GaAs since graphite is softer than the semiconductor: this also heats well in the RF field. Next a conical Cu pressure-spreader is positioned on top to

spread the applied weight evenly over the sample surface. Finally, the whole stack is carefully placed into a tubular chamber, made of glass so that it is not heated by the RF field, with the RF coil positioned around the stack. A glass rod slides into the chamber, with adjustable weights attached to its top. 300 kPa pressure is applied to the sample throughout the soldering process, governed by these weights.

The chamber is pumped down to 10^{-5} mbar. To melt the solder, several pulses of 1 kW, 500 kHz RF are administered by an Eleotech AG RF driver machine. A bi-metallic strip attached to the nickel hotplate indicates temperature. The target temperature is 250^oC, much higher than the 156^oC required to melt the In solder, in order to melt the $AuIn_2$ compound as well. Successful soldering can be identified by the appearance of characteristic droplets of In formed around the sample edge.

4.6.3 Substrate Removal Etching Process

Following soldering, the sample is ready for the etching step of the procedure. A similar approach to the method reported in [50] and [51] is adopted. First, the bulk of the 500 μm of GaAs substrate must be removed. This is achieved in a bromine etching step. The etchant is composed of a mixture of 1:10 bromine to methanol. The sample is mounted on to a molybdenum plate with Logitech plasticised wax on a hotplate, ensuring that the sample sides are coated with wax. This is then screwed on to a teflon jig which is resistant to the chemo-mechanical bromine etch (as is the Mb plate). Inside a fume cupboard, the jig is placed upside-down on to a grease-proof paper sheet on top of a glass plate laden with ~30 ml of bromine etch, and moved steadily in a figure eight pattern by hand for 1.5 minutes. Other than the weight of the chuck, no additional pressure is applied by hand, the chuck is simply guided around the polishing plate. After this time, the sample is quickly washed with methanol to remove any traces of the bromine etchant, and then doused with copious amounts of DI water, and blown dry with clean air. The bromine etch and greaseproof paper must be refreshed as they degrade quickly, and the bromine etch evaporates rapidly. At this point the sample thickness can be tested. The etch rate is approximately 100 μm per minute. These steps continue until approximately 100 μm substrate remain. The sample is then washed, dried, and

removed from the molybdenum jig. The wax holding the sample on to the molybdenum plate is then removed on a hotplate, and the sample is soaked in Ecoclear^{TM} to remove the wax, and then cleaned in the standard way with acetone, IPA and DI water. An alternate method to Bromine etching would be to lap and polish away the substrate as described in section 4.2.1.

Following bulk substrate removal, selective etching of the etch-stop layers can commence. The sample, still attached to the Cu submount is mounted on to a 1.5 cm diameter pyrex disc which is resistant to all of the etches used. Plasticised wax (also resistant to the etchants) is used to hold the sample in place, and protect the sample edges. It is important to cover all of the metal submount with wax to avoid this being etched and contaminating the etchant flow. Moreover, using a microscope, it must be ensured that the sample sides are covered to avoid lateral etching of the DBR and gain region. However, coating of the top surface should be avoided to prevent the formation of un-etched areas on the final sample surface.

Once mounted, each of the etch-stop layers detailed in figure 4.10 must be etched. The first layer is the remaining ~100 μm of GaAs substrate. The etchant chosen for this step is a hydrogen peroxide, ammonium hydroxide (H_2O_2:NH_4OH) solution, known to be an effective etchant of GaAs, with a selectivity of up to 30 to the AlGaAs layer beneath [50]. The solution is mixed at 24:1 30% H_2O_2 solution with 25% NH_4OH, giving an etch rate of 6-8 μm/minute. It has a lifetime of 45 minutes before it starts to degrade after mixing, and so must be mixed just before etching commences.

To remove this relatively large amount of GaAs, the etching step is approximately 15 minutes long, the etchant at the sample surface must be constantly replenished for the duration of this time to ensure smooth etching, and removal if waste products. For this reason, a 'jet-etcher' rig is used. The rig is designed to provide a continuous, laminar flow of etchant over the sample surface, with controllable flow. Constructed of PTFE, teflon, and stainless steel, all resistant to the etchant, the rig consists of a reservoir filled with etchant, and a pump which cycles the etchant up to a delivery tube positioned over the surface of the sample. The sample is held over the reservoir for the etchant

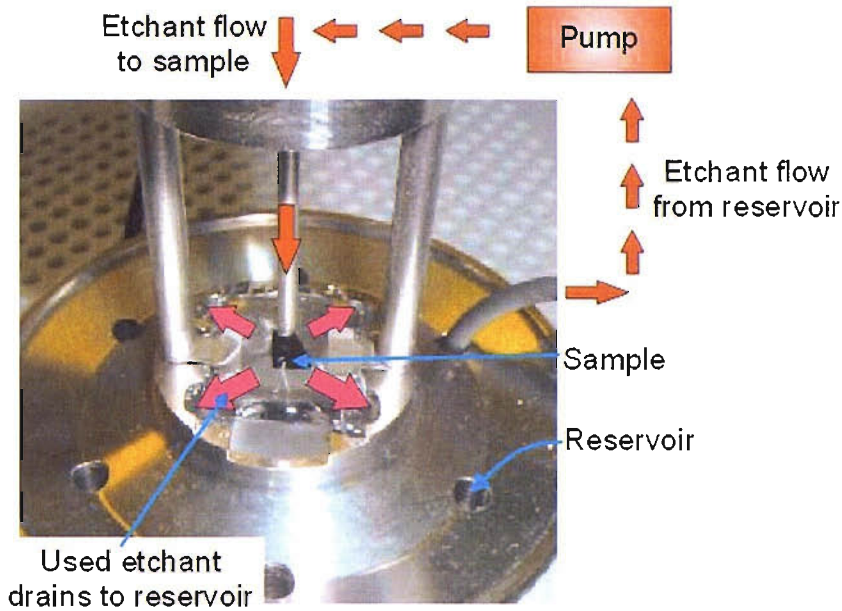

FIGURE 4.12: Photograph of jet etcher rig at Southampton. The etchant is constantly refreshed at the sample surface by the cyclic flow pumped from the reservoir. The reservoir is a PTFE beaker not shown in the picture.

to drain back. A photograph of a similar rig constructed for processing of this type at Southampton is shown in figure 4.12.

Towards the end of the 15 minute long etching step, the sample surface begins to change colour passing through violet to green as only a thin film of GaAs is left. Once the colour changing ceases, the GaAs has been removed. Etching is halted as soon as this is observed, and the sample is immediately doused with copious amounts of DI water to remove any etchant residue that might continue to slowly etch the AlGaAs beneath, or contaminate the next step in the etching process. The sample is then dried with nitrogen.

Next, the 300 nm layer of $Al_{0.85}Ga_{0.15}As$ is etched. This composition is chosen over pure AlAs to provide good selectivity to the GaAs etching in the previous step as the small amount of gallium present stabilises the film against oxidation by the etchant. This layer is etched very efficiently by 40% hydrofluoric acid (HF). The sample is held with a pair of tweezers, lowered into a beaker of HF, and stirred in the acid for 45 seconds. This is sufficient to remove all of the $Al_{0.85}Ga_{0.15}As$, and with its excellent selectivity ($\geq 10^7$ [51]) to the GaAs beneath, leaves a surface with excellent flatness. Once again,

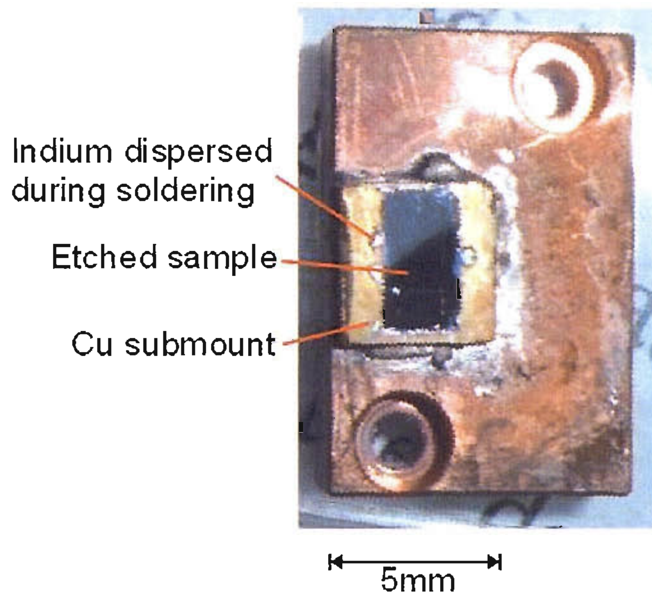

FIGURE 4.13: Photograph of the etched, mounted sample. The surface has the characteristic grey colour of GaAs, and small droplets of indium are observable around its edges, displaced during the soldering step.

the sample is immediately doused with copious amounts of DI water to halt the etching, and dried with nitrogen to prevent contamination of the next step.

The next etch-stop layer as in figure 4.10 is the 20 nm GaAs. A very weak H_2O_2:NH_4OH solution is used with a pH of 7.05. Just a couple of drops of NH_4OH are required in 50 ml of H_2O_2, and the solution is stable for several hours. The sample is stirred in the beaker of etchant as before, and then immediately doused with DI water after 60 seconds. Then quickly on to the final step of 70 nm AlAs before it oxidises, etched with HF as before for 30 seconds, followed by DI water and drying. These two extra etch steps appear unnecessary at first, however, the defects in GaAs etch much more quickly than a perfect crystal, and may result in rectangular pits in the layer. The extra steps give an opportunity for these pits to be eliminated via lateral etching and undercutting, and the GaAs layer of just 20 nm also limits their maximum possible depth.

The sample that remains appears as a characteristic GaAs grey colour, with excellent optical quality finish as shown in figure 4.13. However, there is some evidence of unetched sample at the edge. The epitaxial layers that remain are only 7 μm thick, so the quality of the surface is indicative of the good quality of the indium solder layer below.

4.6.4 Substrate-Removal Results

Following substrate removal, the back of the sample DBR is now bonded directly to the copper heatsink with a 5 μm layer of indium, and the heat can be immediately evacuated without having to travel through the bulky substrate. Referring to equation 4.3.2, it can be seen that the thickness d is now reduced to just the thickness of the DBR, making heat removal from the gain region much more efficient.

Unfortunately, samples processed in this way are difficult to analyse before processing since pumping of the active region must either be through the bulk GaAs substrate, or the DBR, both of which absorb all of the pump light before it reaches the active region. Consequently, comparison before and after processing of the sample is not possible. However, the success of this technique in improving the performance and power achievable from a VECSEL are clear in the published work [46, 47, 48].

The sample processed using this method in thesis was sample QT1770, an antiresonant VECSEL with the same structure as QT1544 which was characterised in chapter 3. A two mirror, 0.8% output coupling cavity was formed with the processed QT1770 identical to that used for CW lasing characterisation described in section 3.5. Lasing efficiency curves for the sample are shown in figure 4.14

Since it was not possible to characterise QT1770 before processing, we cannot determine whether or not its threshold and lasing power in this CW cavity have been improved as a result. However, in comparison with data for QT1544, the unprocessed chip whose CW lasing properties are shown in section 3.5, some conclusions can be drawn.

Initially, the performance of QT1770 appears good. However, the threshold is higher at pump powers of 347-370 mW compared with 240-340 mW for QT1544 (shown in figure 3.10). Moreover, its maximum lasing power is only 75 mW compared with $>$120 mW for QT1544 (shown in figure 3.9), and it doesn't appear to be as efficient. However, these attributes are associated with a misaligned growth.

What is interesting to observe is that unlike QT1544's dramatic increase in threshold pump power (P_{th}) with increasing temperature ($\sim$100 mW for a temperature increase of

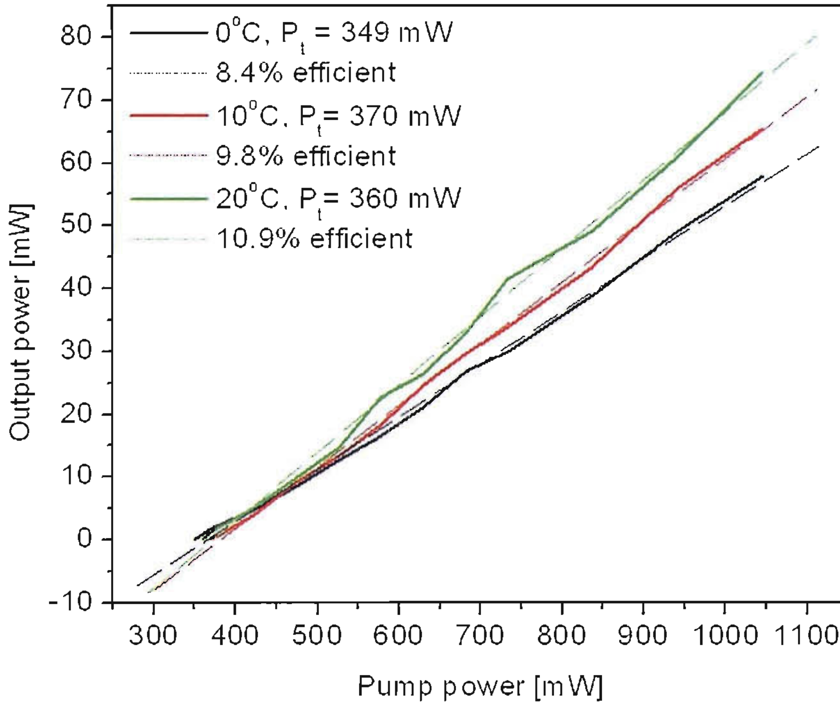

FIGURE 4.14: CW lasing performance of QT1770 at various sample temperatures. The sample substrate has been removed to improve its thermal properties. Note that no thermal rollover is observed.

20^oC), QT1770's threshold appears to remain relatively unchanged for such a temperature increase. Moreover, calculation of a value of characteristic temperature for QT1770 using the method described in section 3.5.3 yields a T_0 of 171 K at 5^oC, compared with a value of ~95 K calculated for QT1544 at 5^oC. This shows the dramatically reduced thermal dependence of processed QT1770 compared with unprocessed QT1544, and is comparable with the typical values for strained InGaAs quantum well lasers of ~200 K [9], indicating that the substrate removal technique has been successful in improving the thermal properties of the VECSEL.

4.7 Conclusions

A great advantage of VECSELs is that no post-growth processing is required for the device to oscillate. However, the operation of VECSELs can be greatly improved by employing some of the processing techniques discussed in this chapter.

Back-surface angle polishing has been demonstrated as a successful method for eliminating satellite pulses that may appear in the laser output as a result of reflections from the back surface of the SESAM or gain chip. The corresponding improvement in the autocorrelation of a 500 fs pulsed VECSEL after the back surface polish clearly demonstrated the success of this process.

Thermal properties of VECSELs were discussed, and their key role in limiting the power obtainable from a device highlighted. Two different approaches to improving the thermal properties of VECSELs were investigated. The first was direct bonding of heatspreader windows to the front surface of the gain chip. A successful bond to an active wafer was not obtained, and this is thought to be due to a degradation in the surface quality of the wafer over time. However, this method has been proved to be a very successful approach to thermal management in VECSELs elsewhere, and it is expected that with newer samples with better surface quality, a heatspreader device can be realised at Southampton. The problems associated with inserting such a device into a ML-VECSEL cavity were highlighted, and the solution of using an AR-coated, wedged, or thin heatspreader was proposed.

Substrate removal was also investigated as a second method for improving the gain chip thermal properties. A reverse-grown VECSEL was soldered to a heat sink, and then the substrate removed in a selective etching process. The resulting device did not give high powers, but this is thought to be due to a poorly grown structure, rather than its thermal properties. The characteristic temperature of the device was calculated, and shown to be much higher than that of an analogous unprocessed device, demonstrating the success of this technique in improving the VECSELs thermal properties. It is clear from this two-fold improvement in characteristic temperature, that for the future of the VECSEL work contained in this thesis, proper thermal management must be employed in further devices.

Bibliography

[1] Hoogland, S. *et al.* Passively mode-locked diode-pumped surface-emitting semiconductor laser. *IEEE Photonics Technology Letters* **12**, 1135–1137 (2000).

[2] Garnache, A. *et al.* Sub-500-fs soliton-like pulse in a passively mode-locked broadband surface-emitting laser with 100 mW average power. *Applied Physics Letters* **80**, 3892–3894 (2002).

[3] Hoogland, S., Roberts, J. S. & Tropper, A. C. Soliton operation of a sub-500fs passively mode-locked surface-emitting laser at more than 10 GHz repetition rate. In *Conference on Lasers and Electro-Optics (CLEO) US 2003 (Postdeadline session)* (Baltimore, U.S.A., 2003).

[4] Garnache, S. H. A. *et al.* Picosecond pulse generation with 1.5 μm passively mode-locked surface-emitting semiconductor laser. *Electronics Letters* **39**, 846–847 (2003).

[5] Hoogland, S., Garnache, A., Sagnes, I., Roberts, J. S. & Tropper, A. C. 10-GHz train of sub-500-fs optical soliton-like pulses from a surface-emitting semiconductor laser. *IEEE Photonics Technology Letters* **17**, 267–269 (2005).

[6] Logitech ltd. Website (2006). URL `http://www.logitech.uk.com/`.

[7] Torrance, K. W., McAneny, J. & Robertson, M. Wax mounting, backlapping and chemo-mechanical polishing of 150mm (6 inch) GaAs wafers. In *The International Conference on Compound Semiconductor Manufacturing Technology*, 13 (Vancouver, Canada, 1999).

[8] Vossen, J. L. & Kern, W. *Thin Film Processes* (Academic Press Inc., 1978).

[9] Coldren, L. A. & Corzine, S. W. *Diode Lasers and Photonic integrated Circuits* (John Wiley and Sons Inc., 1995).

[10] Schmid, M. *et al.* Optical in-well pumping of a vertical-external-cavity surface-emitting laser. *Applied Physics letters* **84**, 4860–4862 (2004).

[11] Häring, R. *et al.* High-power passively mode-locked semiconductor lasers. *IEEE Journal of Quantum Electronics* **38**, 1268–1275 (2002).

[12] Kemp, A. J. *et al.* Thermal management in vertical-external-cavity surface-emitting lasers: Finite-element analysis of a heatspreader approach. *IEEE Journal of Quantum Electronics* **41**, 148–155 (2005).

[13] Maclean, A. J. *et al.* An analysis of power scaling and thermal management in a 1060nm VECSEL with a diamond heatspreader. In *Conference on Lasers and Electro-Optics (CLEO)*, JWB21 (Long Beach, California, USA, 2006).

[14] Tropper, A. C. & Hoogland, S. H. Extended cavity surface-emitting semiconductor lasers. *Progress in Quantum Electronics* **30**, 1–143 (2006).

[15] Giesen, A., Hügel, H., Voss, A., Brauch, U. & Opower, H. Scalable concept for diode-pumped high-power solid-state lasers. *Applied Physics B: Lasers and Optics* **58**, 365–372 (1994).

[16] Ioffe physico-technical institute: New semiconductor materials. characteristics and properties. Website (1996-2005). URL `http://www.ioffe.rssi.ru/SVA/NSM`.

[17] Wikipedia. Website (2006). URL `http://www.wikipedia.org/`.

[18] Padture, N. P. & Klemens, P. G. Low thermal conductivity in garnets. *Journal of the American Ceramics Society* **80**, 1018–1020 (1997).

[19] Incorpera, F. P. & de Witt, D. P. *Fundamentals of Heat and Mass Transfer* (John Wiley & Sons, 1990), third edn.

[20] Hastie, J. E. *et al.* A 0.5W, 850nm $Al_xGa_{1-x}As$ vecsel with intra-cavity silicon carbide heatspreader. In *Annual Meeting of the IEEE Lasers and Electro-Optics Society*, TuAA2 (Glasgow, Scotland, UK, 2002).

[21] Element six: Thermal material properties. Website (2001-2006). URL `http://www.e6.com/e6/uploaded_files/Thermal%20Material%20properties.pdf`.

[22] The engineering tool box: Air properties. Website (2005). URL `http://www.engineeringtoolbox.com/air-properties-d_156.html`.

[23] Babic, D. I., Dudley, J. J., Streubel, K. & Mirin, R. P. Double-fused 1.52-μm vertical-cavity lasers. *Applied Physics Letters* **66**, 1030 (1995).

[24] Alford, W. J., Raymond, T. D. & Allerman, A. A. High power and good beam quality at 980 nm from a vertical external-cavity surface-emitting laser. *Journal of the Optical Society of America B* **19**, 663–666 (2002).

[25] Hastie, J. E. *et al.* A 0.5W, 850nm $Al_xGa_{1-x}As$ vecsel with intra-cavity silicon carbide heatspreader. *SPIE proceedings* **5137**, 201–206 (2003).

[26] Hastie, J. E. *et al.* High power CW red VECSEL with linearly polarized TEM_{00} output beam. *Optics Express* **13**, 77–81 (2005).

[27] Hastie, J. E. *et al.* Microchip vertical external cavity surface emitting lasers. *Electronic Letters* **39** (2003).

[28] Hastie, J. E. *et al.* Red microchip VECSEL array. *Optics Express* **13**, 7209–7214 (2005).

[29] Hopkins, J.-M. *et al.* Tunable, single-frequency, diode-pumped 2.3 μm vecsel. In *Conference on Lasers and Electro-Optics (CLEO) 2006*, CThM3 (Long Beach, California, U.S.A., 2006).

[30] Haisma, J., Spierings, B. A. C. M., Biermann, U. K. P. & van Gorkum, A. A. Diversity and feasibility of direct bonding: A survey of a dedicated optical technology. *Applied Optics* **33**, 1154 (1994).

[31] Liau, Z. L. & Mull, D. Wafer fusion: A novel technique for optoelectronic device fabrication and monlithic integration. *Applied Physics Letters* **56**, 737–739 (1990).

[32] Haisma, J., Spierings, G. A. C. M., Michielsen, T. M. & Adema, C. L. Surface preparation and phenomenological aspects of direct bonding. *Philips Journal of Research* **49**, 23–46 (1995).

[33] Yablonovitch, E., Hwang, D. M., Gmitter, T. J., Florez, L. T. & Harbison, J. P. Van der Waals bonding of GaAs epitaxial liftoff films onto arbitrary substrates. *Applied Physics Letters* **56**, 2419–2421 (1990).

[34] Liau, Z. L. Semiconductor wafer bonding via liquid capillarity. *Applied Physics letters* **77**, 651–653 (2000).

[35] SurfaceNet GmbH. Website (2003). URL `http://www.surfacenet.de/`.

[36] Adachi, S. GaAs, AlAs, and $Al_xGa_{1-x}As$: Material parameters for use in research and device applications. *Journal of Applied Physics* **58**, R1–R29 (1985).

[37] Surface-tension.de: Surface tension values of some common test liquids for surface energy analysis. Website (2004). URL `http://www.surface-tension.de/`.

[38] Plöβl, A. & Kräuter, G. Wafer direct bonding: tailoring adhesion between brittle materials. *Materials Science and Engineering* **R25**, 1–88 (1999).

[39] Spierings, G., Haisma, J. & Michielsen, T. Surface-related phenomena in the direct bonding of silicon and fused-silica wafer pairs. *Philips Journal of Research* **49**, 47–63 (1995).

[40] Tong, Q.-Y. & Gösele, U. *Semiconductor Wafer Bonding* (John Wiley & Sons, 1999).

[41] Svelto, O. *Principles of Lasers* (Plenum Press, New York, 1998), fourth edn.

[42] Palik, E. D. *Handbook of optical constants of solids.*

[43] Lindberg, H. *et al.* Mode locking a 1550 nm semiconductor disk laser by using a GaInNAs saturable absorber. *Optics Letters* **30**, 2793–2795 (2005).

[44] Paschotta, R. *et al.* Soliton-like pulse-shaping mechanism in passively mode-locked surface-emitting semiconductor lasers. *Applied Physics B: Lasers and Optics* **75**, 445–452 (2002).

[45] Kuznetsov, M., Hakimi, F., Sprague, R. & Mooradian, A. High-power (>0.5-W cw) diode-pumped vertical-external-cavity surface-emitting semiconductor lasers with circular TEM_{00} beams. *IEEE Photonics Technology Letters* **9**, 1063–1065 (1997).

[46] Lutgen, S. *et al.* 8-W high-efficiency continuous-wave semiconductor disk laser at 1000 nm. *Applied Physics Letters* **82**, 3620–3622 (2003).

[47] Chilla, J. *et al.* High power optically pumped semiconductor lasers. In *Photonics West: Solid State Lasers XIII* (San Jose, California, USA, 2004).

[48] Aschwanden, A. *et al.* 2.1-W picosecond passively mode-locked external-cavity semiconductor laser. *Optics Letters* **30**, 272–274 (2005).

[49] S, W. & Lee, C. C. Fluxless process of fabricating In-Au joints on copper substrates. *IEEE Transactions on Components and Packaging Technologies* **23**, 377–382 (2000).

[50] LePore, J. J. An improved technique for selective etching of GaAs and $Ga_{1-x}Al_xAs$. *Journal of Applied Physics* **51**, 6441–6442 (1980).

[51] Yablonovitch, E., Gmitter, T., Harbison, J. P. & Bhat, R. Extreme selectivity in the lift-off of epitaxial GaAs films. *Applied Physics Letters* **51**, 2222–2224 (1987).

Chapter 5

Fibre Amplification of VECSEL Pulses

5.1 Introduction

From its birth in the 1950s, the field of fibre optics saw rapid development as silica fibres emerged as solutions to the problem of loss in optical fibre communications systems [1]. The availability of these low-loss fibres also led to the birth of the new field of nonlinear fibre optics in the early 1970s [2]. The idea of doping silica fibres with rare-earth elements added a further dimension to the field, notably with the invention of the erbium doped fibre amplifier (EDFA) in 1985 [3]. The EDFA revolutionised in the field of optical fibre communications; systems became all-optical in the telecommunications window at 1.5 μm. However, the advantages and applications of this fibre amplifier technology have not been restricted to the field of optical communication, nor to within the 1.5 μm telecoms band. Rare-earth doped fibres have proved themselves to be attractive candidates for the amplification of short optical pulses up to high peak powers, and at a range of wavelengths [4, 5, 6, 7, 8, 9].

The ML-VECSELs described in this thesis are designed to give an output train of ultra-short pulses with wavelength in the 1030-1040 nm region. This wavelength is within the broad gain window of ytterbium doped fibre amplifiers (YDFAs) (975-1200 nm), a now

well-established fibre amplifier technology [6, 7, 10, 11, 12]. With a wide expertise in these rugged, thermally robust, high power amplifiers, and in the ultra-stable, ultra-short pulse production from compact all-semiconductor VECSELs based at Southampton University, it was a natural step to marry these two technologies together, drawing on the advantages of each.

This chapter describes three sets of experiments carried out to obtain the first demonstration of VECSEL pulses amplified in ytterbium-doped fibre (YDF) master oscillator power amplifier (MOPA), with average output powers of up to 187 W achieved [12]. A qualitative analysis of YDFA operation is described, then preliminary experiments to find VECSEL designs suitable for MOPA seeding are presented, followed by the high power amplification of suitable VECSEL seed pulses, and compression of the output down to 291 fs pulse lengths. It should be noted that it is not within the remit of this thesis to present a quantitative analysis of the modelling for these experiments. This was carried out by Pascal Dupriez from the Optoelectronics Research Centre at the University of Southampton.

5.2 Yb-Doped Fibre Amplifier Theory

Interest in Yb^{3+} as a laser and amplifier ion has grown dramatically in the last decade [13, 14]. With its simple energy level structure, well-separated upper level, broad absorption and emission spectrum, and freedom from excited state absorption, Yb^{3+} has proved itself as an efficient active ion for incorporation not only into fibre amplifiers, but also YAG-based disk lasers and rods [15, 16].

5.2.1 Ytterbium Fibre Spectroscopy

The absorption and emission spectra of the Yb^{3+} ion in a silica glass host are shown in figure 5.1, accompanied by an energy level diagram showing the $^2F_{7/2}$ ground state and the $^2F_{5/2}$ excited state manifolds with the energy level structure proposed by Pask et al [13]. It should be noted that in figure 5.1a, the corresponding sublevel transitions (shown in figure 5.1b) are not fully resolved due to strong homogeneous and inhomogeneous

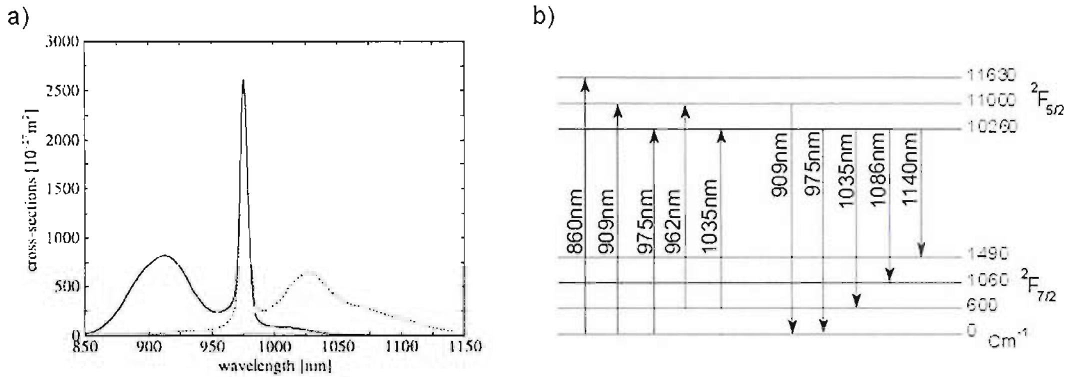

FIGURE 5.1: a) The Yb^{3+} absorption and emission cross section for a germanosilicate host taken from [13] and b) corresponding energy level diagram consisting of 2 manifolds, the ground state manifold consisting of 4 Stark levels, and the excited state manifold with 3 Stark levels. The features of the absorption/emission spectrum, and corresponding transitions are described in the text.

broadening of these optical transitions for Yb in a glass host. Both the absorption and emission spectra show a dominant, narrow peak at 975 nm. This peak relates to transitions between the lowest Stark levels in the ground state, and excited state manifolds. Transitions at this peak are characteristically 3-level in nature. There is a broader feature in absorption at shorter wavelength corresponding to transitions from the lowest Stark level in the ground state manifold to the higher states in the excited manifold (with wavelengths of 860 nm, and 910 nm). The absorption feature a longer wavelength than that of the strong peak at 975 nm corresponds to transitions from the second Stark level in the ground state manifold to the excited state manifold stark levels centred around 1035 nm. The small cross-section of this transition results from the small initial population of the second ground state Stark level.

The broad, long-wavelength peak in emission around 1030 nm is caused by transitions from the lowest Stark level in the excited state manifold to the ground state manifold. As emission moves out into the long wavelength tail of this peak, it becomes more and more 4-level in character as the higher Stark levels in the ground state manifold have little or no population. Finally, the small, short-wavelength feature in emission is due to transitions from the second excited-state Stark level. The small cross section of this transition is due to the small thermal population of this second excited state level, and these transitions are not significant.

5.2.2 Pumping Considerations

When choosing a pump wavelength for a YDFA, there are several elements to consider. Firstly, it is important to remember that it is only possible to generate gain at longer wavelengths than that of the chosen pump radiation. It is clear from the absorption spectrum of Yb that pumping within the strong peak at 975 nm accesses the largest absorption cross-section. This is particularly useful in the cladding pumped configuration when the pump absorption length is long [6].

The slope efficiency with respect to pump absorption of the amplifier is dominated by the ratio of the seed photon energy to that of the pump (known as the quantum defect). Hence, in order to enhance the amplifier conversion efficiency, pumping close to the amplified signal wavelength is desirable to reduce the quantum defect. This is particularly prudent for ytterbium, where the very low quantum defects obtainable allow conversion efficiencies as high as 80% to be achieved [17]. Naturally, another important factor is the relation of both absorption and emission cross sections at the pump wavelength which impacts the pump power requirements, with a larger absorption cross section than emission at the pump wavelength to enable absorption to dominate over stimulated emission. The best choice of pump wavelength is therefore governed by the trade-off between long wavelengths to reduce the pumping defect, and shorter wavelengths to enable absorption to dominate.

As the length of the fibre is increased, the peak wavelength of the gain shifts to longer wavelengths as a result of reabsorption of short wavelength radiation in the extra fibre length. Hence, the amplifier gain spectrum can be tailored by altering the doped length of fibre used in the amplifier.

5.2.3 Pumping Geometry

The fibre amplifiers described in this chapter employ cladding pumping technology [18]. The fibres are double clad with a single-mode, Yb^{3+}-doped core which carries the signal light, surrounded by a larger, undoped, multimode inner cladding into which the pump light is launched (see figure 5.2). There is some overlap between the inner cladding

modes and the core to facilitate absorption of the pump energy by the ytterbium ions. The final outer cladding is a low-index-profiled polymer jacket that promotes efficient guidance of the pump light.

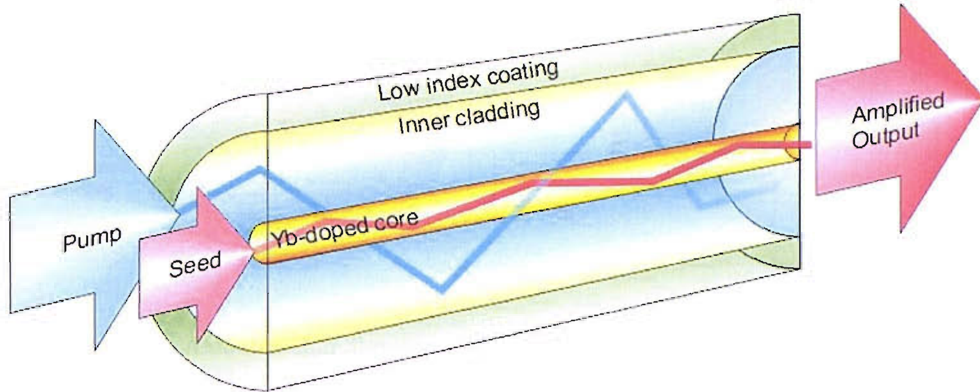

FIGURE 5.2: A fibre section showing the cladding pumping geometry whereby the seed is guided and amplified in the doped core, whilst pump light is guided within the cladding, pumping the Yb^{3+} core in regions where its mode overlaps.

The advantages of this pumping geometry lie in the reduction of restrictions on the pump light. The pump source does not need to emit one single spatial mode in order to achieve high pump launch efficiencies and large alignment tolerances. Moreover, the large inner cladding size allows high powers to be used, coupling into a large spot size, avoiding damage.

Naturally, in this configuration, pump absorption per unit length is lower than in an amplifier where the pump light is launched and guided in the doped core. This means that the amplifier length required to achieve significant pump absorption is longer, resulting in increased impact of dispersion and nonlinear effects on the propagating pulse. Eventually in amplifier design, an amplifier length is chosen that provides a reasonable compromise between these length-dependent processes, and the length-dependent peak gain tuneability.

5.2.4 Fibre Characteristics

A typical cross-section of the cladding pumped fibre amplifiers used in this chapter is shown in figure 5.3. The fibre has a step-index geometry with a uniform index profile

core, surrounded by a slightly lower index inner cladding, and then an even lower index outer cladding.

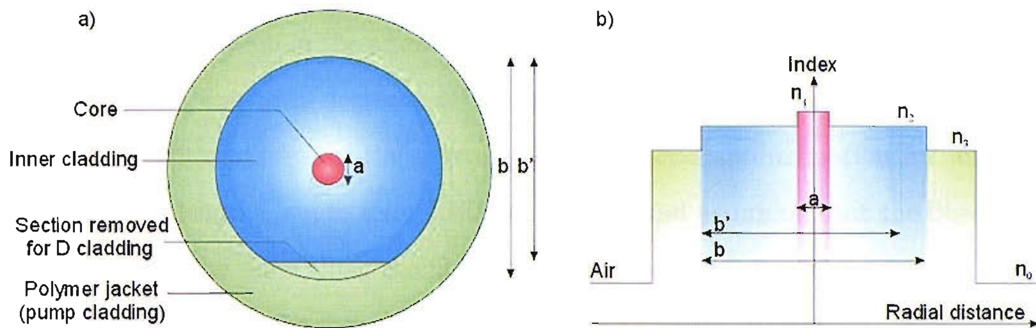

FIGURE 5.3: a) A double-clad fibre cross-section with doped core, inner cladding (which may be D-shaped in design), and outer cladding polymer jacket. b) The step-index profile typical of the YDFA fibres used in the work presented in this thesis.

When designing a fibre amplifier, it is important to consider the modes that may propagate in the fibre. A D-shaped cladding design may be employed to introduce loss for skew rays that allow pump radiation to propagate undesirably in a helical mode that does not overlap with the core at all and hence is not absorbed [14]. Ideally, the core will only support the single mode of the seed since higher order modes can provide spatial distortions of the fibre output, leading to reduced beam quality, and can also couple energy into undesirable modes and corresponding reduction in efficiency. Therefore, it is important that the amplifier is a single mode fibre.

The parameter used to determine how many modes are supported by an optical fibre is the V parameter [2]. It is defined as

$$V = k_0 \frac{a}{2} \sqrt{n_1^2 - n_2^2} \tag{5.2.1}$$

where $k_0 = 2\pi/\lambda$, λ is the wavelength of the light, a is the core diameter, n_1 is the core refractive index, n_2 is the cladding refractive index, and $\sqrt{n_1^2 - n_2^2}$ ($= n_0 sin\theta_{max}$) is the numerical aperture of the fibre, the dimensionless number that characterizes the range of angles over which the fibre can accept or emit light. A step-index fibre supports a single mode if $V < 2.405$: above this number the fibre becomes multi-mode.

5.2.5 Gain Saturation Model

In order to achieve optimal operation from a YDFA, it is important to consider the effect of gain saturation in the amplifier, whereby a decrease in gain is seen as the signal power increases due to a decrease of the population inversion level in the amplifier. Using the Yb^{3+} amplifier in the 4 level regime (a good approximation for amplified signals at wavelengths longer than 1040 nm [6, 13]), and assuming that the fibre cross-section remains the same along the fibre length (according to design and fabrication), it is possible to describe the increase of a CW signal along the fibre as

$$\frac{dI_{sig}}{dz} = N_2\sigma_e I_{sig} \tag{5.2.2}$$

where I_{sig} is the signal irradiance in Wcm^{-2}, z is the direction of the axis of the fibre, σ_e is the emission cross-section, and N_2 is the second level population

$$N_2 = \frac{N_0}{1 + I_{sig}/I_{sat}} \qquad I_{sat} = \frac{\hbar\omega}{\sigma_e\tau} \tag{5.2.3}$$

where N_0 is the photonless population, I_{sat} is the saturation irradiance of the fibre, τ is the upper state lifetime. By substituting this into equation 5.2.2, we obtain the expression

$$\frac{dI_{sig}}{dz} = N_0\sigma_e \frac{1}{\frac{1}{I_{sig}} + \frac{1}{I_{sat}}}. \tag{5.2.4}$$

Integrating by parts, equation 5.2.4 becomes

$$ln\left[\frac{I_{out}}{I_{in}}\right] + \frac{I_{out} - I_{in}}{I_{sat}} = N_0\sigma_e L \tag{5.2.5}$$

where I_{in} is the VECSEL seed intensity, and I_{out} is the intensity of the amplified signal that emerges from the amplifier. We can define amplifier gain (G) as

$$G = \frac{I_{out}}{I_{in}} \quad (5.2.6)$$

Which can be expressed as $G = P_{out}/P_{in}$.

We define G_0 as the unsaturated gain, and in the limit of small intensities ($I_{in} << I_{sat}$), as with the input power of the VECSEL seed in these experiments, relating back to equation 5.2.5, it can be seen that $\frac{I_{out}-I_{in}}{I_{sat}}$ tends to zero, and so

$$I_{out} = exp(N_0 \sigma_e L) I_i n = G_0 I_{in} \quad (5.2.7)$$

In this small signal regime, the amplifier gain is large, and the signal is unable to extract all of the available gain efficiently. Instead, detrimental effects such as amplified spontaneous emission (ASE - described in section 5.2.7) see higher gain, and there is a risk that these effects will begin to dominate.

However, as I approaches I_{sat}, either with a higher power seed, or as the signal is amplified along the fibre length, we approach the saturated regime. Here, to the first order, G_0 scales linearly with pumping rate, and so equation 5.2.5 can be approximated to

$$lnG + \frac{(G-1)I_{in}}{I_{sat}} = lnG_0 \quad (5.2.8)$$

The available gain does not increase as rapidly along the amplifier length in this regime, and as the signal level increases, the amplifier saturates and cannot produce any more output power. However, the signal is able to extract gain efficiently from the amplifier in this regime, and so, it is advantageous to run the amplifier with slight gain saturation to suppress detrimental effects such as ASE.

A simple calculation of I_{sat} for the YDFA described in section 5.3 using values of τ ≈1.5 ms and σ_e ≈400×10^{-27} taken from [6], yields a saturation power (P_{sat}) of ~100 mW for a seed wavelength of 1052 nm. This is beyond the capabilities of the VECSELs presented in this chapter, and thus, the importance of having a long enough

fibre to allow the saturated regime to be reached is clear, and the risk of detrimental effects dominating is particularly high if this length is not reached quickly enough.

5.2.6 Pulse Propagation in Optical Fibre

When considering the propagation of an ultra-short pulse along an optical fibre, it is important to consider the effects that it will experience. The broad bandwidth of an ultra-short pulse means it is particularly sensitive to dispersion effects. Moreover, the high peak power of the pulse may also excite a nonlinear response in the propagating medium.

Pulse propagation in an optical fibre can be understood in terms of the nonlinear Schrödinger equation with gain, given by [2] as:

$$\frac{\partial A}{\partial z} + \frac{\alpha}{2}A + \frac{i\beta_2}{2}\frac{\partial^2 A}{\partial T^2} + \frac{\beta_3}{6}\frac{\partial^3 A}{\partial T^3} = i\gamma\left(|A|^2 A + \frac{i}{\omega_0}\frac{\partial}{\partial T}(|A|^2 A) - T_R A\frac{\partial |A|^2}{\partial T}\right) \quad (5.2.9)$$

where T is time in the frame of reference moving with the pulse at the group velocity, A is the pulse amplitude, assumed to be normalized such that $|A|^2$ represents the optical power. α is the absorption coefficient or fibre attenuation, β_2 is the group velocity dispersion (GVD) parameter, β_3 is the third order dispersion, ω_0 is the central frequency of the pulse spectrum, or carrier frequency, γ is the nonlinear parameter, and T_R is the Raman time constant. These terms are explained in the remainder of this section.

5.2.6.1 Chromatic Dispersion

The first effect to consider is that of chromatic dispersion. This governs the β_2 term in the nonlinear Schrödinger equation (NLSE) (equation 5.2.9). In silica-based fibres, there is an inherent material dispersion associated with the propagation of ultra-short pulses that arises due to the linear response of the bound electrons in silica. Since the broad pulse spectrum is composed of a range of wavelengths, each travelling at different speeds given by $c/n(\omega)$ (where c is the speed of light in a vacuum, n is the wavelength-dependent

refractive index of the propagation medium, well approximated by the Sellmeier equation [2], and ω is the frequency of the light), each spectral component of the pulse travels at a different speed. At 1 μm, negative dispersion is introduced by this material component.

A second, much smaller contribution to chromatic dispersion is that of waveguide dispersion. The light guided inside a single mode fibre is not entirely contained within the core; the mode penetrates out into the cladding. Consequently, the pulse sees an effective index which is a combination of core and cladding indices, dependent on this overlap. Of the pulse's broadband spectrum, the shorter wavelength components are most confined within the core [2], and so see higher effective index as their mode penetrates less into the cladding. Material dispersion remains small and negative at 1 μm, and so the net chromatic dispersion experienced by the pulse is dominated by material dispersion, and remains negative. This net dispersive effect acts to broaden the pulse as it propagates, since there is a time delay in the arrival of all the spectral components of the pulse.

5.2.6.2 Fibre Nonlinearities

In intense optical fields, the response of any dielectric to light becomes nonlinear. The response of bound electrons under the influence of the electric field, gives rise to third order nonlinear effects in silica, governing the β_3 term in the NLSE (equation 5.2.9). The majority of the nonlinear effects in optical fibre result from the phenomenon of nonlinear refraction, the intensity-dependence of the refractive index caused by the Kerr nonlinearity, the elastic response of the bound electrons. Notably, in self phase modulation (SPM), the optical field experiences a self-induced phase shift as it propagates along the fibre. SPM is responsible for a broadening of the pulse optical spectrum as it travels along the amplifier, a favourable effect in a short pulse amplifier as it produces a chirped pulse with a dramatically broadened spectrum, which has great potential for pulse compression (as shown later in this chapter).

It is common for an SPM-induced spectral broadening of a Gaussian pulse to be accompanied by an oscillatory structure covering the entire pulse spectrum [2]. The spectrum is seen to contain many peaks, with the outermost being the most intense. Typically,

the number of peaks depends on the maximum phase shift induced by the SPM, and scales linearly with it as in figure 5.4. The oscillatory behaviour can be understood as an interference between the components of the pulse with the same frequency (and chirp), but different phase. It is the phase difference that causes constructive or destructive interference.

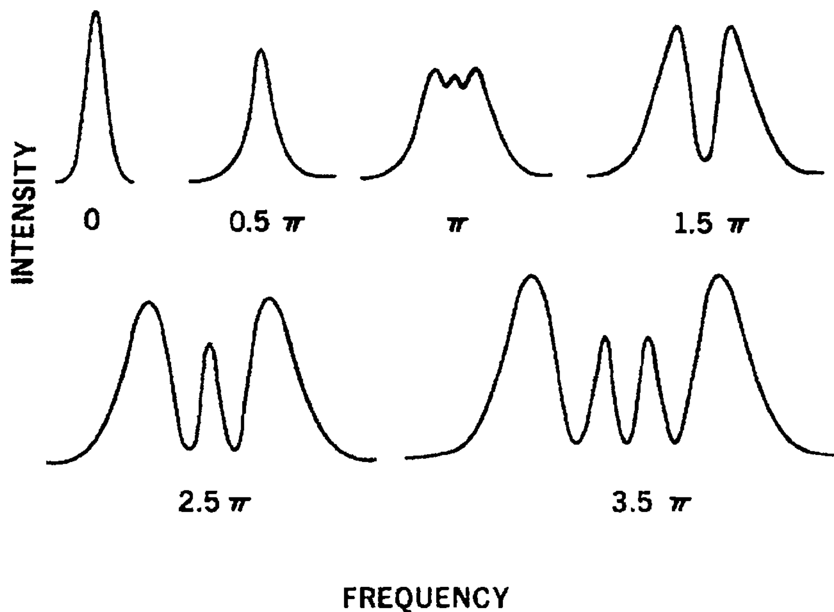

FIGURE 5.4: Calculated SPM-broadened frequency spectra for a Gaussian pulse, showing the oscillatory behaviour of the spectral evolution, taken from [19]. Spectra are labelled by maximum phase shift at the peak of the pulse.

Further third order nonlinear effects arise due to the inelastic response of the bound electrons in silica to an intense optical field. This gives rise to stimulated inelastic scattering, whereby energy is exchanged with the nonlinear medium through creation and annihilation of phonons. These effects manifest themselves in silica as stimulated Raman and Brillouin scattering (SRS and SBS). These can act to decrease the efficiency of the amplifier, coupling energy into an undesirable long-wavelength Stokes wave. Stimulated Brillouin scattering does not extract significant power in the experiments described in this thesis, since the Brillouin gain has a narrow bandwidth accessed only by high spectral density signals, not demonstrated by broadband, ultra-short optical pulses. However, in the amplifiers described in this chapter, stimulated Raman scattering, with its large gain bandwidth, readily accessed by short pulse signals, is a problem. SRS creates a parasitic Stokes wave propagating in the same direction as the amplifying signal, and

is of particular concern as a limiting factor for the maximum output power achievable from the amplifier.

5.2.7 Amplified Spontaneous Emission

An important problem in the operation of optical amplifiers is the phenomenon of amplified spontaneous emission (ASE). As the amplifier is pumped, the fraction of atoms raised to the upper level is very large. The broad emission spectrum of Yb (shown in figure 5.1a) provides ample opportunity for the decay of these atoms in the form of fluorescence. The high gain of the YDFA enables sufficient spontaneous emission fluorescence power to be emitted within the solid angle subtended by the fibre mode, and hence become coupled in, and guided in a regime where it is strongly amplified by the YDFA. The ASE builds up alongside the signal amplification, acting to degrade the signal-to-noise ratio of the amplifier output. Moreover, when the gain of the amplifier is high enough, the fraction of spontaneous emission coupled along the length of the fibre is able to reach intensities comparable to I_{sat} of the amplifier and deplete the population inversion or saturate the gain. ASE of EDFAs has been extensively studied, and theoretical models exist to consider in the design of an amplifier to minimise its undesirable effects [3, 20].

5.2.8 Accessing the Parabolic Regime

There exists an interesting amplification regime in which to run a fibre amplifier, known as the parabolic regime. First shown by Fermann et al, this regime can be seen in high gain optical fibres with normal dispersion in the propagation of short pulses, where the pulse will propagate self similarly with exponential scaling of amplitude and temporal width [21]. Combined with spectral broadening resulting from SPM, the parabolic pulses exhibit strictly linear chirp, and so facilitate ideal compression to a clean, transform limited ultra-short pulse. The parabolic pulses are exact, asymptotic solutions of the nonlinear Schrödinger equation with constant gain (equation 5.2.9). A graph demonstrating this asymptotic evolution with time is shown in figure 5.5.

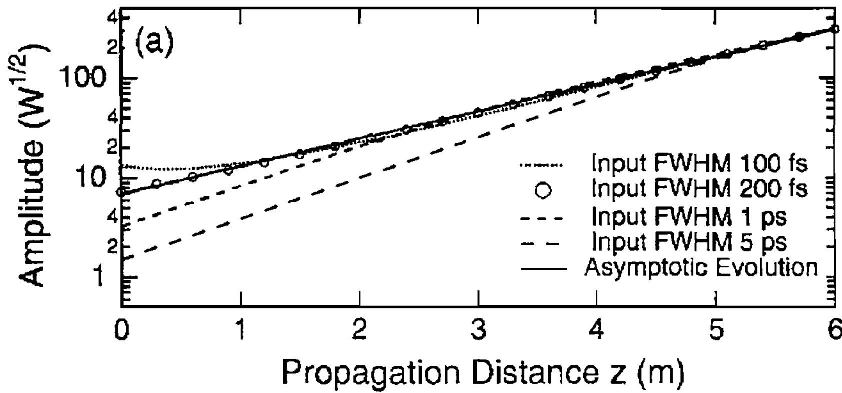

FIGURE 5.5: Simulation results showing the evolution of pulse amplitude as a function of propagation distance for Gaussian pulses of durations between 100 fs and 5 ps, compared with calculated asymptotic result taken from [21].

The asymptotic pulse characteristics are determined only by the incident pulse energy, and the amplifier parameters. The initial pulse shape determines the rate at which the pulse evolves towards the asymptotic solution, but it is possible for any pulse to access the parabolic regime with sufficient input energy and fibre length. As the amplifier gain is increased, the exponential growth of the pulse amplitude and width correspondingly increase. This causes the pulse amplitude to reach the asymptotic limit within a shorter fibre length.

Before reaching the asymptotic limit of the parabolic regime, the compressed pulse has characteristic low amplitude pedestal, demonstrating that the parabolic regime is not yet accessed. The pedestal gradually gets smaller as the pulse approaches the parabolic limit, where it finally disappears.

5.3 Preliminary Experiments: 1035 nm VECSEL with near-single-mode YDFA

First attempts were made to amplify VECSEL pulses in a single amplification stage. The fibre used for these preliminary experiments was provided by SPI lasers plc. It had a core diameter of 10 μm, and cladding diameter of 125 μm. The cladding had a circular profile which was unfavourable for the experiments, since this allowed skew cladding modes to propagate, and prevented efficient absorption of the pump radiation in the fibre core.

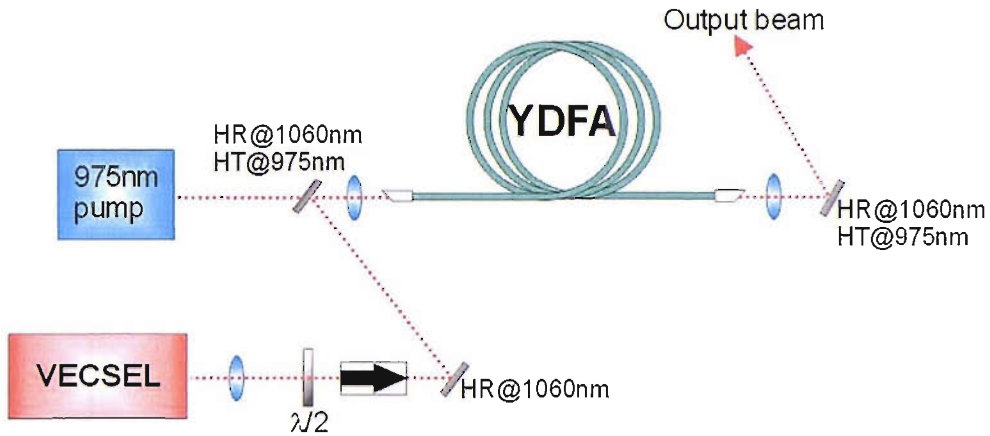

FIGURE 5.6: Preliminary experimental setup. Amplification occurs in one fibre stage pumped with a 915 nm diode stack. Signal feedback into the VECSEL cavity is prevented by a free-space isolator. Dichroic mirrors are used to combine and separate pump and signal light.

The fibre inner guide had a numerical aperture of 0.12, and corresponding V number of 3.49 at 1040 nm, and so more than one mode could propagate. The supplier of the fibre did not provide all of the fibre specifications, consequently, the dopant concentration is not known. The experimental setup is shown in figure 5.6. The fibre was angle-cleaved to prevent parasitic oscillation. A free-space isolator was used to prevent feedback into the VECSEL cavity. The co-propagating pump was radiation from a 915 nm, 26 W average power diode stack with launch efficiency of 55%.

Initially, the master oscillator selected for this amplifier was a 1035 nm, 1 GHz ML-VECSEL. The antiresonant VECSEL gain sample of design described in Chapter 2 was mode-locked using the Stark SESAM. Longer transform limited pulses of 1.09 ps were selected since the mode-locking in this regime, not using the Stark effect, gave very stable operation, essential to avoid damage to the amplifier caused by the cessation of lasing, often observed at room temperature with the Stark VECSEL. The seed pulses are shown in figure 5.7.

The seed VECSEL was thermally tuned to 1040 nm operation in order to access the gain of the amplifier, and a corresponding reduction in pulse length to 780 fs was observed, although no precise spectral data are available for this pulse. The seed device output power was 36 mW, and the launch efficiency was 60%. The amplifier length

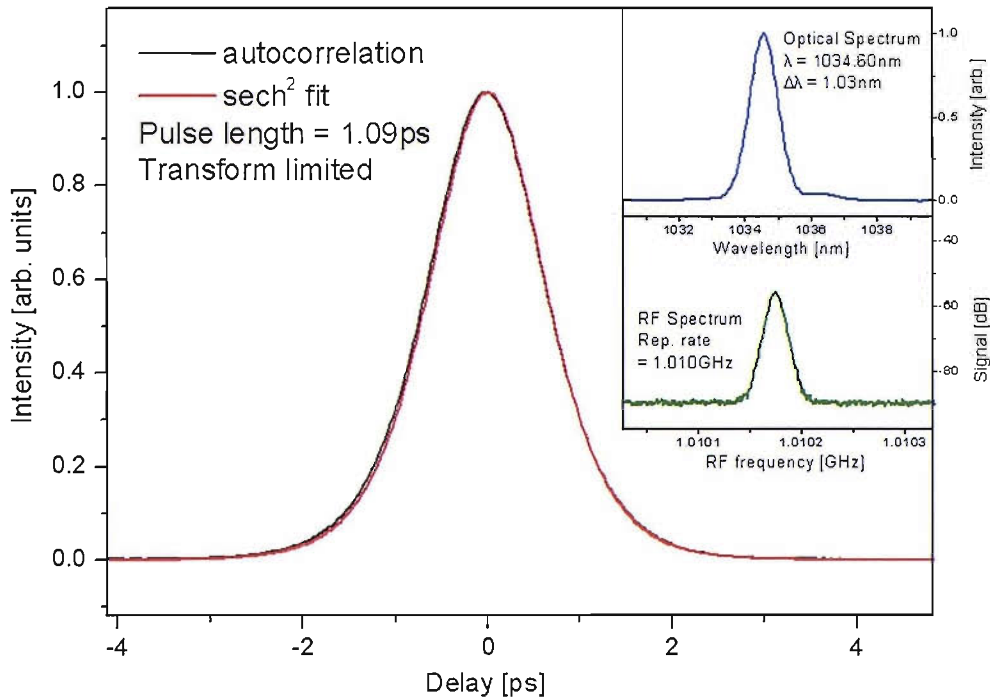

FIGURE 5.7: VECSEL seed pulse intensity autocorrelation, optical spectrum (inset) and RF spectrum (inset). The VECSEL lasing wavelength was 1035 nm, with a corresponding pulse length of 1.09 ps. Thermal tuning of the VECSEL allowed longer wavelengths to be reached, with a corresponding reduction in pulse length as the Stark regime is accessed.

was optimised for operation with this seed at 7 metres. The amplified spectrum and corresponding intensity autocorrelation are shown in figure 5.8. The output pulses were observed to have several satellites in varying regimes, indicative of some disruption to the output thought to be attributable to instabilities in VECSEL output caused by feedback of the amplifier signal into the VECSEL cavity (although this was minimised with the use of an isolator).

Further degradation of the output was thought to be due to the increasing ASE powers observed. The output spectrum shows a small amount of broadening which could be attributable to SPM, but without clean output pulses was not advantageous for any sort of pulse compression. The large peaks in the ASE spectrum to the long-wavelength side of the spectrum, and the incremental growth in the amount of long wavelength ASE observed in comparison to the pulse spectrum, indicate that the seed pulses failed to extract the stored energy effectively. As a result, increasing pump power was simply

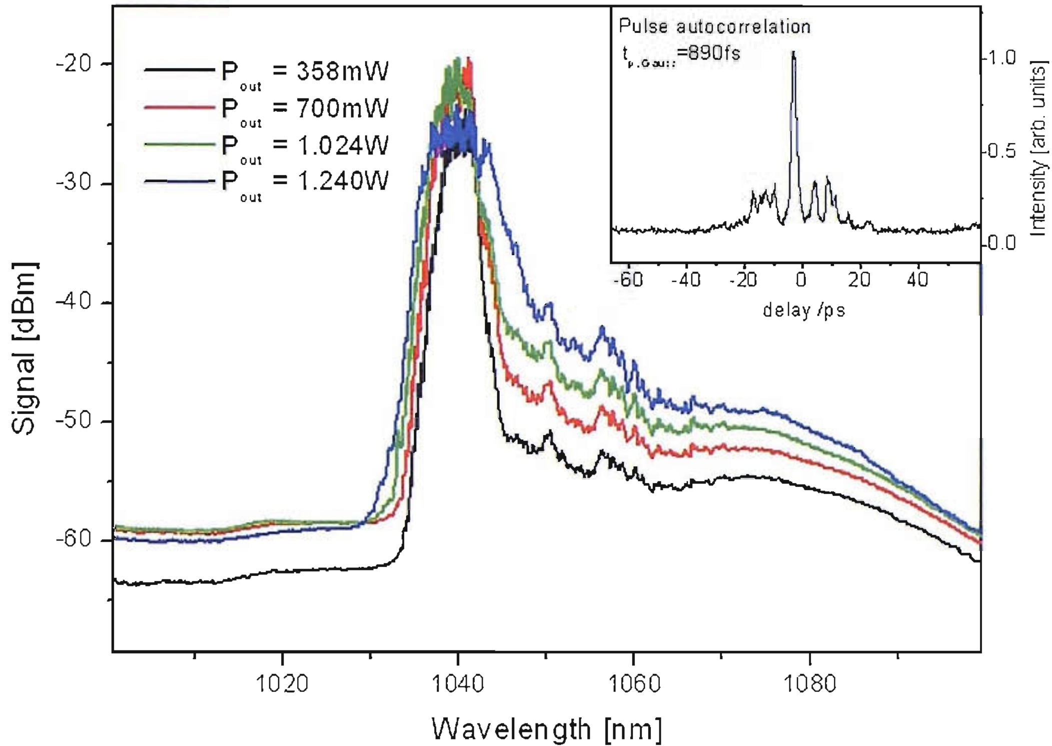

FIGURE 5.8: Output optical spectrum from YDFA seeded with a 1040 nm VECSEL. Notice the undesirable rise in long-wavelength ASE with increasing pump power. The intensity autocorrelation of the output pulse is inset, showing a satellite regime indicative of disruption to the amplifier output. The output powers shown here are the total integrated output power of the amplifier.

coupled into increasing ASE power. It was concluded that in order to access the gain of the fibre more effectively, further optimisation was required.

In order to attempt to optimise the amplifier output, a number of experiments were undertaken. Firstly, the fibre was tightly coiled in order to encourage more efficient absorption of the pump by preventing undesirable cladding modes from propagating, and force a more single-mode core. Also, the pump and seed were counter-propagated to better match signal intensity to gain in the fibre. Moreover various lengths of fibre were tried, however, no marked improvement was achieved. It was decided that modifications should be made to the seed VECSEL.

5.3.1 1052 nm VECSEL with Near Single-Mode YDFA

In order to access the gain seen at longer wavelengths in the ASE spectrum of the YDFA used in the previous section, it was necessary to build a VECSEL seed laser with an output at longer wavelengths than are commonly used at Southampton. This section describes the use of a 1052 nm VECSEL master oscillator to seed the YDFA setup used in the previous section. The VECSEL was required to be portable, and stable for many hours with room temperature operation. In order to access this long-wavelength range, an unoptimised gain sample was investigated. The structure design was similar to the one described in Chapter 2, including 6 InGaAs/GaAs quantum wells grown above a 27.5-pair AlAs/$Al_{0.84}Ga_{0.16}As$ DBR mirror designed for lasing at 1040 nm. When the sample was characterised, it was noticed that the photoluminescence of the quantum wells across the wafer varied greatly (figure 5.9). Through careful selection and cleaving of the wafer, samples with regions of long wavelength gain were found, and low power, long wavelength lasing was achieved.

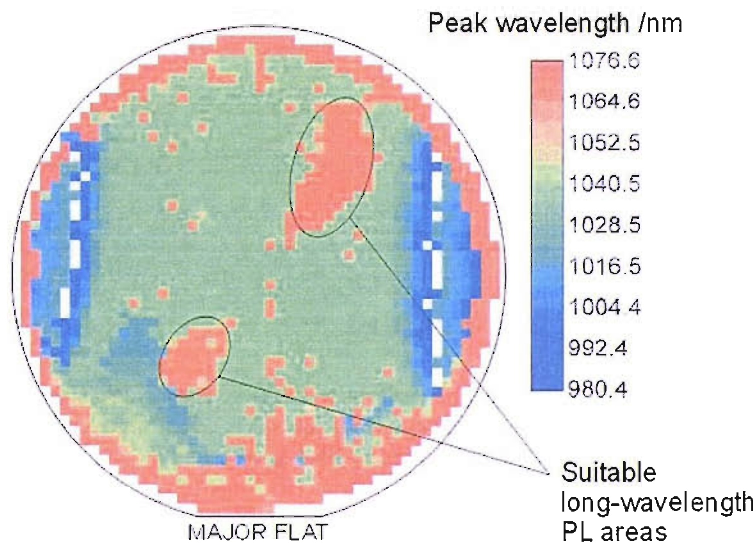

FIGURE 5.9: Map of peak photoluminescence measured across the surface of an unoptimised VECSEL gain sample showing potential regions to be used to obtain long wavelength lasing. This image was taken by Dr John Roberts at the EPSRC III-V Facility in Sheffield.

Because of the shift from the usual operating wavelengths, no ac Stark SESAMs were available to mode-lock and obtain ultra-short pulses, since the effect is only observed over the short 3 nm or so band-edge of the excitons in the SESAM quantum well. In

order to mode-lock the long wavelength VECSEL, a SESAM similar to that described in section 2.4.1.1 was used, provided by the Keller group at ETH Zurich. The structure incorporates a single InGaAs/GaAs quantum well grown by low temperature MBE to give a modulation depth of ~1%; the bleaching response is bitemporal, with a 130 fs fast component, and a 4 ps recovery time. The laser was tuned to a centre wavelength of 1052 nm at room temperature by position on the gain sample. It emitted 5 ps pulses with a repetition frequency of 910 MHz and a lower average power of 24 mW. The VECSEL seed pulse autocorrelation and spectrum are shown in figure 5.10.

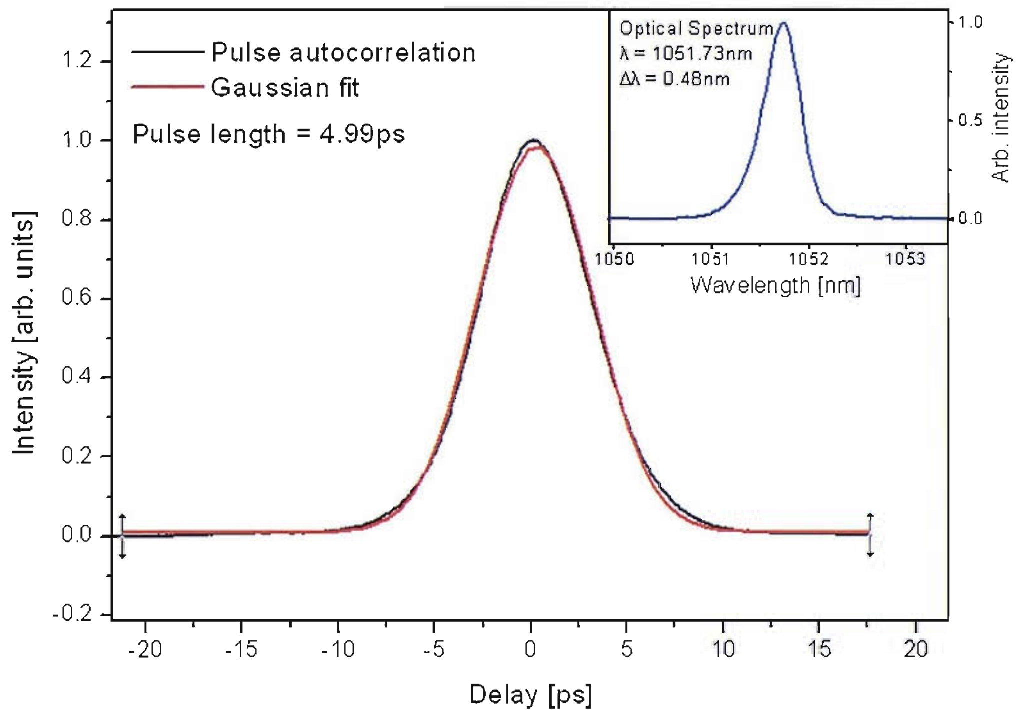

FIGURE 5.10: Pulse intensity autocorrelation and optical spectrum of 1052 nm seed VECSEL, optimised for long wavelength operation to seed the YDFA described above. The pulse is 1.47 times transform limited.

Due to the unoptimised growth of the sample that permitted this long-wavelength operation, much sample degradation was observed on the surface of the sample, in the form of oxidation. This is thought to be caused by the unoptimised growth of the strain compensating layers in the sample. However, careful and frequent cleaning of the sample surface, and storing it under a flow of nitrogen gas within the cavity allowed maintenance of long wavelength lasing at a constant average power of 24 mW for the duration of the experiments.

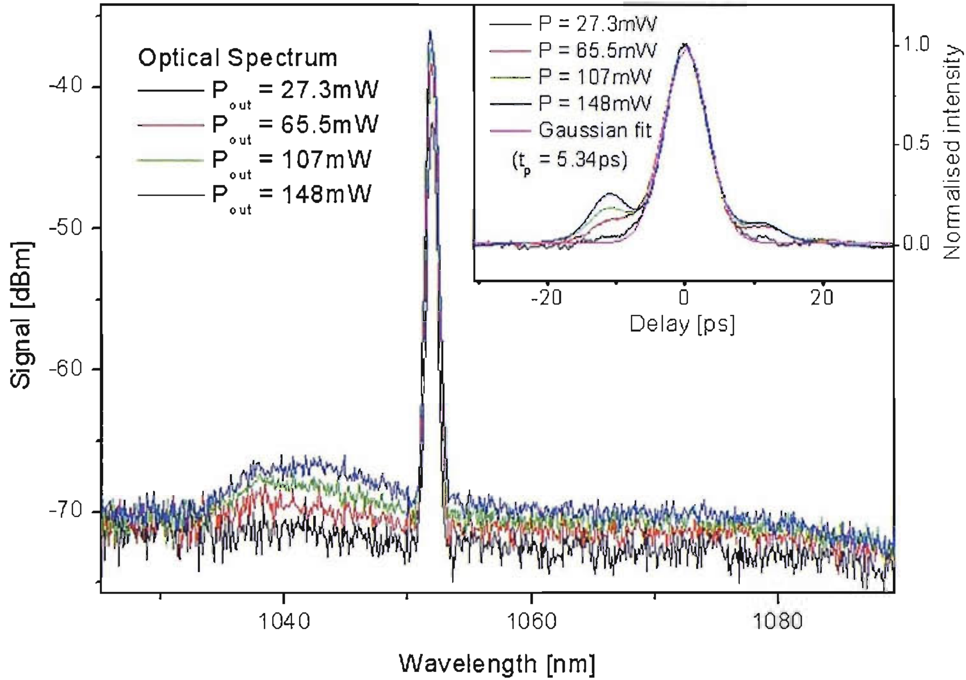

FIGURE 5.11: Optical spectrum and pulse intensity autocorrelation (inset) for amplified 1052 nm VECSEL pulses. Note the dramatic reduction in ASE power. The output powers shown here are the average powers of the amplified radiation only.

The seed pulses were launched into the one-stage Yb-doped fibre amplifier as before. The output spectrum and corresponding pulse intensity autocorrelations are shown in figure 5.11. A decrease in the amount of ASE observed in comparison with the output spectrum for the same YDFA, seeded with a 1040 nm VECSEL (see figure 5.8) can be seen, with an extra 6 dBm of extinction gained, demonstrating that this longer wavelength seed can extract the stored energy of the amplifier much more efficiently.

The output pulse intensity autocorrelations (inset in figure 5.11) show the pulse broadening effects of chromatic dispersion, and also develop large pedestals or satellites thought to be due to the effects of SPM, although the expected dramatic spectral broadening associated with SPM is not seen. Despite this promising amplification, the lack of spectral broadening due to SPM shows that pulse energies are not high enough to excite nonlinear effects sufficiently to draw on their advantages. Moreover, the poor output power achieved from the amplifier, due to the poor absorption of the pump light in the core as it instead propagates in undesirable cladding modes, renders this amplifier inefficient.

5.4 VECSEL-MOPA: 1055 nm VECSEL with near-single-mode cladding pumped power amplifier stage

Following these disappointing results from the one-stage amplification YDFA, a more sophisticated amplifier design was sought. A high power MOPA design was employed. This system had already proved itself in experiments amplifying a gain switched diode seed with 20 ps pulses, and 1 GHz repetition rate up to 321 W average power [11]. The VECSEL offers many advantages over the gain-switched diode: it produces clean, stable pulses with much shorter pulse lengths than the gain switched diode in a much cleaner output beam, and with a much higher output power (10 mW compared with 30 μW), the VECSEL eliminated the need for an extra preamplification stage.

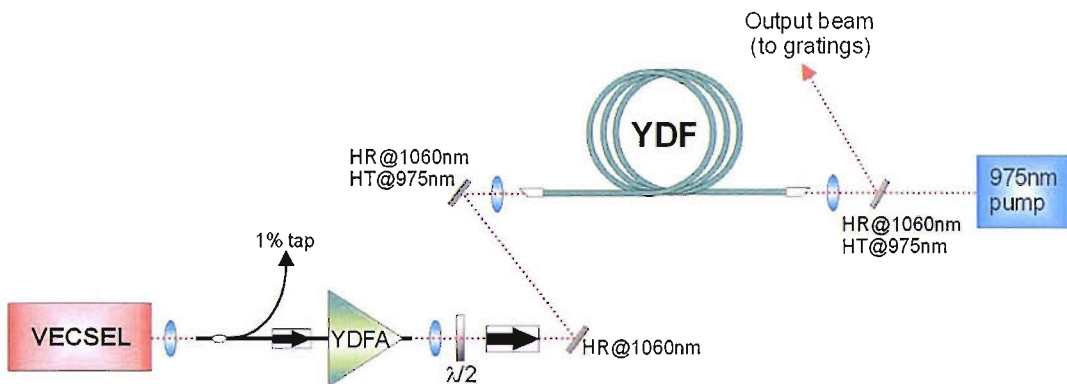

FIGURE 5.12: Experimental setup for high power VECSEL-MOPA experiments. One preamplification stage is used to amplify the VECSEL pulses to a suitable power to saturate the high power amplifier.

The design of the MOPA used for these experiments is shown in figure 5.12. Seed VECSEL pulses at 1055 nm are first pre-amplified to approximately 1 W in a YDFA. These pulses are then amplified in a further ytterbium doped fibre to high powers of up to 184 W. The output from the MOPA is then compressed externally using a free-space grating pair, to obtain pulse lengths as short at 291 fs.

5.4.1 1055 nm VECSEL Seed

The MOPA system used for these experiments was again optimised for amplification around 1060 nm. In order to access the high power regimes within the fibre's capabilities,

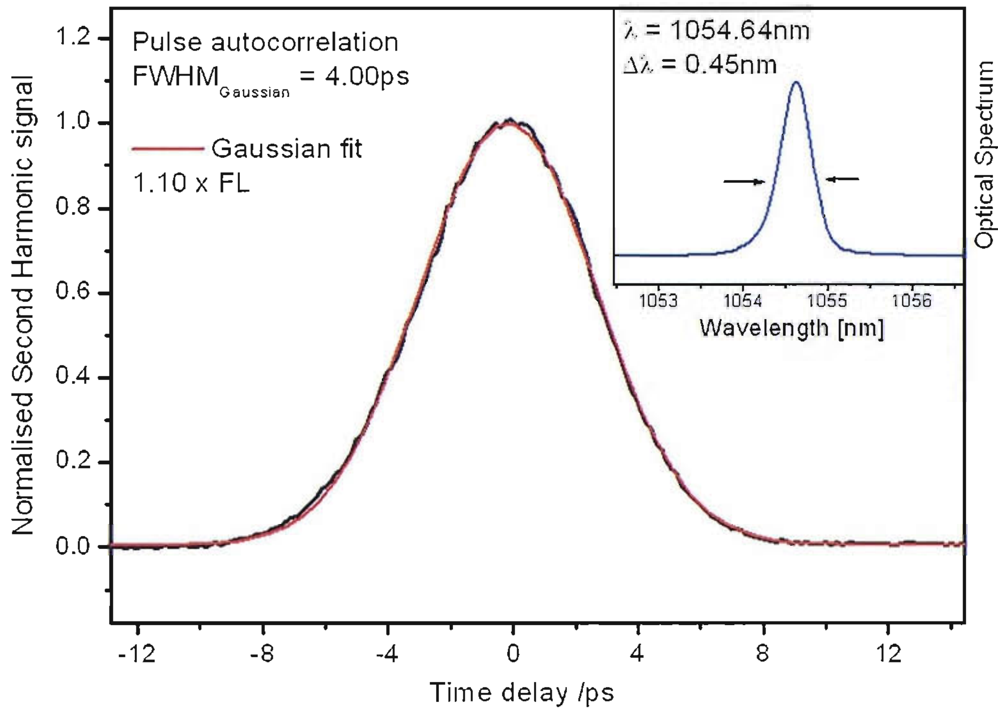

FIGURE 5.13: Pulse intensity autocorrelation and optical spectrum of 1055 nm seed VECSEL, optimised for long wavelength operation to seed a high power MOPA. The pulse is 1.10 times transform limited.

and following the success of the 1052 nm VECSEL in the previous section, a 1055 nm VECSEL master oscillator was developed. The laser was required to be portable, and stable for many hours with room temperature operation. Significant degradation of the VECSEL gain sample used in the previous experiment had occurred, and so the 1040 nm designed gain wafer with long wavelength growth areas was investigated further, to find another piece of long wavelength gain sample.

This time, even longer wavelength lasing was achieved at 1055 nm but with a low average power of only 8 mW. Without the availability of a Stark SESAM at this wavelength, the VECSEL was again mode-locked using the bitemporal SESAM provided by the Keller group, producing 4 ps pulses at a 1 GHz repetition rate that were close to transform limited (see figure 5.13). Despite this unoptimised growth, and sample degradation observed, again, careful and frequent cleaning of the sample surface, and storing it under a flow of nitrogen gas within the cavity allowed maintenance of long wavelength lasing at a constant average power for the duration of the experiments.

5.4.2 Pre-Amplifier

A double-clad, ytterbium doped preamplifier was used for the experiments. It was supplied by SPI, and incorporates their GTWave architecture, facilitating multi-point pump injection into the cladding. The output is single mode, and in the experiments described here, the amplifier was pumped by two 915 nm diodes giving a total of 6 W average pump power. The core diameter was 6 μm with a NA of 0.12, and inner cladding diameter of 125 μm, corresponding to a truly single-mode V number of 2.14. A length of 6 m of fibre was used, optimised for amplification at 1060 nm.

5.4.3 High Power Amplifier

The high power fibre amplifier used to reach the high output powers achieved in the experiment was constructed in the ORC at the University of Southampton. The fibre was double clad, with core diameter 25 μm, D-shaped cladding diameter 400 μm/360 μm for the longer/shorter axis, and NA$<$0.05. The fibre length was chosen to be 12 m for optimal amplification at 1060 nm. The amplifier was pumped with up to 360 W (260 W launched) average power from a diode stack with wavelength centred at 975 nm.

The large core of this fibre would typically allow the amplifier to have multimode operation, however, the small NA design of this fibre forces it towards single mode excitation with a V number of $<$3.72. Indeed, the amplifier output was measured to have an M^2 value of only 1.1, confirming operation close to single mode excitation.

5.4.4 VECSEL-MOPA Results

The slope efficiency of the VECSEL-MOPA is shown in figure 5.14. A 77% optical-to-optical power efficiency was seen, with a maximum amplified average output power of 184 W achieved for a launched pump power of 260 W. However, at this highest power, pulse degradation was seen due to the onset of SRS and increased levels of ASE, consequently, data from pulses amplified to 160 W average power will be presented in this chapter.

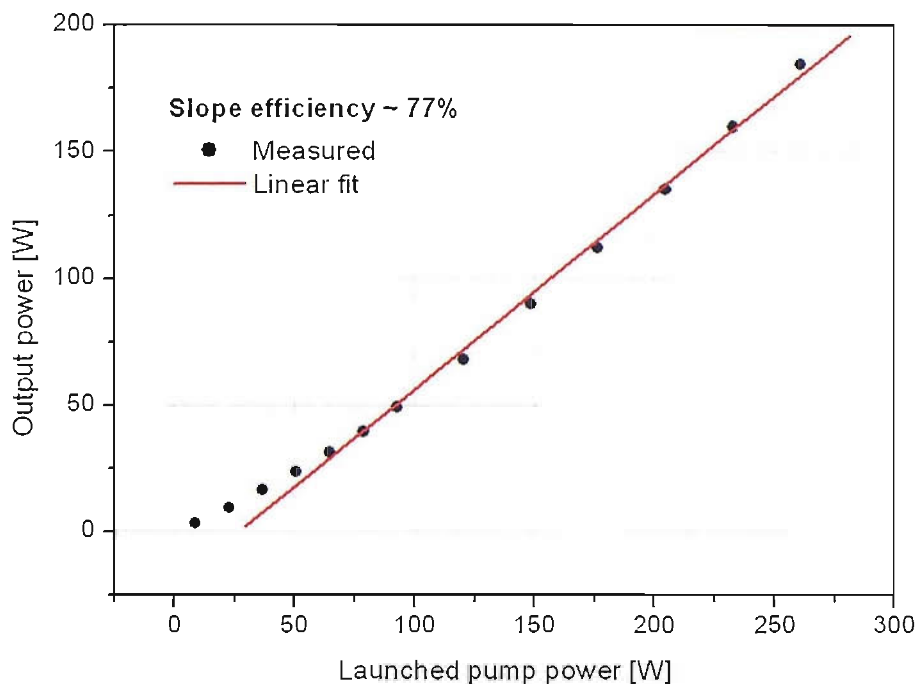

FIGURE 5.14: Graph to show amplified average output power for different values of launched pump power. The maximum input pump power was 360 W, with a launch efficiency of 72%. VECSEL-MOPA optical to optical slope efficiency is 77%.

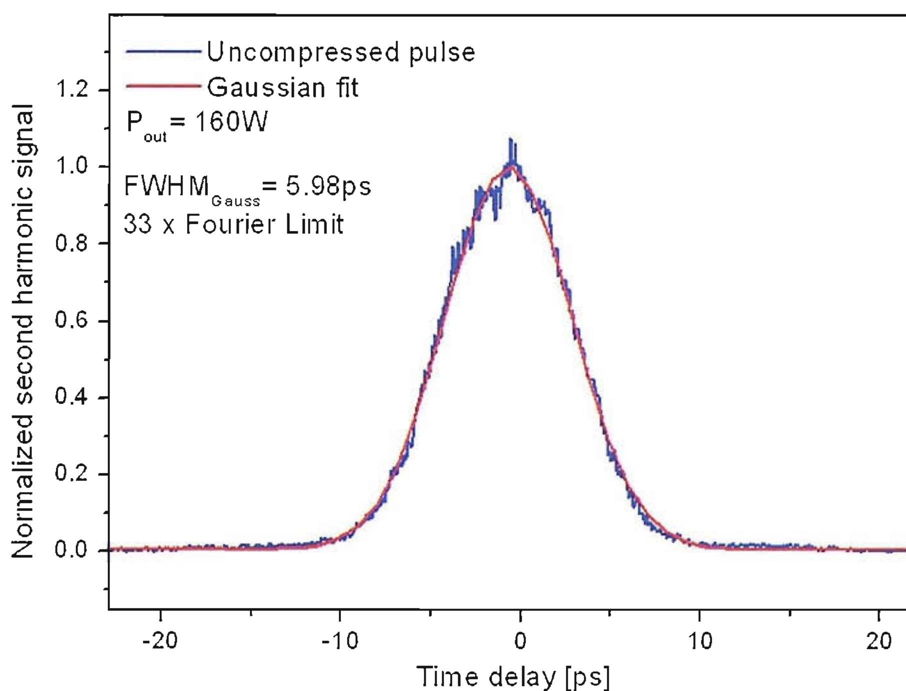

FIGURE 5.15: Intensity autocorrelation of amplified output pulse from VECSEL-MOPA at an average power of 160 W. The pulse is measured to be 6 ps long, and has a Gaussian profile.

The amplified pulse intensity autocorrelation at 160 W average output power is shown in figure 5.15. The pulse has experienced broadening due to chromatic dispersion effects, and is now 6 ps long, maintaining its Gaussian profile. This corresponds to a pulse energy of 138 nJ, and a peak power of 28 kW.

The corresponding amplified output spectra are shown in figure 5.16. Figure 5.16a is the optical spectrum shown with logarithmic intensity, and clearly shows the build-up of ASE around the pulse spectrum with increased pump power, however, it was calculated from the spectrum that 95% of the output power was contained within the pulse, the output powers discussed here are corrected for this factor.

Figure 5.16b shows the linear-scaled optical spectrum with VECSEL optical spectrum included for reference. Here, the spectral broadening effects of SPM can clearly be seen, with the spectrum broadening from 0.45 nm seed bandwidth to approximately 9 nm amplified bandwidth at 160 W average output power. This corresponds to a highly chirped, 33 times Fourier-limited pulse at 160 W, suitable for pulse compression down to a few hundreds of femtoseconds.

The tops of the spectra are strongly modulated, demonstrating that the amplifier had not accessed the parabolic regime where a smooth, parabolic spectral shape would be seen. This modulation effect is typical of an SPM broadened optical spectrum for a Gaussian pulse propagating in the non-parabolic regime, as discussed in section 5.2.6.2.

5.4.5 External Pulse Compression

The highly chirped pulses with broad optical spectra in the output of the MOPA are ideal for pulse compression. Many methods are available for pulse compression, including the use of tailored photonic crystal fibres [22], fibre gratings [23], and the use of various free-space gratings [24]. In order to demonstrate that compression of these pulses was possible, free-space bulk gratings were used. The setup was by no means ideal: the gratings were bulky, and could only tolerate a small fraction of the output power without damage. The aim of this experiment was purely to demonstrate that compression is possible, not to optimise the process.

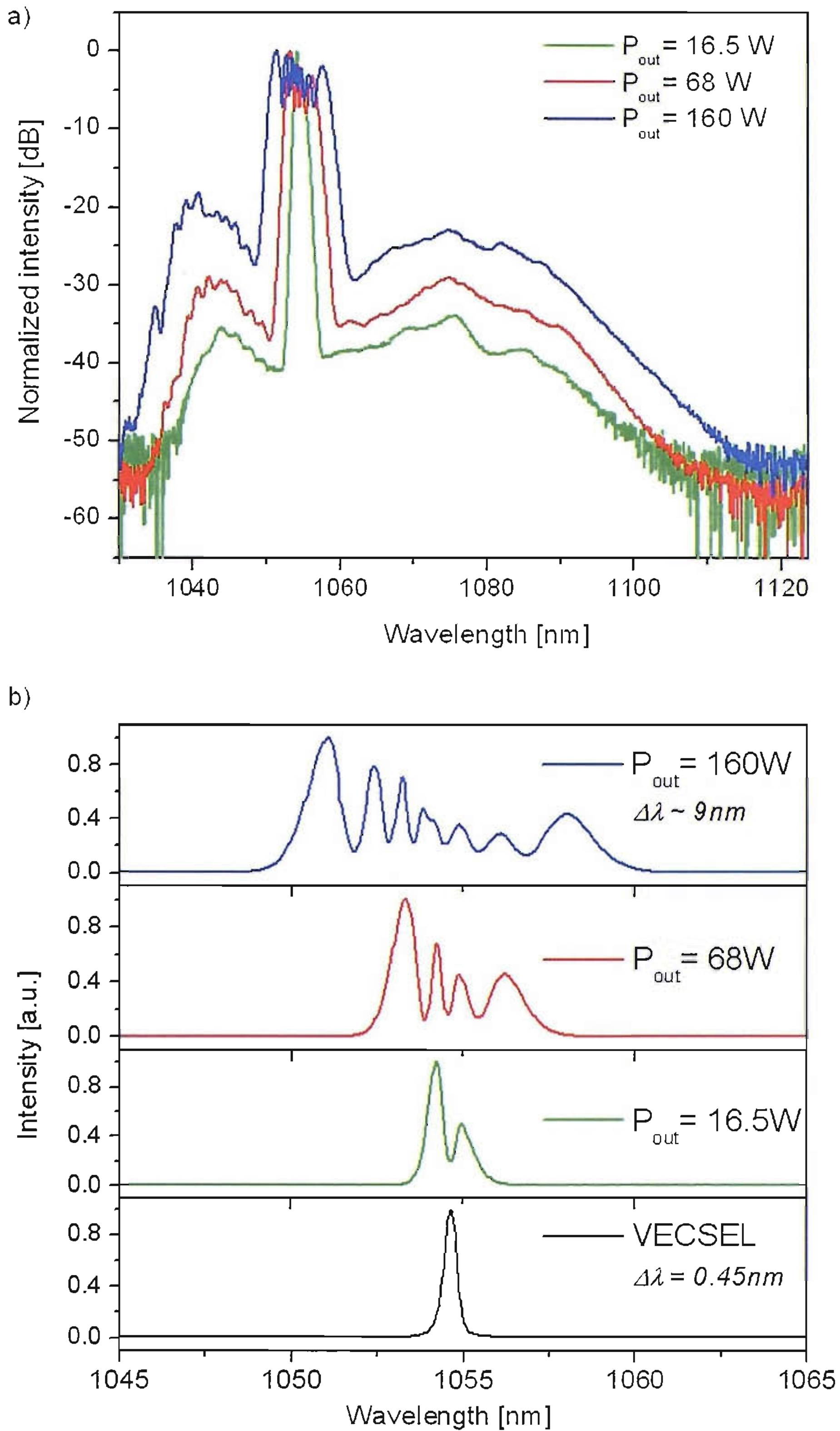

FIGURE 5.16: Optical spectra of amplified output from VECSEL-MOPA on a) logarithmic scale, and b) linear scale, showing the effects of SPM-induced spectral broadening, and ASE.

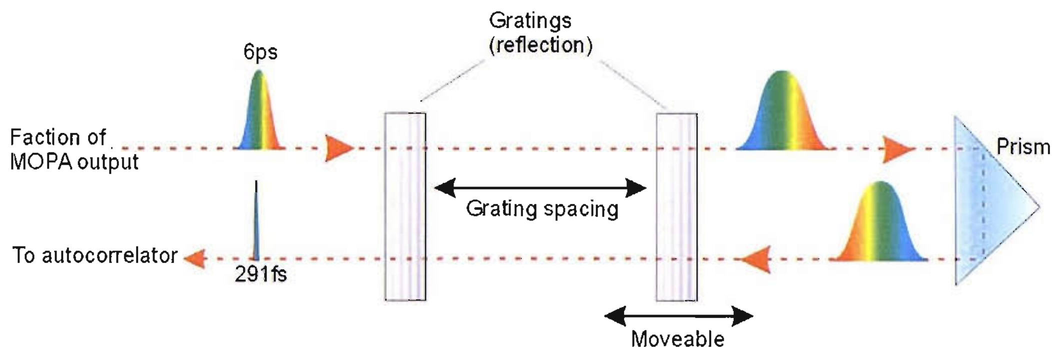

FIGURE 5.17: Schematic of pulse compression setup. The free space bulk blazed gratings have 830 lines per mm, and are cut for first order diffraction.

The gratings selected were first order blaze-cut with 830 grooves per mm. The experimental concept is shown in figure 5.17. A small fraction of the output power was launched into the grating pair. The pulse is reflected by the pair once, stretching it, then it is retro-reflected back along the path it took, where the gratings act to compress it to a length much shorter than its incident length. This process is optimised by varying the grating spacing to introduce just the right amount of dispersion to compensate for the initial chirp of the pulse, and capitalise on its broad spectral bandwidth to form a short, near-transform-limited pulse.

An intensity autocorrelation of a compressed pulse is shown in figure 5.18. The pulse length was measured to be 291 fs at 160 W average output power. This was the shortest compressed pulse achieved, with the onset of pulse degradation observed at higher powers, as seen in figure 5.19. A large pedestal can be seen in the pulse intensity autocorrelation, with the compressed pulse measured to contain 75% of the total pulse energy. The pedestal is a product of the compression of a modulated spectrum as seen in the amplifier output.

The incident pulses were 33 times transform limited, with a length of 6 ps, and a 9 nm bandwidth. The compressed pulses were measured to be 291 fs long, with the same bandwidth, corresponding to 1.6 times the Fourier limit. If a perfect grating pair could be found, that could handle the full power of the amplified output, and compress without loss, this would correspond to a peak power of 550 kW. In reality, no such gratings exist,

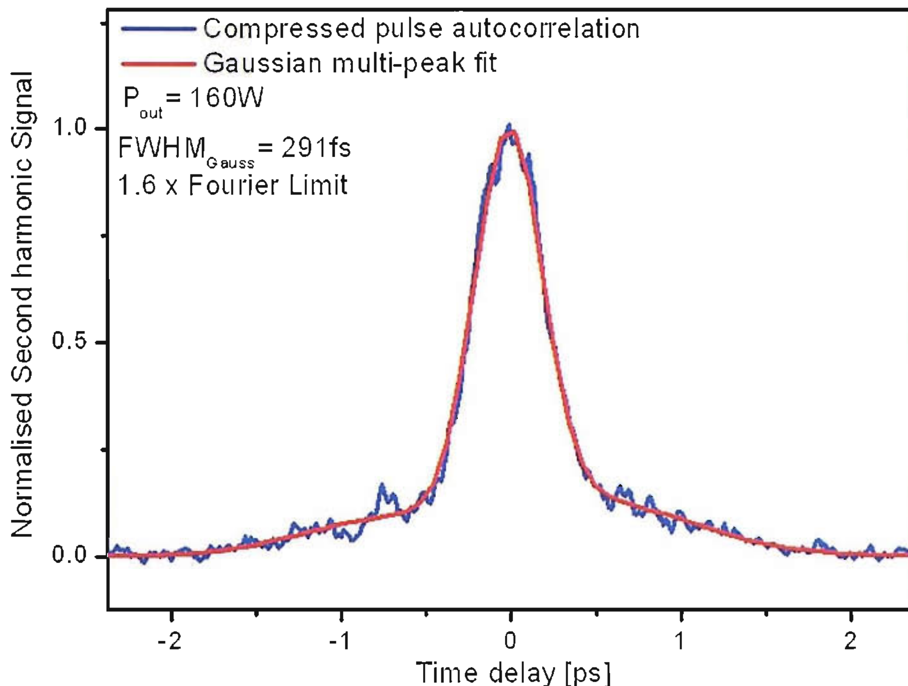

FIGURE 5.18: Compressed pulse from VECSEL-MOPA at 160 W average power. The pulse is multi-Gaussian fit in the Origin 7 program, and the pulse length is measured to be 291 fs. Only a fraction of the output power was coupled into the grating pair to achieve this compression.

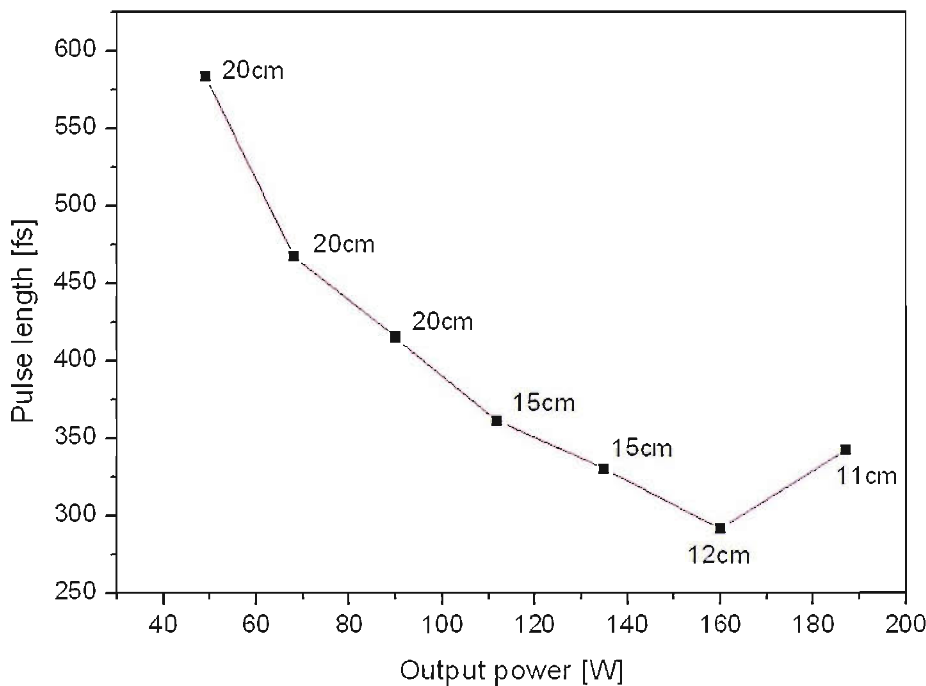

FIGURE 5.19: Compressed pulse length as a function of average VECSEL-MOPA output power. Note that the optimal compression is achieved at 160 W average power, above which, pulse degradation is seen.

however, high tolerance, low loss, gold gratings for this application do exist, and it is also possible to envisage carrying out compression in a fiberised device.

5.4.6 Limitations and Damage

The maximum average amplified power attained in these experiments was limited to 187 W, however, at this power, degradation of the amplifier output was seen, with dramatic increases in ASE power, and SRS, accompanied by a reduction in pulse compressibility. When operating a MOPA system, it is imperative that the seed is launched into the fibre, and operating all the time that the YDFAs are being pumped. If the seed signal is interrupted in any way, the amplifier may self-lase, or experience massive thermal load from all its stored pump energy, resulting in damage to the fibre.

In the high power MOPA described above, these limitations are even more prudent since the high power MOPA is also sensitive to changes in the output from the preamplifying YDFA. Output from the VECSEL was observed to be stable, and of constant polarisation. However, the YDF used as a pre-amp in these experiments is not polarisation-maintaining, and the high power isolator that its output passed through into the high power YDFA is polarisation dependent. Consequently, any alterations in the polarisation of the output from the pre-amp could result in the final amplifier ceasing to be seeded, and hence experiencing damage. It was observed in the experiments that the pre-amp was very sensitive to thermal polarisation-altering effects and despite efforts being made to compensate for this by twisting the fibre, seeding did cease on occasion.

The damage to the fibre ends observed on these occasions is shown in figure 5.20. a) and b) show 2 damaged whole fibre cross-section (with polymer jacket cladding stripped), c) shows a damaged core, and d) shows a side-profile of the damage. These damage defects tend to start at the fibre ends, and propagate down the fibre. In order to prevent propagation deep into the fibre, the ends of the fibre are attached to water-cooled heat-sinks, which dissipate the energy responsible for the damage, and prevent it propagating more than a few centimetres down the fibre.

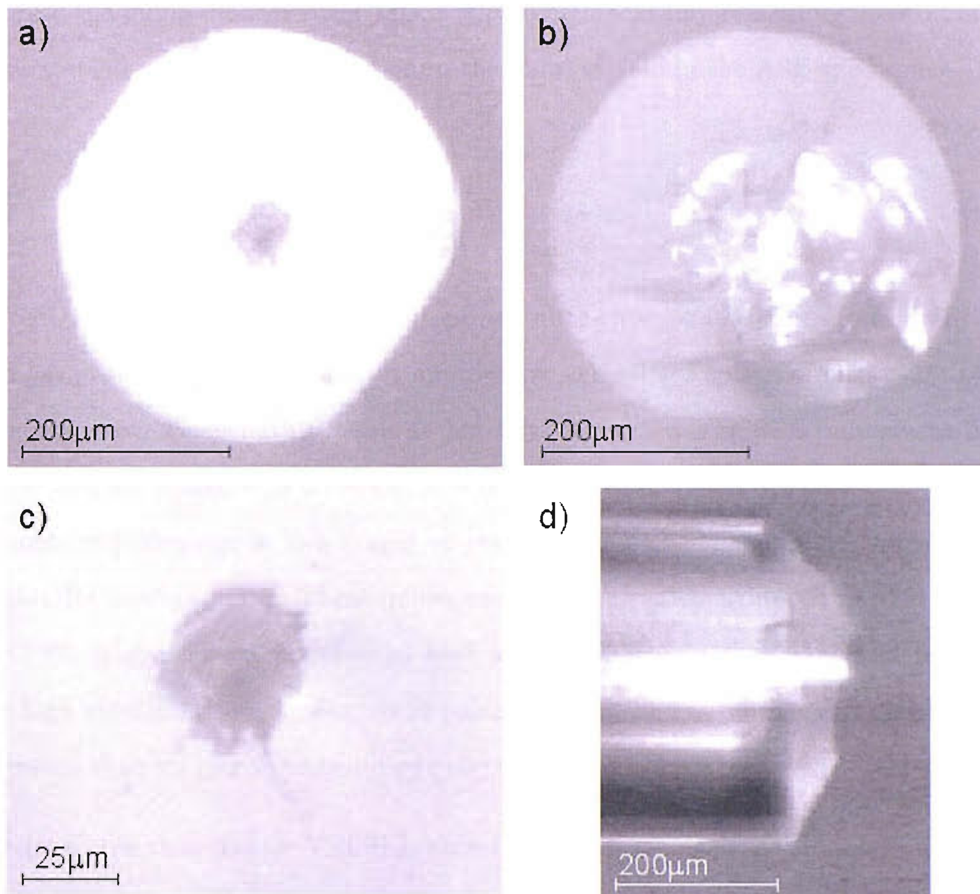

FIGURE 5.20: Images of damaged fibre ends. a) and b) show inner cladding cross-sections, c) shows a damaged fibre core, and d) shows the profile of a damaged fibre facet.

A further restricting effect can be that of ASE, which acts to deplete the population inversion of the amplifier. Moreover, the onset of SRS can also be a limitation, where the amplified signal itself pumps the Raman Stokes wave. Both of these effects act to rob the amplified signal of power, decreasing the efficiency of the amplifier. They can also lead to parasitic lasing, and damage. In these experiments, both were limitations to the amount of power achieved. As soon as power was seen to be channelled into either effect, the experiment had to be stopped for fear of damaging the amplifier.

Noise of the amplifier is a further limitation to the quality of the output. VECSELs are very low noise, stable pulsed sources, but for a MOPA, this is not so. It is quite simple to remove the noise effects of mechanical vibrations from the system through engineering. Then, the majority of the noise in the amplifier is attributable to the pump. It is possible to employ a locking technique similar to the approach used in [25] to actively

stabilise the pump diodes. After this it is predicted that any remaining noise would be attributable to spontaneous emission in the fibre, as seen in the ASE spectrum.

5.5 Conclusions

The MOPA approach to achieving high-power, ultra-short, stable pulses from a VECSEL seed has proved itself as a promising approach to achieving a source of ultra-short pulses using low cost, wavelength tunable technology. Amplified VECSEL pulses with up to 187 W average power, 6 ps duration, at a repetition rate of ~1 GHz have been achieved through amplification in two stages of ytterbium-doped fibre amplifier, operating in the MOPA configuration. These pulses were compressed to a duration of 291 fs. The VECSEL is therefore a preferential seed for the MOPA, with its spectral flexibility, and high repetition rate, stable, short pulses at much higher powers, and shorter pulse durations than its gain switched diode counterpart.

It is predicted that shorter VECSEL pulses such as those achieved from a Stark mode-locked VECSEL could enable us to access parabolic amplification, running the VECSEL-MOPA in its optimal operation regime. It has been modelled that, in this regime, with a 1040 nm, 40 mW average power, 500 fs VECSEL seeding the MOPA described in this chapter, pulse compression down to 100 fs is possible [26]. Moreover, with the processing methods discussed in chapter 4 to achieve higher power output directly from a VECSEL, with current records standing at 2.1 W average output power from a 4 ps pulse ML-VECSEL [27], and tens of Watts CW already achieved [28], it is possible to envisage a VECSEL-MOPA with only one stage of amplification, with the gain of the high power fibre directly accessed by the high power output from a processed VECSEL. Also, a low power single-mode YDFA is of interest as a route to achieving one or two Watts average power 100 fs pulses from a Southampton VECSEL seed.

These amplified devices are very attractive for applications in THz generation, where ultra-short pulses at high power can be used to drive arrays of THz antennae for parallel acquisition of THz images of thousands of pixels for homelands security applications.

At Southampton as part of the TeraSec consortium, we recently made the first demonstration of room temperature THz generation, using a compact all-semiconductor device based on a 40 mW average power, 1 μm, 500 fs VECSEL, and low-temperature grown GaAsSb antennae [25]. This device has recorded one pixel of a THz image in 1 second. With an amplified VECSEL, an area of 100 by 100 pixels could be driven. The high repetition rates attainable from a VECSEL make this amplified output attractive for a cheap method of optically clocking highly integrated circuits (discussed further in chapter 6). And furthermore, as higher peak powers are accessed, this higher repetition rate approach is ideal for high throughput materials processing applications, where current systems deliver a few microjoules at low repetition rates of a few kilohertz.

Bibliography

[1] Gambling, W. A. The rise and rise of optical fibers. *IEEE Journal on Selected Topics in Quantum Electronics* **6**, 1084–1093 (2000).

[2] Agrawal, G. P. *Nonlinear Fiber Optics* (Academic Press, 2001), third edn.

[3] Desurvire, E. *Erbium-Doped Fibre Amplifiers* (John Wiley and Sons Inc., 2002).

[4] Mears, R. J., Reekie, L., Jauncey, I. M. & Payne, D. N. Low noise erbium-doped fiber amplifier operating at 1.54 μm. *Electronics Letters* **23**, 1026–1028 (1987).

[5] Desurvire, E., Simpson, J. R. & Becker, P. C. High-gain erbium-doped traveling-wave fiber amplifier. *Optics Letters* **12**, 888–890 (1987).

[6] Paschotta, R., Nilsson, J., Tropper, A. C. & Hanna, D. C. Ytterbium-doped fiber amplifiers. *IEEE Journal of Quantum Electronics* **33**, 1049–1056 (1997).

[7] Limpert, J., Liem, A., Gabler, T., Zellmer, H. & Tünnermann, A. High-average-power picosecond Yb-doped fiber amplifier. *Optics letters* **26**, 1849–1851 (2001).

[8] Smart, R. G. *et al.* 20 dB gain thulium-doped fluorozirconate fibre amplifier operating at around 0.8 μm. *Electronics Letters* **27**, 1123–1124 (1991).

[9] Yamada, M. *et al.* Pr^{3+}-doped fluoride fiber amplifier module pumped by a fiber coupled master oscillator/power amplifier laser diode. *IEEE Photonics Technology Letters* **9**, 321–323 (1997).

[10] Limpert, J. *et al.* High-power femtosecond Yb-doped fiber amplifier. *Optics Express* **10**, 628–638 (2002).

[11] Dupriez, P. *et al.* 321 W average power, 1 GHz, 20 ps, 1060 nm pulsed fiber MOPA source. In *OFC 2005*, PDP3 (Anaheim, USA, 2005).

[12] Foreman, H. D. *et al.* High power femtosecond source based on passively modelocked 1055-nm VECSEL and Yb-fibre power amplifier. In *Advanced Solid State Photonics (ASSP) 2006* (Lake Tahoe, USA, 2006).

[13] Pask, H. M. *et al.* Ytterbium-doped silica fiber lasers: Versatile sources for the 1-1.2 μm region. *IEEE Journal of Selected Topics in Quantum Electronics* **1**, 2–13 (1995).

[14] Tünnermann, A. *et al.* The renaissance and bright future of fibre lasers. *Journal of Physics B: Atomic, Molecular and Optical Physics* **38**, S681S693 (2005).

[15] Brauch, U., Giesen, A., Karszewski, M. & Stewen, C. Multiwatt diode-pumped Yb:YAG thin disk laser continuously tunable between 1018 and 1053 nm. *Optics Letters* **20**, 713–715 (1995).

[16] Honea, E. C. *et al.* High-power dual-rod Yb:YAG laser. *Optics Letters* **25**, 805–807 (2000).

[17] Pask, H. M. *et al.* Operation of cladding-pumped Yb^{3+}-doped silica fibre lasers in 1 μm region. *Electronics Letters* **30**, 863–865 (1994).

[18] Snitzer, E., Po, H., Hakimi, F., Tumminelli, R. & McCollum, B. C. Double-clad offset core Nd fiber laser. In *Optical Fiber Sensors*, PD5 (Washington, DC, USA, 1988).

[19] Stolen, R. H. & Lin, C. Self-phase-modulation in silica optical fibres. *Physical Review A* **17**, 1448–1453 (1978).

[20] Desurvire, E. & Simpson, J. R. Amplification of spontaneous emission in erbium-doped single-mode fibers. *Journal of Lightwave Technology* **7**, 835–845 (1989).

[21] Fermann, M. E., Kruglov, V. I., Thomsen, B. C., Dudley, J. M. & Harvey, J. D. Self-similar propagation and amplification of parabolic pulses in optical fibers. *Physical Review Letters* **84**, 6010–6013 (2000).

[22] Südmeyer, T. *et al.* Nonlinear femtosecond pulse compression at high average power levels by use of a large-mode-area holey fiber. *Optics Letters* **28**, 1951–1953 (2003).

[23] Broderick, N. G. R., Taverner, D., Richardson, D. J., Ibsen, M. & Laming, R. I. Optical pulse compression in fiber Bragg gratings. *Physical Review Letters* **79**, 4566–4569 (1997).

[24] Svelto, O. *Principles of Lasers* (Plenum Press, New York, 1998), fourth edn.

[25] Wilcox, K. G., Foreman, H. D., Roberts, J. S. & Tropper, A. C. Timing jitter of 897 MHz optical pulse train from actively stabilised passively modelocked surface-emitting semiconductor laser. *IEEE Journal of Quantum Electronics* **42**, 159–160 (2006).

[26] Dupriez, P. *et al.* High-power, single-mode picosecond fiber laser based on amplification of a passively mode-locked 1055-nm VECSEL. In *Conference on Lasers and Electro-Optics (CLEO)*, CThJ3 (Long Beach, California, USA, 2006).

[27] Aschwanden, A. *et al.* 10 GHz passively mode-locked external-cavity semiconductor laser with 1.4 W average output power. *Applied Physics Letters* **86**, 131102 (2005).

[28] Chilla, J. *et al.* High power optically pumped semiconductor lasers. In *Photonics West: Solid State Lasers XIII* (San Jose, California, USA, 2004).

Chapter 6

High repetition rate VECSEL

6.1 Introduction

High repetition rate lasers have many applications is areas such as optical clocking of highly integrated circuits [1], high bit-rate data transmission [2], and, at higher powers, in rapid throughput laser materials processing. At these multi-GHz repetition rates, a clear constraint upon the device is that it is required to emit ultrashort pulses to avoid pulse overlap. Also, particularly in optical clocking, stability of the laser is crucial, a low noise, low jitter source is fundamental for this application in optimising the amount of usable clock cycle [3].

Previously, high repetition rate sources have relied on harmonic mode-locking whereby several pulses circulate in the cavity at once, with their separation determined by the position of the mode-locking device in a conventional two mirror cavity, or the repetition frequency of the mode-locking device in a ring cavity configuration [4, 5]. The inherent problems with this type of mode-locking lie in the stability, where the noise and pulse-to-pulse jitter caused by polarisation fluctuations in the fibre due to mechanical vibrations, cavity length fluctuations due to temperature variations, and competing supermode noise [6, 7]. Also, with these sources, pulse dropout is a key limiting factor resulting in an unreliable train of irregularly spaced pulses [8]. More recently, solid state lasers have begun to push forward as promising high repetition rate sources [2, 9, 10, 11]. These

sources are unsuitable for cheap mass-production, and prone to Q-switching instabilities, remaining an expensive alternative to the harmonically mode-locked fibre laser.

Compared with many of its solid state and mode-locked fibre laser counterparts, the VECSEL shows great potential as a source of high repetition rate short pulses. Higher repetition rates may be obtained without the need for harmonic mode-locking, by simply shortening the cavity length. VECSELs have already proved themselves to be very low noise lasers, ideal for clocking applications [12]. Moreover, because of the short upper-level lifetime, there is little energy storage in the VECSEL gain medium, rendering VECSELs free from Q-switching instabilities. However, in the early days of VECSEL mode-locking, no miniaturisation of the cavity was attempted, and typical repetition rates of a few GHz were commonplace [13, 14, 15]. It is only more recently that the great potential of VECSELs as novel all-semiconductor sources of stable, ultrashort pulses at very high repetition frequencies has begun to be explored. Tens of GHz repetition rates have been achieved both at Southampton [16, 17], and in other groups [18, 19], through the minaturisation of the VECSEL cavity, where cavity length directly determines the repetition rate. The record currently lies at 50 GHz, where the minaturisation of the typical VECSEL V-cavity configuration has reached its engineering limit [20].

This chapter will outline the challenges of high repetition rate laser design, providing a review of the high repetition rate milestones in the VECSEL field so far, and discussing the limitations of these devices. The fundamental limits of high repetition rate operation are discussed. Then the development of a method for producing VECSEL structures capable of accessing repetition rates above 100 GHz is documented. Characterisations of the structures fabricated are presented, and future steps to realise a final device are outlined.

6.2 Challenges of high repetition rate VECSEL design

Mode-locked VECSEL cavities are designed to fulfill all the requirements outlined in section 2.4. In order to successfully mode-lock using the SESAMs employed in the work presented throughout this thesis, the fluence on the SESAM is required to be an

order of magnitude higher than that on the gain sample. This ensures that the SESAM saturates long before the gain (as discussed in section 2.4.1.1). In the standard 1 GHz VECSEL cavity employed throughout this thesis (cavity length ~15 cm), designed for Stark mode-locking, this is achieved in a Z-cavity configuration, containing a tightly focussing high reflector in the path to the SESAM (see section 2.4). The focal length of this high reflector (typically of the order of a few tens of mm), and hence spot size and corresponding fluence on the SESAM can be altered to achieve stable mode-locking, and varying pulse regimes.

As we move to higher repetition rates, this cavity configuration becomes problematic. At 10 GHz [16, 18], the cavity length is a mere 1.5 cm, requiring intricate cavity design with a V-cavity configuration, precision positioning, and careful engineering of sample mounts in order to accommodate the SESAM, focussing output coupler and gain sample in the cavity, whilst avoiding blocking the incident pump beam. As the cavity is reduced further, it becomes difficult to focus onto the SESAM, and careful engineering and component integration become the only solutions.

6.2.1 10 GHz VECSEL

The first migration into high repetition rate VECSEL operation was made with the Southampton demonstration of a 10 GHz Stark mode-locked, near transform-limited source of sub-500 fs pulses centred at 1034 nm [16, 17]. The laser was essentially a miniaturised version of the sub-500 fs, 1 GHz laser described in section 2.4.2. Shown in figure 6.1a, the 10 GHz cavity length was 1.5 mm, with a V-shaped design, using the antiresonant gain sample described in section 2.2.3.2, and the Stark SESAM detailed in section 2.4.2. The curved output coupler had a 15 mm radius of curvature, chosen to provide good overlap of 120 μm diameter standard diode pump spot, and laser mode on the gain, whilst also providing the necessary focussing on the SESAM to achieve the fluence ratio required to achieve Stark mode-locking.

The resulting 486 fs pulses had sech^2 1.02 times transform limited profiles, giving 30.3 mW average output power, at a repetition rate of 10 GHz, centred at 1034 nm, but tuneable from 1030 to 1040 nm with varying pulse lengths [16]. This demonstration of

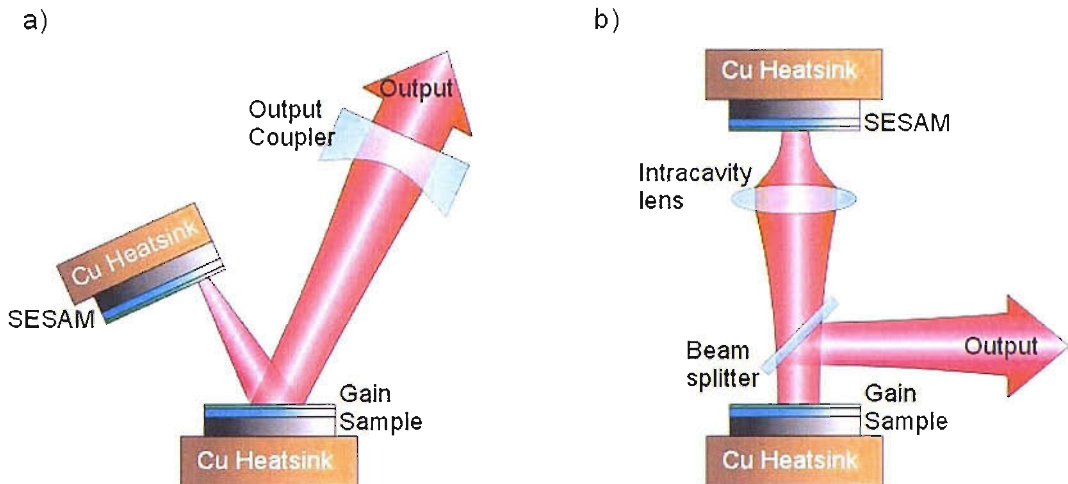

FIGURE 6.1: High repetition rate cavity configurations of a) the 10 GHz VECSEL V-cavity design described in [16] and b)the VECSEL straight cavity design with intracavity lens described in [19].

efficient, stable, high repetition rate operation motivated the further investigations into higher repetition rate devices described in this chapter however, it was evident that if a V cavity were to be employed, an engineering limit would be reached where component minaturisation and focussing in the V configuration would no longer be possible.

Some work has been carried out using an intracavity lens to provide the SESAM focussing required within a VECSEL cavity at a repetition rate of 15 GHz [19]. This straight cavity design, shown in figure 6.1b, incorporated a beam splitter to provide the output, however, the cavity remains complicated, with two intracavity elements again limiting the minimum cavity size possible, and introducing inherent losses. It is thus clear that integration of components, and simplification of cavity configuration is required.

6.2.2 Alternative Saturable Absorbers as a route to 50 GHz

One step towards shorter, simpler VECSEL cavities is to overcome the requirements of focussing within the cavity through modification of the SESAM fluence requirements. This concept necessitates the design of a saturable absorber with a much lower saturation energy than the gain sample, but without sacrificing short-pulse operation. With quantum well SESAM structures, this is not easily achieved, since ultimately, the saturation energies of the SESAM and gain structures are similar as they are based on the

same quantum well structures. In order to pursue this route, alternative, low saturation energy saturable absorber designs must be sought. It is then conceivable to propose a device where saturable absorber and gain structure are incorporated on one epitaxial structure along with a DBR mirror, and the cavity completed with a dielectric output coupler.

Investigations into lower saturation energy saturable absorbers were first reported by Garnache et al in [21]. A self-assembled quantum-dot (QD) SESAM was used to mode-lock a VECSEL. The absorber incorporated 14 layers of InAs/GaAs self-assembled QDs grown at high temperature on top of an AlAs/GaAs DBR. The dots have a large absorption cross-section greater than 10^{-14} cm^2, due to their three-dimensional carrier confinement, ideal for creating a low saturation fluence SESAM suitable for high repetition rate VECSEL mode-locking. The quantum dot density was $\sim 5 \times 10^{10}/\mathrm{cm}^2$, and the absorption per layer was ~0.05%, giving a modulation depth of ~ 1%, comparable to that of a quantum well SESAM, and a low non-saturable loss <0.1%, particularly advantageous for these inherently low-gain devices. But of particular note, the saturation fluence of the QD-SESAM was an order of magnitude smaller than that of the quantum well, greatly reducing the focussing required to saturate it. Unfortunately, this particular device had a long recovery time of ~1 ns, and generated 13 ps pulses in a 300 MHz repetition rate cavity. Further optimisation of the growth of the quantum dots was required to reduce this recovery time, and make a fast saturable absorber for short pulse generation.

Recent developments in the Keller group at ETH Zurich have shown great improvements in quantum dot SESAM growth. Again based on self-assembled InAs QDs, the desired modulation depth (3.1%), nonsaturable losses (0.3%) and low saturation fluence (F_{sat} = 1.7 μJ/cm^2) are achieved with only one layer of low temperature grown dots [22]. Equipped with a saturable absorber and gain structure both requiring a the same modal size, it is possible to overcome the restrictions of focussing within the cavity. A V cavity design is still adopted by the Keller group, but with minaturisation of the cavity elements, repetition rates as high as 50 GHz have been achieved with 3.1 ps pulses at 958 nm with 42 mW average output power, stabilised using an intracavity etalon [20].

At the 50 GHz high repetition rate, a limit of component size engineering truly has been reached. The next step for the QD-SESAM approach is the growth of an epitaxial structure with a DBR, gain region, and integrated QD saturable absorber, to be employed in a simple straight cavity.

6.2.3 Limitations above 50 GHz repetition rates

Once the mechanical limits of cavity configuration are overcome, the next limits to be reached are governed by the mode-locking dynamics of the device in question. This includes the slow recovery of the saturable absorber, the effects of pulse overlap, and saturation of the SESAM.

In order to maintain stable mode-locking, the saturable absorber must be able to recover between pulses. Naturally, if the next pulse arrives before the absorber has recovered fully, the absorber will still be partially saturated, giving a smaller modulation depth, and the pulse will see a weaker pulse-shaping effect. This partial recovery effect will therefore lead to pulse broadening, and destabilisation of the steady state mode-locking. Typical SESAM recovery times are of the order of a few picoseconds, limiting cavity repetition rates to a few hundreds of GHz. For SESAM devices described in this thesis (sections 2.4.2 and 5.3.1) it is the 4 ps slow recovery time component that dominates for this effect. Using $\nu_{RT} = 1/\tau_r$, where ν_{RT} is the repetition rate limit, and τ_r is the absorber recovery time, the limit for full SESAM recovery in a round trip for this 4 ps recovery lies at a repetition rate of 250 GHz.

It is also important to remember that at repetition rates where the pulse base length is longer than the cavity round trip in time, pulse overlap will occur [2]. This dominates over the effect of SESAM partial recovery if the pulse base length is longer than the SESAM recovery time, this will result in a laser output that appears to be more of a continuous-wave output with partial modulations in output power, not the characteristic output of well discriminated pulses expected from a mode-locked laser, this is shown schematically in figure 6.2. Using $\nu_{RT} = 1/\tau_{base}$, where ν_{RT} is the repetition rate limit, and $\tau base$ is the pulse base length, this limit can be calculated. For the 3.1 ps pulses achieved in [20], the base width is 17 ps, giving a pulse overlap repetition rate limit

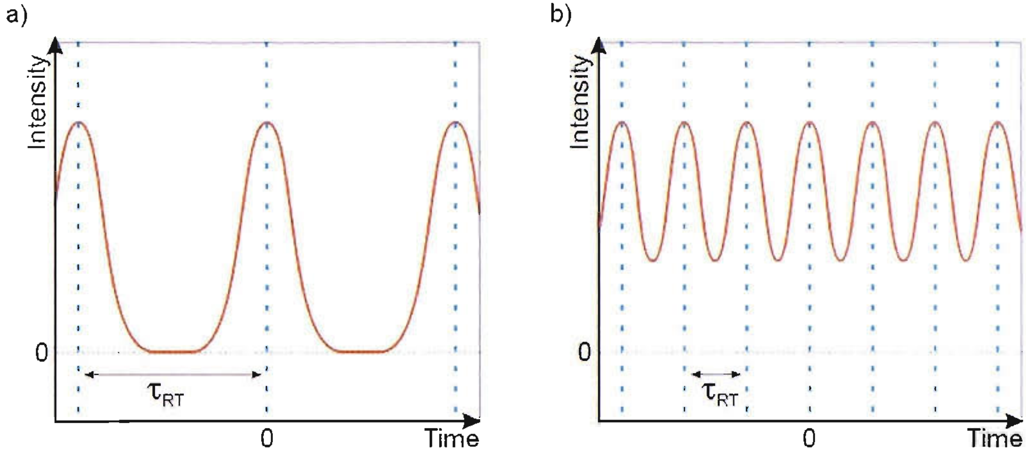

FIGURE 6.2: Representations of ML-VECSEL output for the cases where a) $\tau_{base} << \tau RT$ and b) $\tau_{base}\ \tau_{RT}/2$, showing the potential for pulse overlap as higher repetition rates are accessed by ML-VECSELs [2].

of 58 GHz, very close to the 50 GHz repetition rates already achieved. However, for a sub-500 fs pulse such as that shown in [16], with base width of 2.75 ps, the limit is greatly improved at a repetition rate of 360 GHz.

Another important consideration when designing a high repetition rate laser is intracavity pulse energy. Much as focussing onto a QW-based SESAM is required to saturate the SESAM before the gain sample in the cavity, sufficient fluence upon the SESAM is important to reach the saturation fluence of the device in the first place. In a high repetition rate cavity with a given average intracavity power, the intracavity peak power per pulse is, in turn, less that that of a lower repetition rate laser with the same average intracavity power. Consequently, the threshold fluence for mode-locking is much higher, resulting in the need for either much higher intracavity powers, or much tighter focussing on the SESAM. This is a key limiting factor for the devices fabricated in this chapter, and is discussed further in section 6.6.1.1.

At these higher repetition rates, the resistance of VECSELs to Q-switching instabilities also becomes compromised. The stability criterion against Q-swtching is stated in [23] to be:

$$E_p^2 > E_{satg} E_{sata} \Delta R \tag{6.2.1}$$

where E_p is the intracavity pulse energy, E_{satg} is the saturaton energy of the gain, E_{sata} is the saturation energy of the SESAM and ΔR is the SESAM modulation depth. The right-hand side of this calculation for a Stark SESAM ML-VECSEL yields a threshold value of the order of 0.3×10^{-21} J^2; several orders of magnitude less than E_p^2 for 1 GHz repetition rate VECSELs. However, for repetition rates of ~100 GHz, E_p^2 approaches the stability threshold with values around ~1.5×10^{-21} J^2. Therefore, at even higher repetition rates, or lower pulse energies, the VECSEL may become susceptible to Q-switching instabilities.

6.3 Focussing gain region VECSEL as a route to 100 GHz

Section 2.4.2 describes the dynamic effect of optical Stark effect mode-locking realised at Southampton. Using this effect, and fast surface recombination effects, ultrashort, sub-500 fs pulse lengths are achievable from a ML-VECSEL, pushing the threshold for pulse overlap destabilisation to much higher repetition rates than those predicted with the QD saturable absorber 3.1 ps ML-VECSEL, leaving SESAM saturation and partial saturable absorber recovery threshold as the limiting factors for a high repetition rate laser employing this mode-locking dynamic. However, the Stark SESAM design described in 2.4.2 continues to require intracavity focussing to achieve the desired fluences on gain and SESAM, returning to the problem of a space-limiting, many-component cavity design. Similar to the integrated QD absorber concept in [22], integration of passive with active components is necessary to simplify the cavity and facilitate miniaturisation. This has been investigated as part of the work detailed in this thesis.

If a Stark QW SESAM is to be incorporated into the cavity, different saturation fluences are required on both the SESAM and the gain sample again. It is therefore clear that integration of the gain and SESAM is not feasible. Moreover, there must still be a focussing element in the cavity to provide the saturation fluences required, with smaller spot size on the SESAM than the gain. With cavity lengths of just 1.5 mm required to reach the preliminary goal repetition rate of 100 GHz, it is also clear that a straight-cavity configuration is the most suitable in order to avoid an 'over-crowded' cavity.

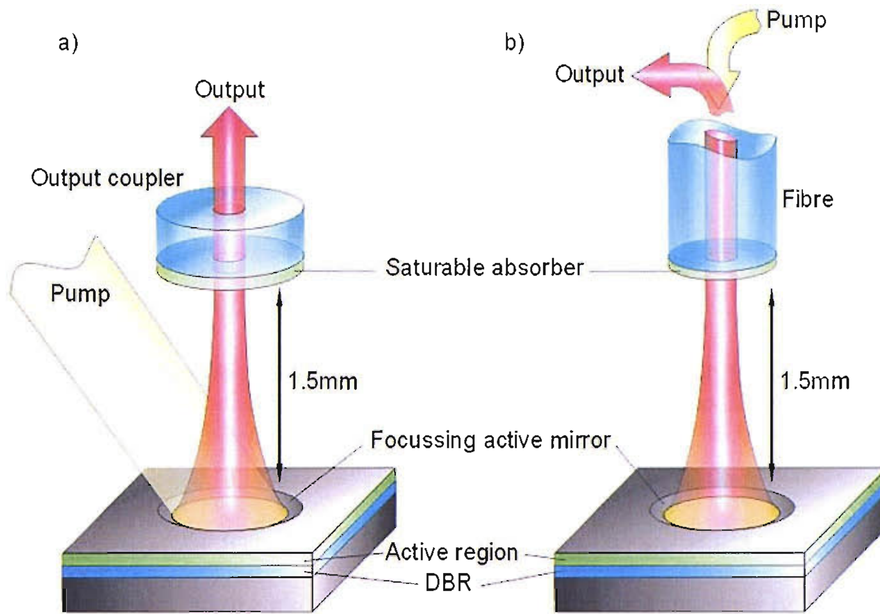

FIGURE 6.3: Schematics of the proposed 100 GHz concept VECSEL cavities, incorporating a focussing active mirror gain sample and completed with a) an output coupler with appropriate Stark SESAM levels incorporated to couple to free-space, and b) fiberised pump launch and SESAM output coupler combined.

The solution investigated in this work involves the integration of the gain sample with the focussing mirror in the production of a focussing gain sample. In order to achieve this, a method for fabricating curved structures in GaAs substrates of the correct dimensions to give the desired focussing, with optical quality surfaces, has been developed. These structures must then have the VECSEL DBR and active region deposited on top, forming a focussing active mirror. It is then possible to conceive a cavity completed with a SESAM output coupler, or possibly even a fibre tip with saturable absorber and mirror layers deposited on, also delivering pump light.

The concept of such a device is shown in figure 6.3. The straight cavity is 1.5 mm long, suitable for achieving the goal repetition rate of 100 GHz. The dimensions of a dish-like structure that would be used to obtain the focussing required for this device are shown schematically in figure 6.4. The mirror dimensions are 150 μm diameter, and $\sim$4 μm deep at the centre. The mirror should be parabolic in shape to fulfill the requirements of mode-focussing within the cavity, however a spherical profile is chosen for ease of fabrication as this approximates well to the base of a parabola at the dimensions proposed.

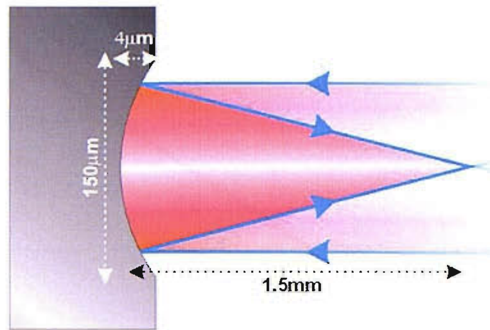

FIGURE 6.4: Cross-section of a proposed curved structure to be fabricated in GaAs, showing the desired dimensions of 150 μm diameter to accommodate a 120 μm pump spot, and 4 μm deep with a spherical profile to give the desired focussing in a 1.5 mm cavity

A stability calculation (method included in appendix B) for the desired structure in a straight, two mirror cavity shows that focussing down to spot sizes of less than 10 μm radius is possible at the edge of the stability limit using such a structure in a 105 GHz cavity (figure 6.5). The remainder of this chapter documents the route taken towards fabricating such a focussing semiconductor gain structure, outlining the challenges of developing a new fabrication technique. Results are shown, and future routes to a final device are outlined.

6.4 Fabricating Optical-Quality Focussing Structures in GaAs Substrates

The first step in realising a high repetition rate ML-VECSEL based on a focussing active mirror is to fabricate optical quality curved structures in a GaAs substrate suitable for overgrowth. Several routes to such a structure can be thought of conceptually, however, there is little in the literature to support fabrication of any structures similar to those attempted in this thesis in GaAs. Two methods attempted are presented.

6.4.1 Direct Drilling of GaAs

The principally investigated method for curved structure fabrication is presented in the following sections, and does not involve the direct patterning of the GaAs substrate.

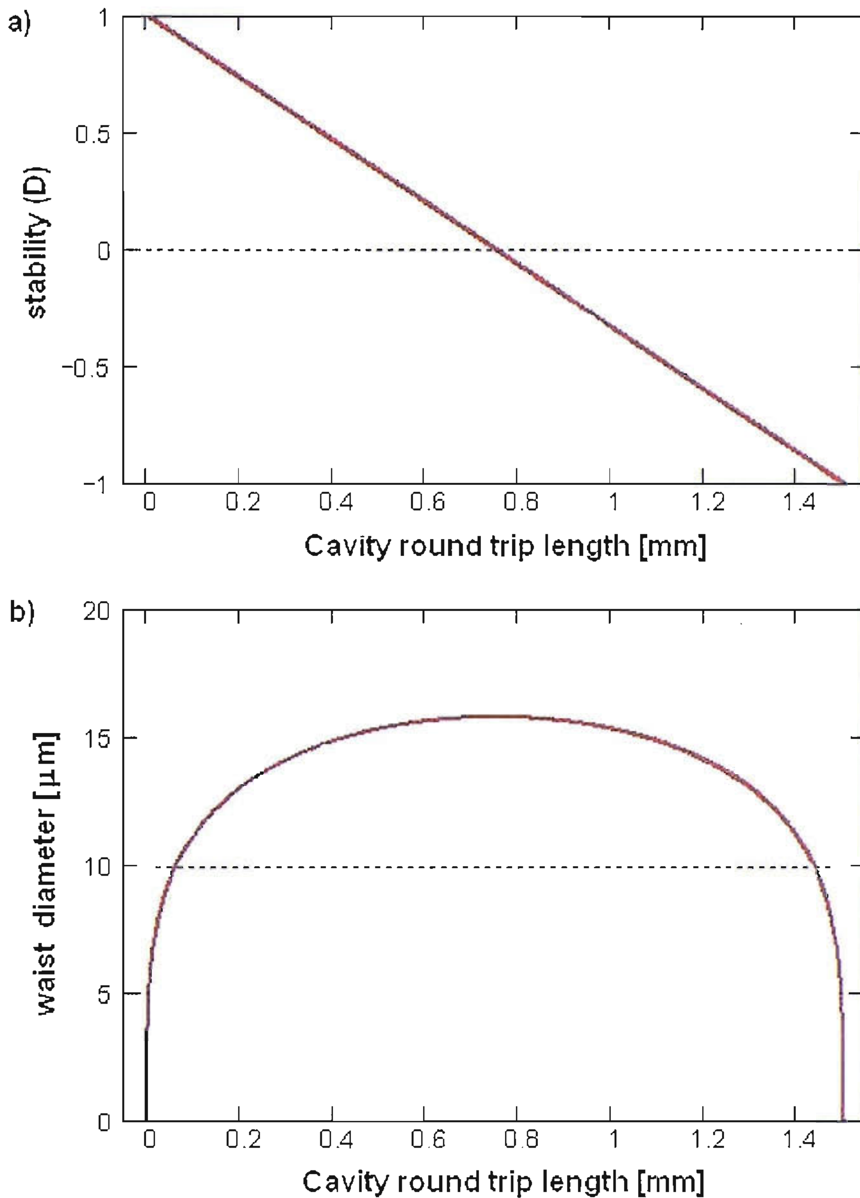

FIGURE 6.5: Stability calculation for the proposed 100 GHz cavity, showing that a 10 μm radius spot is achievable at the edge of cavity stability.

However, for completeness, a directly invasive technique was explored, and the results of such a technique are described in this section. With current mechanical workshop processing accuracies of the order of a micron achievable with standard drill bits, it was considered reasonable to attempt to drill the desired curved structure into the GaAs substrate.

A watchmakers drill column with micron precision was used for this purpose. A drill-bit with the desired dimensions was fabricated by accurately glueing a 1.5 mm diameter

ruby ball lens into a 0.5 mm impression made in the centre of a post designed to fit the drill shaft. Samples of 500 μm thick, undoped GaAs substrate approximately 5 mm $\times$ 5 mm were attached to glass microscope slides with polishing wax. This was then held in place beneath the drill. A drop of either etchant or calcined aluminium polishing slurry was dropped onto the GaAs surface in the spot where the drill makes contact. The drill was then lowered and held onto the sample with contact pressure, turning at a speed of 20 revolutions per minute.

Various drilling recipes were explored, combining both mechanical, and chemical polishing-based drilling. Initially, 5% sodium hypochlorite (NaOCl) solution was used. This is a particularly aggressive etchant of GaAs, with an unstirred, 100% solution etch rate of 1.8 μm/min [24]. The sample was drilled for 5 minutes, and then immediately washed with copious amounts of deionised water to halt etching.

The profile of the resulting structure is shown in figure 6.6. The profile was taken using a FLA Tencor Alphastep P15 profiler with a 2 mg needle load. It shows a deep, $\sim$20 μm wide, circular trench etched around the point of contact of the drill tip with a radius of approximately 40 μm. This is attributed to the rapid movement of sodium hypochlorite in this area, close enough to the ball to move with it, enhanced by the constant replenishing with fresh etchant from the surrounding pool, etching much more readily than the etchant at the centre of the impression. The profile does not exhibit the desired characteristics of an optical quality curved impression.

A more favourable impression was achieved using a method developed to incorporate a combination of mechanical and chemical etching. To avoid trenching, a coarse impression was made using the same drill setup, but with a 0.3 μm particle size calcined aluminium polishing slurry used in place of the sodium hypochlorite etchant. The sample was drilled for 7 minutes. The remaining slurry was then washed off with deionised water, without moving the sample from its position beneath the drill. As before, sodium hypochlorite was then used with the drill for 2 minutes to attempt to improve the surface quality of the resulting structure.

A profile of the impression is shown in figure 6.7. The trenching effects associated with the previous drilling method using only sodium hypochlorite are overcome. A

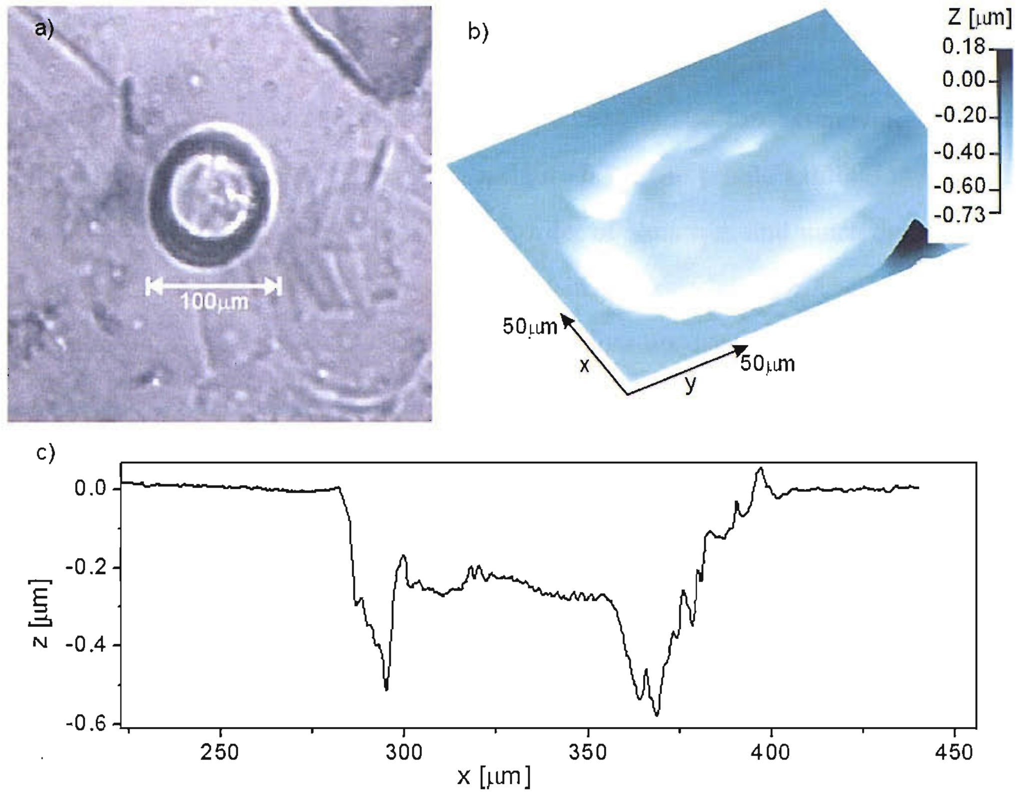

FIGURE 6.6: Results of attempts to drill GaAs with ball-lens drill and sodium hypochlorite solution, showing a) a microscope image of the drilled area, showing etching of the surrounding GaAs, b) a three-dimensional profile of the area, and c) a two-dimensional profile of the drilled region, showing deep etching by the replenished, fast moving sodium hypochlorite solution at the edges of the drill tip, and raised central drilled region where the drill tip was in direct contact with the GaAs, with little etchant movement or replenishment.

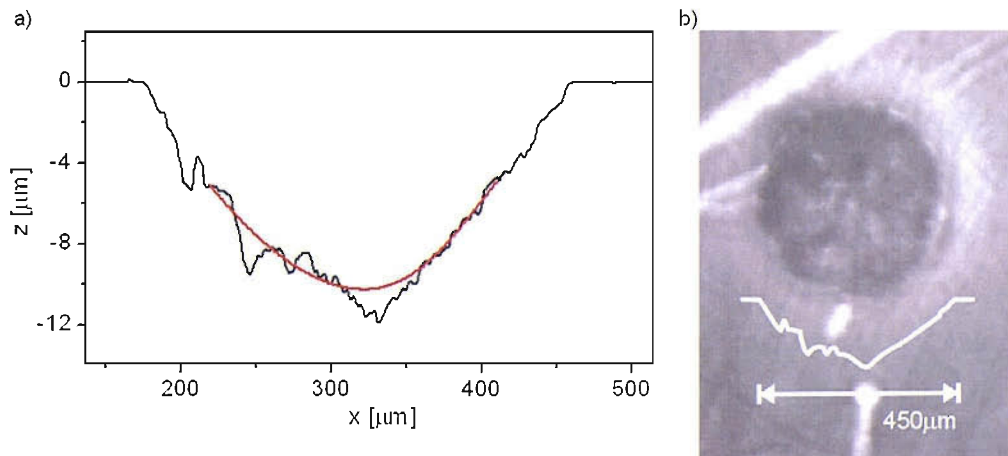

FIGURE 6.7: Results of attempts to drill GaAs with ball-lens drill in a 2 step chemomechanical process using polishing slurry, and etchant. a) A profile of the drilled structure (black) with smoothed fit (red) used to calculate the potential focussing properties of the structure. b) A microscope image of the impression showing it's dull appearance, indicative of poor surface quality

dramatically smoothed fit to the base of the profile in figure 6.7a shows the potential of this technique for producing curved structures with the desired dimensions, the focal length extrapolated from the fit is very approximately 900 μm. However, the surface quality of the impression is very poor. In figure 6.7a, the profile exhibits much surface roughness, with peak to valley values of the order of a micron, and much deviation from a smooth, curved profile. Also, in figure 6.7b, a microscope image of the impression, the impression centre appears dull, indicating that it does not have an optical-quality finish.

Further refinements of the drilling technique for the fabrication of focussing mirrors in GaAs could be made by investigating finer polishing slurries, and a method for ensuring an even flow of sodium hypochlorite etchant across the drilled area, constantly removing etch by-products and supplying fresh etchant. Moreover, a drill tip that moves not only radially in the x-y plane, but also rolls in the z direction could be designed and implemented. However, the work detailed in this thesis concentrates on an alternative method for fabrication of the desired structures, focussed on achieving the desired optical quality finish, as detailed in the remainder of this section.

6.4.2 Imprint Lithography

The principal method developed to produce the dish-like structures in GaAs requires a combination of lithography and etching. Shown schematically in figure 6.8, first, the desired structure is patterned into resist that is spun onto the GaAs substrate (steps a and b). This is then etched via the inductively coupled plasma (ICP) method, to transfer the pattern into the GaAs substrate beneath (step c). Finally, the structure will be overgrown by Metalorganic Chemical Vapor Deposition (MOCVD) with the desired mirror and active layers. The lithography step was carried out in the Nanomaterials rapid prototyping facility cleanroom at the University of Southampton, whilst the etching of the samples described in this thesis was carried out at the EPSRC III-V Semiconductor Facility in collaboration with Dr Geoff Hill at the University of Sheffield. These structures were then characterised, and their suitability for overgrowth ascertained. MOCVD growth was carried out by Dr John Roberts and Dr Andrey Krysa at the EPSRC III-V Semiconductor Facility at the University of Sheffield.

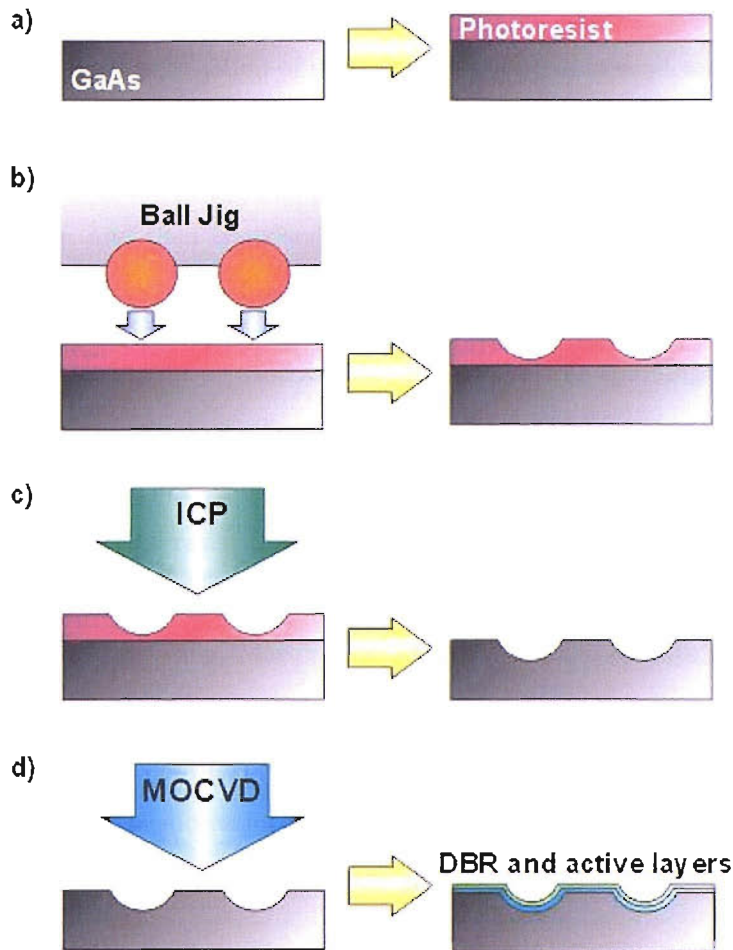

FIGURE 6.8:
Schematic detailing the steps in the process developed to create focussing optical quality structures in GaAs.
a) Photoresist is spun onto a cleaned GaAs substrate.
b) The resist is patterned with the desired structure.
c) This pattern is then transferred into the GaAs substrate below via an ICP etch step.
d) Finally, the patterned GaAs is overgrown by MOCVD with the desired epitaxial layers.

6.4.2.1 Imprint Lithography: Historical Aspect

The idea of imprinting patterns into materials has been adopted for centuries to produce both decorative and functional items. Indeed, the fabrication process of a compact disc relies on this technique to pattern thermoplastic polymers for data storage. Most patterning processes in the semiconductor industry employ lithographical techniques to transfer patterns in a resist material through to a semiconductor substrate material

[24]. In 1995, this principle was adapted by Chou et. al. to meet demands for low-cost, high-throughput mass-production of sub-micron structures in semiconductor substrates [25]. Entitling the technique 'Nanoimprint Lithography', they successfully fabricated sub-25 μm vias, trenches and dot-arrays by pressing a mould into a thin thermoplastic polymer layer, and then transferring the three dimensional pattern through to the substrate using reactive ion etching.

The nanoimprint technique as described in [26] involves the spinning of a thin (50 nm) polymer photoresist layer on a silicon substrate. The sample is then heated well above the glassy transition temperature of the resist, and a mould pressed into the resist. The mould is left in the resist until it cools, and is then removed, leaving behind its impression. A smooth removal is aided by the application of a mould release agent to the mould prior to imprinting. More recent advances in the nanoimprint process include roller nanoimprint lithography where a sample is run through a printing-press style arrangement [27], and multilayer resist methods on non-flat surfaces [28, 29] to name but a few. Also, with its successful application to high throughput nanoscale lithography [30], nanoimprint lithography machines are gradually becoming commercially available [31, 32].

6.4.3 Southampton Micro-Imprint Technique

As a solution to the challenges of transferring mechanical machining down to the nanometre scale, the nanoimprint technique has proved itself a successful method for fabricating structures with feature sizes of the order of a few nanometres [33]. However, the feature sizes desired for this project are much larger (see figure 6.4). It is clear that the fabrication of the desired structures lies between the scales of two technologies; mechanical machining suitable for millimetre-scale features, and the nano-processing techniques described above. However, when considering a suitable fabrication method, the optical quality surface finish required on the final dish structure dictated that a modified imprint lithography approach was most suitable, and led to the first investigations into

micro-imprint lithography for the fabrication of optical surface quality dish-like structures in GaAs. This is the first time in imprint lithography that a structure designed to be curved in three dimensions has been fabricated.

The method described below is a result of many fabrication trials to arrive at a feasible technique with reasonable reliability:

1. Samples of GaAs substrate very approximately 5 mm by 5 mm are cleaved from a substrate wafer. Their bottom left corner is scratched to enable reproducible navigation of the sample throughout the imprint, etch and growth stages. They are then cleaned using the standard wash steps described in section 4.5.2.

2. Photoresist is spun onto the sample surface. Spinning is carried out on a standard spin coater. The sample is held in place with a vacuum, one drop of photoresist is dropped onto the center of the sample surface. The resist is filtered through a 0.2 μm pore-size polypropylene Whatman Puradisc^{TM} filter to remove any contaminating particulates. The sample is then spun at 4000 rpm for 60 seconds.

3. The sample is removed from the spinner, and then hard baked for 60 seconds on a hotplate at 115 ^{o}C, then removed from the heat, and stored ready for imprinting. At this point, if thicker resist is required, steps 2 and 3 can be repeated to form a thicker layer of resist.

Imprinting is carried out using a customized watchmakers drill. The drill has micron precision, and is free from any rocking action which may deform the imprinted pattern. The rig is shown in figure 6.9. Imprinting jigs were made to fit into the shaft of the drill. For the larger imprints, these were constructed of ruby ball lenses, sunk into a glass layer on top of a stainless steal plate with a rod that fits the drill shaft screwed into the back. These jigs could be easily cleaned by standard methods (section 4.5.2). For smaller imprints, ruby ball lenses were stuck into drilled recesses in an aluminium jig that fits the drill shaft. These jigs were more difficult to clean as the glue is not resistant to the solvents used, so the ball lenses were removed and cleaned separately, then re-attached. The imprinting method follows:

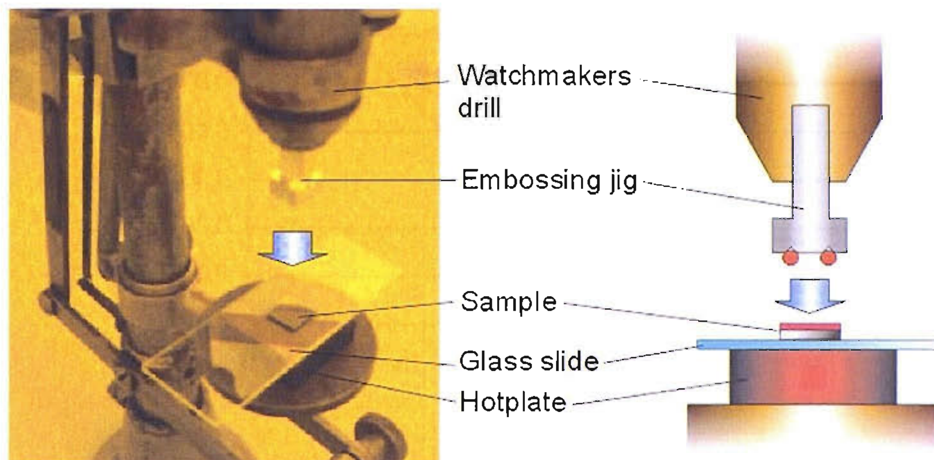

FIGURE 6.9: Diagram and photograph of the rig used for micro-imprinting of resist spun on GaAs substrate. The imprinting jig fits into the shaft of the micron-precision watchmakers drill, and has ruby ball lenses of the desired size attached.

1. The sample with a baked resist layer is placed on a hot glass slide, and heated to 165 ^{o}C on a hot plate for 1.5 minutes, above the glassy transition temperature of the resist (120 ^{o}C).

2. Using the glass slide to hold the sample, this is then placed on a heated metal plate, also at 165 ^{o}C, underneath the imprinting jig on the customised watchmakers drill.

3. The drill is lowered, and held with a finger pressure of 170×10^{6} Pa on the sample for 30 seconds, giving the resist time to cool to below its glassy transition temperature of 120 ^{o}C.

4. The drill is then raised, and the sample removed. The pattern is now hard baked into the resist, suitable for analysis.

5. Samples are stored face-up in individual, clean boxes, in a yellow room. If Shipley 1813 resist samples are transported, they are carried in a dark box to prevent curing of the resist by ambient light. This is not a problem for PMMA.

The nanoimprint techniques developed by Chou et. al. employ a mould release agent to prevent the mould sticking in the resist [26]. This approach was tried in the micro-imprint technique described above. A thin layer of silicone oil, stable to 250 ^{o}C, was sprayed onto the mould prior to imprinting. However, there was no noticeable improvement in the quality of the impression. Moreover, the silicone oil was difficult to

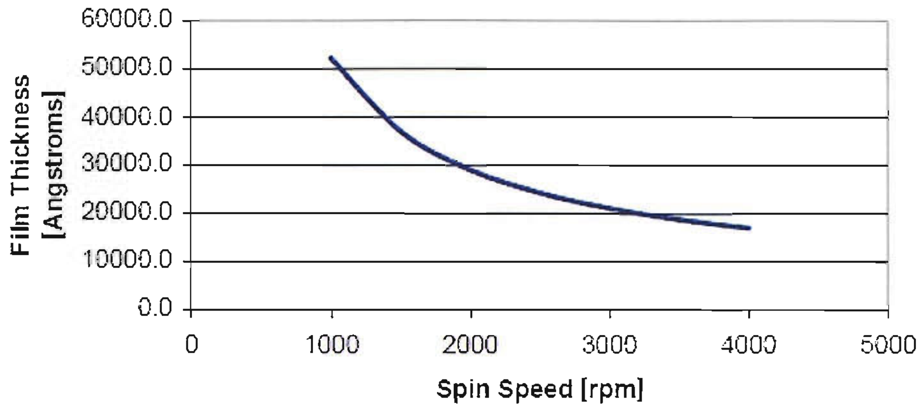

FIGURE 6.10: Spin characteristics of PMMA 950 A11 photoresist from [34]. Note that at 4000 rpm, the spinning speed used in the technique described in this section, the resist thickness is approximately 1.7 μm.

clean from the sample surface after imprinting as suitable solvents would damage the photoresist layer.

Initial micro-imprint trials were carried out on Si substrates to reduce the cost of developing such a challenging technique. A Shipley 1813 photoresist was used, which spun to give a thickness of 1.2 μm. In order to build up a suitably thick layer of resist to imprint, multiple layers of resist were spun on top of each other with a hard bake before each next layer. Shipley 1813 was later replaced by polymethyl-methacrylate (PMMA) 950. PMMA was chosen for its etch characteristics described in section 6.4.4.1, however, it also had favourable spin characteristics, shown in figure 6.10, giving a resist thickness of ~1.7 μm for 4000 rpm spins. This thickness was advantageous for these techniques since fewer layers of resist would be required. Trials with ball lenses with diameters of 1.5 μm were less successful as the resist tended to stick to the ball, even when mould release agent was employed, and the resulting imprint was of poor quality (as in figure 6.11). It was decided to resort to ball-lenses with a much smaller diameter (300-790 μm) to improve the imprinting quality and reproducibility of these initial trials, and modify the cavity length of the final device accordingly.

In later trials with GaAs substrates it was discovered that the brittle nature of GaAs in comparison with Si is a problem. The GaAs had a tendency to break under the pressure of the imprint into the 1813 resist. To try to overcome this problem, since it would ultimately have no effect on the quality of the undoped DBR layers that were

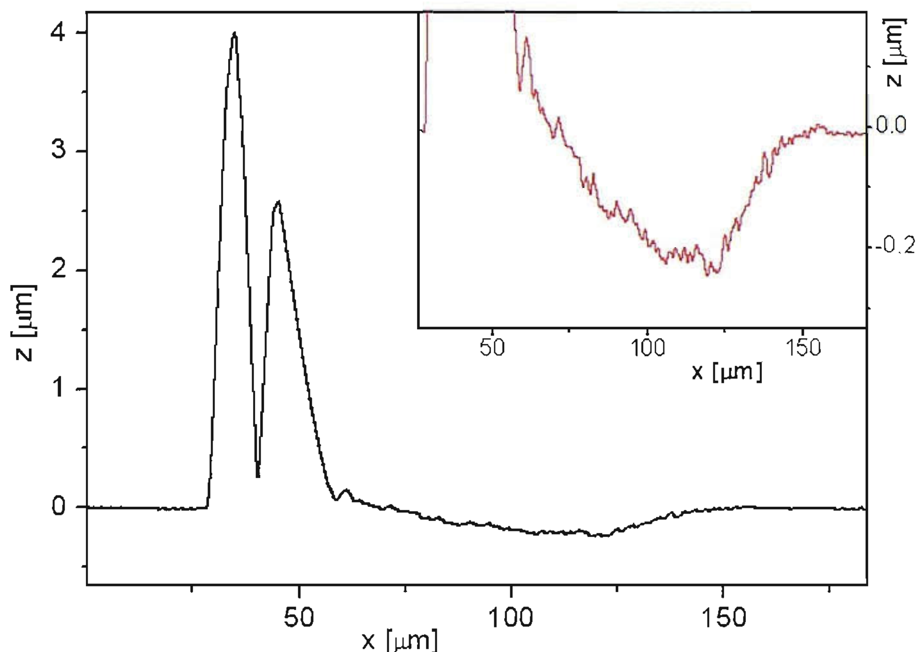

FIGURE 6.11: Imprint made in 2.4 μm thick Shipley 1813 photoresist on a Si substrate. A 1.5 μm diameter ruby ball lens was used to imprint. Note the resist displaced from the imprint appears as a large mound on the left hand side of the imprint. A zoom in on the base of the imprint (inset) shows the poor quality of the imprint, and deviation from a spherical shape.

to be deposited on top of the structure, a GaAs substrate with doping was used. The introduction of a small amount of Si in the doping process acted to strengthen the crystal slightly, and reduce the tendency for cracking. However, the n-doped GaAs was still much more brittle that Si.

Some of these problems with the imprinting technique are shown in figure 6.12. In 6.12a, cracking of the substrate beneath the photoresist can be seen propagating away from the imprinted area. Figure 6.12b shows an area where resist has been lifted away with the ball lens as it was removed. Figure 6.12c clearly demonstrates cracking of the substrate beneath the imprinted area, showing a square-shaped cracking pattern that is indicative of cleave lines along the crystal lattice lines. Also the ridged areas of resist can be seen around the imprint's edge. Finally, figure 6.12d shows a dramatic smashing of a substrate by the imprint process.

A further problem with this fabrication method can be seen in figure 6.13: the imprint is deformed, with a raised area in the centre. This is thought to be caused by a relaxing

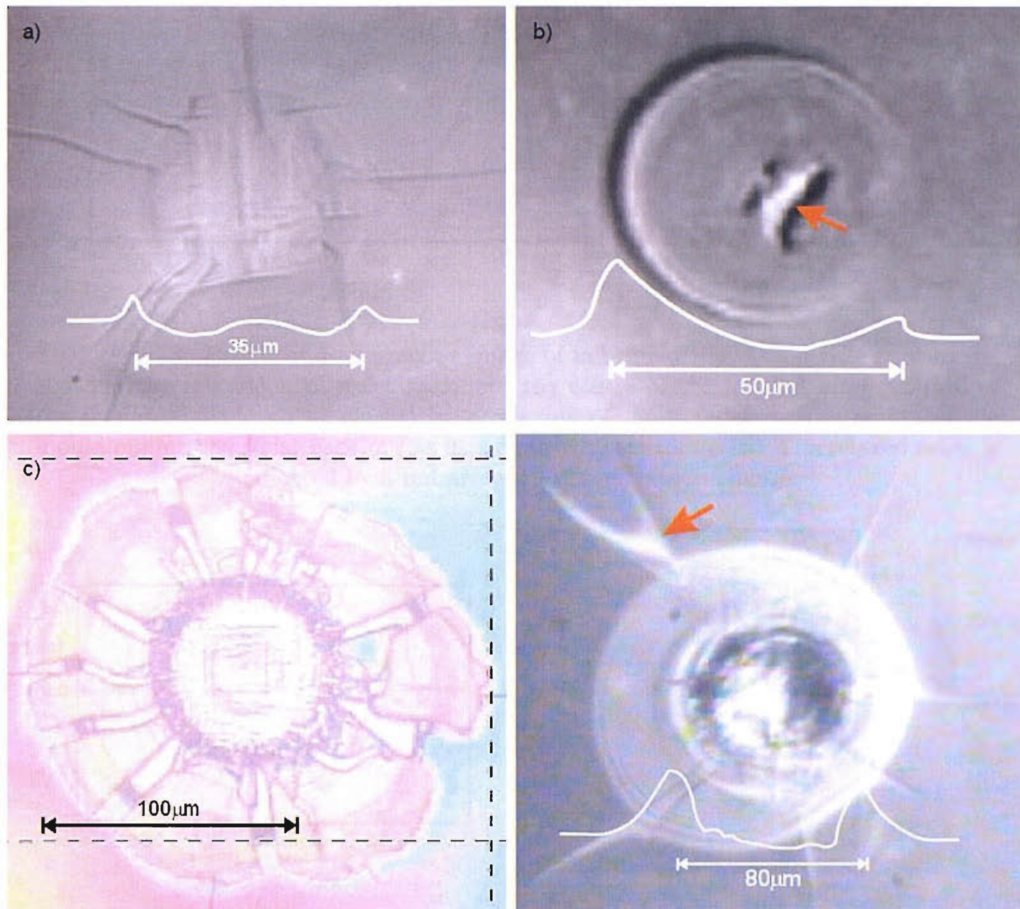

FIGURE 6.12:
Various examples of unsuccessful imprintings.
a) Substrate damage incurred during imprinting beneath the photoresist layer. 1.7 μm thick PMMA950 on n-doped GaAs imprinted with 500 μm ball lenses, showing cracking beneath imprinting in lattice-formation, and cracks propagating across GaAs surface from the imprinted area.
b) Resist lift-off. 2 μm thick PMMA950 on n-doped GaAs imprinted with 400 μm ball lens, showing a region (indicated by red arrow) where resist has lifted off from the substrate during mould removal.
c) Substrate damage. 1.5 μm thick Shipley 1813 on undoped GaAs, imprinted with 300 μm ball lens, showing cracking in lattice-pattern beneath imprinted region, and structure of resist mounds around imprinting edge.
d) Substrate damage. 2 μm thick PMMA950 on undoped GaAs, imprinted with 300 μm ball lens, showing a 'smashing' of the substrate beneath the resist layer (propagating cracks indicated by red arrow). Shown in white on a, b and d are 2-D profiles of the structures.

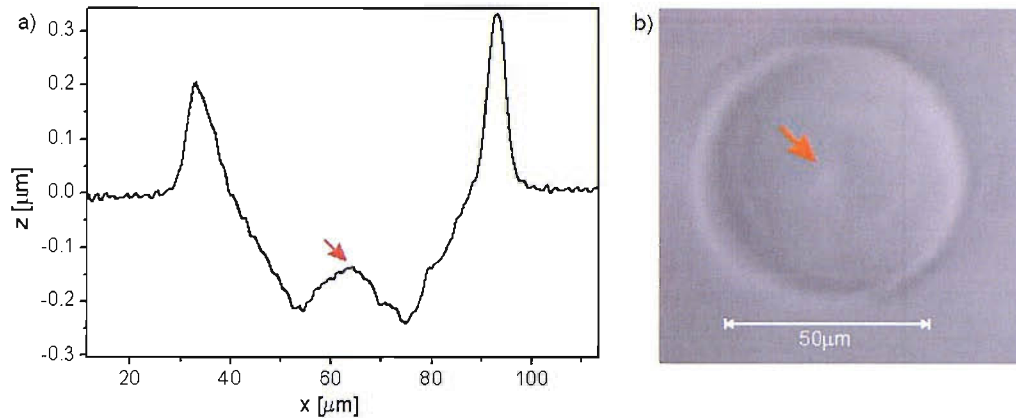

FIGURE 6.13: Profile and microscope image of imprinted PMMA on GaAs substrate, showing the relaxation of resist back into the centre of the imprint after removal of the mould, thought to be caused by a relaxing of unset resist, or the action of the mould pulling the resist back out as it is removed from the resist. The relaxed resist is indicated by a red arrow on the microscope image.

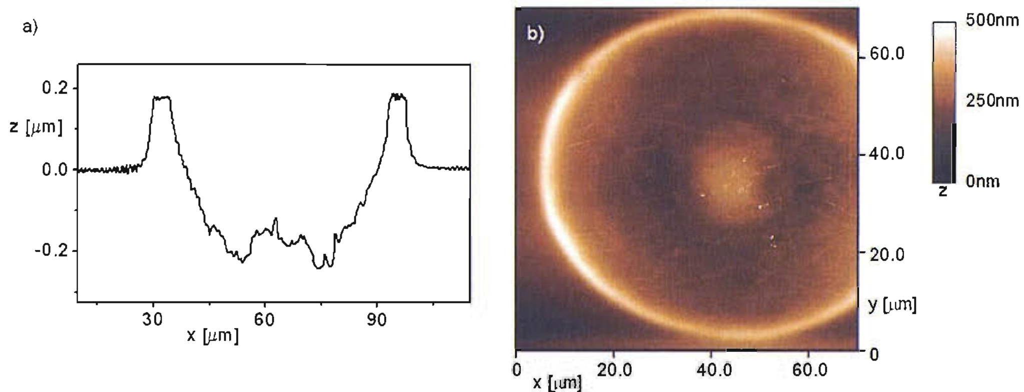

FIGURE 6.14: Profile and AFM image showing the transferral of the pattern of relaxed resist into the GaAs substrate following etching. The AFM is a useful tool to observe the optical quality of the surface of the transferred imprint. Apart from the relaxed region, the surface quality of the transferred imprint looks favourable, with few features to jeopardise its optical quality.

of resist that has not set properly, back into the centre of the imprint when the mould is removed. The resist may also be pulled up in this area by the mould as it is removed. This effect is seen regularly across the imprints made, particularly with larger ball sizes, and greatly reduces the reproducibility of good structures. The occurrence of this effect has been reduced as much as possible by leaving the mould in the resist for longer (up to 5 minutes) allowing it to cool and set, but has not been completely overcome. The transferral of this relaxed pattern into the GaAs substrate after etching is shown in figure 6.14

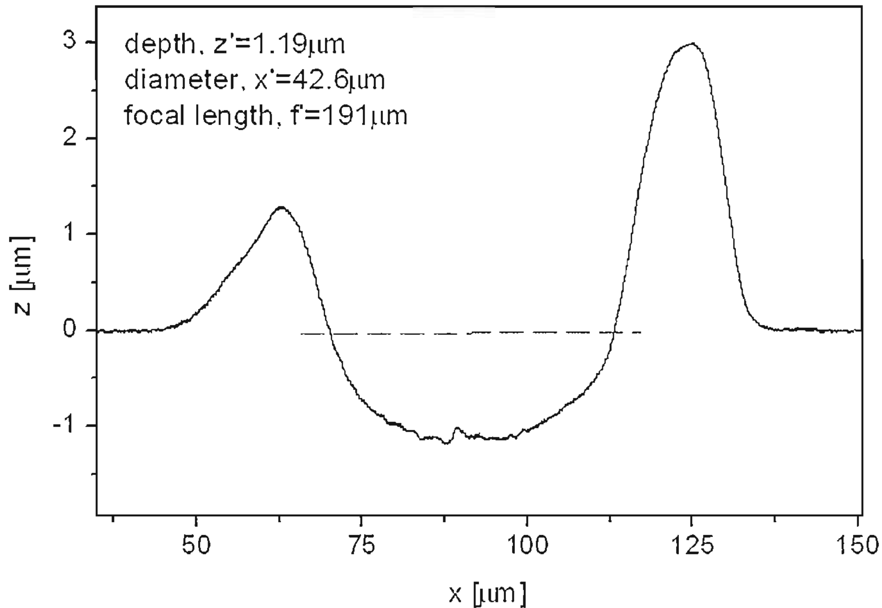

FIGURE 6.15: Profile of 1.7 μm-thick PMMA on n-doped GaAs, imprinted with 400 μm diameter ball-lens jig, shown with expanded vertical scale. Note the large regions of displaced resist at the edge of the imprint. Structuring of the base of the imprint is minimal, and is later seen to disappear during ICP etching of the sample.

Despite these limitations to the technique, imprints with promising profiles were achieved. For the rest of this chapter, we will follow one such imprint through to the overgrowth stage. Its imprinted profile is shown in figure 6.15. The imprint was made by a 400 μm ball lens jig in PMMA 950 via the method described above. The base of the imprint (below the dashed red line) is 1.19 μm deep and 42.6 μm in diameter. This corresponds to a focal length of 191 μm. Some structuring of the base of the imprint is present in the profile, however, since the profile is displayed on a greatly exaggerated vertical scale, this is considered to be minimal. The large raised sections at the edge of the imprint are thought to be composed of resist displaced from the imprint.

6.4.4 Pattern transfer into the GaAs substrate via dry-etching techniques

Following imprinting, referring to figure 6.8c, the next step is to transfer the pattern from the resist into the GaAs substrate below. The technique chosen to achieve this is dry etching, relying on plasma driven chemical reactions or energetic ion beams to

remove material. This category of etch is highly directional, ideal for this application as horizontal etching and undercutting of the imprinted pattern observed with wet etching techniques would act to deform the imprint.

Initial trials were carried out using an ion beam mill dry etch in the ORC cleanroom facility at Southampton. However, the resulting surface quality was poor. Ion beam milling relies on a highly collimated beam of ions to sputter material from the sample surface, not a chemical reaction that will carry its by-products away [24]. Consequently the sample surface showed a ridged post-etch topography, thought to be caused by a flow of ions and etch by-products across the surface. This led to an uneven structure within the imprints themselves, and across the whole sample surface, unsuitable for overgrowth, and application to the final device.

6.4.4.1 Inductively Coupled Plasma (ICP) Etching Method

A more favourable approach is that of reactive ion etching (RIE), where a directional plasma of reactive ions is directed at the sample, reacting chemically at the surface to create highly volatile compounds that quickly disperse. The reactive ion etching presented in this section was carried out at the EPSRC National facility for III-V technology at the University of Sheffield in collaboration with Dr Geoff Hill. The etching is enhanced by the inductively coupled plasma (ICP) technique.

A schematic of the ICP chamber is shown in figure 6.16. The precursor gases flow into the etching chamber through an inductive element; a coil carrying a time-varying electric current. This generates an RF electric field which acts to break-down the gases, forming, and sustaining a high density plasma of reactive species which then serve to chemically etch the sample. The coil is external to the chamber, consequently, the generation of contaminants from this electrode is not a problem. Control of the RF power supplied to the coil allows unique control of the plasma density.

The substrate table is RF-biased independently of the inductively coupled RF plasma. This creates directional electric fields at the substrate, allowing control of the ion energy and direction of bombardment at the substrate separately from the plasma density. This

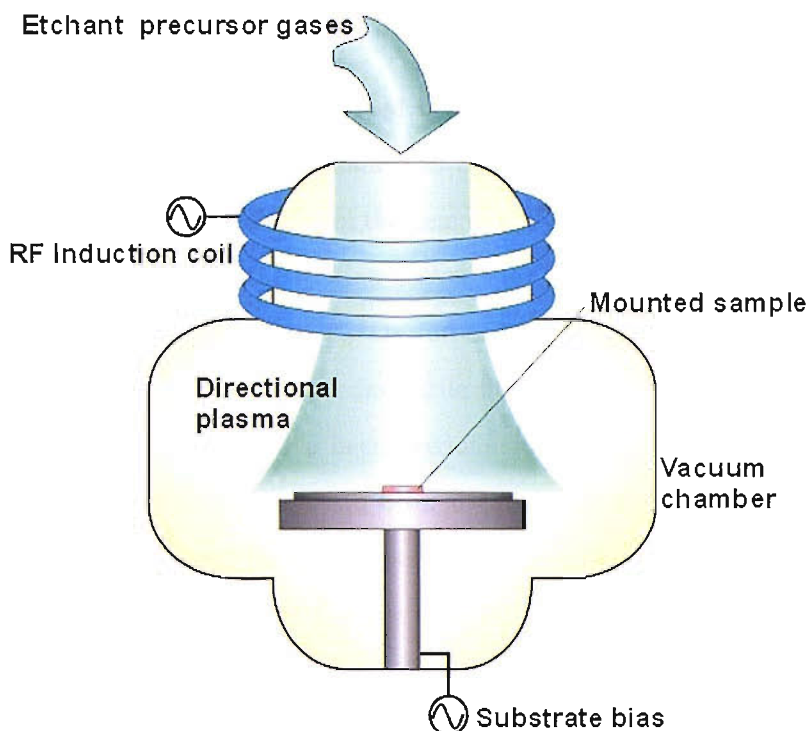

FIGURE 6.16: Schematic of an inductively coupled plasma reactive ion etching chamber. The precursor gases are flowed through an inductive element where a high-density plasma is formed, this is then directed at the backside cooled sample, which is located on an independently RF biased plate. The reactive species in the plasma chemically etch the sample surface.

separate control facilitates highly anisotropic etches as the chemical etching is assisted by the kinetic energy of the incoming ions, and the vertical etch rate far exceeds the horizontal.

The anisotropy of this type of etching is further enhanced by the low pressures used in ICP-RIE as scattering within the gas is minimised. Moreover, this low pressure facilitates some physical sputtering, ideal for removal of nonvolatile products and resist. However, the lower pressure also reduces the effect of convective cooling within the chamber, which can lead to excessive heating of the sample. To overcome this effect, the sample electrode is actively cooled with thermal contact enhanced by helium backside cooling.

6.4.4.2 Southampton-Sheffield ICP Etch Recipe

For the purposes of the etching described in this chapter, a unique etch recipe was required. The first challenge to overcome was that of efficiently etching GaAs. Plasma etching was initially developed to meet the demands of silicon microelectronics processing technology. Consequently, most routine ICP recipes exist for Si etching, and are based on fluorine atom plasmas such as CF_4/O_2 and SF_6/O_2 [35]. GaAs is practically unetchable in these plasmas since it forms involatile fluorides [36]. Furthermore, previously successful GaAs etch recipes have been predominantly based on CCl_2F_2 [37, 38, 39], but these freon-based techniques have been shown to produce etched surfaces lacking the optical quality required for this project [40, 41]: moreover, legislation against the production of CCl_2F_2 means that this gas is no longer a viable option for production of etched GaAs devices.

To overcome these limitations, a recipe based on silicon tetrachloride ($SiCl_4$) was developed. $SiCl_4$ has been used as an etchant for GaAs for some time [42], with its potential for highly anisotropic etches independent of the lattice orientations exposed highlighted at gas pressures lower than 10 mTorr [43]. This is ideal for application to the etching described in this chapter where multiple orientations will be exposed during the etch. The addition of argon has shown further improvements in the orientation independence of the etch particularly at the base of the structure formed [44].

Uniquely, for the fabrication of the devices conceived in this chapter, it is important that there is as close as possible to a 1:1 etch rate between the GaAs and the resist. This poses a problem for the dry etching technique since resists are designed to provide high resistance to etchants. The eventual choice of PMMA 950 resist for the imprinting stage in this chapter had advantages for etch rate since it is notoriously weak as a dry etch resist, and hence gave less selectivity than other resists to the ICP etch. Our trials showed ten times less selectivity for GaAs with PMMA than GaAs with Shipley 1813 resist for the same etch parameters. However, in order to reach 1:1 etch rates further steps had to be taken. In [44], the authors allude to the ability of argon to effectively sputter involatile materials from the sample surface when included in a $SiCl_4$ etch. It

was decided to flow a large amount of Ar into the chamber with the $SiCl_4$ throughout the etching to sputter the PMMA from the sample surface.

The ICP-RIE etching was carried out in an Oxford Plasma Tech Plasma Lab System 100 [45]. A series of experiments were run to determine the etch recipe required to achieve the best compromise between the capabilities of the machine, and the proximity to 1:1 etch rates. The final recipe was carried out at a chamber pressure of 2.4 mTorr, and used 90 W of RF power supplied to the sample holder, 1000 W power supplied to the ICP coil, 10 sccm helium provided for substrate cooling, 4 sccm $SiCl_4$ for etching of the GaAs, and 30 sccm Ar to sputter the PMMA.

The $\sim$5 mm $\times$ 5 mm sample was held onto the centre of a 6-inch Si wafer using fomblin oil. This was loaded into the loading chamber of the ICP system. The loading chamber was then evacuated, and the wafer transferred into the main, evacuated ICP chamber. The resist thickness was monitored using a 980 nm laser interferometer to ascertain when all of the resist had been removed. The etch time varied depending on the number of samples etched at once, since the pressure and active species concentration is affected by the amount of volatile etch by-product present. The pressure limit for the chamber was set to 3 mTorr, and this was not exceeded. For the data presented in this section, the PMMA on n-doped GaAs sample was loaded into the reactor with one other, and the etch time was 11 minutes.

6.4.4.3 ICP Etch Results

The resulting profile is shown in figure 6.17, compared with the original imprint (shown also in figure 6.15). The etch rate was measured to be 3:5 (PMMA:GaAs), and correspondingly, with dimensions of 33.5 μm diameter and 904 nm deep, the focal length of the structure has reduced to 156 μm (from f=191 μm pre-etch). The base profile of the structure has improved, and it is thought that the original structuring may have been a weak region of raised resist that was readily sputtered by the argon, a particulate of contaminant that was dislodged in the pre-etch cleaning stage, or a spurious feature in

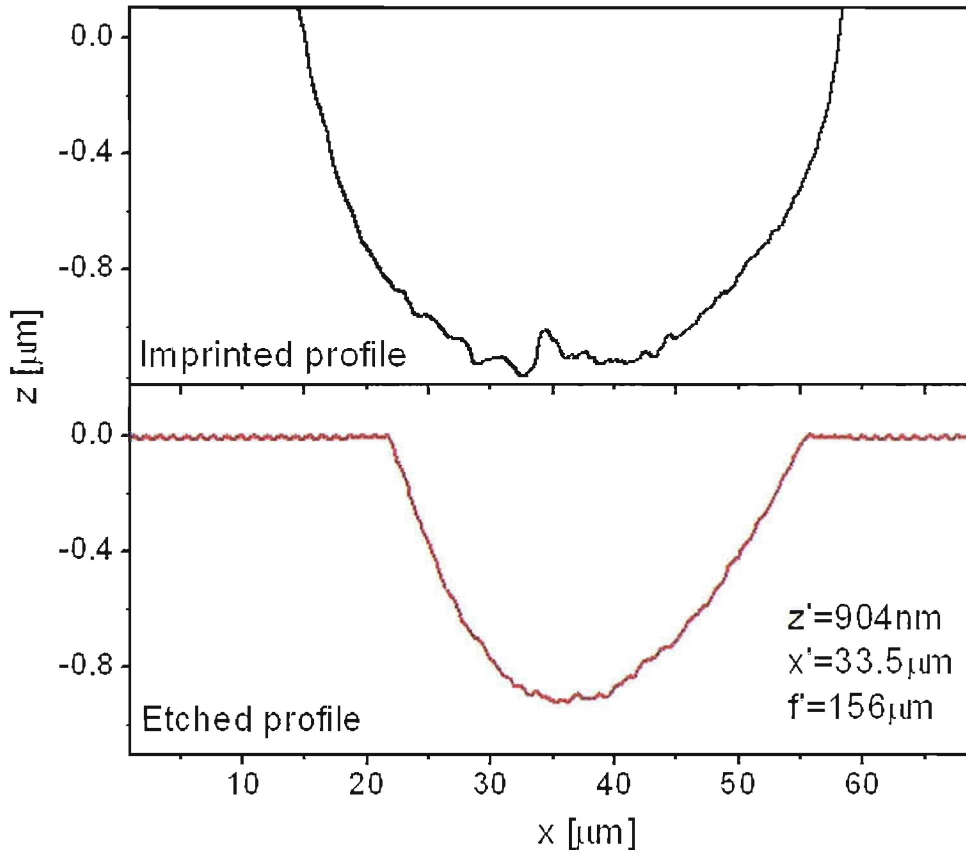

FIGURE 6.17: Profile of ICP etched imprint in GaAs (red) compared with original imprint in PMMA (black - also shown in figure 6.15). Etching was halted before the raised pattern of displaced resist was transferred into the GaAs. The structuring of the base of the imprint observed before etching is eliminated in the etch process.

the original profile. Etching was ceased before all of the PMMA was removed, consequently, the raised pattern of the displaced resist at the edge of the imprint seen in the PMMA is not transferred through to the substrate.

6.5 Overgrowth and Characterisation

Following ICP etching, the sample must be overgrown with the suitable mirror and active layers in order to realise the final device. The project currently lies at this stage. No mirror or active layers have been grown at present, but the structures have been tested for GaAs overgrowth. Results of this overgrowth are detailed in this section.

To our knowledge, this project will be the first time that any structure as complicated as a DBR has been grown on a curved GaAs substrate. There are many factors to consider when attempting the growth, and very little exists in the literature for guidance. In creating a curved structure in the GaAs substrate, other lattice planes and orientations are exposed for which growth rates are different [46]. This may result in a DBR across which the central wavelength of the stopband varies transversely. However, the structures proposed in this thesis have promising dimensions for overgrowth since they are so shallow [47]. Moreover, it may be possible to optimise the growth quality by adjusting machine parameters such as temperature and growth rate [48].

Prior to growth, the samples were cleaned as detailed in section 4.5.2, and then washed with copious amounts of deionised water that had been filtered in an ELGA Purelab UHQ II purifier: the water is pre-purified by reverse osmosis to remove 98% dissolved solids, organics, bacteria and colloids. Then it passes through an organic adsorption process, and an ion exchange stage. Then a 0.05 μm filter cartridge to remove any particulate matter and bacteria, and then a short-wave UV chamber to remove any trace organics through photo-oxidation. The sample is finally dried with a dry nitrogen flow. This renders the surface free of contaminants, and suitable for overgrowth.

Overgrowth was performed at the EPSRC III-V facility in Sheffield by Dr John Roberts and Dr Andrey Krysa. 1 μm of GaAs was grown by MOCVD (see section 3.2) as a test to determine if overgrowth of the structures is possible.

A profile and microscope image of the overgrown structure are shown in figure 6.18. Due to a loss of facilities at Southampton, a KLA Tencor Alphastep 500 located at Merck Chemicals is now used to profile the imprint. It has a needle load of 3.9 mg. The structure is that shown in figures 6.15 and 6.17, and so can be followed through from initial imprinting to etching and finally to overgrowth. Overgrowth appears to be successful: the low resolution data acquisition software used in conjunction with the microscope gives a low resolution profile image in figure 6.18, but direct observation of the microscope image before acquisition showed much higher resolution, and the overgrown structure surface appeared to be smooth; no large defects in the growth were

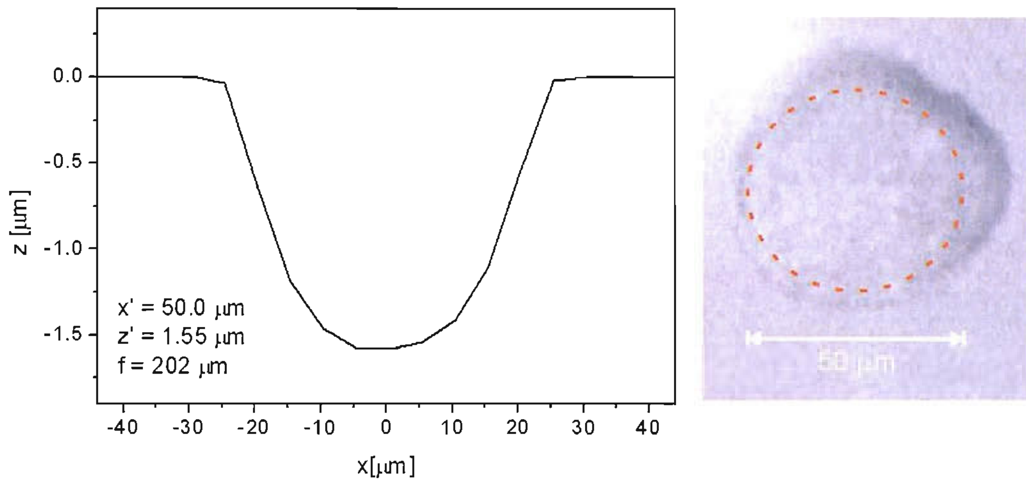

FIGURE 6.18: Profile and microscope image of imprinted n-doped GaAs sample from figure 6.17, overgrown with 1 μm of GaAs. The area profiled is shown with a red dashed line on the microscope image.

observed. The circular imprinted region profiled is indicated by a red circle, 50 μm in diameter, on the microscope image.

The profile shows a spherical shape, with greatly exaggerated z scale to emphasize the good profile. The focal length of the structure is calculated to be 202 μm, close to the 191 μm of the original imprint. The profile is measured to be deeper and wider than pre-overgrowth. It is thought that this discrepancy arises from off-centre profiles being recorded previously. The depth may also be due to a more rapid growth of GaAs on the flat substrate surrounding the imprint than on the imprint itself. No deformation of the imprint from the desired shape has been observed in overgrowth, so it is concluded that the effects of different crystal orientations experiencing different growth rates does not affect the spherical shape of the structure. However, the increase in focal length of the structure is indicative of a decrease in its curvature. This may be due to increased growth rates in the base of the imprint compared with the side-walls. With the use of smaller diameter ball lenses to form the imprint resulting in shorter focal lengths than desired, this effect is advantageous in increasing the focal length of the structure.

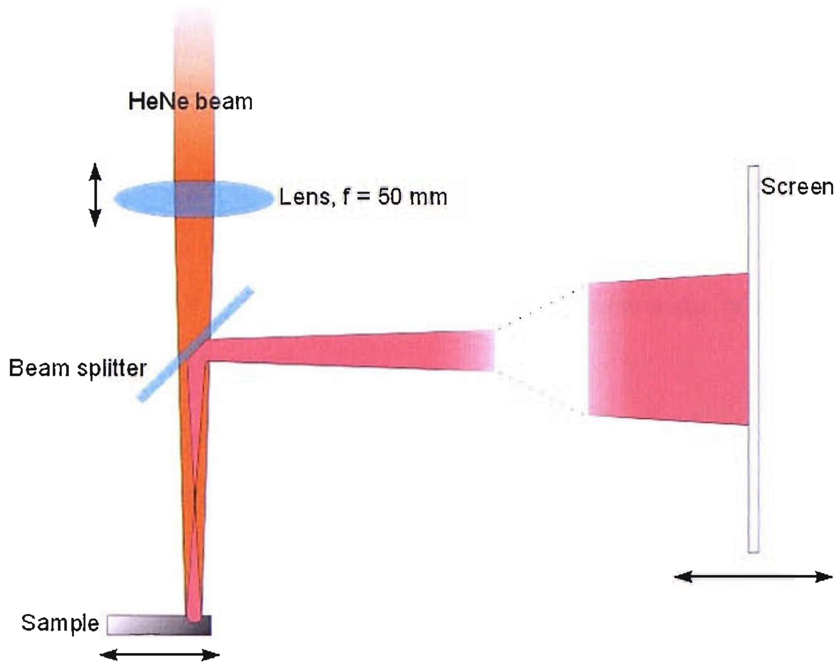

FIGURE 6.19: Experimental setup for optical characterisation of overgrown imprinted GaAs sample. The reflected HeNe beam is projected onto the moveable screen, and measured at two known distances in order to calclate the beam divergence as described in the text.

6.5.1 Optical Characterisation of the Overgrown Structure

In order to ascertain the optical quality of the overgrown structure, a method was devised to analyse its reflection of a focussed helium neon laser (HeNe) beam (λ=632 nm), using the experimental setup shown in figure 6.19. The HeNe was focussed onto the imprinted and overgrown sample using a 50 mm focal length lens, selected to give a beam waist of ω_1=33.5 μm at its focus, close to the dimensions of the structure to be analysed. The sample was positioned normal to the beam on a translation stage at the focus; the surface was observed with a microscope camera, and translated to find the overgrown structure on the surface.

The light reflected and refocussed by the sample was diverted to a moveable screen, positioned at a distance much greater than the Rayleigh distance ($Z_R = \pi\omega_0^2/\lambda$; the order of a few micrometers in this case) from the structure's focus. Thus, for simplicity, all measurements were taken in the far field, where beam divergence after the structure's focus can be assumed linear, and can be written as

$$\theta = \frac{\lambda}{\pi \omega_2}. \tag{6.5.1}$$

Where θ is the half angle of the diverging beam, found by measuring the difference in the beam waist at two positions a relatively large distance apart (Δz=20 cm) on the screen to minimise error in this measurement. ω_2 is the new waist of the beam focussed by the structure.

Since the structure is positioned at the focus of the HeNe, the calculation of its focal length is greatly simplified; the properties of the incident beam need not be included, only the waist size at the HeNe focus (ω_1) is required. The focal length (f) is then calculated using the following Gaussian optics equation:

$$f = \frac{\omega_1 \omega_2 \pi}{\lambda}. \tag{6.5.2}$$

This yielded an experimental value of f = 234 μm for the structure, close to the value of 202 μm measured from the overgrown imprint.

A photograph of the image produced by the structure on the screen is shown in figure 6.20. The focusing effect of the structure could be easily identified by slightly translating the sample, moving the structure out of the HeNe focus (figure 6.20b), and observing the changes in the reflected beam. When centred on the structure (figure 6.20a), the image shows the central circular beam reflected by the structure. Concentric rings are also observable around the edge of the central spot, thought to be caused by divergence from the edges of the structure since the focussed beam is of similar dimensions to the structure.

A beam profile of the reflected beam was taken to ascertain surface quality of the structure through its ability to reflect a Gaussian beam. The x and y profiles are shown in figure 6.21. There is little discrepancy between them indicating that the structure has neglegible astigmatism. Both show a smooth, Gaussian profile, indicating that the structure is of high spherical quality and has not distorted the beam greatly. The fringes observed on the screen are identifiable in the beam profiles.

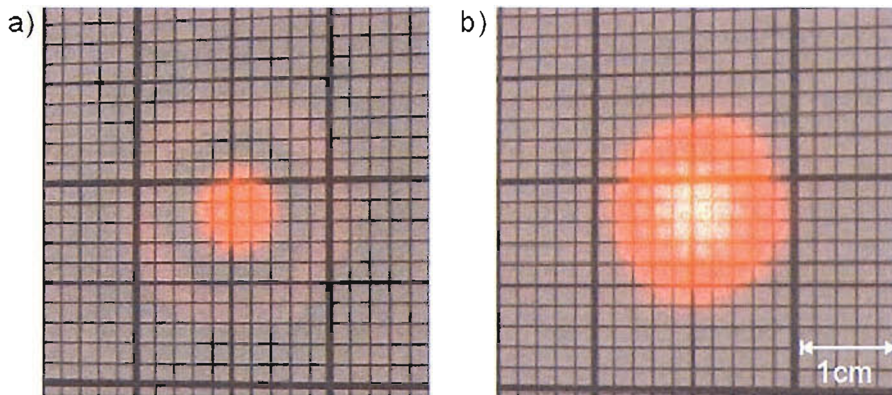

FIGURE 6.20: Photographs of the images produced by the reflected beam when projected onto the screen at an arbitrary distance from the sample when a) the HeNe is focussed on the structure, and b) when the structure is moved out of the focus. Note the rings present in a) that result from diffraction from the edges of the structure.

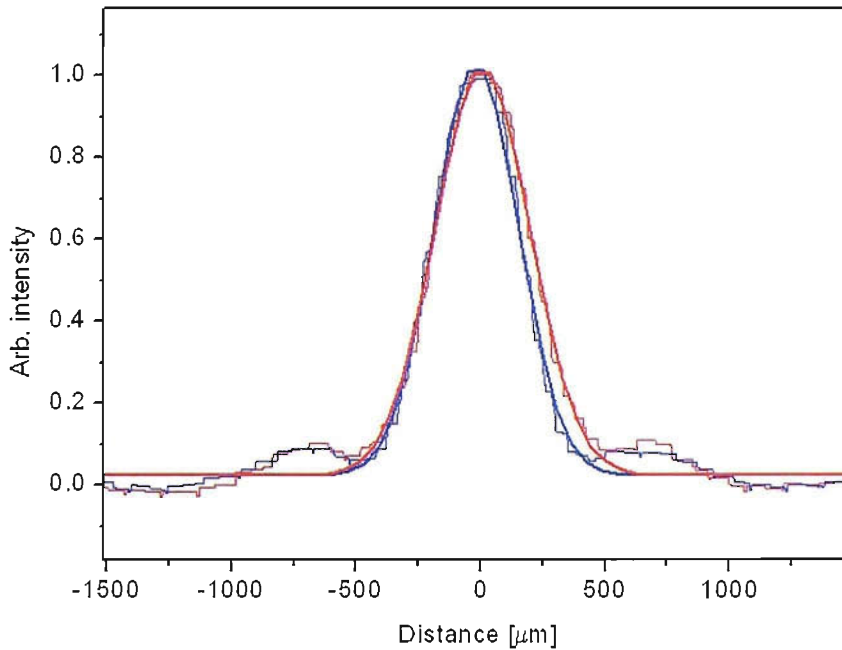

FIGURE 6.21: Spatial beam intensity profiles of HeNe beam reflected by the imprinted and overgrown structure taken at an arbitrary distance from the sample. The x-profile is shown in red and the y-profile in blue with corresponding Gaussian fits in bold. Steps in the collected data are factors of the beam detector itself due to the low intensity of the reflected beam, and are not real features caused by the structure.

6.6 Focusing Gain Region VECSEL Device Outlook

The next step in this project is to MOCVD-grow an antiresonant VECSEL gain structure of the design detailed in 2.2.3.2 suitable for Stark mode-locking on top of the patterned GaAs. Transverse characterisation of the reflectivity of the DBR can then be carried out to ascertain the growth variation across the structure from the shift in central wavelength of the DBR stopband. If the currently achieved curved structure dimensions are used (as in figure 6.18), pumping of a ~30 μm diameter spot by a Ti:Sapphire laser could be employed. The photoluminescence of the structure can be characterised and CW lasing achieved as in chapter 3.

6.6.1 Mode-Locking of the focusing Gain Region VECSEL

In order to Stark mode-lock the high repetition rate laser, the limits discussed in section 6.2.3 must be considered. The parameters outlined in section 6.2.3 for a Stark mode-locked laser with 500 fs pulses give a pulse overlap limit of 360 GHz repetition rate, but more significantly, the SESAM recovery time limit is reached first, at 250 GHz, corresponding to a 4 ps recovery time. The other important factor to consider is that of SESAM saturation since as repetition rate increases, the energy per pulse decreases, decreasing the fluence upon the SESAM until the point where it is no-longer possible to saturate the SESAM.

6.6.1.1 Saturation Fluence Considerations

The saturation fluence of a Stark SESAM has been measured to be 56 μJ/cm^2 [49]. In a 1 GHz cavity such as that presented in section 2.4.2, with for example, 30 mW average output power, and 0.7% output coupling, the pulse peak energy incident on the SESAM in a typical 30 μm diameter spot corresponds to a fluence of 606 μJ/cm^2. This is far above the 56 μJ/cm^2 saturation fluence of the SESAM. At 10 GHz, as presented in section 6.2.1, the fluence is correspondingly 60.6 μJ/cm^2 in the same 30 μm diameter spot, still saturating the SESAM. However, at 100 GHz, assuming 30 mW average output power, a spot diameter of 30 μm on the SESAM gives a fluence of just 6.06 μJ/cm^2.

This is not sufficient to saturate the SESAM. A spot size of just 5.6 μm diameter is required to reach the SESAM saturation fluence at 30 mW average output power, or an increase of average output power to 277 mW for a 30 μm diameter spot.

It should be remembered that the etched and overgrown structure presented in 6.18 does not possess the desired focusing properties for a 100 GHz laser. With a focal length of 202 μm, using the ABCD matrix calculations of cavity stability shown in appendix B, graphs are obtained for the stability of the cavity, and corresponding SESAM spot sizes. These are shown in figure 6.22.

The stability calculations show that the more desirable, small spot sizes are achievable at the edge of the cavity stability. At a cavity length of 0.35 mm, the corresponding round trip length is 0.7 mm, giving a repetition rate of 430 GHz. The corresponding waist radius on the SESAM is 6.75 μm, giving a fluence of 6.97 $\mu J/cm^2$ at 30 mW average power, much lower than the 56 $\mu J/cm^2$ required to saturate. Moving out to 0.40 mm cavity lengths, with a corresponding round trip length of 0.80 mm, and repetition rate of 375 GHz, the waist size becomes 3.64 μm radius, corresponding to a fluence of 27.4 $\mu J/cm^2$, still not adequate to saturate the Stark SESAM. Moreover, these cavity lengths are too short, with high repetition rates that are above the threshold for SESAM recovery time (250 GHz), preventing the SESAM from fully recovering before the next pulse arrives. Also, they lie just above the threshold for pulse overlap (360 GHz). Hence, in order to use this etched and overgrown device in a high repetition rate Stark mode-locked VECSEL cavity, design of a modified, reduced saturation fluence Stark SESAM with a faster recovery time, and sub-500 fs pulses must be implemented.

6.6.2 Future steps for the High Repetition Rate Stark ML-VECSEL project

The future steps for this project are clear: a longer cavity design, enabled by a longer focal length imprinted structure closer to the dimensions initially proposed in this work (figure 6.4) provides lower repetition rates, and hence would allow mode-locked operation below the thresholds for pulse overlap and SESAM recovery, but above 100 GHz. The problems of SESAM saturation for a device of these dimensions were outlined in section

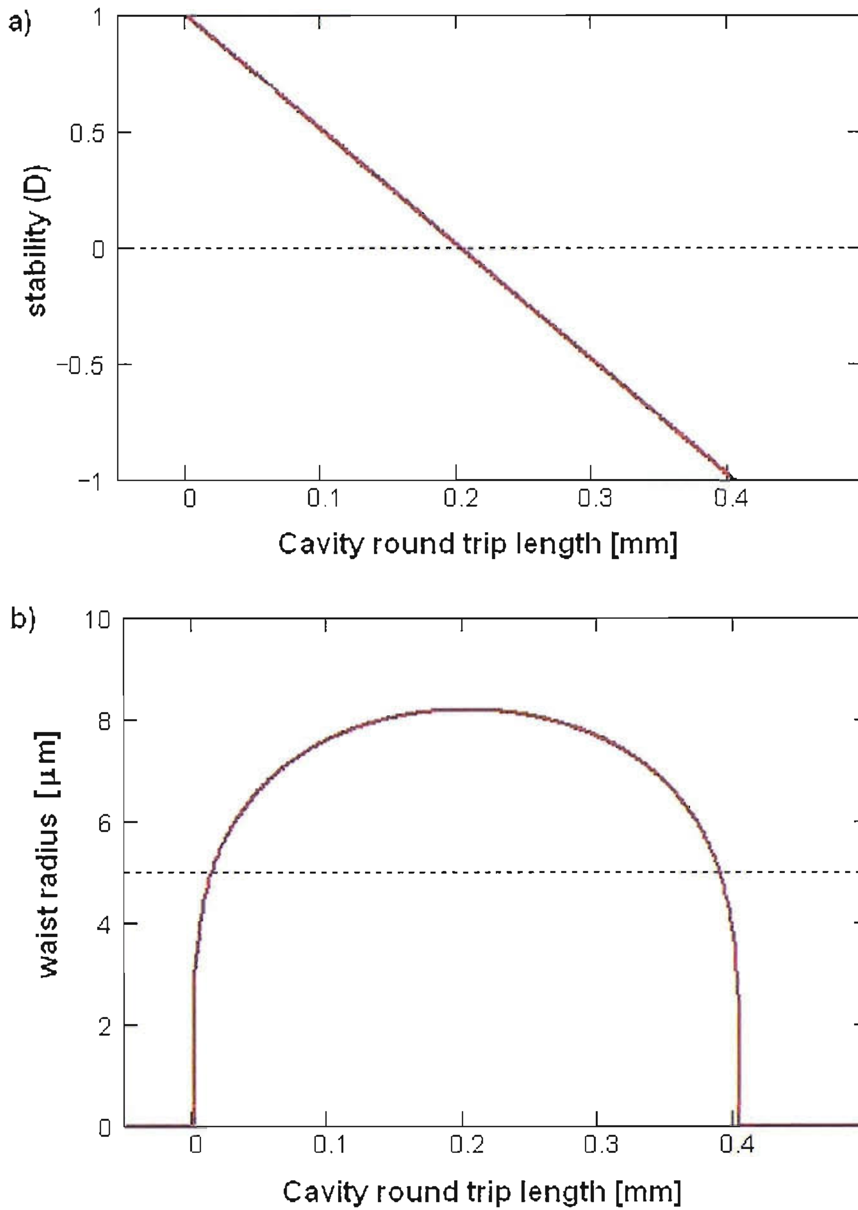

FIGURE 6.22: Graphs to show the stability calculations for the overgrown imprint shown in figure 6.18 as a function of cavity length, and corresponding SESAM spot sizes. Note that the required focusing to small spot sizes is achievable only at the edge of the cavity stability.

6.6.1.1. The stability calculation for a cavity incorporating the proposed f = 1.5 mm structure, shown previously in figure 6.5, indicates that focusing to spot radii smaller than 10 μm is possible, a corresponding average power of approximately 100 mW would be required to saturate the current Stark SESAM in this cavity. The thermal management methods introduced in section 4 could be employed to reach these higher average powers, increasing the fluence on the SESAM accordingly. Moreover, further increases in average output power could also be accessed through more careful epitaxial growth of the active structures in the first instance.

Modifications to the SESAM design could raise the thresholds of SESAM recovery and pulse overlap to higher repetition rates, allowing the device to be constructed using the existing overgrown structures. Such a SESAM would incorporate some of the features suggested in section 2.4.2.3. The window layer of the SESAM structure could be designed to have a lower bandgap than that of the spacer layer. This would encourage carriers out of the quantum well, and to the sample surface, enhancing the surface fast recombination effect, encouraging a faster recovery of the SESAM [50]. The quantum well could be moved closer to an E-field resonance to increase the SESAM modulation depth, increasing the strength of the SESAM's pulse shaping effect, and hence decreasing the pulse length [51].

Further improvements in SESAM design could also be made by implementing some of the techniques presented in [52] for decreasing the saturation fluence of SESAM structures. The 'low-field-enhancement resonant-like SESAM device' (LOFERS) [53] structure implements a DBR top layer extended by one quarter wave, to increase the cavity enhancement factor inside the SESAM, making the E-field intensity inside the SESAM almost equal to that outside of the structure, more like a resonant system, 11 times more than that of a classical SESAM device. Consequently, the saturation fluence of this device should be 11 times lower than a classical SESAM. In the Stark SESAM, this idea of closer to resonant operation is implemented in the same way as increasing the modulation depth of the SESAM; by altering the thickness of the front spacer layer to move the quantum well closer to the peak of the intensity inside the microcavity.

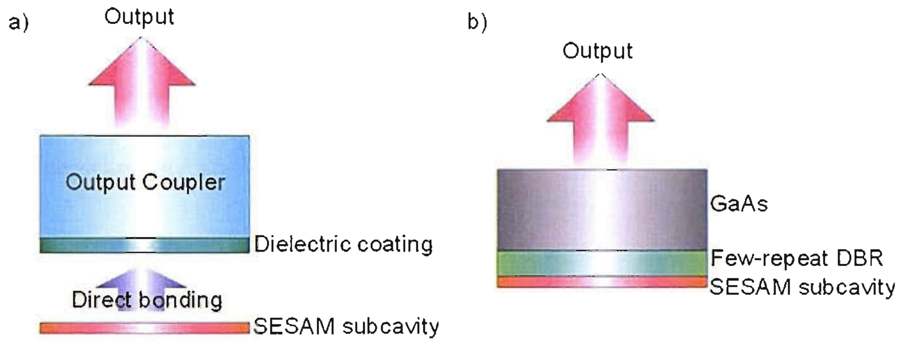

FIGURE 6.23: Schematics of the SESAM output coupler devices conceived for completion of the high repetition rate VECSEL cavity proposed in this chapter. a) Shows the concept of directly bonding the appropriate epitaxially lifted off absorber layers onto an appropriate dielectric mirror. b) Shows the concept of a reduced reflectivity DBR SESAM where the amount of output coupling depends on the number of repeats of the DBR.

6.6.2.1 SESAM Output Coupler

The requirements of the high repetition rate cavity proposed in this chapter dictate that the output coupler must also incorporate the saturable absorber. Two configurations in which this is possible are considered briefly here, and shown in figure 6.23: firstly, the SESAM spacer layer, quantum well, and window layer could be epitaxially lifted from the substrate as in [54], and bonded directly onto the output coupler which already has the appropriate dielectric coating [55] (figure 6.23a). Secondly, the SESAM structure could be re-designed with a modified DBR with fewer repeats to give a lower reflectivity. This would enable some output coupling through the back of the DBR (figure 6.23b). The amount of output coupling would be determined by the number of DBR repeats.

Two output coupling devices are considered for the high repetition rate devices proposed in this thesis. They were shown schematically in figure 6.3. The first (figure 6.3a) uses a free-space output coupler. This could be replaced by the output coupling DBR SESAM, or indeed, the output coupler could have the relevant dielectric coatings deposited, and the epitaxially lifted SESAM spacer layers and quantum well directly bonded. For the fiberised output coupler with pump delivery down the fibre, shown in figure 6.3b, it is not so simple. Since the pump light is launched through the output coupler, the modified DBR SESAM is not suitable as the majority of the pump will be absorbed by the GaAs substrate and the GaAs in the DBR, preventing efficient pumping of the

gain sample, and causing excessive heating of the SESAM structure, so the epitaxially lifted and re-bonded structure would be required. Of course, there will also be some absorption in the spacer layers of the epitaxially lifted off structure, but this would be negligible since the GaAs would be so thin.

6.7 Conclusion

A micro-imprint lithography technique has been developed for the fabrication of curved, optical quality structures in GaAs substrates, suitable for overgrowth with the appropriate layers to create focusing active mirror structures for incorporation in high repetition rate Stark mode-locked VECSEL cavities. The technique involves the imprinting of PMMA resist, followed by transferral of the imprinted structure into the GaAs substrate below, and finally overgrowth of the structure with the appropriate epitaxial layers. So far, structures with focal lengths of $\sim$200 μm have been successfully overgrown with GaAs buffer layers, demonstrating the feasibility of the technique. The routes taken to develop the technique have been documented in this chapter.

The limitations of pulse overlap, SESAM recovery, and SESAM saturation have been identified for the proposed high repetition rate devices, and threshold values calculated for the range of devices discussed. In order to realise a high repetition rate VECSEL using the imprinted and overgrown structures, it is necessary to either produce structures with longer focal lengths, or modify the Stark SESAM to permit higher repetition rates. Possible methods for this are proposed. This includes implementation of a modified Stark SESAM design, with the quantum well located closer to a peak in the field intensity within the microcavity of the SESAM to increase the modulation depth of the device leading to stronger pulse shaping, and shorter pulses, and also to a reduced saturation fluence of the SESAM. Also, methods to reduce the recovery time of the SESAM by encouraging faster surface recombination times through reduction of the bandgap of the window layer material are suggested. Increases of the average output power, and hence the fluence on the SESAM are proposed through the thermal management techniques

introduced in Chapter 4. Finally, designs to obtain the necessary SESAM output coupler device have been conceptualised.

These devices have the potential to generate very stable, ultra-high repetition frequency trains of ultrashort pulses from a compact, cheap package, with the advantages of the excellent beam quality attributed to VECSELs. Such a source would be an attractive alternative to unstable harmonically mode-locked sources, and expensive solid state devices currently used for high-bit-rate data transmission, optical clocking, and even high-throughput materials processing.

Bibliography

[1] Miller, D. A. B. Optics for low-energy communication inside digital processors: quantum detectors, sources, and modulators as efficient impedance converters. *Optics Letters* **14**, 146–148 (1989).

[2] Krainer, L. *et al.* Compact Nd:YVO_4 lasers with pulse repetition rates up to 160 GHz. *IEEE Journal of quantum electronics* **38**, 1331–1338 (2002).

[3] Hinton, G. *et al.* The microarchitecture of the pentium 4 processor. *Intel Technology Journal* **5**, 1–13 (2001).

[4] Usechak, N. G., Agrawal, G. P. & Zuegel, J. D. Tunable, high-repetition-rate, harmonically mode-locked ytterbium fiber laser. *Optics Letters* **29**, 1360–1362 (2004).

[5] Yoshida, E. & Nakazawa, M. 80 200 GHz erbium doped fibre laser using a rational harmonic mode-locking technique. *Electronics Letters* **32**, 1370–1372 (1996).

[6] Guina, M. & Okhotnikov, O. G. Harmonically mode-locked laser stabilized by semiconductor saturable absorber modulated with the residual pump. *Applied Physics B: Lasers and Optics* **75**, 127–130 (2002).

[7] Wu, C. & Dutta, N. K. High-repetition-rate optical pulse generation using a rational harmonic mode-locked fiber laser. *IEEE Journal of Quantum Electronics* **36**, 145–150 (2000).

[8] Horowitz, M., Menyuk, C. R., Carruthers, T. F. & Duling, I. N. Pulse dropout in harmonically mode-locked fiber lasers. *Intel Technology Journal* **12**, 266–268 (2000).

[9] Krainer, L., Paschotta, R., Moser, M. & Keller, U. 77 GHz soliton modelocked Nd:$YV0_4$ laser. *Electronics Letters* **36**, 1846–1848 (2000).

[10] Spühler, G. *et al.* 40 GHz pulse generating source with less than 350 fs timing jitter. *Electronics Letters* **38**, 1031–1033 (2002).

[11] Zeller, S. C. *et al.* Passively mode-locked 40-GHz Er:Yb:glass laser. *Applied Physics B: Lasers and Optics* **76**, 787–788 (2003).

[12] Wilcox, K. G., Foreman, H. D., Roberts, J. S. & Tropper, A. C. Timing jitter of 897 MHz optical pulse train from actively stabilised passively modelocked surface-emitting semiconductor laser. *IEEE Journal of Quantum Electronics* **42**, 159–160 (2006).

[13] Hoogland, S. *et al.* Passively mode-locked diode-pumped surface-emitting semiconductor laser. *IEEE Photonics Technology Letters* **12**, 1135–1137 (2000).

[14] Garnache, A. *et al.* Sub-500-fs soliton-like pulse in a passively mode-locked broadband surface-emitting laser with 100 mW average power. *Applied Physics Letters* **80**, 3892–3894 (2002).

[15] Häring, R. *et al.* Picosecond surface-emitting semiconductor laser with >200mW average power. *Electronics Letters* **37**, 766–767 (2001).

[16] Hoogland, S., Garnache, A., Sagnes, I., Roberts, J. S. & Tropper, A. C. 10-GHz train of sub-500-fs optical soliton-like pulses from a surface-emitting semiconductor laser. *IEEE Photonics Technology Letters* **17**, 267–269 (2005).

[17] Hoogland, S., Roberts, J. S. & Tropper, A. C. Soliton operation of a sub-500fs passively mode-locked surface-emitting laser at more than 10 GHz repetition rate. In *Conference on Lasers and Electro-Optics (CLEO) US 2003 (Postdeadline session)* (Baltimore, U.S.A., 2003).

[18] Aschwanden, A. *et al.* 10 GHz passively mode-locked external-cavity semiconductor laser with 1.4 W average output power. *Applied Physics Letters* **86**, 131102 (2005).

[19] Jasim, K. *et al.* Picosecond pulse generation from passively modelocked vertical cavity diode laser at up to 15 GHz pulse repetition rate. *Electronics Letters* **40**, 34–36 (2004).

[20] Unold, H. J. *et al.* 50-GHz mode-locked vecsels: An integrable alternative to high-repetition-rate solid-state lasers. In *Advanced Solid State Photonics (ASSP) 2006*, TuA2 (Lake Tahoe, U.S.A., 2006).

[21] Garnache, A. *et al.* Pico-second passively mode locked surface-emitting laser with self-assembled semiconductor quantum dot absorber. In *Conference on Lasers and Electro-Optics (CLEO) Europe 2001*, 130 (Munich, Germany, 2001).

[22] Lorenser, D. *et al.* Towards wafer-scale integration of high repetition rate passively mode-locked surface-emitting semiconductor lasers. *Applied Physics B: Lasers and Optics* **79**, 927932 (2004).

[23] Hönninger, C., Paschotta, R., Morier-Genoud, F., Moser, M. & Keller, U. Q-switching stability limits of continuous-wave passive mode locking. *Journal of the Optical Society of America B* **16**, 46–56 (1999).

[24] Williams, R. *Modern GaAs processing techniques* (Artech House Inc., 1990), second edn.

[25] Chou, S. Y., Krauss, P. R. & Renstrom, P. J. Imprint of sub-25 nm vias and trenches in polymers. *Applied Physics Letters* **67**, 3114–3116 (1995).

[26] Chou, S. Y., Krauss, P. R. & Renstrom, P. J. Nanoimprint lithography. *Journal of Vacuum Science and Technology B* **14**, 4129–4133 (1996).

[27] Tan, H., Gilbertson, A. & Chou, S. Y. Roller nanoimprint lithography. *Journal of Vacuum Science and Technology B* **16**, 3926–3928 (1998).

[28] Yu, Z., Gao, H., Wu, W., Ge, H. & Chou, S. Y. Fabrication of large area subwavelength antireflection structures on Si using trilayer resist nanoimprint lithography and liftoff. *Journal of Vacuum Science and Technology B* **21**, 2874–2877 (2003).

[29] Zhang, W. & Chou, S. Y. Multilevel nanoimprint lithography with submicron alignment over 4 in. Si wafers. *Applied Physics Letters* **79**, 845–846 (2001).

[30] Li, M., Chen, L., Zhang, W. & Chou, S. Y. Pattern transfer fidelity of nanoimprint lithography on six-inch wafers. *Nanotechnology* **14**, 3336 (2002).

[31] Li, M., Tan, H., Kong, L. & Koecher, L. Four-inch photo-curable nanoimprint lithography using NX-2000 nanoimprintor. In *Emerging Lithographic Technologies VIII*, 209–212 (Santa Clara, California, USA, 2004).

[32] Tan, H., Kong, L., Li, M., Steere, C. & Koecher, L. Current status of nanonex nanoimprint solutions. In *Emerging Lithographic Technologies VIII*, 213–221 (Santa Clara, California, USA, 2004).

[33] Guo, L. J. Recent progress in nanoimprint technology and its applications. *Journal of Physics D: Applied Physics* **37**, R123 R141 (2004).

[34] Chestech Ltd. Website (2003-2005). URL `http://www.chestech.co.uk/950Aspinspeed.pdf`.

[35] Vossen, J. L. & Kern, W. *Thin Film Processes* (Academic Press Inc., 1978).

[36] Smolinsky, G., Chang, R. P. & Mayer, T. M. Plasma etching of III-V compound semiconductor materials and their oxides. *Journal of Vacuum Science Technology* **18**, 12–16 (1981).

[37] Donnelly, V. M. & Flamm, D. L. Anisotropic etching in chlorine-containing plasmas. *Solid State Technology* **April**, 161–166 (1981).

[38] Hu, E. L. & Howard, R. E. Reactive-ion etching of GaAs and InP using $CCl_2F_2/Ar/O_2$. *Applied Physics Letters* **37**, 1022–1024 (1980).

[39] Klinger, R. E. & Greene, J. E. Reactive ion etching of GaAs in CCl_2F_2. *Applied Physics Letters* **38**, 620–622 (1981).

[40] Rawal, D. S. *et al.* Anisotropic etching of GaAs using CCl_2F_2/CCl_4 gases to fabricate 200 μm deep via holes for grounding MMICs. *Journal of the Electrochemical Society* **150**, G395–G399 (2003).

[41] Rawal, D. S. *et al.* Study of reactive ion etching process to fabricate reliable via-hole ground connections in GaAs MMICs. In *International Conference on Compound Semiconductor Manufacturing Technology* (CS Mantech, 2004).

[42] Stern, M. B. & Liao, P. F. Reactive ion etching of GaAs and InP using $SiCl_4$. *Journal of Vacuum Science and Technology B: Microelectronics and Nanometer Structures* **1**, 1053–1055 (1983).

[43] Li, J. Z., Adesida, I. & Wolf, E. D. Orientation dependent reactive ion etching of GaAs in $SiCl_4$. *Applied Physics Letters* **45**, 897–899 (1984).

[44] Sonek, G. J., Wolf, E. D., Ballantyne, J. M. & Li, J.-Z. $SiCl_4$ reactive ion etching for GaAs optical waveguides. *Journal of Lightwave Technology* **LT-3**, 1147–1150 (1985).

[45] Oxford instruments plc. Website (1996-2005). URL `http://www.oxinst.com/`.

[46] Yoshikawa, A. *et al.* A self-aligned ridge substrate laser fabricated by single-step MOVPE. *Journal of Crystal Growth* **93**, 843–849 (1988).

[47] Roberts, J. Private communication (2005).

[48] Gregušová, D. *et al.* Investigation of the GaAs-pyramids overgrowth using MOCVD. *Journal of Crystal Growth* **248**, 417420 (2003).

[49] Grange, R. Nonlinear optical characterization of the SESAM QT1627 (2005). Private communication.

[50] Garnache, A., Sermage, B., Teissier, R., Saint-Girons, G. & Sagnes, I. A new kind of fast quantum-well semiconductor saturable absorber mirror with low losses for ps pulse generation. In *IEEE IndiumPhosphide-Realted-Materials*, 247–250 (Santa-Barbara, CA, USA, 2003).

[51] Keller, U. *et al.* Semiconductor saturable absorber mirrors (SESAMs) for femtosecond to nanosecond pulse generation in solid-state lasers. *IEEE Journal of Selected Topics in Quantum Electronics* **2**, 435–453 (1996).

[52] Spühler, G. J. *et al.* Semiconductor saturable absorber mirror structures with low saturation fluence. *Applied Physics B: Lasers and Optics* **81**, 27–32 (2005).

[53] Weingarten, K. J., Spühler, G. J., Keller, U. & Krainer, L. GigaTera AG. U.S. Patent 6,538,298 B1 (2003).

[54] Yablonovitch, E., Gmitter, T., Harbison, J. P. & Bhat, R. Extreme selectivity in the lift-off of epitaxial GaAs films. *Applied Physics Letters* **51**, 2222–2224 (1987).

[55] Yablonovitch, E., Hwang, D. M., Gmitter, T. J., Florez, L. T. & Harbison, J. P. Van der Waals bonding of GaAs epitaxial liftoff films onto arbitrary substrates. *Applied Physics Letters* **56**, 2419–2421 (1990).

Chapter 7

Conclusions

The work of this thesis has been dedicated to the optimisation of passively mode-locked VECSELs. Design and characterisation of suitable gain samples and SESAMs has been documented with particular emphasis on their application to mode-locked operation. Optimisation of ML-VECSEL performance through post-growth processing of gain and SESAM chips has been investigated. The suitability of ML-VECSELs as seeds for high power MOPAs has been assessed with promising results. And the processing steps to achieving a high repetition rate VECSEL have been developed.

7.1 Characterisation of VECSEL Samples

In chapter 3 the methods used in this thesis to characterise VECSEL samples were outlined, employing the techniques described in [1]. Examples of experimental application of each technique to various samples used throughout the work presented were shown. Reflectivity spectra were taken to assess the quality of the DBR mirror of the sample, and identify the microcavity resonance wavelength. Typical reflectivities of >99.9% were measured over a broad stopband from 1000-1100 nm. Photoluminescence collected from the side of the sample was analysed in order to directly probe the emission characteristics of the quantum wells, free from structural modulations, to assess whether they were grown with suitable detuning from the design and lasing wavelength, and characterise the shift of this wavelength with temperature and incident pump power, typical shifts of

0.03 nm/K were measured. Photoluminescence was also collected from the front surface of the sample to analyse the emission of the whole sample incorporating the modulation effects of the structure; data were collected for varying temperatures and pump powers again, to assess the corresponding spectral shifts, measured typically to be 0.1 nm/K, highlighting the requirement for QW wavelength detuning from that of the structure in design to allow for heating of the structure under pumping conditions. PL power data were also collected, and the quantum efficiency of the sample was calculated from this, and found to be ~0.5.

Finally, CW lasing experiments are carried out with the gain chip held at incremental temperatures. Data were collected from these characterisations to enable asses

7.2 Post-Growth Processing of VECSELs

Wafer fabrication techniques employed in this thesis as possible routes to achieving improved lasing characteristics were presented in chapter 4. Undesirable satellite pulses observed in the pulse autocorrelation of an un-processed Stark ML-VECSEL, corresponding to sample back-surface reflections, were successfully eliminated through angle polishing of the back surface of the gain and SESAM chips.

Thermal management of VECSELs is key to the realisation of higher power devices, and improved slope efficiencies. Two approaches to thermal management were attempted as part of this thesis: direct bonding to an intra-cavity heat spreader window, and substrate removal. In initial trials, samples of GaAs substrate were successfully bonded to Sapphire heat spreaders, however, no successful bonds to active samples were obtained. It was proposed that this was a result of surface degradation of the active samples available preventing a successful bond.

A reverse-growth VECSEL gain sample was processed to remove the bulky GaAs substrate, and directly solder the back of the DBR to a heat-sink. Successful lasing was achieved with the processed sample, and although the operation was not optimal due to poor growth, the characteristic temperature of the sample was calculated, and shown to be greatly improved over that of an unprocessed sample of the same design at a value

of T_0=171 K (c.f. 95 K pre-processing), and comparable to that of optimised strained InGaAs QW-diodes.

7.3 Fibre Amplification of VECSEL Pulses

The application of ML-VECSELs as seeds for Yb-doped fiber amplifiers was investigated in chapter 5. The ML-VECSEL is well suited to this application, not only because of its favorable pulse properties over other semiconductor sources, but also for the ease with which the high quality output beam may be launched into the core of a single mode fibre. The high peak power pulses from such a source may find application in fields such as materials processing, THz generation, and optical clocking.

Preliminary experiments were carried out using a single-stage Yb-doped fibre amplifier configuration, identifying the need for longer wavelength emission from the VECSEL seed in order to efficiently access the emission cross-section of the fibres employed, which are designed for λ=1060 nm operation. A suitable long-wavelength seed was constructed and lased at λ=1055 nm; no Stark-SESAMs were available at this wavelength, hence, the pulses produced were of picosecond length. However, this ML-VECSEL was successfully used to seed a 2-stage master oscillator power amplifier. Pulses were amplified to 184 W average power with some temporal broadening to a 6 ps pulse duration due to chromatic dispersion. Dramatic spectral broadening to $\Delta\lambda$=9 nm was observed as a result of self-phase modulation, making the output pulses ideal for external compression. Pulse lengths of <300 fs were achieved after compression in a bulk-grating pair, demonstrating the suitability of this technique for achieving high peak power, high repetition rate, femtosecond pulses.

7.4 High Repetition Rate VECSELs

Because of the compactness of the cavity elements, resilience against Q-switching instabilities in ML-operation, and the inherent tailorability of the external cavity, ML-VECSELs have been identified as suitable sources of high repetition rate, pulsed output,

suitable for applications such as optical clocking of highly integrated circuits. Chapter 6 presented the methods developed in this thesis as a route to realising such a VECSEL. Limitations of the maximum achievable repetition rates were discussed, highlighting the problems of pulse overlap, and issues relating to SESAM recovery time as possible problems for such high repetition rate lasers.

The challenges to achieving such a device were discussed, highlighting the necessity for integration of cavity components in order to reach the millimeter-scale cavity lengths required to access desired repetition rates above 100 GHz. The major problem encountered in this integration is the need for intracavity focusing on the SESAM to achieve a smaller modal size there than on the gain chip and ensure that the SESAM saturates before the gain to create the window of net gain that permits the pulse to oscillate, and shapes it. Fabrication of a focusing gain structure was suggested as a solution to this problem, incorporated in a cavity with a Stark SESAM output coupler. Focusing on the SESAM to achieve a smaller modal size there than on the gain chip and ensure that the SESAM saturates before the gain to create the window of net gain that permits the pulse to oscillate, and shapes it. Fabrication of a focusing gain structure was suggested as a solution to this problem, incorporated in a cavity with a Stark SESAM output coupler.

A method for fabricating such a curved structure in GaAs was devised, using a micro-imprint technique. Some overgrowth of the fabricated structures was achieved, giving promising results. The structures produced had shorter than desired focal lengths, and the likely repetition rates they may produce in a cavity were calculated to be above both the thresholds for pulse overlap and incomplete SESAM recovery. Methods to achieve the Stark SESAM output coupler were also proposed.

7.5 Future Work

The work contained in this thesis provides key foundations in the development and application of ML-VECSELs. Thermal management of VECSELs is now an integral part of many of the current devices, both through integration of heatspreader windows, and

substrate removal; it is clear that such techniques could be instrumental in improving the performance of the devices presented in this thesis, and should be implemented in future devices, allowing higher powers to be reached, and lasing efficiencies to be improved.

The successful demonstration of the use of a ML-VECSEL to seed a high power fibre amplifier provides several avenues of further investigation. The gratings used in the experiments described in this thesis for external compression had low damage thresholds, and high losses, a more optimal grating pair could be sourced to allow compression of the total power emitted by the VECSEL-MOPA to fs-pulses. Polarisation-maintaining fibres were proposed to overcome the problem of polarisation switching in the pre-amplifier that lead to critical damage of the final amplifier stage in the experiments described, and the need for a pre-amplifier designed for shorter wavelength amplification of Stark-ML pulses was identified. The possibility of accessing the parabolic amplification regime using a 500 fs-pulsed VECSEL to seed a MOPA was discussed, and since the work of this thesis, such amplification has been demonstrated giving 100 fs pulse lengths after compression [2]. Moreover, the powers achieved in the pre-amplification stage alone are sufficient for application to some short-pulsed work, so it is possible to conceive a single-stage fibre amplified VECSEL emitting 1 W of average power in femtosecond pulses.

For the high repetition rate VECSEL, further optimisation of the micro-imprint technique to produce the desired focal-length structures must be performed. Alternatively, a suitably short recovery-time SESAM capable of producing shorter pulses could be designed. Successful overgrowth of a complete VECSEL structure must also be completed. Routes to fabricating a SESAM-output-coupler were suggested, such a device must be fabricated in order to realise a final high-repetition rate VECSEL device via the design proposed in this thesis.

The techniques and experiments presented in this work are concentrated on VECSELs operating in the 1 μm spectral region. However, it is intuitive that such operation principles may be applied at any VECSEL wavelength through appropriate design of the relevant semiconductor structures, and inclusion of intracavity elements with low loss at the design wavelength.

Bibliography

[1] Tropper, A. C. & Hoogland, S. H. Extended cavity surface-emitting semiconductor lasers. *Progress in Quantum Electronics* **30**, 1–143 (2006).

[2] Dupriez, P. *et al.* High-power, single-mode picosecond fiber laser based on amplification of a passively mode-locked 1055-nm VECSEL. In *Conference on Lasers and Electro-Optics (CLEO)*, CThJ3 (Long Beach, California, USA, 2006).

Appendix A

Multilayer Calculations

The multilayer method used to calculate the properties of the VECSEL and SESAM structures described in this thesis is rigorously defined by Tropper et al [1]. A basic description of the method is included here for completeness, but the reader is directed to [1] for the thorough discussion.

Multilayer Calculation Theory

Consider a monochromatic lightwave propagating through a multilayer structure composed of N-1 homogeneous layers on an infinite substrate. At one interface inside the structure, located at position z_i between layers i and $i+1$ with refractive indices n_i and n_{i+1} respectively, the electric field can be written as:

$$E_i(z_i) = A_i^+ e^{ik_i z_i} + A_i^- e^{-ik_i z_i} \tag{A.0.1}$$

where $A_i^{\pm} e^{\pm ik_i z_i}$ is the forward/backward propagating wave with amplitude $A_i^{\pm}$, and wavenumber k_i at layer i for a given wavelength λ and an incident angle θ outside of the structure is given by:

$$k_i = \frac{2\pi}{\lambda} n_i cos\left(arcsin\left(\frac{n_0}{n_i} sin(\theta)\right)\right) \tag{A.0.2}$$

where n_0 is the refractive index of the incident medium.

The E-field and its derivative should be continuous at the interface resulting in the conditions:

$$A_i^+ e^{ik_i z_i} + A_i^- e^{-ik_i z_i} = A_{i+1}^+ e^{ik_{i+1} z_i} + A_{i+1}^- e^{-ik_{i+1} z_i} \tag{A.0.3}$$

$$k_i (A_i^+ e^{ik_i z_i} - A_i^- e^{-ik_i z_i}) = k_{i+1} (A_{i+1}^+ e^{ik_{i+1} z_i} - A_{i+1}^- e^{-ik_{i+1} z_i}). \tag{A.0.4}$$

In the structure, the 0th layer is the air-structure interface, and the Nth layer is the substrate. Therefore, the lightwave encounters N discontinuous interfaces with 2N unknowns related by 2N boundary equations of the form above. This system of equations can be incorporated into one matrix equation of the form **Mx=b**; in which **M** is a 2N $\times$ 2N matrix containing the phase factors $e^{\pm ik_i z}$, known from the structural and refractive index properties of the structure as described in chapter 2; **x** is a column vector containing the unknown e-filed amplitudes $A_i^{\pm}$; **b** is a column vector containing the known E-field amplitudes ($A_0^+ = 1$ and $A_N^- = 0$), with zeros in all other positions.

We introduce the notation $L_{ij}^{\pm} = e^{\pm ik_i z_j}$ and $K_{ij}^{\pm} = k_i e^{\pm ik_i z_j}$ for compactness, and the matrix equation takes the form:

$$\begin{pmatrix} L_{00}^- & -L_{10}^+ & -L_{10}^- & 0 & 0 & 0 & 0 & 0 & \dots & 0 \\ -K_{00}^- & -K_{10}^+ & K_{10}^- & 0 & 0 & 0 & 0 & 0 & \dots & 0 \\ 0 & L_{11}^+ & L_{11}^- & -L_{21}^+ & -L_{21}^- & 0 & 0 & 0 & \dots & 0 \\ 0 & K_{11}^+ & -K_{11}^- & -K_{21}^+ & K_{21}^- & 0 & 0 & 0 & \dots & 0 \\ 0 & 0 & 0 & L_{22}^+ & L_{22}^- & -L_{32}^+ & -L_{32}^- & 0 & \dots & 0 \\ 0 & 0 & 0 & K_{22}^+ & -K_{22}^- & -K_{32}^+ & K_{32}^- & 0 & \dots & 0 \\ \dots & \dots & \dots & \dots & \dots & \dots & \dots & \dots & \dots & \dots \\ \dots & \dots & \dots & \dots & \dots & \dots & \dots & \dots & \dots & \dots \\ 0 & 0 & 0 & 0 & 0 & \dots & 0 & L_{N-1N-1}^+ & -L_{N-1N-1}^- & -L_{NN-1}^+ \\ 0 & 0 & 0 & 0 & 0 & \dots & 0 & -K_{N-1N-1}^+ & -K_{N-1N-1}^- & K_{NN-1}^+ \end{pmatrix} \begin{pmatrix} A_0^- \\ A_1^+ \\ A_1^- \\ A_2^+ \\ A_2^- \\ A_3^+ \\ \dots \\ \dots \\ A_{N-1}^- \\ A_N^+ \end{pmatrix} = \begin{pmatrix} -L_{00}^+ \\ K_{00}^+ \\ 0 \\ 0 \\ 0 \\ 0 \\ \dots \\ \dots \\ 0 \\ 0 \end{pmatrix}$$

The solutions to the equation are found by inverting **M**, or, as in this thesis, using an LU decomposition method in an Igor programme written by S. Hoogland.

From this, the intensity distribution inside the structure can be achieved readily, aswell as the reflectivity, and other properties. Moreover, a source term may be added, allowing the structural effects on quantum well emission to be modelled as in [1].

Bibliography

[1] Tropper, A. C. & Hoogland, S. H. Extended cavity surface-emitting semiconductor lasers. *Progress in Quantum Electronics* **30**, 1–143 (2006).

Appendix B

VECSEL Cavity Design

The following is a Mathcad design program for a 4 mirror ML-VECSEL cavity used in this thesis. The ABCD matrix approach to Gaussian beam propagaton is used as described in [1, 2, 3].

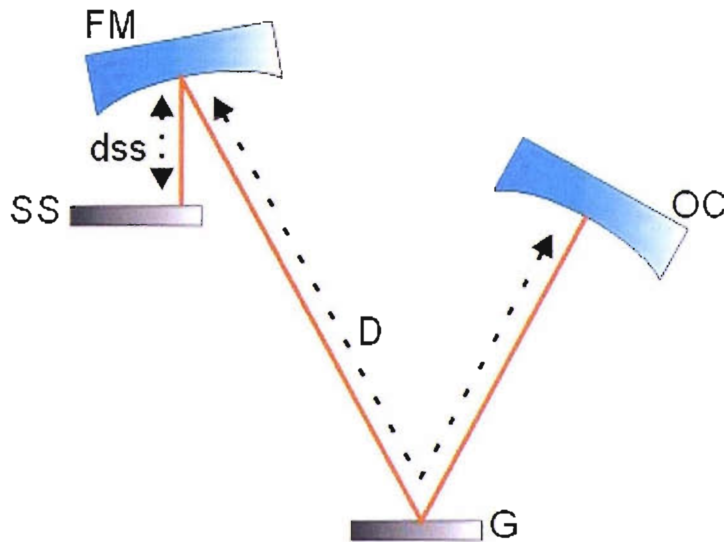

FIGURE B.1: Four mirror VECSEL cavity: G = VECSEL gain chip, OC = Output coupler, FM = SESAM focussng mirror, SS = SESAM, D = cavity long arm length (output coupler to SESAM focusing mirror distance), dss = distance from SESAM focusing mirror to SESAM.

~1GHz Z-cavity design for 1 μm ML-VECSEL

hb = Planck's constant/2π

cl = speed of light

Roc = radius of curvature of the output coupler

RFM = radius of curvature of the SESAM focusing mirror

ABCD transfer matrices

MLarm(D): matrix for free space propagation along distance D

MSarm(dss): matrix for free space propagation along distance dss

Mocx and *Mocy*: matrices in x and y planes for output coupling spherical mirror

Mfmx and *Mfmy*: matrces in x and y planes for SESAM focusing mirror including angular incidence.

Definition of units, constants and parameters (may be re-defined later in program):

$\mu s := 10^{-6} \cdot sec \quad \mu m := 10^{-6} \cdot m \quad hb := 6.64 \cdot 10^{-34} \cdot joule \cdot sec \quad cl := 3 \cdot 10^{8} \cdot m \cdot sec^{-1} \quad mW := 10^{-3}$

refractive index: $n := 1$

laser wavelength: $\lambda := 1.035 \cdot 10^{-3}$

Roc: $foc := \frac{50}{2}$ RFM: $ffm := \frac{25}{2}$

1/2 angle between 2 arms of VECSEL:

$\theta a := \frac{\pi}{180} \cdot 15$

1/2 angle between 2 arms of SESAM:

$\theta s := \frac{\pi}{180} \cdot 6$

Length of long arm: $D := 100$

Distance FM-SESAM: $dss := 20$

Definition of ABCD transfer matrices of cavity in x and y planes:

$$\mathrm{MLarm}(D) := \begin{pmatrix} 1 & D \\ 0 & 1 \end{pmatrix} \qquad \mathrm{MSarm}(dss) := \begin{pmatrix} 1 & dss \\ 0 & 1 \end{pmatrix}$$

$$\mathrm{Mocx} := \begin{pmatrix} 1 & 0 \\ \frac{-1}{foc} & 1 \end{pmatrix} \qquad \mathrm{Mocy} := \begin{pmatrix} 1 & 0 \\ \frac{-1}{foc} & 1 \end{pmatrix}$$

$$\mathrm{Mfmx} := \begin{pmatrix} 1 & 0 \\ \frac{-\cos(\theta s)}{ffm} & 1 \end{pmatrix} \qquad \mathrm{Mfmy} := \begin{pmatrix} 1 & 0 \\ \frac{-1}{ffm \cdot \cos(\theta s)} & 1 \end{pmatrix}$$

$$\mathrm{Mcavityx}(D, dss) := \mathrm{MSarm}(dss) \cdot \mathrm{Mfmx} \cdot \mathrm{MLarm}(D) \cdot \mathrm{Mocx} \cdot \mathrm{MLarm}(D) \cdot \mathrm{Mfmx} \cdot \mathrm{MSarm}(dss)$$

$$\mathrm{Mcavityy}(D, dss) := \mathrm{MSarm}(dss) \cdot \mathrm{Mfmy} \cdot \mathrm{MLarm}(D) \cdot \mathrm{Mocy} \cdot \mathrm{MLarm}(D) \cdot \mathrm{Mfmy} \cdot \mathrm{MSarm}(dss)$$

Calculation of stability of cavity as a function of dss

Stability zones (dss):

$$\mathrm{stabilityx}(D, dss) := \frac{\mathrm{tr}(\mathrm{Mcavityx}(D, dss))}{2}$$

$$\mathrm{stabilityy}(D, dss) := \frac{\mathrm{tr}(\mathrm{Mcavityy}(D, dss))}{2}$$

$$dss := 1.07 \cdot ffm, 1.0701 \cdot ffm .. 5 \cdot ffm$$

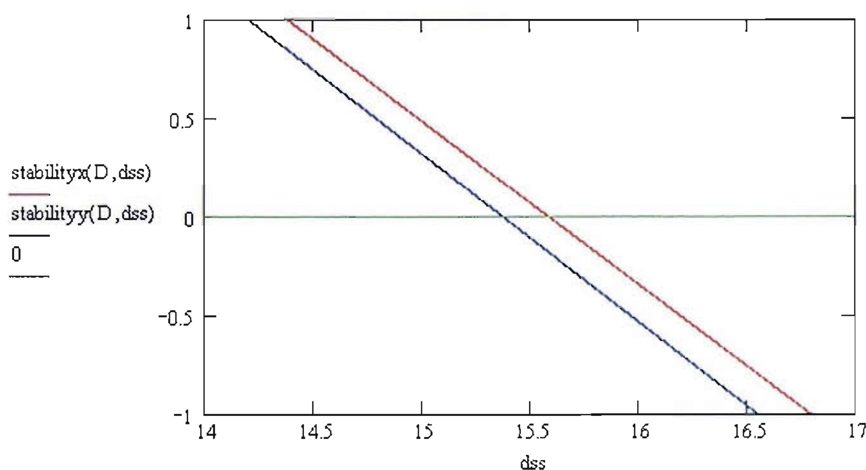

(Zero-pont is most stable)

Calculation of the mode waist size (ws) on the SESAM

Waist on SESAM:

$$wsxz(D,dss) := \mathrm{if}\left[\mathrm{Im}\left(\sqrt{\frac{-Mcavityx(D,dss)_{1,0}}{Mcavityx(D,dss)_{0,1}}}\right) = 0, \sqrt{\frac{\lambda}{\pi}}\cdot\left(\frac{-Mcavityx(D,dss)_{0,1}}{Mcavityx(D,dss)_{1,0}}\right)^{\frac{1}{4}}, 0\right]$$

$$wsyz(D,dss) := \mathrm{if}\left[\mathrm{Im}\left(\sqrt{\frac{-Mcavityy(D,dss)_{0,1}}{Mcavityy(D,dss)_{1,0}}}\right) = 0, \sqrt{\frac{\lambda}{\pi}}\cdot\left(\frac{-Mcavityy(D,dss)_{0,1}}{Mcavityy(D,dss)_{1,0}}\right)^{\frac{1}{4}}, 0\right]$$

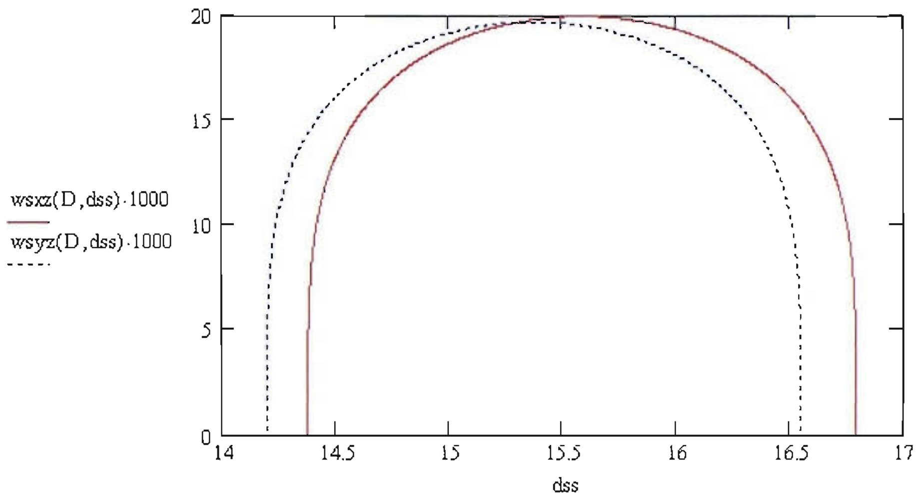

Showing the waist size on the SESAM as a function of the distance from the SESAM to the focusing mirror.

Calculation of the mode waist size (ws) on the gain chip

Waist laser in long arm FM-OC:

$$wxz(D,dss) := \mathrm{if}\left[\mathrm{Im}\left(\sqrt{\frac{-Mcavityx(D,dss)_{1,0}}{Mcavityx(D,dss)_{0,1}}}\right) = 0, \frac{wsxz(D,dss)}{\sqrt{\left(\frac{dss}{\frac{ffm}{\cos(\theta s)}} - 1\right)^2 + \left(\frac{\pi \cdot wsxz(D,dss)^2}{\lambda \cdot \frac{ffm}{\cos(\theta s)}}\right)^2}}, 0\right]$$

$$wyz(D,dss) := \mathrm{if}\left[\mathrm{Im}\left(\sqrt{\frac{-Mcavityy(D,dss)_{1,0}}{Mcavityy(D,dss)_{0,1}}}\right) = 0, \frac{wsyz(D,dss)}{\sqrt{\left(\frac{dss}{ffm \cdot \cos(\theta s)} - 1\right)^2 + \left(\frac{\pi \cdot wsyz(D,dss)^2}{\lambda \cdot ffm \cdot \cos(\theta s)}\right)^2}}, 0\right]$$

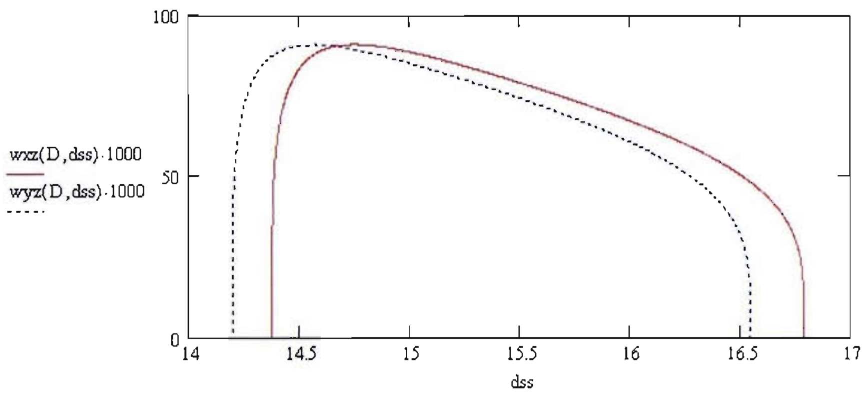

A suitable dss may be chosen to provide a waist radius at the gain chip that is mode matched with the pump spot (60 μm).

Bibliography

[1] Kogelnik, H. & Li, T. Laser beams and resonators. *Applied Optics* 5, 1550–1567 (1966).

[2] Hanna, D. C. Astigmatic gaussian beams produced by axially asymmetric laser cavities. *IEEE Journal of quantum electronics* 5, 483–488 (1969).

[3] Svelto, O. *Principles of Lasers* (Plenum Press, New York, 1998), fourth edn.

Appendix C

Selected Publications

1. Tropper, A. C., Foreman, H. D., Garnache, A., Wilcox, K. G. & Hoogland, S. H. Vertical-external-cavity semiconductor lasers. Journal of Physics D: Applied Physics **37**, *R75R85* (2004).

2. Foreman, H. D. et al. High power femtosecond source based on passively mode-locked 1055-nm VECSEL and Yb-fibre power amplifier. In Advanced Solid State Photonics (ASSP) 2006 (Lake Tahoe, USA, 2006).

3. Wilcox, K. G., Foreman, H. D., Roberts, J. S. & Tropper, A. C. Timing jitter of 897 MHz optical pulse train from actively stabilised passively modelocked surface emitting semiconductor laser. IEEE Journal of Quantum Electronics **42**, *159160* (2006).

4. Dupriez, P., Malinowski, A., Sahu, J. K., Jeong, Y., Nilsson, J., Richardson, D. J., Foreman, H. D., Wilcox, K. G., Tropper, A. C., Morier-Genoud, F., Keller, U., and Roberts, J. S. High-power, single-mode picosecond fiber laser based on amplification of a passively mode-locked 1055-nm VECSEL. In Conference on Lasers and Electro-Optics (CLEO), CThJ3 (Long Beach, California, USA, 2006).

5. Dupriez, P., Finot, C., Malinowski, A., Sahu, J. K., Nilsson, J., Richardson, D. J., Wilcox, K. G., Foreman, H. D. & Tropper, A. C. High-power, high repetition rate picosecond and femtosecond sources based on Yb-doped fiber amplification of VECSELs. Optics Express **14** (21), *9611-9616* (2006)

6. Wilcox, K. G., Rutz, F., Wilk, R., Foreman, H. D., Roberts, J. S., Sigmund, J., Hartnagel, H. L., Koch, M. and Tropper, A. C. Terahertz imaging system based on LT-GaAsSb antenna driven by all-semiconductor femtosecond source. Electronics Letters **42** (20), (2006).